STRUCTURAL & ELECTRONIC PROPERTIES OF SOME EARLY TRANSITION METAL OXIDES

C. M. Jewell

The Royal Institution of Great Britain
& University College, London

Thesis submitted for the degree of Doctor of Philosophy from the
University of London
2003

ProQuest LLC
789 East Eisenhower Parkway
P.O. Box 1346
Ann Arbor, MI 48106-1346

Abstract

Low-dimensional spin systems with $S = ½$ and a singlet ground state attract intensive research efforts because of the quantum nature of their ground state. Since the discovery of the singlet plaquette CaV_4O_9 compound more attention has been paid to chemical analogues with $S = ½$, V^{4+} (d^1) ions. For example, the V_2O_5 network exhibits the characteristics of layered and crystallographic shear structures and there is a large vanadium oxide bronze family, $M_xV_2O_5$ (M = alkali, alkaline earth metals), which shows several original [V_2O_5] networks. For this reason, the atomic architectures of V_2O_5 and its derivatives provide a stage where various lower-dimensional quantum critical phenomena can be realised.

Compounds in the series $Li_xV_2O_5$ were synthesised via soft chemistry methods and characterised structurally and magnetically via high-resolution x-ray and neutron diffraction and magnetisation measurements using a SQUID magnetometer. Additional weaker peaks observed in certain of the diffraction patterns suggested the occurrence of charge ordering of vanadium ions in an incommensurately modulated superstructure for some of the ε-$Li_xV_2O_5$ and ε'-$Li_xV_2O_5$ phases. Having discovered a possible magnetic transition ($T_f \sim 25$ K) in one of these dilute-spin phases, $Li_{0.50}V_2O_5$, believed to be associated with the low-dimensional, chain-like arrangement of the V^{4+} ($S = ½$, d^1) cations over the non-magnetic V^{5+} ($S = 0$, d^0) network, a local probe, μSR, was applied to investigate its ground state and the ground states of other members of the series $Li_xV_2O_5$ with $x = 0.55$, 0.64 and 0.72 which also exhibit interesting magnetic behaviour. Lack of oscillation in the μSR data revealed the absence of any long-range magnetic order for $Li_{0.50}V_2O_5$, $Li_{0.55}V_2O_5$, $Li_{0.64}V_2O_5$, and $Li_{0.72}V_2O_5$, supportive of a true one-dimensional ground state, suggesting the formation of domains of one-dimensional antiferromagnetic chains, consistent with the Bonner-Fisher model for low-dimensional magnetic behaviour which provided a good fit to the SQUID data collected.

Acknowledgements

Firstly many thanks must go to my supervisor **Mark Green** for all his help and advice over the past four years. Thank you too **"The Green Group"** – especially **Donna** for hot desk room solidarity (and her amazing brain power) and **Tom** for many useful discussions and suggestions.

On a technical note, thanks must also go to Richard Ibberson at HRPD, Philip King at EMU and Wouter Van Beek and Hermann Emerich at BM1B for all their help collecting data, and to Alex Lappas for helping to collect and interpret the EMU data.

Thanks to my family – **Dad, Emma, Mike, Stephen, Helen, Margaret, Karen** and **Robin** for all their encouragement, general interest and for never failing to be impressed when I needed to feel impressive; also thank you **Anne & Grant** and the rest of the Castleberg family for a great summer over in Santa Barbara while I was at UCSB. Warmest thanks must go to **Uncle Jim** for his proofreading services and I must also say a very grateful thank you to the trustees of the H. L. & M. T. Jewell discretionary settlement for all their help over the last five years.

THANK YOU to all my friends, especially **Nens, Gemma, Jane, Laura, Kate, Katie,** the members of **Saracens WRFC, UCLUWRFC** and all the other people who made it fun.

Finally, thanks must go to **Holly** for letting me ramble about chemistry and generally looking after me...

This thesis is dedicated to **Mum**: I hope she would have been proud.

"Do not stand at my grave and weep;
I am not there. I do not sleep.
I am a thousand winds that blow.
I am the diamond glints on snow.
I am the sunlight on ripened grain.
I am the gentle autumn rain.
When you awaken in the morning's hush
I am the swift uplifting rush
Of quiet birds in circled flight.
I am the soft stars that shine at night.
Do not stand at my grave and cry;
I am not there. I did not die."

Anon.

Contents

Table Captions

Table Captions

Chapter One

Introduction

This chapter provides an overview of the chemistry relevant to this thesis. Intercalation chemistry is introduced (section 1.1), and some current aspects of the electronic and magnetic behaviour of transition metal oxides such as superconductivity (section 1.1.2) and charge ordering (section 1.2) are discussed. Finally, the structure and notable features of vanadium oxides are reviewed (section 1.3), with particular emphasis on the literature and reported structures of $Li_xV_2O_5$; the system investigated in this project (section 1.4).

1.1 Intercalation

Intercalation reactions have been well documented since the reaction of graphite with potassium vapour [1] sparked a new wave of investigations in this area. Typical intercalation reactions are reversible, occurring around room temperature and conserving the morphology of the host lattice, which may range from three-dimensional framework structures to zero-dimensional molecular lattices. A good example is the reaction of lithium with layered titanium disulphide (TiS_2) as shown in *equation 1.1*:

$$Li \rightleftharpoons Li^+ + e^- + TiS_2 \rightleftharpoons Li^+[TiS_2]^-$$

Equation 1.1

TiS_2 layers are reduced by lithium metal and the lithium cations formed are taken up into vacant interlayer sites as charge compensation for the negative layer charge caused by electron transfer. The final product is slightly expanded in the direction perpendicular to the layers [2]. Intercalation reactions with layered host lattices occur more widely, probably due to the ability of layered structures to adjust their interlayer separation to cater for the geometry of the guest molecule, and therefore offer greater opportunity than other host lattice dimensionalities. An example of this would be the plethora of species successfully intercalated into double hydroxide systems, offering many new applications in areas such as drug delivery [3-7]. Layered intercalates are characterised by strong intralayer bonding and weaker interlayer interactions. The layers may be electrically neutral, as found in graphite for example, or they may be charged, for example negatively charged titanate layers in $K_2Ti_4O_9$. Neutral layered systems have a connected network of empty lattice sites between the layers, with predominantly van der Waals bonding, whereas the layers in charged systems are held together by electrostatic forces and the interlayer sites are partially or completely filled

by ions or a combination of ions and solvent molecules. The negative layer system, $K_2Ti_4O_9$, for example, intercalates a molecular ion, 1,1'-dimethyl-4,4'-bipyridinium [8, 9], which carries a double positive charge; whereas graphite intercalates both negatively charged species such as the molecular ion HSO_4^- [8, 9], as well as positively charged species such as alkali cations like K^+.

Intercalation can affect the chemical and electronic properties of the guest species and/or the host lattice: the potential for tailoring these effects to produce specific properties makes these reactions relevant to a broad range of applications. For example: intercalation of alkali metals or hydride ions into tungsten oxide (WO_3) to form tungsten bronzes with electrochromic interactions [8]; intercalation of oxygen into $YBa_2Cu_3O_x$ and other perovskite-related cuprates so as to optimise T_C of superconductors [8]; intercalation and deintercalation of lithium into $LiMn_2O_4$ or Li_xCoO_2 cathode materials in solid state lithium batteries [8]. These examples will be discussed in more detail hereafter.

1.1.1 Tungsten Bronzes

Intercalation of alkali metal ions into tungsten oxide, WO_3, produces a system in which there are interstitial cations of one element and mixed valency cations of another element, as shown by *equation 1.2*:

$$xK^+ + WO_3 + xe^- \rightarrow K_xW^{6+}{}_{1-x}W^{5+}{}_xO_3.$$

Equation 1.2 – Intercalation of potassium into tungsten oxide [8]

White WO_3 has a perovskite structure: a framework of corner-sharing WO_6 octahedra, shown in *figure 1.1*, forming a three-dimensional network of interconnected channels along which alkali cations can migrate.

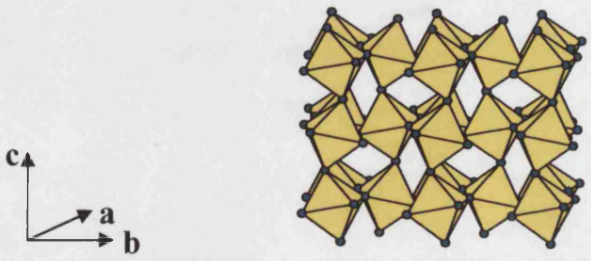

Figure 1.1 – Structure of Tungsten Oxide, WO_3.

On intercalation of alkali metal cations, electrons enter the *5d* bands of tungsten, which are empty in $W(d^0)O_3$, and the material darkens due to absorption of light associated with *d-d* transitions. The extra electrons produce metallic conductivity rather than the insulating behaviour of WO_3. The speed and reversibility of the intercalation reaction makes possible a rapid and reversible colour change: these materials find applications in thin film electrochromic devices and glass coatings.

1.1.2 Superconductivity

Superconductors have several unique features including zero resistance to the flow of electrical current, implying indefinite flow of a "supercurrent", and "perfect diamagnetism", shown by the expulsion of a magnetic field below the critical field H_C. The properties of superconductors have great potential in applications of electricity supply, shielding magnetic fields and transport. Discovery of superconductivity in mercury in 1911 [8], has led to the observation in many metals of such phenomena, including several early transition metals such as lanthanum, titanium, vanadium, molybdenum and niobium [10-12]. Prior to 1986, the highest critical temperature, T_C, for the superconductor to metal transition was just over 20K, in the alloys Nb_3Ge and Nb_3Sn. The discovery of superconductivity in a La-Sr-Cu-O phase with a T_C of about 36K [10, 13] was followed by the synthesis of $YBa_2Cu_3O_7$ (T_C = 93K [14]) and other complex cuprates of Bi, Tl and Hg with T_C values up to 135K [8, 15].

In these so-called high T_C superconductors it is mixed valency copper cations that are seen as the key to superconducting behaviour. Creation of mixed valency cations may be associated with insertion of interstitial anions into a structure; in $YBa_2Cu_3O_x$, for example, the oxidation state of copper is dependent upon the oxygen content, x: mixed Cu^+ and Cu^{2+}, when $x = 6$; entirely Cu^{2+}, for $x = 6.5$; a mixture of Cu^{2+} and Cu^{3+}, when $x = 7$. This may be regarded as an intercalation reaction where extra oxygen is introduced into the $x = 6$ structure, causing oxidation of copper and transformation in the electronic properties from a semiconductor to a superconductor for $x = 7$.

There are two copper sites in $YBa_2Cu_3O_x$, as shown in *figure 1.2*. One site, nominally Cu^{2+}, is square pyramidally coordinated by oxygen atoms for $6 \leq x \leq 7$, while the second copper site is sensitive to oxidation, having linear coordination when $x = 6$, as Cu^+, changing to square planar coordination as extra oxygen is intercalated and it is

oxidised to Cu^{2+}. This oxidation also causes a change from a tetragonal to an orthorhombic unit cell, as the four-fold rotation axis parallel to the *c*-axis that is present when $x = 6$ is reduced to a two-fold axis when oxygen is intercalated at the 0, ½, 0 position.

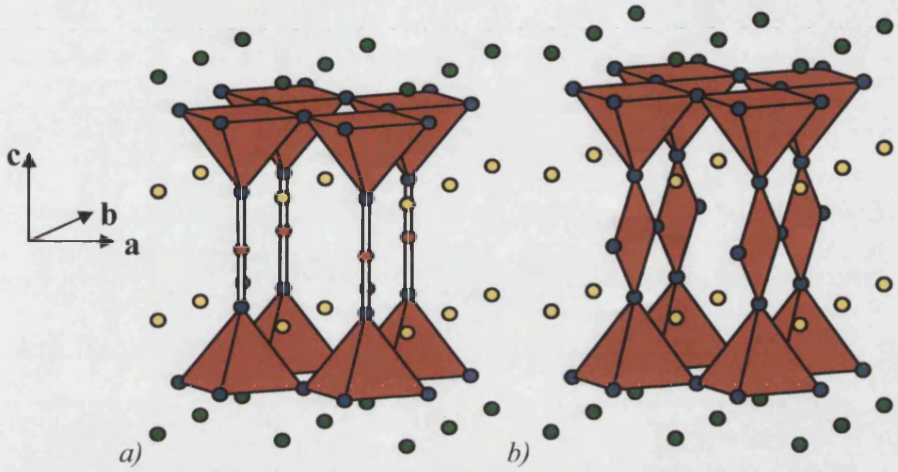

Figure 1.2 – Structures of a) $YBa_2Cu_3O_6$ and b) $YBa_2Cu_3O_7$ [8]. Copper ions are shown in red, oxygen in blue, barium in green and yttrium in yellow.

The cuprate superconductors are also good examples of the way in which electronic properties may be strongly affected by the dimensionality. For example, T_C for the series $TlBa_2Ca_{n-1}Cu_nO_{3n+2}$ increases as the connectivity between the Cu-O layers increases: for n = 1, T_C = 80K; for n = 2, T_C = 108K and for n = 3, T_C = 125K. The structures of this series are shown in *figure 1.3*.

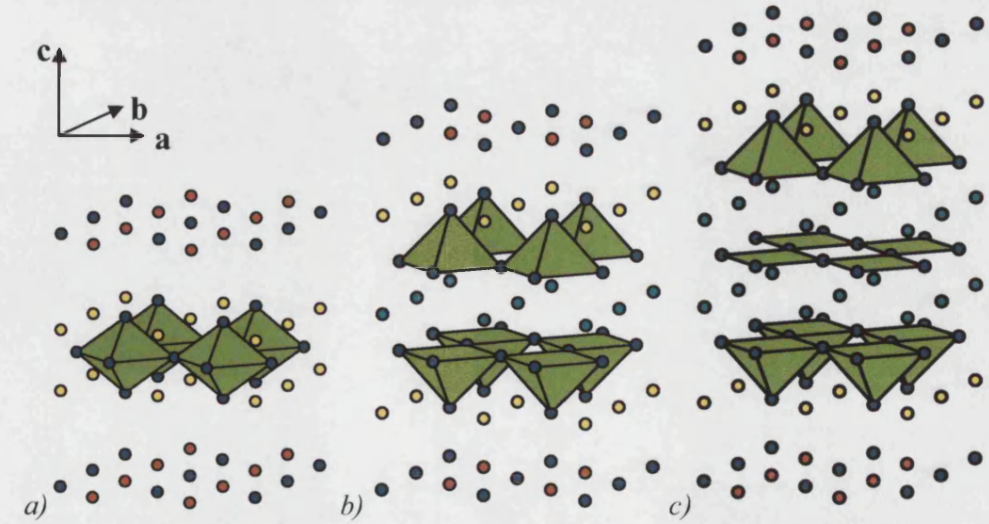

Figure 1.3 – Structure of the n = 1, 2 and 3 members of the $TlBa_2Ca_{n-1}Cu_nO_{3n+2}$ series: a) $TlBa_2CuO_5$; b) $TlBa_2CaCu_2O_7$; c) $TlBa_2CaCu_3O_9$.. Copper atoms are shown in green, oxygen in blue, thallium in red, barium in yellow and calcium in light blue.

1.1.3 Lithium Batteries

There is currently huge interest in developing advanced lithium batteries for applications such as mobile telephones, laptop computers and zero emission vehicles.

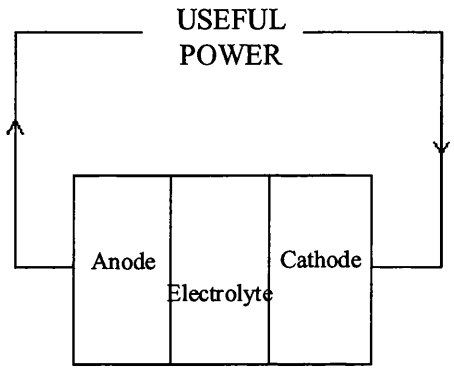

Figure 1.4 – Schematic of a secondary lithium battery [8].

For optimal cell voltage, an anode of high lithium activity is needed, ideally lithium metal. To this goal, various lithium-based alloys and lithium-carbon intercalation compounds have been investigated [16-18]. Electrolytes must have high lithium ion conductivity, for example a lithium salt such as $LiCF_3$-COO, $LiClO_4$ or $LiPF_6$ dissolved in a non-aqueous solvent like propylene carbonate, or a polar polymer like poly(ethylene oxide), PEO [19-21].

Candidate cathodes in lithium batteries are all intercalation host structures that have empty channels: structures capable of supporting lithium ions, and a mixed valence species in the framework that is able to accept and release electrons. The first materials to be considered [22] were layered chalcogenides such as TiS_2, which accepts Li^+ into empty layers of octahedral sites separating TiS_2 sheets, with an accompanying reduction of titanium to give mixed valence Ti^{4+} and Ti^{3+} in the product. Since then, materials such as $LiCoO_2$ and $LiMn_2O_4$ (*equations 1.3-4*) have been investigated and are used as cathodes, although both have disadvantages [23-25]. Cobalt is relatively expensive and toxic, while conversion of Mn^{4+} to Mn^{3+} involves a structural distortion due to the Jahn-Teller effect in Mn^{3+} octahedra, which causes deterioration in the electrolyte-cathode interfacial integrity and consequently loss in battery performance on cycling [8].

$$LiCoO_2 - xLi^+ - xe^- \rightarrow Li_{1-x}Co^{3+}{}_{1-x}Co^{4+}{}_xO_2$$

Equation 1.3 – Deintercalation of lithium ions from $LiCoO_2$

$$LiMn_2O_4 - xLi^+ - xe^- \rightarrow Li_{1-x}Mn^{3+}_{1-x}Mn^{4+}_{1+x}O_2$$

Equation 1.4 – Deintercalation of lithium ions from $LiMn_2O_4$

It can be seen from these examples that intercalation with transition metal oxides as host lattice can produce systems with interesting electronic properties, due to their ability to accept and release electrons to guest molecules to produce mixed valency. For some early transition metal oxides, there is also potential for low-dimensional magnetic behaviour, where a d^0 configuration is reduced through intercalation to a mixed d^0/d^1 system. This mixture of magnetic and non-magnetic ions raises the possibility of low-dimensional magnetic behaviour through charge ordering in suitable intercalated systems.

1.2 Charge Ordering and Low Dimensionality

The coexistence of ions with distinct valences is observed in some transition metal compounds, for example Fe^{2+} and Fe^{3+} in Fe_3O_4, V^{4+} and V^{5+} in NaV_2O_5, Mn^{3+} and Mn^{4+} in $La_{1-x}Sr_xMnO_3$, and Cu^{2+} and Cu^{3+} in $Sr_{14-x}Ca_xCu_{24}O_{41}$. Rare earth compounds based on Sm, Eu, Tm and Yb ions frequently exhibit a mixed divalent and trivalent state. In these mixed-valence compounds, allowance must be made for the charge degrees of freedom of the 3d or 4f ions in addition to the spin and orbital degrees of freedom when considering the magnetic behaviour. A distinction can be made between homogenously and inhomogenously mixed-valence compounds. In the former, there is essentially a single ion property where the magnetic ion hybridises with the sea of conduction electrons. Examples of this type of mixed-valency include rare-earth materials such as SmS, TmSc, SmB_6 and $YbInCu_4$ [26-28]. In the case of inhomogenously mixed-valence compounds, the 3d or 4f electrons can hop between the magnetic ions with different valences, assisted in some cases by thermal motion. Below a transition temperature there is a distinct charge ordering [29], where different oxidation states are localised onto crystallographically distinct sites. The causes of this ordering include a range of electronic and structural factors such as electrostatic forces, resulting in distinct oxidation states adopting different geometries despite having the same coordination. It can be difficult to detect charge ordering with direct methods, but its occurrence can significantly influence the physical properties of a material. In particular, where the ordered ions are a mixture of magnetic and non-magnetic ions, this can influence the magnetic behaviour and is capable of producing low-dimensional

magnetic behaviour, as ordering of magnetic ions onto a distinct site may allow correlation or ordering of spins to occur, leading to novel magnetic behaviour such as that observed in $Nb_{12}O_{29}$ [30, 31] and NaV_2O_5 [32, 33] discussed in detail later. True low-dimensional behaviour is produced by having chains of magnetically active atoms separated from one another by large distances; hence materials containing bulky organic ligands often give the most attractive low-dimensional properties as the interchain interactions are much smaller than the intrachain interactions. It is more difficult to achieve extensive separation between magnetic chains in condensed phases, making true low-dimensional character much more rare. However, condensed inorganic oxides have been found to exhibit comparable low-dimensional properties to those observed in organometallic compounds through charge ordering in the structure, as will be exemplified in the following sections.

1.2.1 Fe_3O_4

Magnetite, Fe_3O_4, has an inverse spinel structure, as shown in *figure 1.5*, in which one third of the iron ions are tetrahedrally coordinated with four oxygen ions and the remaining two thirds are octahedrally coordinated with six oxygen ions. The tetrahedral A sites are occupied by Fe^{3+} ions, and the octahedral B sites are occupied by a mixture of Fe^{3+} and Fe^{2+} ions. The formula may be rewritten as $[Fe^{3+}]_{tet}[Fe^{2+}Fe^{3+}]_{oct}O_4$.

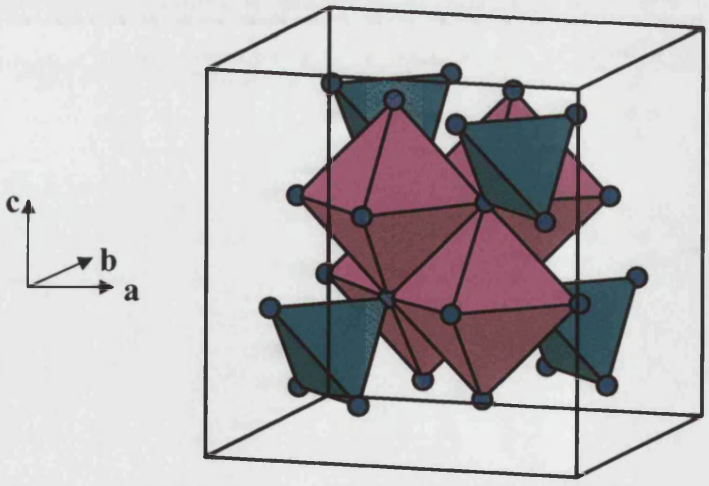

Figure 1.5 – Polyhedra in Fe_3O_4, tetrahedral in light blue containing Fe^{3+} ions, octahedra in pink containing mixture of Fe^{3+} and Fe^{2+} ions.

The metal-insulator transition, known as the Verwey transition, is observed in magnetite at $T_{CO} \approx 124K$ and is probably the first experimental realisation of the charge-ordering

phenomenon [34, 35]. There is an increase in electrical resistivity of two orders of magnitude on going from the high temperature phase to the low temperature phase at T_{CO} [36]. The electrical conduction and the Verwey transition occur on the B site sublattice. Above T_{CO} there is electron hopping in the B sites, but below the Fe^{2+}-Fe^{3+} ions order on the octahedral sites. Verwey proposed a model for the charge ordering of alternating chains of Fe^{2+} and Fe^{3+} cations along the [110] direction, shown in *figure 1.6*, however, this has not been verified by the neutron scattering studies made by Fujii *et al.* [37] and recent x-ray scattering experiments give a confusing picture of the charge ordering below the Verwey transition: one resonant x-ray experiment gives no indication of charge ordering below T_{CO} [38], while two other similar experiments do show charge ordering phenomena [39, 40]. The latter proposes a charge order on the B sites that differs from the model proposed by Verwey. These contradictory results demonstrate the complexity of charge ordering, and the difficulty of studying it with direct methods.

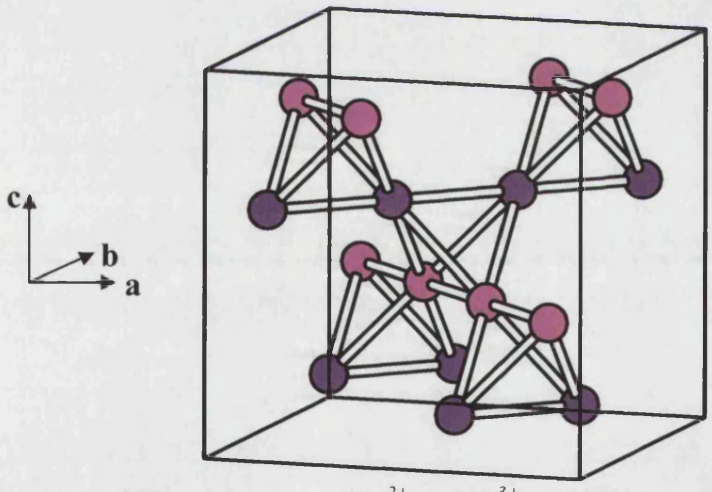

Figure 1.6 – Ordered structure of Fe^{2+} and Fe^{3+} at the B sites in inverse spinel Fe_3O_4 proposed by Verwey [34].

1.2.2 $La_{1-x}Sr_xFeO_3$

One end compound in this series, $LaFeO_3$, $x = 0$, is an antiferromagnetic insulator with a d^5 configuration of iron, characterised by high Neél temperature, $T_N = 738K$. The other end, $SrFeO_3$, $x = 1$, is an antiferromagnetic metal with $T_N = 134K$. The solid solution system, $La_{1-x}Sr_xFeO_3$, is antiferromagnetic with a Neél temperature that decreases with doping level, x. For $x > 0.1$, above T_N the material is semiconducting or conducting, while below T_N there is a steep increase in resistivity and insulating behaviour in the

antiferromagnetic phase, at least for $x \leq 0.7$. For $x \approx 0.67$ the resistivity increases abruptly at approximately 207K, due to simultaneous charge and spin ordering in a superlattice structure [36, 41, 42] as shown in *figure 1.7*. The charge disproportionation at $x \approx 0.67$ was first observed by Mössbauer spectroscopy [43], which showed two kinds of iron sites with nominal charges Fe^{3+} and Fe^{5+} in the ratio 2 : 1. The Fe^{5+} valence is unusual, but this valency and the ordering of iron sites were confirmed by neutron scattering measurements [44]. The structural change of the lattice upon charge ordering was studied using electron diffraction [45]. In this case, change in the physical properties (resistivity) is directly linked to charge ordering in the sample, which has been established using neutron and electron diffraction [36].

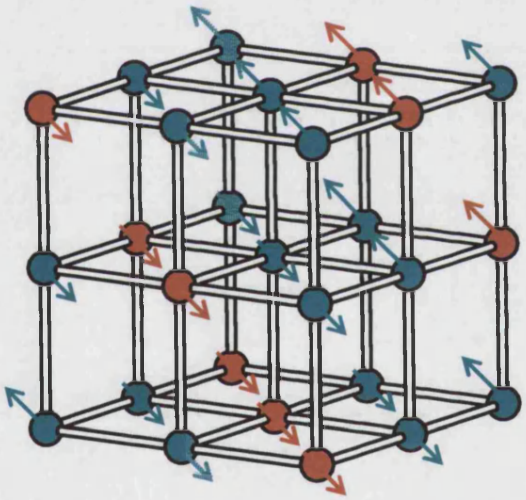

Figure 1.7 – Charge and spin ordering in $La_{0.33}Sr_{0.67}FeO_3$ [36]. Fe^{3+} shown in blue, Fe^{5+} shown in red.

1.2.3 $Sr_{14-x}Ca_xCu_{24}O_{41}$

$Sr_{14}Cu_{24}O_{41}$ has a composite structure made up of alternating layers of Cu_2O_3 spin ladders and CuO_2 spin chains separated by layers of strontium atoms. A spin ladder is somewhere between a one-dimensional magnet and a two-dimensional magnet, and is composed of spin chains which have an interchain coupling of comparable strength to the intrachain coupling [46]. Good examples of spin ladders include $SrCu_2O_3$, $La_{1-x}Sr_xCuO_{2.5}$ and $Sr_2Cu_3O_5$, shown in *figures 1.8-9*. The system $Sr_{n-1}Cu_{n+1}O_{2n}$ with odd n is a $\frac{1}{2}(n+1)$-leg spin ladder due to the strips of a CuO_2 square lattice with $\frac{1}{2}(n+1)$ Cu^{2+} ions across their width that make up the structure. Theoretical calculations predict that

even-leg ladders have a ground state with spin singlet pairs and the first excited state is separated by a spin gap energy, while odd-leg ladders are gapless [47], and this assertion is supported by the results of neutron and μSR experiments [48, 49].

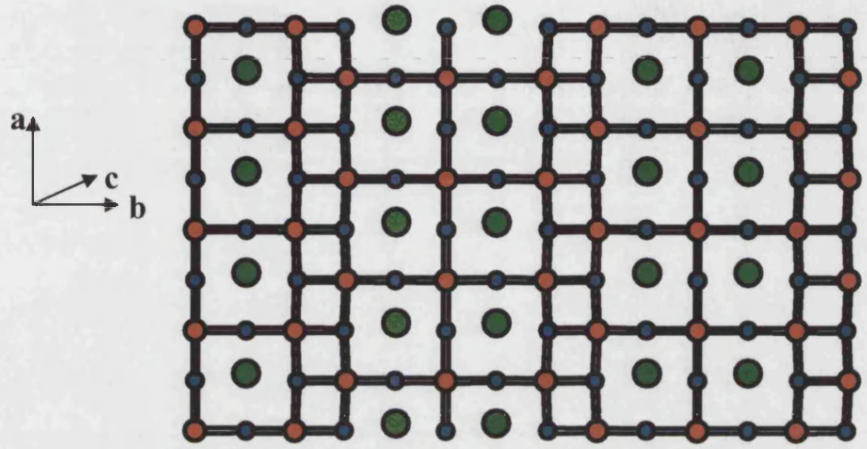

Figure 1.8 – Three-leg spin ladder $Sr_2Cu_3O_5$, strontium in green, copper in red, oxygen in blue.

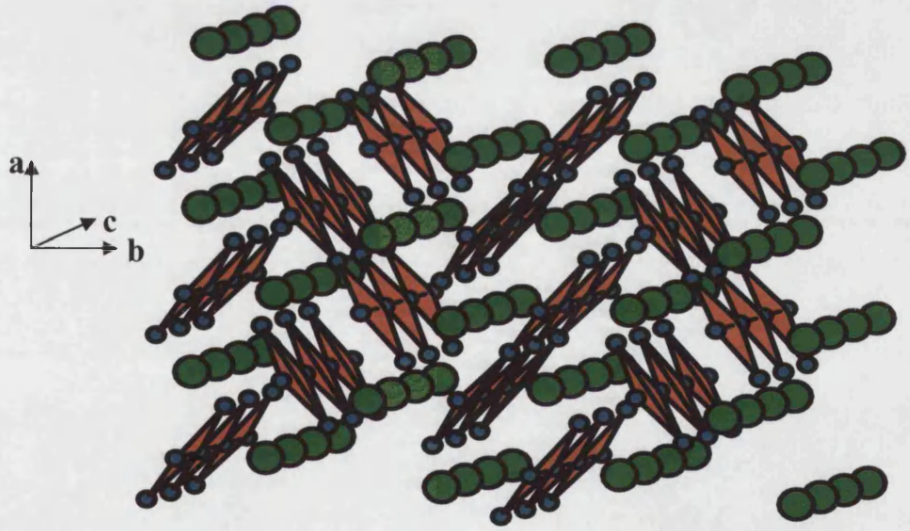

Figure 1.9 – $La_{1-x}Sr_xCuO_{2.5}$ two-leg spin ladder.

The "phone number" compound, $Sr_{14}Cu_{24}O_{41}$ can be doped easily and the hole-doped phases, $Sr_{14-x}Ca_xCu_{24}O_{41}$, become superconducting under pressure. The potential for superconductivity is one of the reasons for interest in spin ladders. The layered structure of alternating Cu_2O_3 and CuO_2 sheets separated by strontium and calcium layers is shown in *figure 1.10*.

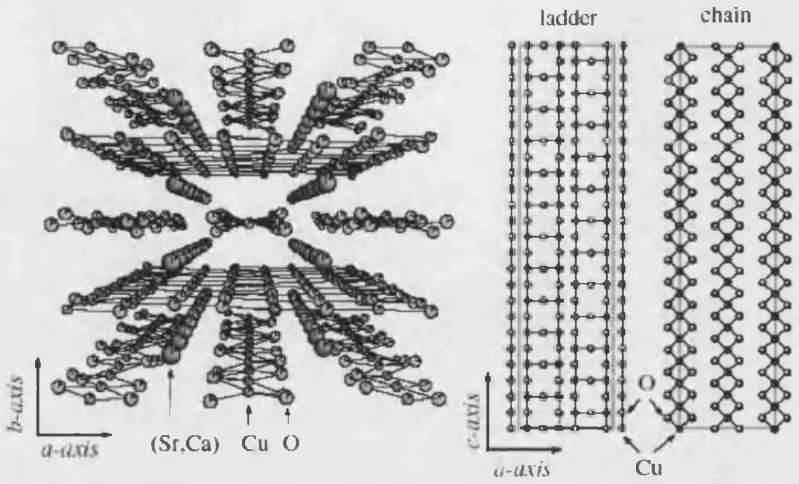

Figure 1.10 – Left figure shows the crystal structure of $Sr_{14-x}Ca_xCu_{24}O_{41}$ viewed in perspective along the c-axis. Right figure shows the crystal structure of two-leg ladder and chain viewed in perspective along the b-axis [50].

The Cu_2O_3 layers consist of two-leg spin ladders. The approximately 180° copper-oxygen-copper bonds give rise to a strong antiferromagnetic-type superexchange coupling between the copper spins along the legs and rungs. The CuO_2 planes are composed of spin chains where copper is four-coordinated by oxygen in a square planar arrangement, forming CuO_4 plaquettes. These share edges to make up chains.

Independent of the calcium concentration, the average copper valence in $Sr_{14-x}Ca_xCu_{24}O_{41}$ is $Cu^{2.25+}$; in other words, the compound is intrinsically hole-doped. Previous neutron diffraction and x-ray scattering experiments [51] have shown that in $Sr_{14}Cu_{24}O_{41}$ the holes are located solely in the chains, producing a well-defined charge ordered alternating dimer chain structure with six holes per formula unit, where one formula unit consists of a chain ten copper ions in length.

In an alternating chain there are two spin-spin interactions, as shown in *figure 1.11.*

Figure 1.11 – Exchange interactions in an alternating chain.

In this case the interactions are intra-dimer and inter-dimer interactions, and for the doped phase $Sr_{2.5}Ca_{11.5}Cu_{24}O_{41}$, these have been found to be antiferromagnetic inter-dimer and ferromagnetic intra-dimer interactions [52]. The alternation constant, α, has been calculated to be $\alpha = 0.1$ [53].

Doping with calcium for strontium would not be expected to alter the concentration of holes since the two elements are isovalent. However, neutron diffraction measurements [54] have shown that calcium substitution distorts the crystal structure in such a way as to bring oxygen atoms into a position directly below some of the copper atoms in the ladder layers, providing a possible path for holes to migrate between the two layers. It is believed the application of pressure further distorts the structure with a corresponding increase in hole migration to the ladders, with superconductivity occurring at a critical hole concentration on the ladders [29, 53]. Thus the partial destruction of charge ordering in the chains and their action as a charge reservoir for the spin ladders is linked to superconductivity under pressure in the highly doped phases.

1.2.4 $La_{2-x}Sr_xNiO_4$

Introduction of strontium in place of lanthanum in La_2NiO_4 is equivalent to the introduction of positive "holes" in the structure; for certain doping levels, cooperative ordering of holes and nickel spins is observed [36]. When $0.2 \leq x < 0.5$, the system is semiconducting below room temperature and metallic above 600K, but for $x = {}^1/_3$ the resistivity increases sharply at 240K, indicative of a charge ordering transition. A similar, weaker, effect is apparent at 340K for $x = ½$, suggesting it also undergoes a charge ordering transition around this temperature [55]. Substitution with isovalent cations, for example replacement of strontium with barium or calcium and replacement of lanthanum with neodymium, have no effect on the charge ordering transition, indicating that the transition is stabilised by the commensurate value of the hole number. In other words, charge ordering is only observed for a rational doping of Ni^{3+}: values of x such as 1, ½ or ${}^1/_3$. The ordering leads to the formation of "charge stripes", and some examples for different doping levels are shown in *figure 1.12*. This ordered stripe arrangement has been confirmed by the observation of superlattice spots in electron diffraction [55, 56] and by more recent neutron diffraction experiments [57].

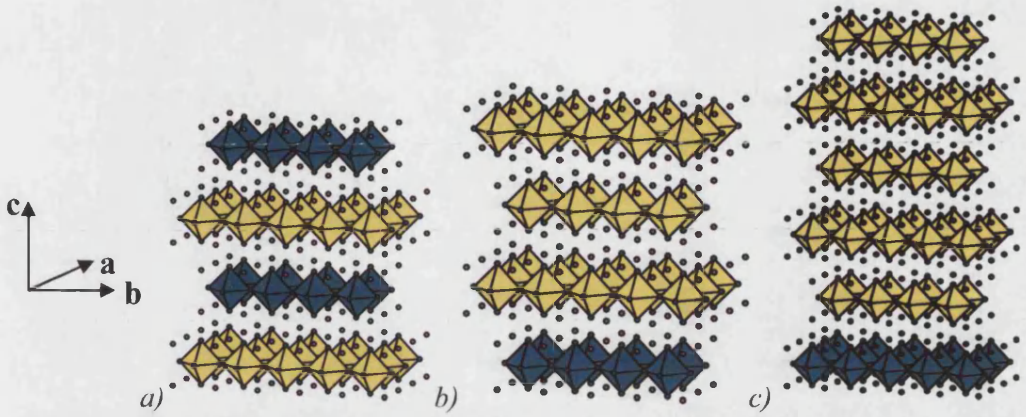

Figure 1.12 – Different doping levels of $La_{2-x}Sr_xNiO_4$, a) x = 1; b) x = 0.5; c) x = 0.33. $Ni^{2+}O_6$ octahedra are shown in yellow and $Ni^{3+}O_6$ octahedra are shown in blue.

1.2.5 $R_{1-x}A_xMnO_3$

It has recently been found that certain distorted perovskite manganates, $R_{1-x}A_xMnO_3$, including $La_{1-x}Sr_xMnO_3$, $Nd_{1-x}Sr_xMnO_3$ and $Pr_{1-x}Ca_xMnO_3$, exhibit a metal-insulator transition that is highly sensitive to magnetic fields and leads to colossal magnetoresistance (CMR) [58-60]. It has been known since the 1950s that electron hopping via the double exchange interaction (*figure 1.13*) between adjacent Mn^{3+} and Mn^{4+} ions requires ferromagnetic ordering, as the electron can hop to a neighbouring site only if the t_{2g} orbitals are aligned in a parallel fashion [61-63]. The electron transfer between adjacent sites *i* and *j* is described in terms of the transfer integral t_{ij}. When dopant ions are introduced, the average ionic radius of the perovskite A site decreases and there is an increase in the orthorhombic distortion, resulting in reduced electron transfer [36]. With this reduced transfer, other electronic instabilities such as charge or orbital ordering may become more important and compete with the ferromagnetic double exchange interaction.

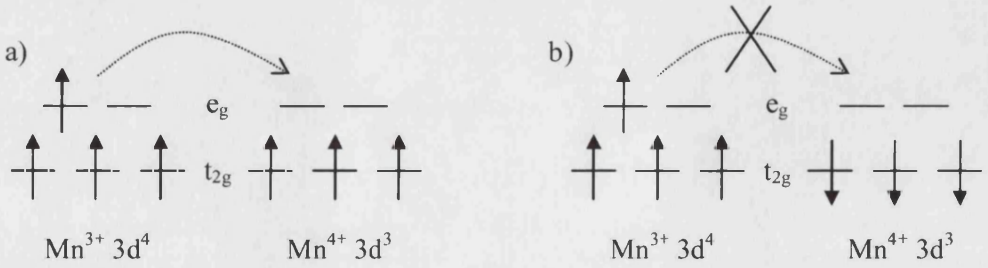

Figure 1.13 – Schematic of the double exchange mechanism. Electron hopping is favoured if a) neighbouring ions are ferromagnetically aligned and not if b) neighbouring ions are antiferromagnetically aligned or disordered in a paramagnetic state.

This competition produces some interesting magnetoresistive and magnetostructural phenomena, in particular, when the doping, x, is close to the commensurate value $x = ½$, charge-ordering. The zero field charge ordered state is characterised as being an insulator with increasing resistivity as temperature decreases. The transfer integral, t_{ij}, of electrons of Mn^{3+} ions to the Mn^{4+} ions with parallel spin direction at neighbouring sites increases in applied magnetic fields, hence the kinetic energy due to the transfer integral, which favours the ferromagnetic metallic state, becomes superior to the Coulomb interaction among Mn^{4+} ions and Mn^{3+} ions that favours an insulating state. Consequently, in magnetic fields the insulating phase is suppressed [29]; in other words, the charge ordered state can be relaxed to a ferromagnetic state by application of an external magnetic field [36, 64, 65].

For example, $Nd_{1-x}Sr_xMnO_3$ is a ferromagnetic metal for $x > 0.3$, but for doping levels around $x = ½$ the ferromagnetic state changes into a charge ordered insulating state below $T_{CO} = 160K$, which accompanies orbital and antiferromagnetic spin ordering [66-69]. In $Nd_{0.5}Sr_{0.5}MnO_3$, the charge ordered transition shifts to a lower temperature as the external field increases, and above 7T remains metallic as the temperature is decreased, without charge ordering [64]. A similar effect is observed for $La_{0.5}Ca_{0.5}MnO_3$ [70] and recent x-ray scattering experiments on $La_{1-x}Sr_xMnO_3$ [71] showed a transition driven by orbital ordering at $T_C = 145K$, which is subtly different from the charge ordering picture proposed by neutron scattering experiments [72] and elastic constant measurements [73].

The charge ordered insulating state appears to be extended over a wider doping region when the bandwidth is narrowed: for example, in $Pr_{1-x}Ca_xMnO_3$ it is observed over $0.3 < x \leq 0.5$ [68]. A larger external field is needed to destroy the charge ordered insulating state in $Pr_{0.5}Ca_{0.5}MnO_3$ than in the corresponding neodymium/strontium compound. Neutron and x-ray scattering on $Pr_{1-x}Ca_xMnO_3$ ($x = 0.40$ and 0.50) revealed charge ordering in the *a-b* plane accompanied by orbital ordering [68, 74]. The onset of spin ordering occurs at a lower temperature than charge ordering in this series [36] and the microstructure of charge ordering in $Pr_{1-x}Ca_xMnO_3$ observed using electron microscopy revealed competition between orbital and charge degrees of freedom [75]. The field induced transition from ferromagnetic metal to charge ordered insulator in $Pr_{0.3}Ca_{0.7}MnO_3$ becomes irreversible below 40K, and is accompanied by a change in resistivity of more than ten orders of magnitude. This irreversible transition can be

triggered not only by external magnetic field or pressure [76, 77], but also by x-ray [78] and light irradiations [79], and by an electric field [80] raising possibilities for application in magnetoelectronic devices [36].

As illustrated by these examples, charge ordering in the distorted perovskite manganates is dependant on the combination of ions chosen to occupy the A perovskite sites in $R_{1-x}A_xMnO_3$ and the amount of doping (value of x) [29, 36].

1.2.6 $La_{2-2x}Sr_{1+2x}Mn_2O_7$

These compounds are the n = 2 Ruddlesden-Popper phases where the MnO_2 bilayer repeats as shown in *figure 1.14* for the parent compound, $La_2SrMn_2O_7$, where x, the nominal hole number per manganese ion site, is zero.

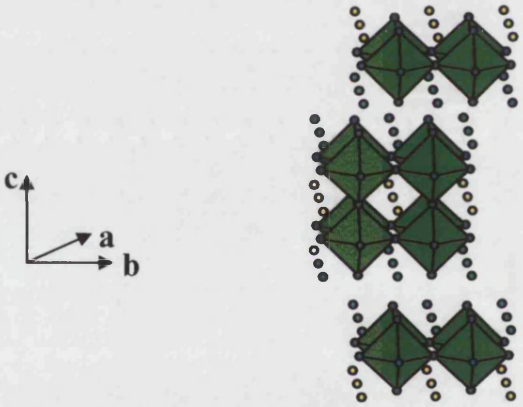

Figure 1.14 – $La_2SrMn_2O_7$ Ruddlesden-Popper n = 2 phase.

Resistivity measurements on the $x = 0.3$ phase [81] have shown anisotropic behaviour, with the resistivity along the c-axis significantly larger than that within the *ab* plane [36]. The c-axis resistivity, ρ_c, has a sharp maximum at approximately 100K, above which semiconducting behaviour is observed and below which metallic behaviour is observed. This drop in resistivity below 100K is linked to the occurrence of three-dimensional spin ordering: weak antiferromagnetic interlayer coupling has been confirmed by magnetisation and neutron experiments [82]. Behaviour within the *ab* plane differs: a broad maximum in the resistivity, ρ_{ab}, is observed around 270K. Coupled with magnetisation measurements, it is thought that below 270K there are in-plane two-dimensional ferromagnetic correlations. Between 100K and 270K, the $x = 0.3$ compound shows ferromagnetic metallic behaviour arising from confinement of the holes within the MnO_2 bilayer [36]. Below 100K, ρ_c steeply decreases indicating a very

fast change from incoherent to coherent charge dynamics. The magnetoresistance was found to be weakly dependent upon field orientation: within the plane, there was an enhanced magnetoresistance around 100K and 270K, whereas along the *c*-axis the temperature of the observed maximum increased with a magnetic field, while the maximum resistivity value decreased. The in-plane magnetoresistance is much smaller than the interplane magnetoresistance [81].

The charge-transport properties, including magnetoresistance, are observed to be quite sensitive to the doping level, as was the case for the perovskite manganites previously discussed. This is shown by comparison of the behaviour of the resistivity of the $x = 0.4$ lanthanum strontium manganite with the $x = 0.3$ phase just described. In the $x = 0.4$ phase, both the in-plane and interplane resistivities show a slow increase in resistivity with decreasing temperature, down to $T_C = 126K$ where they both have a steep decrease in resistivity by more than two orders of magnitude, exhibiting metallic behaviour below T_C. Application of a magnetic field suppresses the resistivity above T_C, effectively moving the resistivity maximum towards higher temperature [83].

The charge ordered state in these phases have been found to be of the same type as that found in the perovskite manganites, having the same complex relationship with spin and orbital ordering [36, 84].

1.2.7 $Nb_{12}O_{29}$

Monoclinic $Nb_{12}O_{29}$ is composed of 4x3 blocks of NbO_6 octahedra, which are edge and corner shared as shown in *figure 1.15*.

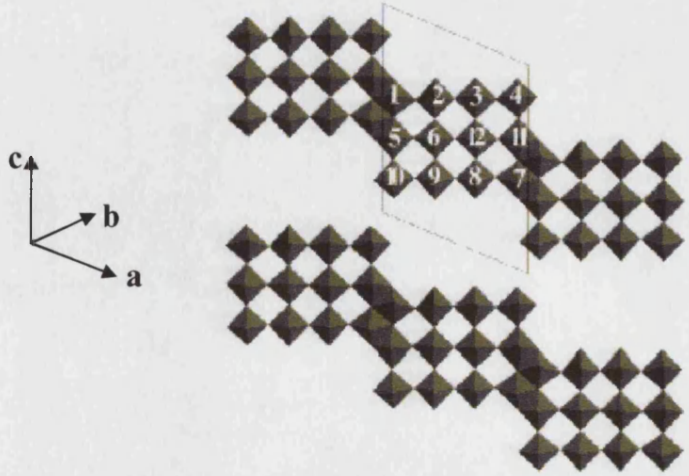

Figure 1.15 – The structure of $Nb_{12}O_{29}$ made up of edge-sharing NbO_6 octahedra, obtained from neutron diffraction [30].

Susceptibility and conductivity measurements have shown that this system is metallic at all temperatures, and that it undergoes antiferromagnetic ordering at 12K [30]. This magnetic ordering is unexpected given the low concentration of unpaired electrons present: the formula may be written as $Nb^{4+}{}_2Nb^{5+}{}_{10}O_{29}$, where Nb^{5+} has a d^0 electronic configuration and Nb^{4+} has a d^1 configuration, in other words there are two unpaired electrons per block. Susceptibility measurements showed that approximately half of the unpaired electrons present are localised, the rest being itinerant: there is one localised spin in every twelve. The most likely product of this dilute spin system would be the formation of a spin glass, where the spins are frozen at low temperature in a disordered arrangement, but in $Nb_{12}O_{29}$ the spins are arranged in a well-defined arrangement that allows antiferromagnetic coupling. μSR experiments were carried out to confirm the existence of a long-range ordered state in this material [31] and low temperature neutron diffraction experiments were undertaken to determine the ordered structure below 12K [30], which is shown in *figure 1.16*.

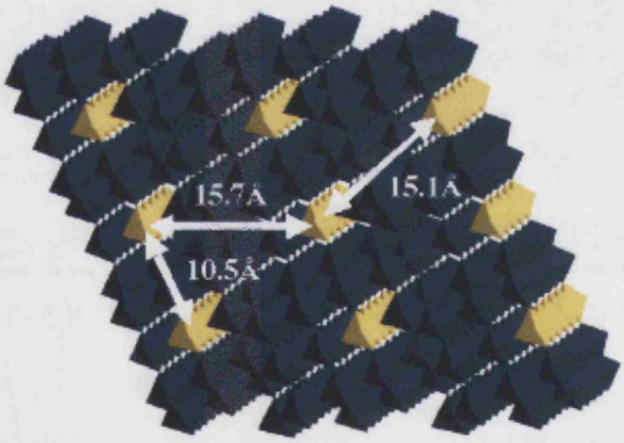

Figure 1.16 – The charge-ordered structure of $Nb_{12}O_{29}$, blue octahedra Nb^{5+}, yellow octahedra Nb^{4+}.

Nb^{4+} octahedra are corner shared to form chains along the *b*-axis, thus allowing the formation of a long-range ordered magnetic state despite the low proportion of localised spins. Corner shared octahedra have a larger Nb-Nb separation than that found in edge-shared octahedra, leading to less of the direct metal-metal overlap which results in metallic properties, instead favouring localised behaviour. In this compound therefore it is the mixture of corner and edge shared octahedra within the structure that is responsible for the coexistence of localised and itinerant electrons [30]; charge ordering of non-magnetic d^0 ions and magnetic d^1 ions onto these crystallographically distinct

sites is responsible for the production of a one-dimensional magnetic state with a much larger chain separation than was previously reported in condensed oxides: approximately double those reported in magnetic condensed copper oxides such as dichlorobi(thiazole) copper, shown in *figure 1.17*, which has chain separations of approximately 7Å and 9Å, compared with the 10Å and 15Å separations observed in $Nb_{12}O_{29}$ [30].

Figure 1.17 – Dichlorobi(thiazole) copper (II), chains of magnetic copper ions are shown in red.

1.2.8 NaV_2O_5

NaV_2O_5 was initially believed to consist of two leg spin ladders, in the $P2_1mn$ space group, with each ladder having one leg made up of V^{4+} ions and the other of V^{5+} ions [85]. However, four recent, separate structural investigations have shown that the structure is centrosymmetric with Pmmn space group [86-89], in agreement with ^{51}V NMR experiments that show the presence of only one type of vanadium atom at room temperature [90, 91]. This compound is a mixed-valence system with an average valence of $V^{4.5+}$ and can be considered as an insulating quarter filled spin ladder [29].

A phase transition occurs in NaV_2O_5 at T_C = 34K. Below T_C the magnetic susceptibility decreases rapidly and lattice distortion to form a $2a$ x $2b$ x $4c$ supercell is observed [92, 93]. This distortion and drop in susceptibility was originally thought to be due to a spin-Peierls transition [92]. A spin Peierls transition occurs when a quasi-one-dimensional s = ½ Heisenberg antiferromagnetic chain is coupled to three-dimensional lattice vibrations, causing the chain to distort into pairs as a function of temperature. Above the transition, the magnetic behaviour is that of a one-dimensional antiferromagnet; below, the dimerisation of the spin lattice system leads to alternating

exchange constants, as for any alternating chain. The dimerisation increases progressively and reaches a maximum at zero temperature [46]. There are not many examples of inorganic spin-Peierls compounds, $CuGeO_3$ (T_{SP} = 14K), shown in *figure 1.18*, was the first of these to be discovered [94, 95]: NaV_2O_5 was thought to be the second [92].

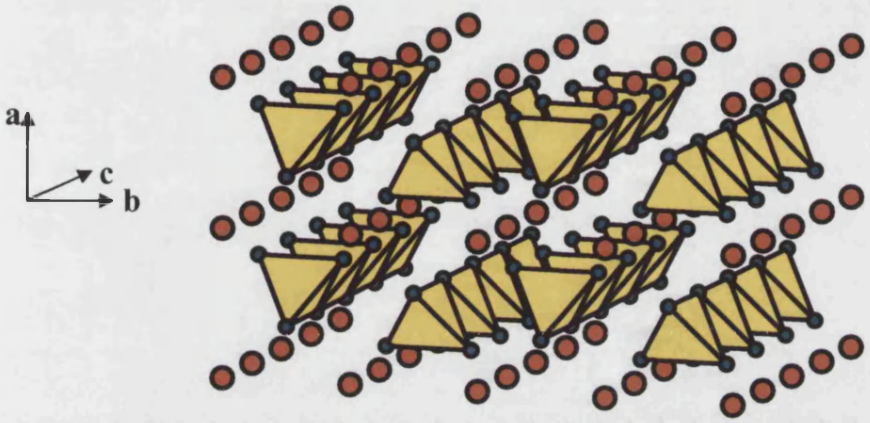

Figure 1.18 – $CuGeO_3$ (Copper is shown in red, Germanium in yellow and Oxygen in blue).

However, the lattice distortion in NaV_2O_5 is not due to a spin-Peierls transition as originally thought, but rather to the onset of charge order. This has been established by ^{51}V NMR: one line for the average $V^{4.5+}$ site is observed above T_C, splitting to two lines for inequivalent V^{4+} and V^{5+} sites below T_C [32, 91]. Comparison of elastic constant measurements of NaV_2O_5 and $CuGeO_3$ by Goto *et al.* [29] gives an insight into the similarities and differences between a spin Peierls transition and a charge order transition.

Thermal expansion and specific heat measurements gave evidence for two consecutive transitions at 33K and 34K [96]. The first of these is the charge ordering transition and recent synchrotron x-ray diffraction experiments have established the second transition to be an orthorhombic-monoclinic phase transition [97]. However, despite numerous studies [29, 32, 92, 97-99] the charge ordered structure has yet to be incontrovertibly established in this compound. All experiments give a zigzag charge order, but some give fully charged ladders while others give charge ordering only in alternate ladders, some examples are shown in *figure 1.19*. The fully charged models agree with NMR results previously mentioned, as they involve only oxidation states V^{4+} and V^{5+}, whereas the alternate zigzag ladder models would give three inequivalent sites for the oxidations states V^{4+}, V^{5+} and $V^{4.5+}$ [29].

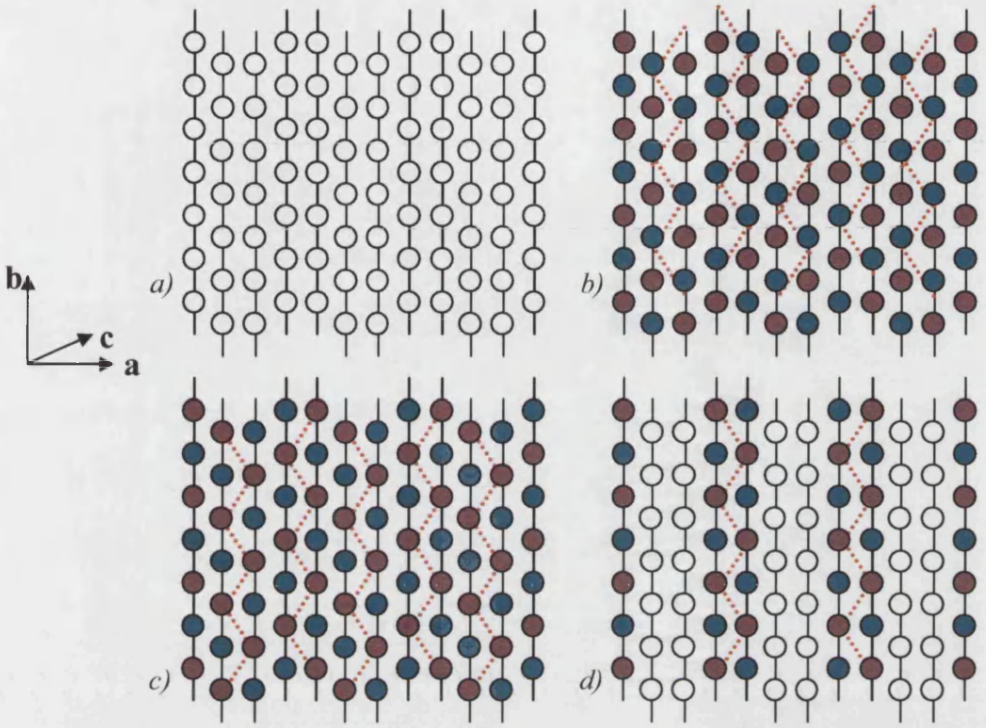

Figure 1.19 – Suggested models for zigzag charge ordering models in NaV_2O_5, V^{4+} shown as purple circle, V^{5+} shown as blue circle, $V^{4.5+}$ shown as open circles, "zigzag" magnetic interactions shown in red [29, 100] a) one vanadium site, average $V^{4.5+}$ oxidation state; b) repeating pattern ABAABABB…; c) repeating pattern AABBAABB…; d) oxidation states V^{4+}, V^{5+} and $V^{4.5+}$ repeating ACCABCCB…

1.3 Vanadium Oxides

There are many kinds of vanadium oxides, exhibiting a wide range of structural and electronic properties [101]. There are four principal oxides: vanadium monoxide, VO; vanadium sesquioxide, V_2O_3; vanadium dioxide, VO_2 and vanadium pentoxide, V_2O_5; however, a number of other phases of intermediate composition have been identified and the lower oxides in particular have wide ranges of homogeneity [102].

V_2O_5 loses oxygen reversibly on heating, a property that makes it a versatile catalyst, used in the oxidation of organic compounds by air or oxygen, and the reduction of alkenes and aromatic hydrocarbons by hydrogen, for example [102]. More importantly, it is used in the contact process for the manufacture of sulphuric acid to catalyse the oxidation of SO_2 to SO_3 [102]. V_2O_5 dissolves in acids to produce salts of the angular $[VO_2]^+$ ion, and in alkalis producing colourless solutions containing the tetrahedral orthovanadate ion $[VO_4]^{3-}$. At intermediate pH a series of hydrolysis-polymerisation reactions occur producing isopolyvanadates such as $KVO_3.H_2O$, K_3VO_4,

$Na_xV_2O_7$ and $Na_6V_{10}O_{28}.18H_2O$, which contain various combinations of tetrahedral, bipyramidal or octahedral vanadium species [102]. The wide applications of vanadium pentoxide, in pure form or via its numerous compounds, have made it the focus of much attention for many years [103]. Structurally the V_2O_5 network is viewed as exhibiting the characteristics of layer and crystallographic shear structure. Its formula yields a wide vanadium oxide bronze family $M_xV_2O_5$ (M = alkali, alkaline earth metals), showing several original $[V_2O_5]$ networks.

VO_2 is formed by mild reduction of V_2O_5 and has a rutile-like structure at room temperature, shown in *figure 1.20*.

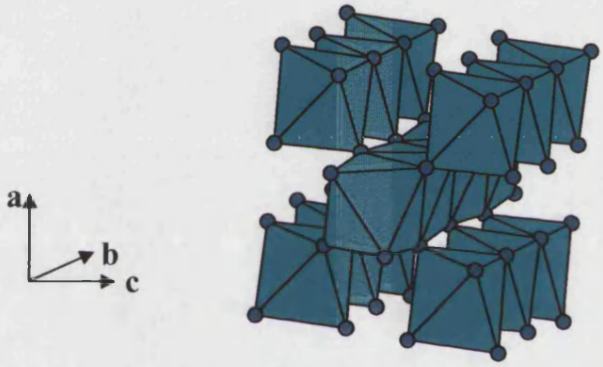

Figure 1.20 – Rutile structure of VO_2 [104].

Low temperature x-ray diffraction and ^{51}V NMR studies on metastable polymorphs of VO_2 have confirmed the formation of V^{4+}-V^{4+} pairs that dissociate above the metal-insulator transition at 340K, causing a sharp increase in electrical conductivity [105-108].

Between V_2O_5 and VO_2 there are a succession of phases of general formula V_nO_{2n+1}, including V_3O_7 and V_4O_9, which are shown in *figure 1.21*.

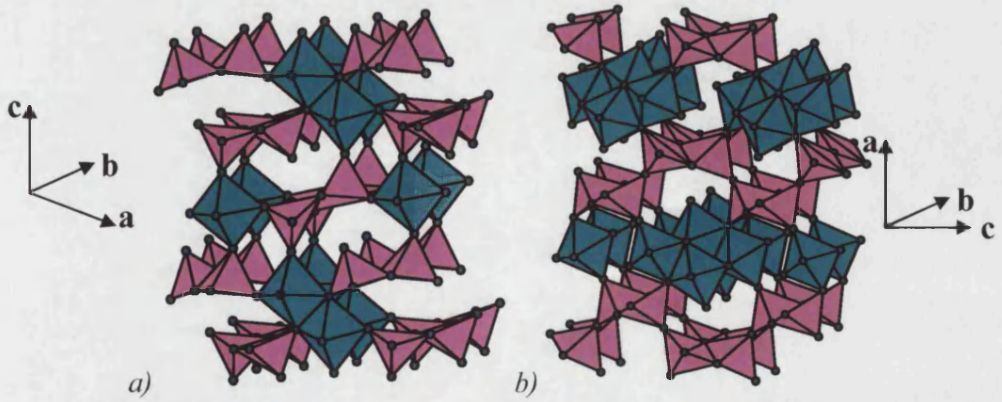

Figure 1.21 – V_nO_{2n+1} phases a) V_3O_7 [109] b)V_4O_9 [110]. VO_5 square pyramids shown in pink, VO_6 octahedra shown in blue.

Further reduction from VO_2 produces a series of chemical shear phases known as the Magnéli phases, of general formula V_nO_{2n-1}, before the sesquioxide V_2O_3 is reached. Examples include V_4O_7, V_5O_9, V_6O_{11}, V_7O_{13} and V_8O_{15}. These phases containing a mixture of V^{4+} (d^1) and V^{3+} (d^2) ions are believed to undergo charge ordering such as that previously discussed for the case of Fe_3O_4 [111]. Although the oxides VO, V_2O_3 and V_3O_5 also conform to the general formula, they are structurally unrelated to the Magnéli phases. [102]

V_2O_3 has a corundum structure and undergoes a metal to insulator transition below about 170K.

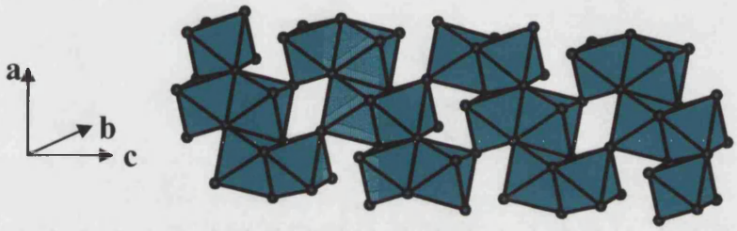

Figure 1.22 – Corundum structure of V_2O_3 [112]: chains of edge-sharing VO_6 octahedra linked through corner sharing.

Incorporation of Cr_2O_3 and Ti_2O_3 to form V_2O_3 "alloy" systems with the general formula $(V_{1-x}M_x)_2O_3$ has been investigated due to their effects in respectively enhancing or suppressing the transition to an insulating state. The system may be manipulated to show one, two or three metal-insulator transitions as a function of temperature, depending on compositional details [111]. On further reduction the corundum structure is retained down to compositions as low as $VO_{1.35}$, after which the metallic monoxide with a rock salt structure is formed (*figure 1.23 [113]*). This is also markedly non-stoichiometric with a composition range from $VO_{0.8}$ to $VO_{1.3}$. At least thirteen distinct oxide phases have been identified between $VO_{\sim 1}$ and V_2O_5 [102].

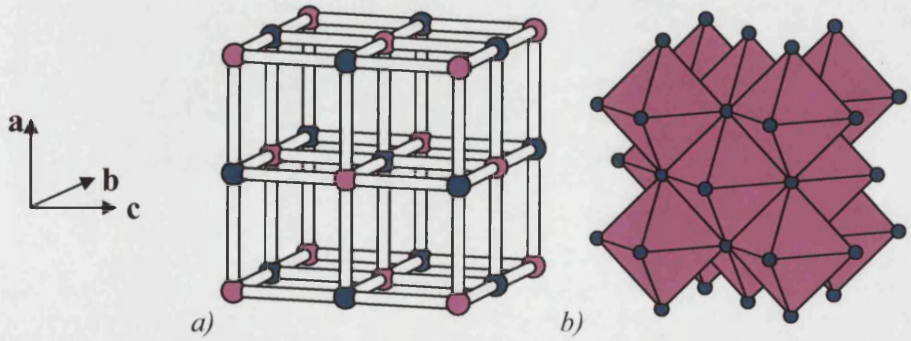

Figure 1.23 – Rocksalt VO structure: a) ball and stick model, vanadium in pink, oxygen in blue; b) polyhedral model showing linking of VO_6 octahedra [113].

1.3.1 V_2O_5 Structure

The first crystallographic data on V_2O_5 was reported by Ketelaar in 1936, and later by Byström et al. [114], then by Bachman et al. [115] and has recently been refined by Enjalbert and Galy [116]. Although vanadium has sometimes been described as having distorted octahedral oxygen coordination in this compound (as would be expected of a d^0 oxide), taking into account a sixth oxygen (2.791Å from Vanadium) as shown in *figure 1.24,* it has been suggested by Galy [103] in a detailed refinement of the structure, that the V_2O_5 structure is better described as $[V_2O_5]_n$ layers built up from VO_5 square-based pyramids sharing edges and corners as shown in *figure 1.24b).* This representation helps to stress the layered structure of the material, the assembly being held together via relatively weak Van der Waals interactions, making it eminently suitable for intercalation.

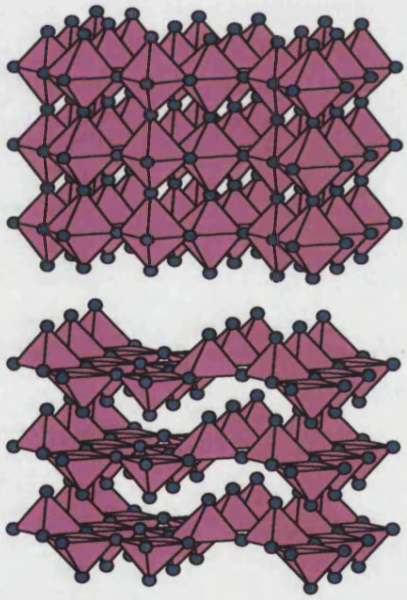

Figure 1.24 – Layered structure of V_2O_5: a) with octahedral coordination of vanadium, b) with square pyramidal coordination of vanadium.

1.3.2 $M_xV_2O_5$ Vanadium Oxide Bronzes

Various kinds of ions may be intercalated between the layers to form the well-known vanadium oxide bronzes, $M_xV_2O_5$ (M = alkaline or alkaline earth metal). They possess extended homogenous ranges of composition, which result from a non-stoichiometric intercalation of *M* cations within the $[V_2O_5]_n$ network. Intercalation of an alkali metal leads to partial reduction of V^{5+} ions to V^{4+} ions to balance the electric charges, shown

by study of NaV_2O_5 with ^{51}V NMR and x-ray scattering experiments [29] though the system was shown to possess a more complex arrangement with higher resolution studies as described previously. The preferred environments of V^{4+} (d^1) and V^{5+} (d^0) ions are very different, making the $M_xV_2O_5$ system a good candidate for charge ordering, which has been observed in NaV_2O_5 (section *1.2.8*), for example.

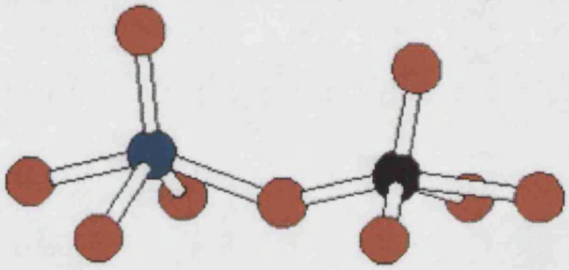

Figure 1.25 – Distinct vanadium environments in NaV_2O_5 corresponding to V^{4+} (blue) and V^{5+} (black).

The localisation of electrons through charge ordering can create low-dimensional character and properties in the case of d^0/d^1 condensed inorganic oxide phases [30, 31]. These compounds have the potential for unique structures as low-dimensional magnets, depending on the arrangement of the magnetic V^{4+}, d^1 ions within each structure; the unusual and distinctive properties of low-dimensional systems make them of great interest [117]. The variation in magnetism and charge ordering observed in the vanadium bronzes is well demonstrated by comparison of NaV_2O_5, CaV_2O_5, MgV_2O_5, CsV_2O_5 and γ-LiV_2O_5. These compounds have similar layered structures with a characteristic arrangement of VO_5 square pyramids sharing edges and corners, yet their magnetic properties are widely different: α'-NaV_2O_5 is a quarter filled spin ladder with $T_C = 35K$ and energy gap $\Delta = 114K$; CaV_2O_5 and MgV_2O_5 have similar two-leg spin-ladder structures but very different energy gaps, ~600K and ~17K respectively; CsV_2O_5 is a dimer system with a spin gap of approximately 160K; γ-LiV_2O_5 has a quasi-one-dimensional zigzag chain structure, and does not show spin gap or magnetic ordering down to 0.5K [101].

The magnetic properties and structures of the vanadium bronzes vary according to the identity of *M*, and the doping level *x* [101, 118]: weak interlayer bonding and transformations by crystallographic shears, slips and/or square pyramid reversal allow the formation of intercalated structures with a variety of stacking arrangements determined by the size, charge and quantity of *M* [103] raising potential for tailoring the properties by adjustment of these factors.

1.4 Lithium Vanadium Oxides, $Li_xV_2O_5$

It is generally agreed that there are seven phases in this system: alpha (α); beta (β); beta' (β'); epsilon (ε), which has been subdivided into ε_1 and ε_2; delta (δ); and gamma (γ). However, the correlation of these phases with x values is disputed, there being several published phase diagrams for the system [103, 119-121]. The discrepancies in these phase diagrams are due either to inaccurate determination of the composition or the differences in synthetic methods employed by different authors. The most comprehensive phase diagram was published by Galy in 1992, and is shown in *figure 1.26*. This covers a range of compositions ($0 < x < 1$) and synthetic methods ($0 < T < 650^{\circ}C$).

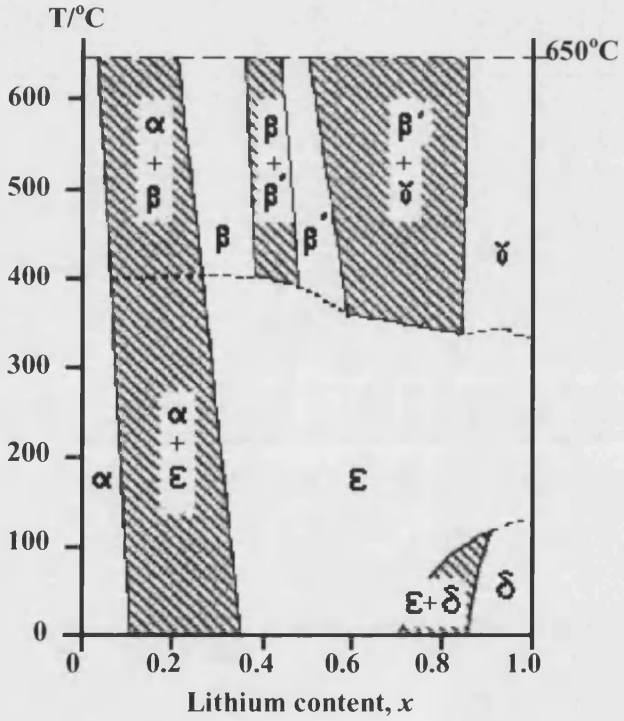

Figure 1.26 – Phase diagram for $Li_xV_2O_5$ published by Galy et al. [103] based on data published by Murphy [120] and Galy [122].

It is evident from *figure 1.26* that there are four thermodynamically stable phases: alpha, beta, beta' and gamma. The α and γ phases may be produced by high temperature and room temperature methods [120, 123, 124], whereas the β and β' phases are only accessible via high temperature methods [103, 125, 126]. The metastable phases epsilon and delta are synthesised by room temperature routes, and in the case of epsilon, via a

phase transition from the delta phase at increased temperature [124, 127]. The temperature dependent transformations between the epsilon, delta and gamma phases have been studied in detail by Galy and co-workers [124, 127]. All the phases that may be synthesised by room temperature wet methods are also accessible by electrochemical methods [128, 129]. The different synthetic methods used complicate the literature on this subject, and we have therefore confined our discussion to phases made through high temperature solid state and room temperature wet methods as these methods have been used to produce detailed structural information rather than performance in electrochemical cells with a view to future use as a battery cathode material [121, 130-138].

1.4.1 Alpha phase: α-$Li_xV_2O_5$

The alpha phase has low lithium content and is isostructural with undoped V_2O_5. This phase is stable up to high temperature as shown in *figure 1.26*, and may be synthesised by all three methods. Structural data have been published by Galy *et al.* [123], from x-ray diffraction data for $Li_{0.04}V_2O_5$ made via high temperature solid-state methods at 650°C. Galy has used the Pmmn space group with origin choice one to represent the structure [139]; consequently all atoms have a displacement of zero along the *y*-axis, the cell depth direction.

Space Group	**Lattice Parameters/Å**		
	a	**b**	**c**
Pmmn	11.460	3.554	4.368
	α	**β**	**γ**
	90	90	90
Atom	**x**	**y**	**z**
Li1	0.5	0	0.397
V2	0.1488	0	0.0993
O3	0.151	0	0.455
O4	0.349	0	0.903
O5	0	0	0.002

Table 1.1 – Atom positions and lattice parameters for α-$Li_xV_2O_5$ as defined by Galy et al. [123] R-factor = 0.13 (published without error-bars).

Some crystallographic data on vanadium oxide and its bronzes have been reported in space group Pmmn using origin choice two, in which the displacement along the *y*-axis is ¼, with corresponding alteration in the *x*-axis and *z*-axis positions, for example that of V_2O_5, given in *table 1.2*. Comparison of these data shows a very slight increase in unit

cell volume to 177.9Å^3 from 176.7Å^3, interestingly entirely due to an increased cell width, represented by parameter **a** in the orthorhombic Pmmn space group.

Space Group	Lattice Parameters/Å		
	a	**b**	**c**
Pmmn	11.3512(3)	3.564(1)	4.368(1)
	α	β	γ
	90	90	90
Atom	**x**	**y**	**z**
V	0.10118(8)	0.25	0.8917(2)
O3	0.1043(4)	0.25	0.531(1)
O4	-0.0689(3)	0.25	0.003(1)
O5	0.25	0.25	0.001(2)

Table 1.2 – Crystallographic data for V_2O_5 [116] (published without error bars).

Like V_2O_5, the alpha phase has one vanadium site, where the metal is square pyramidally co-ordinated by oxygen as shown in *figure 1.27*.

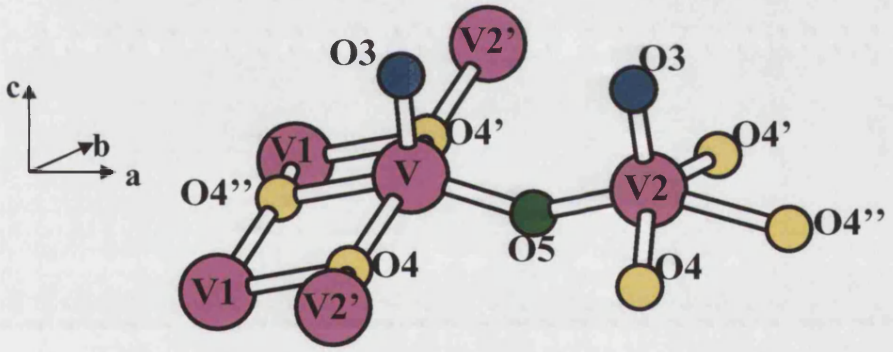

Figure 1.27 – Vanadium environment in V_2O_5 [116]: Vanadium shown in pink, corner-shared oxygen atoms (O5) shown in green, edge shared oxygen atoms (O4) in yellow and apical oxygen atoms (O3) in blue. Atoms are labelled according to tables 1.1-2.

Table 1.3 shows the vanadium-oxygen bond lengths and the vanadium-vanadium distances in α-$Li_{0.04}V_2O_5$ [123], compared with the corresponding lengths and angles in V_2O_5 [116]. There are one short, three similar length and one long vanadium-oxygen bonds in α-$Li_{0.04}V_2O_5$. The oxygen atom located at the apex of the square pyramid has the shortest bond length. This is to be expected since this oxygen atom has only one bond, which will therefore be stronger and shorter than the bonds of oxygen atoms located in shared positions, attached to more than one vanadium atom. The next-shortest bond length is to the oxygen that is corner-shared between two square pyramids. Of the bonds with edge shared oxygen atoms, two of these are the same length and similar in length to the V-$O_{corner\ shared}$ bond, while the third is much longer.

Bond Lengths in V_2O_5 [116]		Bond Lengths in α–$Li_xV_2O_5$ [123]	
Bond	**Bond Length/Å**	**Bond**	**Bond Length/Å**
V-O3	1.58	V-O3	1.55
V-O5	1.76	V-O5	1.76
V-O4	1.88	V-O4	1.78
V-O4'	1.88	V-O4'	1.78
V-O4''	1.99	V-O4''	2.45
V-V1	3.06	V-V1	3.05
V-V2	3.56	V-V2	3.55
V-V2'	3.39	V-V2'	3.41
Bond Angles in V_2O_5 [116]		**Bond Angles in α–$Li_xV_2O_5$ [123]**	
Atoms	**Angle**	**Atoms**	**Angle/°**
O4, O4'-V-O4''	75.40	O4, O4'- V-O4''	89.13
O4, O4'-V-O5	97.13	O4, O4'-V-O5	90.71
O4, O4'-V-O3	104.44	O4, O4'-V-O3	90.31
O4''-V-O3	105.46	O4''-V-O3	109.56
O5-V-O3	104.49	O5-V-O3	104.92
V-O4-V1	104.60	V-O4-V1	90.87
V-O4-V2'	143.27	V-O4-V2	178.25
V-O5-V2	148.44	V-O5-V2'	152.01

Table 1.3 – Comparison of vanadium-oxygen bond lengths and angles and vanadium-vanadium distances for α-$Li_{0.04}V_2O_5$ and V_2O_5.

While the introduction of lithium into the compound causes significant changes to the vanadium-oxygen bond lengths and angles, the vanadium-vanadium distances are almost unchanged. Compared with the vanadium environment in V_2O_5, it can be seen that intercalating even this small amount of lithium is enough to considerably distort the square pyramidal vanadium environment, the observed changes in bond angles suggesting some tendency to puckering, though at relatively small levels since the space group remains unchanged and the overall layered structure made up of chains of edge and corner sharing square pyramids apparently remains intact, and the stacking of layers regular, as shown in *figure 1.28*.

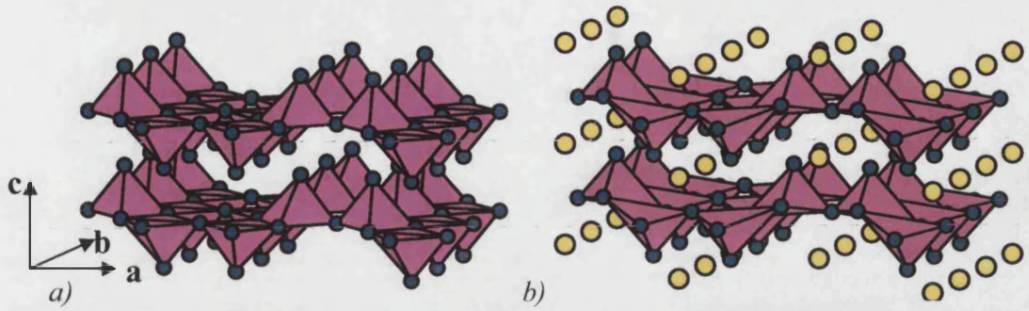

Figure 1.28 – a) Structure of V_2O_5 as published by Galy et al. [116]; b) Structure of α-$Li_xV_2O_5$ as published by Galy et al, Lithium atoms shown in yellow, oxygen in blue and vanadium square pyramids in pink [123].

The puckering angle, μ, is defined by *figure 1.29*, and is representative of the degree of closure of the apical oxygen atoms, and the degree of distortion of two neighbouring corner-shared square pyramids from 180°, the latter giving a simple method for determination of μ: the degree of distortion of the O4''-O5-O4'' angle from 180° (see figures *1.27* and *1.29*).

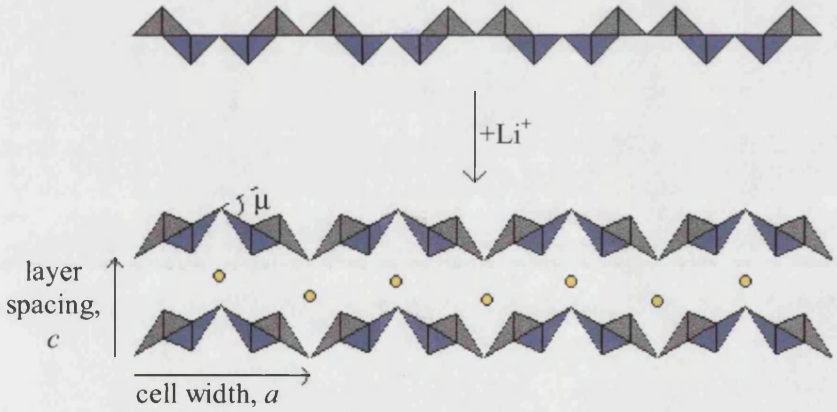

Figure 1.29 – Introduction of lithium into V_2O_5 creating a puckering angle, μ [103].

In V_2O_5 the puckering angle is 0°, in other words, the layers are flat. In the alpha phase, where there is only a small amount of lithium introduced, the puckering angle is expected to be very small. Lithium ions normally require tetrahedral or octahedral coordination with ideal lithium-oxygen distances of 1.97 or 2.14Å respectively [140], however, in this compound the only sites available are eight-fold co-ordinated by oxygen atoms as shown in *figure 1.30*. Lithium-oxygen distances are given in *table 1.4*. Lithium atoms are intercalated along the [010] channels and are coordinated by eight oxygen atoms in a bicapped triangular prismatic arrangement in α-$Li_{0.04}V_2O_5$ [123, 127].

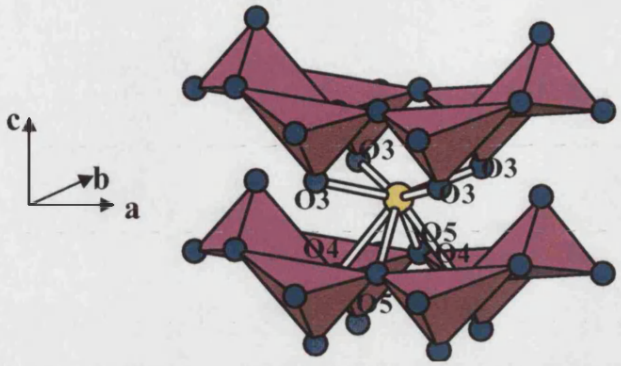

Figure 1.30 – Lithium co-ordination by oxygen within layers of α-$Li_{0.04}V_2O_5$ [123] within V_2O_5 layers. Lithium depicted in yellow, oxygen in blue and vanadium polyhedra in pink. Oxygen atoms are labelled according to table 1.2.

Li-O	Separation/Å
4 x Li-O3	2.56
2 x Li-O5	2.49
2 x Li-O4	2.77

Table 1.4 – Lithium-oxygen separations in α-$Li_{0.04}V_2O_5$ [123].

Galy accounts for the phenomenon of puckering by noting that four of the oxygen atoms coordinating lithium are apex oxygen atoms, which are attracted to the lithium and thus the angle between corner shared square pyramids is closed, causing puckering [103]. However, it should be noted that Galy's published crystallographic data for this alpha phase, α-$Li_{0.04}V_2O_5$, actually gives a negative puckering, not consistent with his prediction. In other words, the angle between corner shared square pyramids is being opened rather than closed, so that the puckering angle, $\mu = -12.34^{\circ}$. This disagreement between prediction and experiment is possibly due to an inaccuracy in the lithium and oxygen positions, since this structure was obtained from x-ray diffraction data, where vanadium, as a heavier atom, would dominate [123]. This could be rectified with the use of neutron scattering techniques.

1.4.2 Beta and Beta' phases: β-$Li_xV_2O_5$ and β'-$Li_xV_2O_5$

β and β' phases are formed only at high temperatures (above 400°C). The β phase has a monoclinic three-dimensional tunnel structure containing vanadium in octahedral and square pyramidal coordination. The layered room temperature structure of chains of edge and corner sharing square pyramids is partially retained with the integration of chains of edge and corner sharing octahedra running perpendicularly to form tunnels. The octahedral layered structures of the beta and beta' phases are formed at high

temperature by a crystallographic shear of the vanadium pentoxide layers followed by a slip and rearrangement of oxygen atoms in the square pyramids to form puckered double layers. The mechanism of this transformation has been described in detail by Galy *et al.* [103]. The beta and beta' phases differ in the mode of insertion of lithium ions [141]. There are three possible sites for cation intercalation in the structure, which is defined by tunnels running parallel to the [010] direction. The site occupation is influenced by the nature and size of the intercalating cation, [142] for example copper is always found in the M3 site, giving the β' phase, while silver occupies the M1 site (β phase). Lithium can occupy both the M1 and M3 sites, giving rise to the β and β' structures [143]. Structural data have been published for three compounds in the beta and beta' phase range by Galy et al. (without error bars) from NMR and x-ray diffraction data [126]. The compositions β-$Li_{0.3}V_2O_5$, β'-$Li_{0.48}V_2O_5$ and β'-$Li_{0.67}V_2O_5$ were synthesised by the reduction of vanadium pentoxide with lithium carbonate (*equation 1.5*) and are discussed in the following section.

$$2V_2O_5 + xLi_2CO_3 \rightarrow 2Li_xV_2O_5 + xCO_2 + \frac{x}{2}O_2$$

Equation 1.5 – reduction of vanadium pentoxide by lithium carbonate at 600°C under vacuum.

$Li_{0.30}V_2O_5$:

Space Group	Lattice Parameters/Å		
	a	b	c
A 2/m	10.03(2)	3.60(2)	15.38(2)
	α	β	γ
	90	110.7	90
Atom	**x**	**y**	**z**
Li1	0.342	0	0.003
V2	0.109	0	0.338
V3	0.119	0	0.120
V4	0.342	0	0.290
O5	0	0	0
O6	0.082	0	0.825
O7	0.096	0	0.628
O8	0.231	0	0.435
O9	0.232	0	0.263
O10	0.274	0	0.109
O11	0.434	0	0.774
O12	0.478	0	0.399

Table 1.5 – Atom positions and lattice parameters for β-$Li_{0.3}V_2O_5$ as defined by Galy et al. [123, 144] R-factor = 0.17.

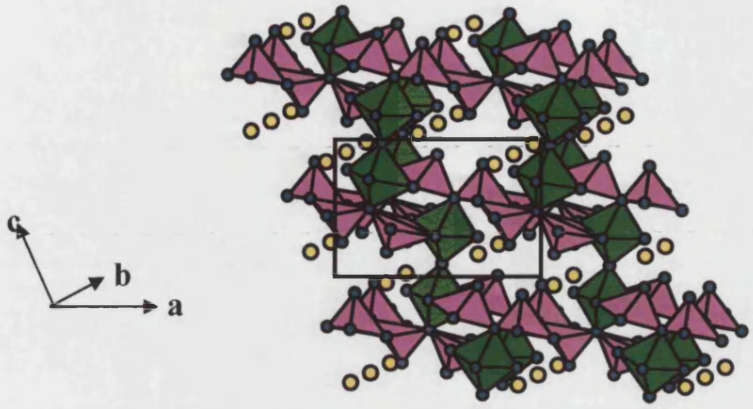

Figure 1.31 – Structure of β-$Li_{0.3}V_2O_5$ as published by Galy et al. [123, 144] vanadium in square pyramidal coordination are shown in pink, vanadium in octahedral sites are shown in green.

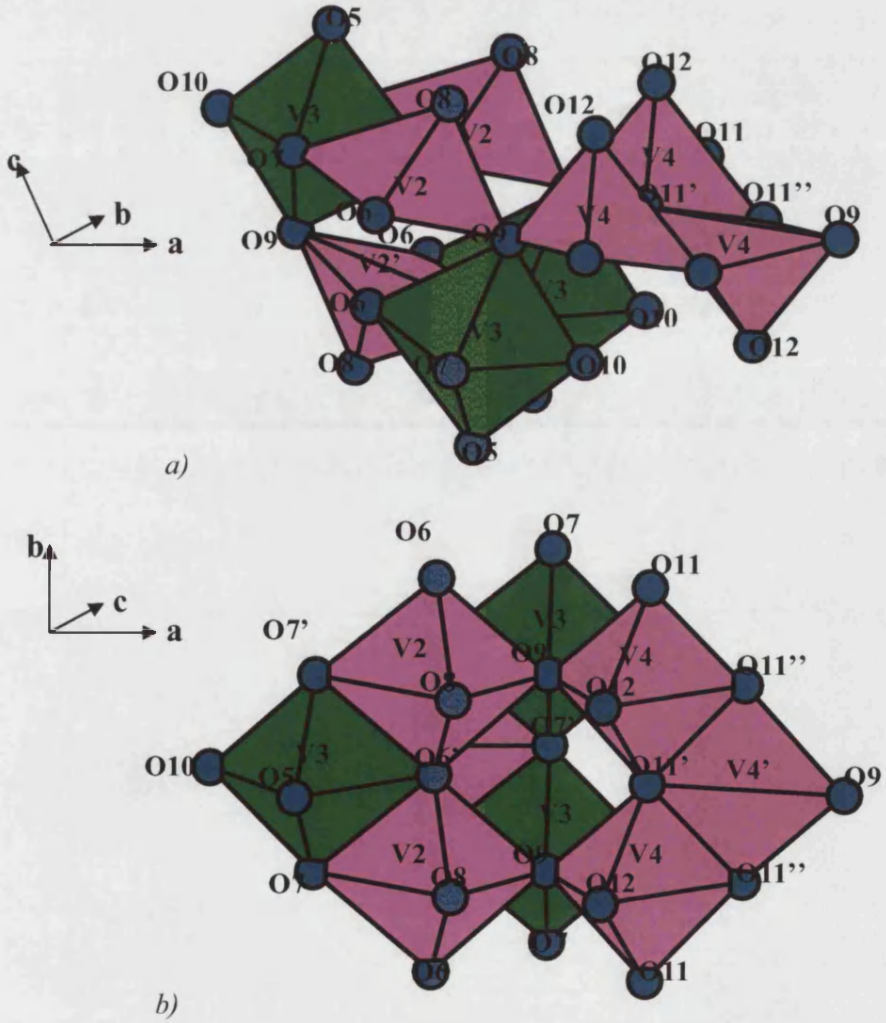

Figure 1.32 – Section of β-$Li_{0.3}V_2O_5$ [123, 144] to show detail of bonding of polyhedra a) viewed down b-axis; b) viewed down c-axis.

As can be seen from *table 1.5*, there are three vanadium sites in this monoclinic compound, one octahedral and two in square pyramidal coordination, as shown in *figure 1.31*. The VO_6 octahedra form chains, integrated into the remaining partial layered structure retained from the orthorhombic, layered structure of the V_2O_5 parent compound. The polyhedra have a complex arrangement of shared corners and edges shown in more detail in *figure 1.32*, from which we can see that the octahedra share edges with one set of square pyramids and corners with the other. *Table 1.6* compares the vanadium-oxygen bond lengths and angles in each set of polyhedra.

Bond Lengths in β–$Li_{0.3}V_2O_5$					
Octahedral Site		**Square Pyramidal Sites**			
V3-O10	1.62	V2-O8	1.56	V4-O12	1.57
V3-O5	1.81	V2-O9	1.96	V4-O9	1.81
V3-O9	2.09	-	-	-	-
V3-O7	1.82	V2-O6	1.82	V4-O11	1.83
V3-O7'	1.82	V2-O6'	1.82	V4-O11'	1.83
V3-O6	2.45	V2-O7	2.29	V4-O11''	2.01
V3-V3	3.60	V2-V2'	3.34	V4-V4'	2.91
V3-V3	5.10	V2-V2	3.60	V4-V4	3.60
V3-V3	5.63	V2-V4	3.48	V4-V2	3.48

Table 1.6 – Bond lengths for β-$Li_{0.3}V_2O_5$.

The integration of VO_6 octahedra into the layered structure influences the square pyramidal vanadium environments. The vanadium-oxygen bond lengths are between those found in V_2O_5 and those found in α-$Li_{0.04}V_2O_5$, as previously detailed [123]. The bond angles show the same trend although the V-O-V angle between corner shared square pyramids is smaller here than in either V_2O_5 [116] or α-$Li_{0.04}V_2O_5$ [123], 134.29°, compared to 148.44° in V_2O_5 and 152.01° in α-$Li_{0.04}V_2O_5$. This angle is more acute than observed in the parent V_2O_5, suggesting that there is puckering in the layers of square pyramids, confirmed by the puckering angle, μ: for this compound, μ = 13.47°. The closing of the angle between corner shared square pyramids is just visible in *figure 1.32*.

The lithium ions have been intercalated in their preferred tetrahedral coordination (*figure 1.33*), and although the lithium-oxygen distances vary somewhat

from the ideal 1.97Å length [145] (*table 1.7*) they are reasonable, confirming that this is a stable lithium site.

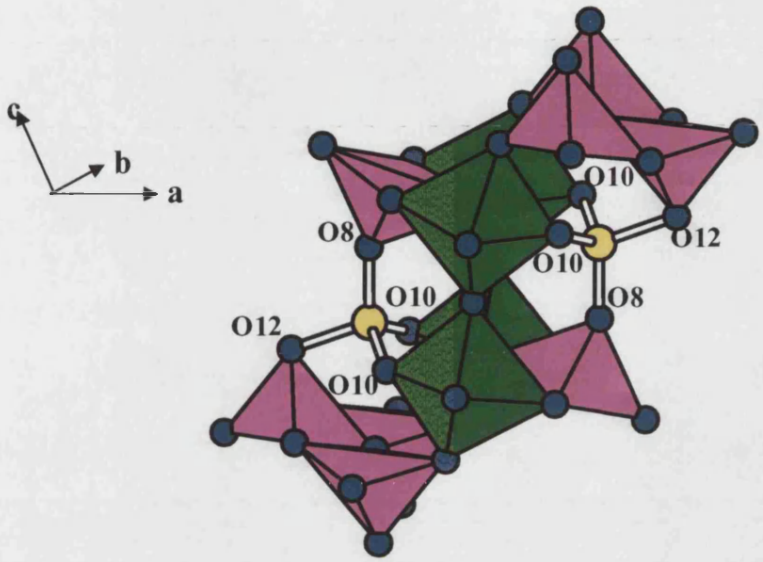

Figure 1.33 – Tetrahedral lithium coordination by oxygen in layered β-$Li_{0.30}V_2O_5$ [123, 144] lithium shown in yellow, VO_6 octahedra in green and VO_5 square pyramids in pink.

Li-O	Separation/Å
2 x Li-O10	2.03
Li-O12	1.99
Li-O8	1.80

Table 1.7 – Lithium-oxygen separations in β'-$Li_{0.48}V_2O_5$ [123, 144].

$Li_{0.48}V_2O_5$:

Space Group	Lattice Parameters/Å					
	a	b	c	α	β	γ
A 2/m	10.09	3.61	15.25	90	108.0	90
Atom	**x**		**y**		**z**	
Li1	0.690		0		0.440	

Table 1.8 – Atom positions and lattice parameters for β'-$Li_{0.48}V_2O_5$ as defined by Galy et al. [125]. R-factor = 0.066.

The slightly increased lithium content from $x = 0.30$ to $x = 0.48$ does not alter the structure of the vanadium oxide framework: there are still three vanadium sites, one octahedral and two in square pyramidal coordination, and only minor differences in the lattice parameters and puckering angle ($\mu = 13.86^{\circ}$). The significant difference is in the position of the lithium atoms: in the $x = 0.48$ compound lithium occupies the M3 site

rather than the M1 site, as defined by Withers *et al* [146], but despite the shift in position, lithium ions are again found in stable tetrahedral coordination.

Li-O	Separation/Å
2 x Li-O10	2.03
Li-O12	2.03
Li-O8	1.82

Table 1.9 – Lithium-oxygen separations in β'-$Li_{0.48}V_2O_5$ [123, 144].

$Li_{0.67}V_2O_5$:

Further increase in the lithium content changes the vanadium oxide framework slightly, changing coordination of one vanadium atom by oxygen from square pyramidal to octahedral. Lithium ions are again tetrahedrally coordinated by oxygen, however, the tetrahedron is more distorted with two lithium-oxygen separations much longer and one much shorter (*table 1.10*) than the ideal 1.97Å [145] for a stable lithium site.

Li-O	Separation/Å
2 x Li-O10	2.23
Li-O12	2.07
Li-O8	1.69

Table 1.10 – Lithium-oxygen separations in β'-$Li_{0.67}V_2O_5$ [122].

1.4.3 Gamma phase: γ-$Li_xV_2O_5$

The gamma phase is commonly thought of as the thermodynamic product in this system [120], and can be synthesised at high temperature with varying lithium content, x, by standard solid-state methods according to Ueda and Galy [101, 103, 147]. Structural data published are for high temperature phases with lithium content, $x = 1$, studied using x-ray diffraction [122, 124, 148, 149]. γ-LiV_2O_5 has been described in two orthorhombic space groups, $Pna2_1$ and Pnma. Two basically identical structures have been published in Pnma; only one will be discussed in detail here. For the sake of continuity, having already referred to Galy's work, we have chosen to use his Pnma structure for comparison with α-$Li_xV_2O_5$, since the reported structures, despite differences in space group, have only minor differences in lattice parameters, and atom environments as represented by bond lengths and angles. γ-LiV_2O_5 has a structure made up of layers of edge and corner-sharing vanadium oxide square pyramids, with two distinct vanadium sites, as described in *table 1.11* and *figure 1.34*.

Space Group	Lattice Parameters/Å		
	a	b	c
Pnma	9.702(5)	3.607(2)	10.664(6)
	α	β	γ
	90	90	90
Atom	**x**	**y**	**z**
Li1	0.163(6)	0.25	0.225(5)
V2	0.3762(5)	0.25	0.4991(5)
V3	0.0661(5)	0.25	0.5995(5)
O4	0.241(2)	0.25	0.633(2)
O5	0.483(2)	0.25	0.770(2)
O6	0.282(2)	0.25	0.376(2)
O7	0.574(2)	0.25	0.451(2)
O8	0.440(2)	0.25	0.046(2)

Table 1.11 – Atom positions and lattice parameters for γ-LiV_2O_5 as defined by Galy et al. [122] R-factor = 0.068.

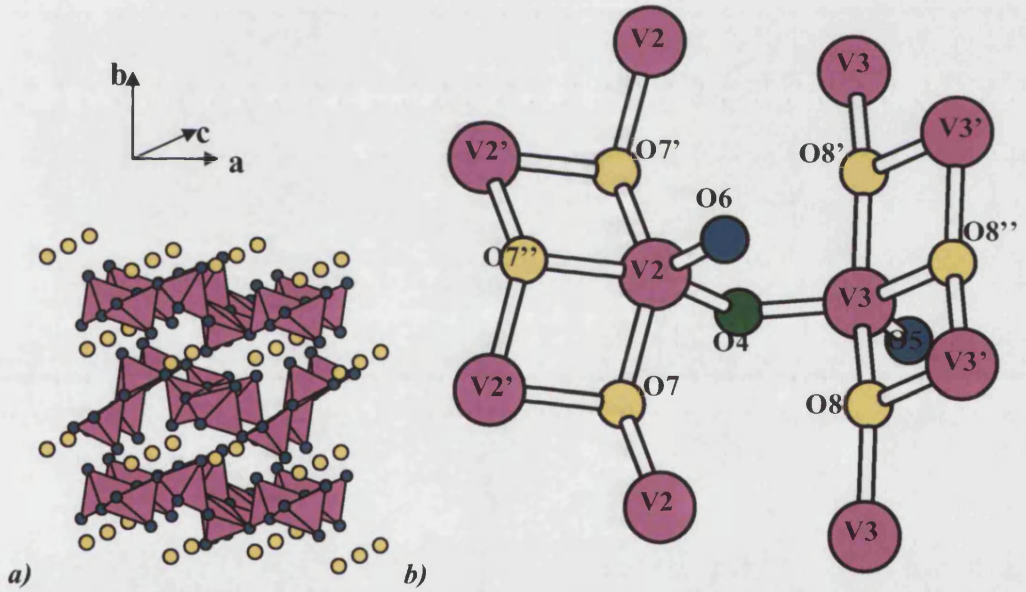

Figure 1.34 – a) Structure of γ-LiV_2O_5 [122] and b) Vanadium environment in γ-LiV_2O_5 [122]. Vanadium atoms are shown in pink, apical oxygen atoms are shown in blue, edge shared oxygen positions in yellow and corner shared oxygen positions in green. Atoms are labelled according to table 1.11.

Table 1.12 gives the bond lengths and angles in γ-$Li_xV_2O_5$. The vanadium environment described here is very different to that reported in α-$Li_{0.04}V_2O_5$ previously discussed, having in general longer bond lengths and less regular angles due to the larger amount of intercalated lithium causing reduction of a greater proportion of vanadium from V^{5+} to V^{4+} and increased distortion within the layers, also evident from the large puckering angle $\mu = 64.65^{\circ}$.

Bond Lengths in γ–LiV_2O_5 [123, 148]			
Bond	**Length /Å**	**Bond**	**Length/ Å**
V2-O6	1.60	V3-O5	1.61
V2-O4	1.94	V3-O4	1.73
V2-O7	1.94	V3-O8	1.89
V2-O7'	1.94	V3-O8'	1.89
V2-O7''	1.99	V3-O8''	1.98
V2-V2'	3.00	V3-V3'	3.07
V2-V2	3.61	V3-V3	3.61
V2-V3	3.19	V3-V2	3.19
Bond Angles in γ–LiV_2O_5 [122]			
Atoms	**Angle/°**	**Atoms**	**Angle/°**
O7/O7'-V2-O7''	80.23	O8/O8'-V3-O8''	75.16
O7/O7'-V2-O4	88.08	O8/O8'-V3-O4	95.32
O7/O7'-V2-O6	111.54	O8/O8'-V3-O5	104.19
O7''-V2-O6	109.88	O8''-V3-O5	111.66
O4-V2-O6	102.58	O4-V3-O5	108.20
V2-O7-V2'	98.77	V3-O8-V3'	104.84
V2-O7-V2	136.54	V3-O8-V3	144.71
V2-O4-V3	120.68	V3-O4-V2	120.68

Table 1.12 – Vanadium-oxygen bond lengths and angles and vanadium-vanadium distances for γ–LiV_2O_5 [122].

Lithium coordination in γ-LiV_2O_5 is octahedral, as shown in *figure 1.35* and described in *table 1.13*. The stability of this arrangement is much superior to that of the bicapped triangular prismatic coordination observed in α-$Li_{0.04}V_2O_5$ [145, 146]. As the amount of lithium intercalated increases, the stability of the guest ions becomes more important: although there is an energy cost to distort the host lattice vanadium oxide layers, this is compensated for by the stability of the intercalated lithium ions, hence γ-$Li_xV_2O_5$ is the thermodynamic product.

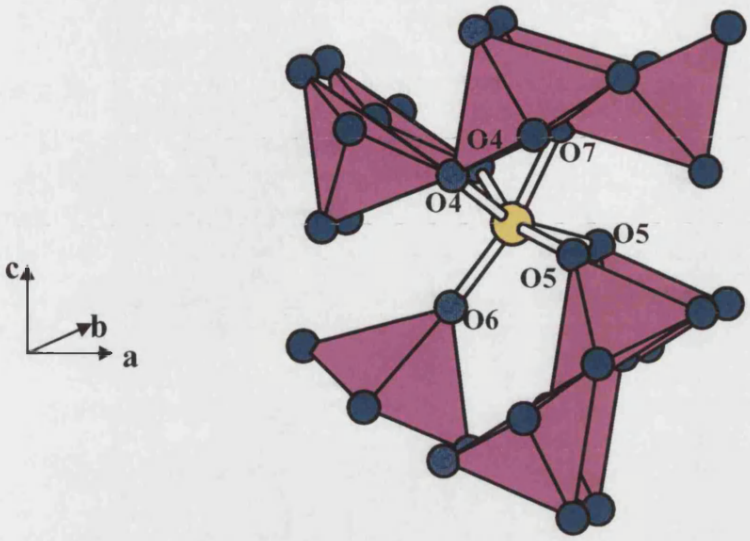

Figure 1.35 - Octahedral lithium coordination by oxygen in layered γ-LiV_2O_5 in space group Pnma [122].

Li-O	Pnma separations/Å
2 x O4	2.25
2 x O5	2.34
O6	1.98
O7	2.07

Table 1.13 – Lithium-oxygen separations in γ-LiV_2O_5 [122].

1.4.4 Epsilon phase: ε-$Li_xV_2O_5$

Originally reported as one phase, it has since been put forward by Rozier, Galy et al. [150] that the range of x values believed to be a single phase, ε-$Li_xV_2O_5$ is in fact made up of two kinds of structures: $0.33 \leq x \leq 0.47$ is made up of ε_1, $0.47 \leq x \leq 0.53$ is a biphasic region containing both ε_1 and ε_2, while $0.53 \leq x \leq 0.70$ contains only ε_2. These phases, which have also been referred to as ε and ε' [145, 151], differ in regard to their behaviour at decreased temperature. According to Rozier *et al*, ε_1 undergoes a doubling of the cell depth and layer spacing, while ε_2 undergoes the same doubling and a slip of a layer, opening the β lattice parameter and transforming to a monoclinic system, foreshadowing transition to the higher lithium content δ phase [152]. Both are metastable phases and may be synthesised at room temperature by soft chemistry [101, 127, 147] or electrochemical methods [121, 130], or by the phase transition at higher temperature of delta $Li_xV_2O_5$ [124]. The room temperature structure of both phases have been studied with neutron, x-ray and electron diffraction, however, although wave

vectors for the incommensurately modulated lithium ordering have been determined [145, 151, 153-155] the structure has not been fully described. Structural data published on this phase is for ε-LiV_2O_5 synthesised via high temperature transformation from δ-LiV_2O_5 at 140°C, studied using x-ray diffraction, and this high temperature phase has been described in the orthorhombic space groups Pmmn, $P2_1mn$, and in $Pmn2_1$ with a doubled layer spacing.

Pmmn [124]:

Space Group	Lattice Parameters/Å		
	a	b	c
Pmmn	11.3552(6)	3.5732(2)	4.6548(3)
	α	β	γ
	90	90	90
Atom	**x**	**y**	**z**
Li1	0.25	0.75	0.284(5)
V2	0.4002(1)	0.25	0.8932(2)
O3	0.1193(3)	0.25	0.5510(7)
O4	0.5733(3)	0.25	-0.0221(6)
O5	0.25	0.25	0.0293(9)

Table 1.14 – Atom positions and lattice parameters for ε-LiV_2O_5 as defined by Satto et al. [124] R-factor = 0.026.

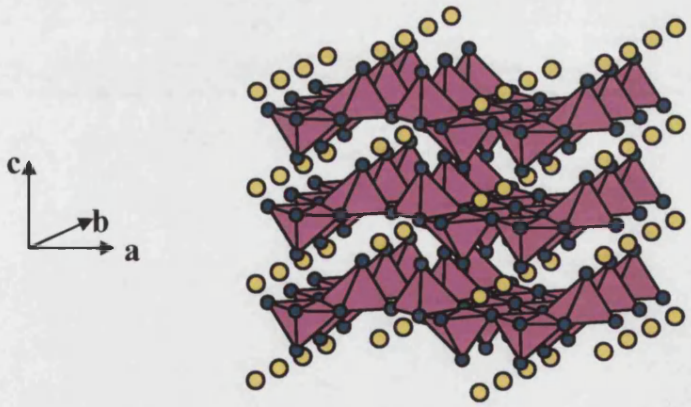

Figure 1.36 – Structure of ε-LiV_2O_5 in space group Pmmn [124].

The Pmmn structure has one vanadium site, implying that there is no ordering of electrons but an average vanadium oxidation state of $V^{4.5+}$ for LiV_2O_5. From *figure 1.36* it can be seen that the layered structure of edge and corner-sharing square pyramids is retained. Comparisons of the vanadium-oxygen bond lengths and angles in this structure (*table 1.15*) show a slightly longer average bond length of 1.85Å compared with 1.82Å

in V_2O_5. The bond angles are slightly different, and there is a puckering angle of μ = 7.46°.

Bond Lengths in ε–LiV_2O_5 [124]	
V-O3	1.61
V-O5	1.82
V-O4	1.91
V-O4'	1.91
V-O4''	2.00
V-V1	3.05
V-V2'	3.57
V-V2	3.41

Table 1.15 – Vanadium-oxygen bond lengths and vanadium-vanadium distances for ε–LiV_2O_5.

The lithium environment here is like that of the alpha phase: a bicapped trigonal prism, as shown in *figure 1.37* with lithium-oxygen separations given by *table 1.16*:

Li-O	Separation/Å
2 x O4	2.35
2 x O5	2.14
4 x O3	2.63

Table 1.16 – Lithium-oxygen separations for ε-LiV2O5 in Pmmn space group [124].

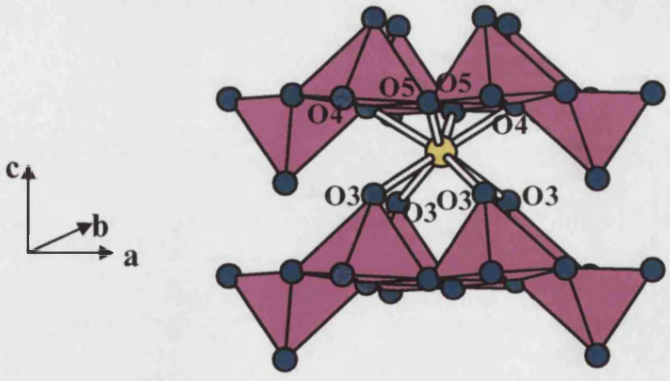

Figure 1.37 – Lithium coordination in ε-LiV_2O_5 in Pmmn space group [124].

It is impossible in this structure for lithium to be tetrahedrally or octahedrally coordinated by oxygen atoms. The cuboctahedral cavities which are available in this phase, and the other published structures, are too large and therefore energetically unstable sites for lithium coordination [145]. For this high concentration of lithium, the

situation differs from that of the alpha phase where the large separation between Li^+ means small mutual influence and therefore simply a disordered arrangement. Here repulsive Li^+-Li^+ forces and/or elastic strain lead to a regular distribution of the intercalated lithium ions, resulting in the formation of an ordered commensurate or incommensurate superstructure. Katzke has worked with electron diffraction to propose a model for the ordering of lithium ions within the structure [145, 151, 153-157] which will be discussed in more detail alongside the relevant experimental work in chapter four.

The reported $Pmn2_1$ structure is likely to be found close to the transition to the delta phase, in which a shift of $^c/_2$ along [001], causing doubling of the layer spacing, is found [127]. Although there are two crystallographically distinct vanadium sites for this structure, vanadium-oxygen bond lengths and angles are identical to those observed in the Pmmn space group, suggesting that the drop in symmetry from Pmmn to $Pmn2_1$ is a consequence solely of the doubling of the layer spacing, *b*, with respect to the Pmmn structure. Since the vanadium environments are not distinct, there is no likelihood of charge ordering to produce separate V^{4+} and V^{5+} sites, there is an average oxidation state of $V^{4.5+}$, as found in Pmmn.

$P2_1mn$ [124]:

Atom	x	y	z
Li1	0.218(2)	0.5	0.280(4)
V2	0.5999(1)	0.5	0.1131(8)
V3	0.4004(1)	0	0.8998(8)
O4	0.621(1)	0.5	0.466(3)
O5	0.383(1)	0	0.568(3)
O6	0.424(1)	0.5	0.000(2)
O7	0.571(1)	0	-0.0455(2)
O8	0.254(2)	0	0.0285(9)

Table 1.17 – Atom positions for ε-$Li_xV_2O_5$ as defined by Satto et al. [124] R-factor = 0.026.

In the $P2_1mn$ space group, lattice parameters are identical to those for the Pmmn representation, and the structure differs only in the details of site degeneracy: the suppression of the mirror plane normal to the *a* axis that is present in Pmmn leads to differentiation of two crystallographic sites for vanadium, allowing the possibility of localisation of electrons for separate V^{4+} and V^{5+} sites. The $P2_1mn$ structure is made up of chains of V2 site square pyramids sharing edges and corners with chains of V3 site

square pyramids, as shown in *figure 1.38*. Degeneracy of oxygen atoms is also affected: each vanadium atom is coordinated by five oxygen atoms occupying four crystallographically distinct oxygen atoms, whereas in the Pmmn structure there are only three crystallographically distinct oxygen sites. This extra site allows the possibility of more variation in vanadium-oxygen bond lengths.

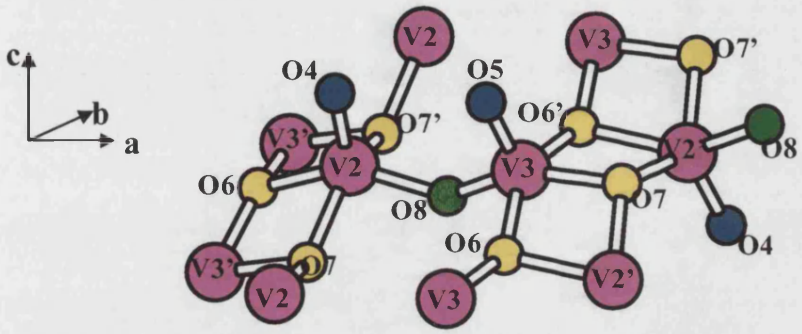

Figure 1.38 – Vanadium environment in ε-LiV_2O_5 as published by Satto et al. in space group $P2_1mn$ [124]. Vanadium atoms are shown in pink, apical oxygen atoms are shown in blue, edge shared oxygen positions in yellow and corner shared oxygen positions in green.

A comparison of bond lengths and angles for the two vanadium sites is given in *table 1.18* and it can be seen from this that one vanadium site is very similar to that found in V_2O_5 (V^{5+}), having an average bond length of 1.80Å compared with 1.82Å for V_2O_5 [116], while the other has longer bonds averaging 1.90Å, similar to those found in VO_2 (V^{4+}). The puckering angle for this structure is $\mu = 7.49°$, close to that for the Pmmn structure.

Bond	Length/ Å	Bond	Length/ Å
V2-O4	1.66	V3-O5	1.56
V2-O8	1.87	V3-O8	1.77
V2-O7	1.96	V3-O6	1.87
V2-O7	1.96	V3-O6	1.87
V2-O6	2.07	V3-O7	1.95
V2-V3'	3.05	V3-V2'	3.05
V2-V2	3.57	V3-V3	3.57
V2-V3	3.41	V3-V2	3.41

Table 1.18 – Comparison of vanadium-oxygen bond lengths and angles and vanadium-vanadium distances for ε–LiV_2O_5.

1.4.5 Delta phase: δ-$Li_xV_2O_5$

This phase is metastable and undergoes a transition to ε-$Li_xV_2O_5$ at about 100°C [124]. Like ε-LiV_2O_5, the delta phase has been reported as a low symmetry version in the $Pmn2_1$ space group, allowing the vanadium oxide layers and lithium atoms to be described independently [127], but it is the only phase to have been reported fully from the study of a room temperature synthesised sample, δ-LiV_2O_5, using both x-ray and neutron diffraction techniques [158, 159] and the Cmcm structure obtained from this study is described below.

Space Group	**Lattice Parameters/Å**		
	a	**b**	**c**
Cmcm	3.6047(2)	9.9157(5)	11.2479(4)
	α	**β**	**γ**
	90	90	90
Atom	**x**	**y**	**z**
Li1	0.5	0.3992(18)	0.25
V2	0	0.2057(2)	0.3987(2)
O3	0	0.0471(4)	0.3728(4)
O4	0	0.2449(4)	0.5745(4)
O5	0	0.2808(6)	0.25

Table 1.19 – Atom positions and lattice parameters for δ-LiV_2O_5 in space group Cmcm [158, 159] R-factor = 0.033.

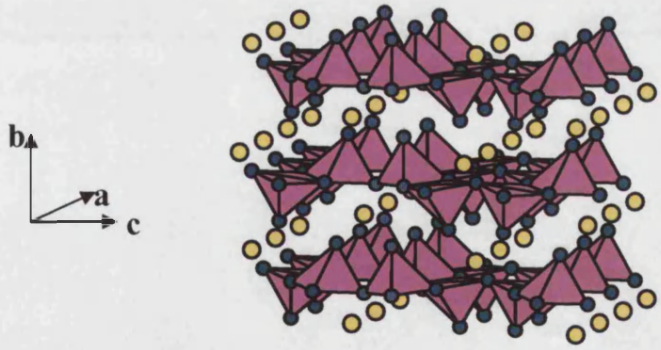

Figure 1.39 – Structure of δ-LiV_2O_5 in space group Cmcm [158, 159].

There is one vanadium site in the Cmcm structure. From *figure 1.39* it can be seen that the layered structure of edge and corner-sharing square pyramids observed in previous phases is retained, although there is a shift in the layers of $^a/_2$ along [100] leading to a doubling of the layer spacing, *b*. Comparison of the vanadium-oxygen bond lengths (*table 1.20*) shows a slight increase in bond length compared with V_2O_5. Average bond

length is 1.85Å, compared with 1.82Å for V_2O_5. The puckering angle $\mu = 11.14^{\circ}$, larger than that observed for α- and ε-$Li_xV_2O_5$ but smaller than in γ-, β- and β'-$Li_xV_2O_5$.

Bond Lengths in δ–LiV_2O_5 [158, 159]	
V-O3	1.60
V-O5	1.83
V-O4	1.89
V-O4'	1.89
V-O4''	2.02
V-V1	2.99
V-V2	3.60
V-V2'	3.40

Table 1.20 – Comparison of vanadium-oxygen bond lengths and angles and vanadium-vanadium distances for δ–LiV_2O_5 [158, 159].

The shift in layers along the cell depth axis [100] creates an octahedral cavity for lithium coordination, shown in *figure 1.40*, much more stable than the bicapped trigonal prism available in the epsilon phase. The lithium-oxygen separations are given in *table 1.21*. The average separation 2.20Å is slightly longer than the ideal 2.14Å for lithium in an octahedral environment [145].

Li-O	**Separation/Å**
2 x O3	2.01
2 x O4	2.44
2 x O5	2.16

Table 1.21 – Lithium-oxygen separations for δ-LiV2O5 in Cmcm space group [158, 159].

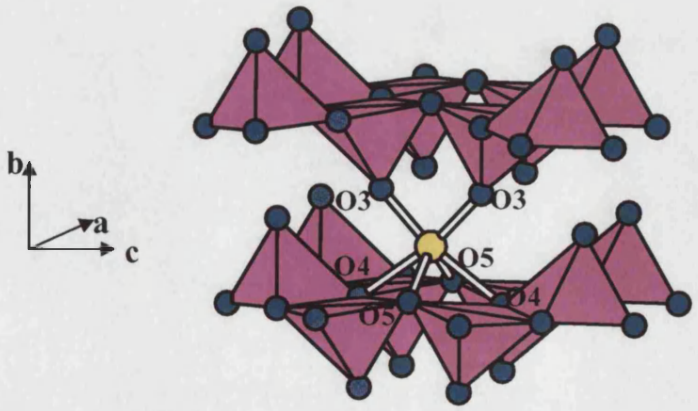

Figure 1.40 – Lithium coordination in δ-LiV_2O_5 in Cmcm space group [158, 159].

Description in the lower symmetry $Pmn2_1$ space group [127] reveals that vanadium and lithium environments in this description are identical to those in the Cmcm description, differing only in their degeneracy: the layer shift of $^{c}/_{2}$ along [001] and subsequent doubling of the layer spacing parameter, *b*, incur the necessity of two vanadium and two lithium sites in the $Pmn2_1$ description.

Although a significant amount of work has been published on the structure of the $Li_xV_2O_5$ phases, it is almost exclusively on the high temperature synthesised phases and almost entirely from x-ray diffraction data. Crystallographic data on the room temperature phases is limited and although there is expected to be a link between room temperature and high temperature structures this has not yet been clearly established, although work by Galy has established mechanisms for transformation between phases at high temperature [103, 124, 127]. Study using both neutron and x-ray diffraction should enable detailed structure solution including the determination of the most appropriate space group where there are current ambiguities: such a study is described in this thesis.

1. K. Fredenhagen and G. Cadenbach, *Z. Anorg. Allg. Chem.*, **158,** (1926).
2. A.J. Jacobson, *Intercalation Reactions of Layered Compounds*, in *Solid State Chemistry, Compounds*, A.K. Cheetham and P. Day, Editors. 1992, OUP: Oxford.
3. A.M. Fogg, J.S. Dunn, S.-G. Shyu, D.R. Cary, and D. O'Hare, *Chem. Mater.*, **10,** 351-355 (1998).
4. A.M. Fogg, J.S. Dunn, and D. O'Hare, *Chem. Mater.*, **10,** 356-360 (1998).
5. A.M. Fogg and D. O'Hare, *Chem. Mater.*, **11,** 1771-1775 (1999).
6. A.M. Fogg, V.M. Green, H.G. Harvey, and D. O'Hare, *Adv. Mater.*, **11,** 1466-1469 (1999).
7. L. Lei, R.P. Vijayan, and D. O'Hare, *J. Mater. Chem.*, **11,** 3276-3280 (2001).
8. A.R. West, *Basic Solid State Chemistry*. 1997, Chichester: J. Wiley and Sons.
9. D. O'Hare, *Inorganic Intercalation Compounds*, in *Inorganic Materials 2nd Edition*, D.W. Bruce and D. O'Hare, Editors. 1996, John Wiley & Sons Ltd.
10. J.G. Bednorz and K.A. Muller, *Z. Phys. B Cond. Matt.*, **64,** 189-193 (1986).

11. G. Xiao, F.H. Streitz, A. Gavrin, Y.W. Du, and C.L. Chien, *Phys. Rev. B,* **35,** 8782-8784 (1987).
12. N.C. Hyatt, G.B. Peacock, I. Gameson, K.L. Moran, M. Slaski, M.O. Jones, A.J. Ellis, Y.E. Gold, R. Dupree, and P.P. Edwards, *Int. J. Inorg. Mat.,* **1,** 87-95 (1999).
13. J.G. Bednorz, M. Takashige, and K.A. Muller, *Europhys. Lett.,* **3,** 379-385 (1987).
14. M.K. Wu, J.R. Ashburn, C.J. Torng, P.H. Hor, R.L. Meng, L. Gao, Z.J. Huang, Y.Q. Wang, and C.W. Chu, *Phys. Rev. Lett.,* **58,** 908-910 (1987).
15. C.N.R. Rao, *J. Mater. Chem.,* **9,** 1-14 (1999).
16. M.W. Wagner, C. Liebenow, and K. Luhder, *J. Power Sources,* **54,** 369-372 (1995).
17. M.W. Wagner, *Electrochim. Acta,* **42,** 1623-1625 (1997).
18. O. Chusid, Y.E. Ely, and D. Aurbach, *J. Power Sources,* **43,** 47-64 (1993).
19. M.W. Wagner, C. Liebenow, and J.O. Besenhard, *J. Power Sources,* **68,** 328-332 (1997).
20. N. Arun, S. Vasudevan, and K.V. Ramanathan, *J. Chem. Phys.,* **119,** 2840-2848 (2003).
21. N. Arun, S. Vasudevan, and K.V. Ramanathan, *J. Chem. Phys.,* **119,** 2849-2853 (2003).
22. B.C.H. Steele, J.M. Shemilt, and D.A. Winn, *Materials Research Bulletin,* **11,** 559-66 (1976).
23. C.J. Pan, Y.J. Lee, B. Ammundsen, and C.P. Grey, *Chem. Mater.,* **14,** 2289-2299 (2002).
24. M.S. Whittingham and P.Y. Zavalij, *Int. J. Inorg. Mater.,* **3,** 1231-1236 (2001).
25. V. Vivier, S. Belair, C. Cachet-Vivier, J.Y. Nedelec, and L.T. Yu, *J. Power Sources,* **103,** 61-66 (2001).
26. C.M. Varma, *Rev. Mod. Phys.,* **48,** 219 (1976).
27. J.M. Lawrence, P.S. Riseborough, and R.D. Parks, *Rep. Prog. Phys.,* **44,** 1 (1981).
28. P. Wachter, in *Handbook on physics and chemistry of rare earths*, K.A. Gschneider and L. Eyrig, Editors. 1994: Amsterdam. p. 177.
29. T. Goto and B. Luethi, *Advances in Physics,* **52,** 67-118 (2003).

30. J.E.L. Waldron, M.A. Green, and D.A. Neumann, *J. Am. Chem. Soc.*, **123,** 5833-5834 (2001).
31. A. Lappas, J.E.L. Waldron, M.A. Green, and K. Prassides, *Phys. Rev. B,* **65,** 134405 (2002).
32. T. Ohama, A. Goto, T. Shimuzu, E. Ninomiya, H. Sawa, M. Isobe, and Y. Ueda, *J. Phys. Soc. Jpn.,* **69,** 2751 (2000).
33. H. Sawa, E. Ninomiya, T. Ohama, H. Nakao, K. Ohwada, Y. Murakami, Y. Fujii, Y. Noda, M. Isobe, and Y. Ueda, *J. Phys. Soc. Jpn.,* **71,** 385-388 (2002).
34. E.J. Verwey, *Nature,* **144,** 327 (1939).
35. E.J. Verwey, P.W. Haayman, and F.C. Romeijn, *J. Chem. Phys.,* **15,** 181 (1947).
36. M. Imada, A. Fujimori, and Y. Tokura, *Rev. Mod. Phys.,* **70,** 1039-1263 (1998).
37. Y. Fujii, G. Shirane, and Y. Yamada, *Phys. Rev. B,* **11,** 2036 (1975).
38. J. Garcia, G. Subias, M.G. Proietti, J. Blasco, H. Renevier, J.L. Hodeau, and Y. Joly, *Phys. Rev. B,* **63,** 054110 (2001).
39. Y. Konoike, T. Toyoda, K. Yamawaki, and S. Sakaki, *Proceedings of the fourth symposium on atomic-scale surface and interface dynamics,* 437 (2000).
40. J.P. Wright, J.P. Attfield, and P.G. Radaelli, *Phys. Rev. Lett.,* **87,** 266 401 (2001).
41. P.D. Battle, T.C. Gibb, and S. Nixon, *J. Solid State Chem.,* **77,** 124 (1988).
42. P.D. Battle, T.C. Gibb, and P. Lightfoot, *J. Solid State Chem.,* **84,** 271-279 (1990).
43. M.S. Takano and Y. Takeda, *Bull. Inst. Chem. Res.,* **61,** 406 (1983).
44. P.D. Battle, T.C. Gibb, and P. Lightfoot, *J. Solid State Chem.,* **84,** 237-244 (1990).
45. J.Q. Li, Y. Matsui, S.K. Park, and Y. Tokura, *Phys. Rev. Lett.,* **79,** 297 (1997).
46. S. Blundell, *Magnetism in Condensed Matter.* Oxford Master Series in Condensed Matter Physics. 2001: Oxford University Press.
47. T.M. Rice, S. Gopalan, and M. Sigrist, *Europhys. Lett.,* **23,** 445 (1993).
48. L.P. Regnault, A.H. Moudden, J.P. Boucher, E. Lorenzo, A. Hiess, A. Vietkin, and A. Revcolevschi, *Physica B,* **259-261,** 1038-1039 (1999).
49. K. Ishii, A. Yamashita, K. Ohishi, J. Akimitsu, R. Kadono, N. Kobayashi, M. Takano, and Z. Hiroi, *Physica B,* **289-290,** 165-167 (2000).

50. T. Nagata, H. Fujino, K. Satoh, N. Yamamori, J. Akimitsu, S. Katano, M. Nishi, K. Kakurai, M. Hiroi, M. Sera, N. Kobayashi, K. Tenya, H. Amitsuka, T. Takigawa, H. Inago, and T. Sakakibara, *J. Phys. Soc. Jpn.,* **70,** 2419-2424 (2001).

51. R.S. Eccleston, *Phys. Rev. Lett.,* **81,** 1701 (1998).

52. J. Akimitsu, K. Ohishi, T. Yokoo, K. Kakuta, H. Fujino, T. Nagata, R. Kadono, M. Nishi, K. Kakurai, and S. Katano, *Physica B,* **289-290,** 157-160 (2000).

53. R. Bewley, R.S. Eccleston, T. Nagata, and J. Akimitsu, *Physica B,* **276-278,** 662-663 (2000).

54. T. Ohta, *J. Phys. Soc. Jpn.,* **66,** 3107 (1997).

55. S.W. Cheong, H.Y. Hwang, C.H. Chen, B. Batlogg, L.W. Rupp, and S.A. Carter, *Phys. Rev. B,* **49,** 7088 (1994).

56. C.H. Chen, S.W. Cheong, and A.S. Cooper, *Phys. Rev. Lett.,* **71,** 2461 (1993).

57. S.H. Lee and S.W. Cheong, *Phys. Rev. Lett.,* **79,** 2514 (1997).

58. Y. Tokura, A. Urushibara, Y. Moritomo, T. Arima, A. Asamitsu, G. Kido, and N. Furukawa, *J. Phys. Soc. Jpn.,* **63,** 3931 (1994).

59. A. Urushibara, Y. Moritomo, T. Arima, A. Asamitsu, G. Kido, and Y. Tokura, *Phys. Rev. B,* **51,** 1113 (1995).

60. Y. Tomioka, A. Asamitsu, H. Kuwahara, Y. Moritomo, and Y. Tokura, *Phys. Rev. B,* **53,** 1689 (1996).

61. C. Zener, *Phys. Rev.,* **82,** 403 (1951).

62. P.W. Anderson and H. Hasegawa, *Phys. Rev.,* **100,** 675 (1955).

63. P.G. De Gennes, *Phys. Rev.,* **118,** 141 (1960).

64. H. Kuwahara, Y. Tomioka, A. Asamitsu, Y. Moritomo, and Y. Tokura, *Science,* **270,** 961 (1995).

65. Y. Tokura, H. Kuwahara, Y. Moritomo, Y. Tomioka, and A. Asamitsu, *Phys. Rev. Lett.,* **76,** 3184 (1996).

66. J.B. Goodenough, *Phys. Rev.,* **100,** 564 (1955).

67. E.O. Wollan and W.C. Koehlar, *Phys. Rev.,* **100,** 545 (1955).

68. Z. Jirak, S. Krupicka, Z. Simsa, M. Dloucha, and S. Vraislav, *J. Magn. magn. Mater.,* **15-18,** 153 (1985).

69. H. Yoshizawa, H. Kawano, Y. Tomioka, and Y. Tokura, *Phys. Rev. B,* **52,** R13145 (1995).

70. P. Schiffer, A.P. Ramirez, W. Bao, and S.W. Cheong, *Phys. Rev. Lett.*, **75,** 3336 (1995).

71. Y. Endoh, K. Hirota, S. Ishihara, S. Okamoto, Y. Murakami, A. Nishizawa, T. Fukuda, H. Kimura, H. Nojiri, K. Kaneko, and S. Maekawa, *Phys. Rev. Lett.*, **82,** 4328 (1999).

72. Y. Yamada, O. Hino, S. Nohdo, R. Kanao, T. Inami, and S. Katano, *Phys. Rev. Lett.*, **77,** 904 (1996).

73. H. Hazama, Y. Nemoto, T. Goto, Y. Tomioka, A. Asamitsu, and Y. Tokura, *J. Phys. Soc. Jpn.*, **71,** 139 (2002).

74. M.V. Zimmermann, J.P. Hill, M. Blume, D. Casa, B. Keimer, Y. Murakami, Y. Tomioka, and Y. Tokura, *Phys. Rev. Lett.*, **83,** 4872 (1999).

75. S. Mori, T. Katsufuji, N. Yamamoto, C.H. Chen, and S.W. Cheong, *Phys. Rev. B,* **59,** 13573 (1999).

76. Y. Tokura, Y. Tomioka, H. Kuwahara, A. Asamitsu, Y. Moritomo, and M. Kasai, *J. Appl. Phys.*, **79,** 5288 (1996).

77. Y. Moritomo, H. Kuwahara, Y. Tomioka, and Y. Tokura, *Phys. Rev. B,* **55,** 7549 (1997).

78. V. Kiryukhin, D. Cax, J.P. Hill, B. Keimer, A. Vigliante, Y. Tomioka, and Y. Tokura, *Nature,* **386,** (1997).

79. K. Miyano, T. Tanaka, Y. Tomioka, and Y. Tokura, *Phys. Rev. Lett.*, **78,** 4257 (1997).

80. A. Asamitsu, Y. Tomioka, H. Kuwahara, and Y. Tokura, *Nature,* **388,** 50 (1997).

81. T. Kimura, Y. Tomioka, H. Kuwahara, A. Asamitsu, M. Tamura, and Y. Tokura, *Science,* **274,** 1698 (1996).

82. T. Perring, G. Aeppli, Y. Moritomo, and Y. Tokura, *Phys. Rev. Lett.*, **78,** 3197 (1998).

83. Y. Moritomo, A. Asamitsu, H. Kuwahara, and Y. Tokura, *Nature,* **380,** 141 (1996).

84. Y. Wakabayashi, Y. Murakami, I. Koyama, T. Kimura, Y. Tokura, Y. Moritomo, K. Hirota, and Y. Endoh, *J. Phys. Soc. Jpn.*, **69,** 2731-2734 (2000).

85. A. Carpy and J. Galy, *Acta Cryst. B,* **31,** 1481 (1975).

86. H.G. von Schnering, Y. Grin, M. Kaupp, R.K. Kremer, O. Jepsen, T. Chattergi, and M. Weiden, *Z. Kristallogr.*, **213,** 246 (1998).

87. H. Smolinski, C. Gros, W. Weber, U. Peuchert, G. Roth, M. Weiden, and C. Geibel, *Phys. Rev. Lett.*, **80,** 5164 (1998).

88. A. Meetsma, J.L. De Boer, A. Damascelli, J. Jugoudez, A. Revcolevschi, and T.T.M. Palstra, *Acta Cryst. C,* **54,** 1558 (1998).

89. M. Onoda and N. Nishiguchi, *J. Solid State Chem.*, **127,** 359-362 (1996).

90. T. Ohama, Y. Isobe, H. Yasuoka, and Y. Ueda, *J. Phys. Soc. Jpn.*, **66,** 545 (1997).

91. T. Ohama, M. Isobe, H. Yasuoka, and Y. Ueda, *Phys. Rev. B,* **59,** 3299 (1999).

92. M. Isobe and Y. Ueda, *J. Phys. Soc. Jpn.*, **65,** 1178 (1996).

93. Y. Fujii, H. Nakao, T. Yosihama, M. Nishi, K. Nakajima, K. Kakurai, M. Isobe, Y. Ueda, and H.J. Sawa, *J. Phys. Soc. Jpn.*, **66,** 326 (1997).

94. M. Hase, I. Terasaki, and K. Uchinokura, *Phys. Rev. Lett.*, **23,** 3651 (1993).

95. M. Hase, *Phys. Rev. Lett.*, **70,** 3651 (1971).

96. M. Koeppen, D. Pankert, R. Hauptmann, M. Lang, M. Weiden, C. Geibel, and F. Steglich, *Phys. Rev. B,* **57,** 8466 (1998).

97. H. Sawa, E. Ninomiya, T. Ohama, and H. Nakao, *J. Phys. Soc. Jpn.*, **71,** 385 (2002).

98. Y. Ueda, H. Yamada, M. Isobe, and T. Yamauchi, *J. Alloy. Cpds.*, **317-318,** 109-114 (2001).

99. L.P. Regnault, J.E. Lorenzo, J.P. Boucher, B. Grenier, A. Hiess, T. Chatterji, J. Jegoudez, and A. Revcolevschi, *Physica B,* **276-278,** 626-627 (2000).

100. J. Riera and D. Poilblanc, *Phys. Rev. B,* **59,** 2667 (1999).

101. Y. Ueda, *Chem. Mater.*, **10,** 2653-2664 (1998).

102. N.N. Greenwood and A. Earnshaw, *Chemistry of the Elements*. 1993, Oxford: Pergamon Press Ltd.

103. J. Galy, *J. Solid State Chem.*, **100,** 229-245 (1992).

104. J. Galy and G. Miehe, *SSSCF,* **1,** 433-448 (1999).

105. J.B. Goodenough, *Phys. Rev.*, **117,** 1442 (1960).

106. Y. Oka, T. Yao, N. Yamamoto, Y. Ueda, and A. Hayashi, *J. Solid State Chem.*, **105,** 271-278 (1993).

107. Y. Oka, T. Yao, and N. Yamamoto, *J. Solid State Chem.*, **112,** 196-198 (1994).

108. Y. Oka, S. Sato, T. Yao, and N. Yamamoto, *Journal of Solid State Chemistry,* **141,** 594-598 (1998).

109. K. Waltersson, B. Forslund, K.A. Wilhelmi, S. Andersson, and J. Galy, *Acta Cryst. B,* **30,** 2644-2652 (1974).

110. K.A. Wilhelmi and C. Waltersson, *Acta. Chem. Scand.,* **24,** 3409-3411 (1970).

111. J.M. Honig, *Transitions in selected transition metal oxides,* in *The metallic and non-metallic states of matter,* P.P. Edwards and C.N.R. Rao, Editors. 1985. p. 261-286.

112. L.W. Finger and R.M. Hazen, *J. Appl. Phys.,* **51,** 5362-5367 (1980).

113. R.E. Loehman, C.N.R. Rao, and J.M. Honig, *J. Phys. Chem.,* **73,** 1781-1784 (1969).

114. A. Bystrom, K.A. Wilhelmi, and O. Brotzen, *Acta Chem. Scand.,* **4,** 1119 (1950).

115. H. Bachmann, F. Ahmed, and W. Barnes, *Zeitschrift fuer Kristallographie, Kristallogeometrie, Kristallphysik, Kristallchemie,* **1961,** 110-131 (1961).

116. R. Enjalbert and J. Galy, *Acta Crys. Sect. C,* **42,** 1467-1469 (1986).

117. K. Katsumata, *Current Opinion in Solid State and Materials Science,* **2,** 226 (1997).

118. Y. Ueda, M. Isobe, and T. Yamauchi, *J. Phys. Chem. Solids,* **63,** 951-955 (2002).

119. B. Pecquenard, D. Gourier, and N. Baffier, *Solid State Ionics,* **78,** 287-303 (1995).

120. D.W. Murphy, P.A. Christian, F.J. DiSalvo, and J.V. Waszczak, *Inorganic Chemistry,* **18,** 2800 (1979).

121. J.M. Cocciantelli, *J. Power Sources,* **34,** 103 (1991).

122. J. Galy, J. Darriet, and P. Hagenmuller, *Rev. Chim. Miner.,* **8,** 509 (1971).

123. J. Galy, A. Hardy, A. Casalot, and M. Pouchard, *Bulletin de Societe Chimie de France,* **1965,** 1056-1065 (1965).

124. C. Satto, P. Sciau, E. Dooryhee, J. Galy, and P. Millet, *Journal of Solid State Chemistry,* **146,** 103-109 (1999).

125. J. Galy, J. Darriet, A. Casalot, and J.B. Goodenough, *J. Solid State Chem.,* 339-348 (1970).

126. J. Hirschinger, T. Mongrelet, C. Marichal, P. Granger, J.M. Savariault, E. Deramond, and J. Galy, *Journal of Physical Chemistry,* **97,** 10301-10311 (1993).

127. J. Galy, C. Satto, P. Sciau, and P. Millet, *J. Solid State Chem.,* **146,** 129-136 (1999).

128. C. Delmas, H. Cognacauradou, J.M. Cocciantelli, M. Menetrier, and J.P. Doumerc, *Solid State Ionics,* **69,** 257-264 (1994).

129. P. Rozier, J.M. Savariault, and J. Galy, *Solid State Ionics,* **98,** 133-144 (1997).

130. J.M. Cocciantelli, M. Menetrier, C. Delmas, J.P. Doumere, M. Pouchard, and P. Hagenmuller, *Solid State Ionics,* **50,** 99-105 (1992).

131. E. Andrukaitis, P.W.M. Jacobs, and J.W. Lorimer, *Solid State Ionics,* **27,** 19-30 (1988).

132. E. Andrukaitis, P.W.M. Jacobs, and J.W. Lorimer, *Solid State Ionics,* **37,** 157-169 (1990).

133. B. Chaloner-Gill, D.R. Shackle, and T.N. Andersen, *Journal of the Electrochemical Society,* **147,** 3575-3578 (2000).

134. J.M. Cocciantelli, M. Menetrier, C. Delmas, J.P. Doumerc, M. Pouchard, and P. Hagenmuller, *Solid State Ionics,* **50,** 99-105 (1992).

135. J.M. Cocciantelli, K.S. Suh, J. Senegas, J.P. Doumerc, J.L. Soubeyroux, M. Pouchard, and P. Hagenmuller, *Journal of Physics and Chemistry of Solids,* **53,** 51-55 (1992).

136. J.M. Cocciantelli, M. Menetrier, C. Delmas, J.P. Doumerc, M. Pouchard, M. Broussely, and J. Labat, *Solid State Ionics,* **78,** 143-150 (1995).

137. C. Delmas, S. Brethes, and M. Menetrier, *Comptes Rendus De L Academie Des Sciences Serie Ii,* **310,** 1425-1430 (1990).

138. C. Delmas, S. Brethes, and M. Menetrier, *Journal of Power Sources,* **34,** 113-118 (1991).

139. *International Tables of Crystallography.*

140. R.D. Shannon, *Acta Crystallographica A,* **32,** 751 (1976).

141. M. Isobe and Y. Ueda, *Materials Research Bulletin,* **34,** 1719-1728 (1999).

142. J. Galy, J. Darriet, A. Casalot, and J. Goodenough, *J. Solid State Chem.,* **1970,** 339 (1970).

143. R.L. Withers, P. Millet, and Y. Tabira, *Zeitschrift Fur Kristallographie,* **215,** 357-363 (2000).

144. J. Galy and A. Hardy, *Bulletin de la Societe Chimique de France,* **1964,** 2808-2811 (1964).

145. H. Katzke, M. Czank, W. Depmeier, and S. van Smaalen, *Philosophical Magazine B-Physics of Condensed Matter Statistical Mechanics Electronic Optical and Magnetic Properties,* **75,** 757-767 (1997).

146. R.L. Withers, J.G. Thompson, and A.D. Rae, *J. Solid State Chem.,* **94,** 404 (1991).

147. J. Galy, P. Millet, C. Satto, and P. Sciau, *J. Solid State Chem.,* **136,** 56-62 (1998).

148. J. Galy and A. Hardy, *Acta. Crys.,* **19,** 432-435 (1965).

149. D.N. Anderson and R.D. Willett, *Acta Crystallographica B (24,1968-38,1982),* 1477-1478 (1971).

150. P. Rozier, *European Journal of Solid State and Inorganic Chemistry,* **33,** 1-13 (1996).

151. H. Katzke, M. Czank, W. Depmeier, and S. van Smaalen, *Journal of Physics-Condensed Matter,* **9,** 6231-6239 (1997).

152. J.M. Savariault and P. Rozier, *Physica B,* **234,** 97-99 (1997).

153. H. Katzke and W. Depmeier, *Phase Transitions,* **59,** 91-104 (1996).

154. H. Katzke, K. Kato, and R.E. Dinnebier, *Zeitschrift Fur Kristallographie,* **214,** 392-397 (1999).

155. H. Katzke, K. Kato, and R.E. Dinnebier, *Zeitschrift Fur Kristallographie,* **214,** 398-401 (1999).

156. H. Katzke and K. Kato, *Zeitschrift Fur Kristallographie,* **214,** 103-107 (1999).

157. H. Katzke, *Zeitschrift Fur Kristallographie,* **216,** 278-283 (2001).

158. R.J. Cava, A. Santoro, D.W. Murphy, S.M. Zahurak, R.M. Fleming, P. Marsh, and R.S. Roth, *J.Solid State Chem.,* **65,** 63-71 (1986).

159. P. Millet, C. Satto, P. Sciau, and J. Galy, *Journal of Solid State Chemistry,* **136,** 56-62 (1998).

Chapter Two

Theory

2.1 Diffraction

In order to describe fully the structure of a crystalline solid, information about the lattice and basis of the compound must be obtained. The lattice, defined through its arrangement of lattice points, specifies the periodic array to which the basis is connected; the basis is the set of atoms, groups of atoms or molecules that make up the unit cell. A lattice is considered to be the set of points with position vector $\vec{R}$, where $\vec{R}$ is calculated from the primitive vectors $\vec{a}$, $\vec{b}$ and $\vec{c}$ as follows:

$$\vec{R} = n_1\vec{a} + n_2\vec{b} + n_3\vec{c}$$

Equation 2.1 – n_i is any integer, negative, zero or positive

The reciprocal lattice is a useful concept in diffraction theory: every direct lattice is associated with a reciprocal lattice. While the direct lattice is used to describe the atomic positions in the crystal, the reciprocal lattice is used to understand the position of diffracted radiation and can be generated by the following three primitive vectors:

$$\vec{a}^* = 2\pi\frac{\vec{b}\times\vec{c}}{\vec{a}.(\vec{b}\times\vec{c})},\ \vec{b}^* = 2\pi\frac{\vec{c}\times\vec{a}}{\vec{a}.(\vec{b}\times\vec{c})},\ \vec{c}^* = 2\pi\frac{\vec{a}\times\vec{b}}{\vec{a}.(\vec{b}\times\vec{c})}$$

Equations 2.2

The reciprocal lattice vectors can only be linear combinations of $\vec{a}^*$, $\vec{b}^*$ and $\vec{c}^*$, with integer coefficients h, k, l, i.e.:

$$\vec{d}^* = h\vec{a}^* + k\vec{b}^* + l\vec{c}^*$$

Equation 2.3

A set of parallel equally spaced lattice planes will contain all the points of a three-dimensional lattice: thus for any family of lattice planes separated by a distance d, there are reciprocal lattice vectors, $\vec{d}^*$, perpendicular to the planes, and vice versa. The magnitude of the vector $\vec{d}^*$ is the reciprocal of the shortest distance between the planes:

$$\left|\vec{d}^*\right| = \frac{1}{d_{hkl}}$$

Equation 2.4

A particular family of planes is thereby uniquely defined by the *hkl* values, known as the Miller indices, of the shortest reciprocal lattice vector. The separation of the planes, d_{hkl}, the wavelength and angle of diffraction are directly related according to Bragg's law. This gives a qualitative expression of the condition for elastic scattering, which is illustrated in *figure 2.1*.

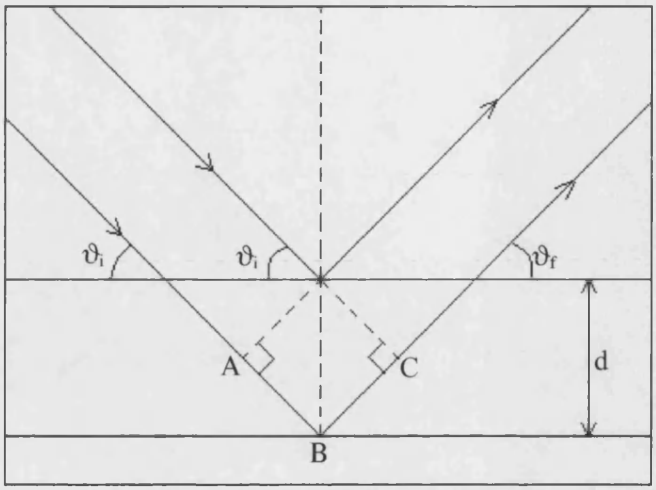

Figure 2.1 – Pictorial description of Bragg's law [1]

In order to observe a sharp peak in the diffracted intensity arising from scattering from successive lattice planes, the diffraction radiation from lattice points must interfere constructively: the difference in path length between the beams must be an integral number of wavelengths. In *figure 2.1*, the difference in path length is equal to AB + BC; thus since AB = BC = $d\sin\vartheta$, the Bragg condition for constructive interference is given by:

$$n\lambda = 2d\sin\vartheta$$

Equation 2.5

The integer n (only positive values) is known as the order of the corresponding reflection.

A geometric representation of the condition for elastic scattering is provided by Ewald's sphere as shown in *figure 2.2*. This construction, in reciprocal space, has O as the origin where the incident wave, k_0, terminates and C as the centre of a sphere of radius equal to λ^{-1}. A diffraction peak will be observed if one or more points, P, lie on the surface of the sphere, coincident with a reciprocal lattice point such that the angle OCP is equal to $2\vartheta_B$.

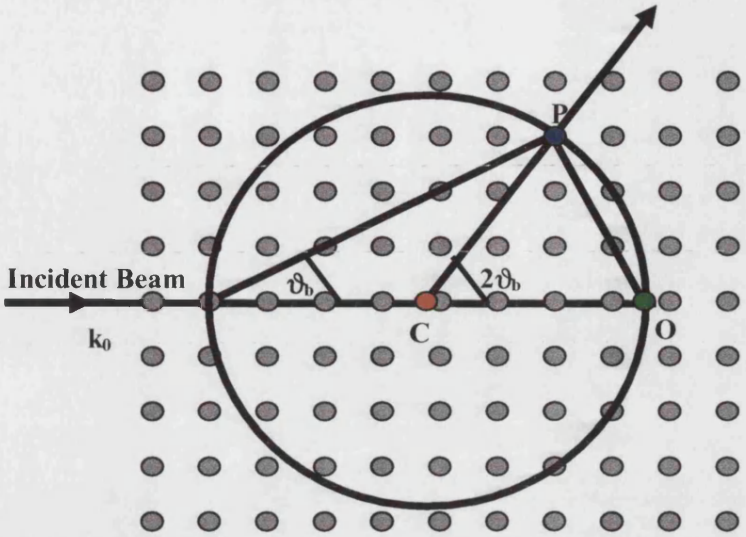

Figure 2.2 – Ewald's sphere – the scattering triangle for elastic scattering in a reciprocal lattice plane

It is the relationship between the Bragg peaks and the arrangement of the composite atoms into *hkl* planes that is the key to the solution of an unknown crystal structure. In a diffraction experiment it is the intensities, I_{hkl}, of the Bragg reflections that are measured in terms of the coherent scattering amplitudes, b_r, of the atomic nuclei and their position in the unit cell. In the case of x-ray scattering, the atomic electrons are responsible for the magnitude of the scattering power; in the case of neutron scattering, it is the nucleus itself that determines the scattering length.

Whatever the nature of the beam, x-ray, neutron or electron, there will be certain classes of *hkl* reflections that are absent from a diffraction pattern. These systematic absences are due to the arrangement of the elements of the basis to give a total destructive rather than constructive interference for certain values of d, which is wholly determined by the symmetry of the given crystal structure.

The intensity of the observed reflections is proportional to the structure factor F_{hkl}:

$$I_{hkl} \propto F_{hkl}^2$$

Equation 2.6

The overall structure factor F_{hkl} is given by *equation 2.7*:

$$F_{hkl}^2 = \left| \sum_{j=1} b_r \exp(-i2\pi(hx_j + ky_j + lz_j) \right|^2 \exp(-W)$$

Equation 2.7 – Where x_j, y_j, z_j are the coordinates of the j^{th} atom, b_r is the scattering length for neutrons (replaced by f_j, the scattering amplitude, for x-rays) and W is the Debye-Waller isotropic temperature factor given by equation 2.8.

$$W_j = \frac{8\pi^2 \sin^2 \vartheta \langle u^2 \rangle}{\lambda^2}$$

Equation 2.8 - $\langle u^2 \rangle$ is the mean square displacement of the atom.

The summation in the structure factor is taken over all the atoms, j, at the x_j, y_j, z_j positions of the unit cell. The Debye-Waller temperature factor takes into account the thermal vibration of the atoms; as shown by *equation 2.8* it is proportional to the mean-square displacement of the jth atom from its regular site. This displacement is non-zero at T=0 (zero-point motion) and increases linearly with temperature. However, in materials where bonding is markedly anisotropic, thermal ellipsoids are used to model the local displacements of the atoms. In this case the Debye-Waller thermal parameter takes the form:

$$\exp\left[-\frac{1}{4}(B_{11}h^2a^{*2} + B_{22}k^2b^{*2} + B_{33}l^2c^{*2} + 2B_{12}hka^*b^* + 2B_{13}hla^*c^* + 2B_{23}klb^*c^* \right]$$

2.1.1 X-Ray Diffraction

X-rays are produced when high-energy charged particles, generally accelerated electrons, collide with matter. The x-ray spectra produced have two components: a broad spectrum of wavelengths known as white radiation, and a number of fixed, monochromatic wavelengths.

In a typical x-ray diffraction experiment, radiation is produced by accelerating a beam of electrons to strike a metal target. The wavelength of the resultant x-rays is dependent on the identity of the target element. Copper is used in a typical experiment, which is shown in *figure 2.3*.

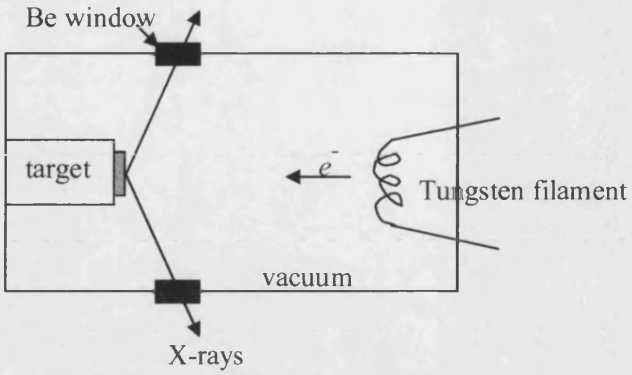

Figure 2.3 – Schematic design of the generation of x-ray radiation through the use of a filament x-ray tube

The electron beam, from a heated tungsten filament, is accelerated towards a continuously cooled anode by a potential difference of approximately 30kV. This x-ray tube is evacuated to prevent oxidation of the filament. The electrons strike the copper target, affixed to the anode, with sufficient energy to ionise some of the copper 1s electrons. An electron in an outer orbital immediately drops down to occupy the vacant 1s level and the energy released in the transition appears as x-radiation.

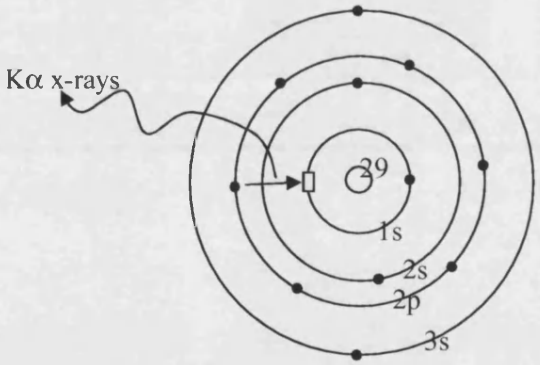

Figure 2.4 – Generation of copper Kα x-rays.

As the copper orbital energies are well defined, the resultant emission of a spectrum of electromagnetic radiation, which happens to be in the x-ray range, leaves the tube through "windows" of beryllium, which has a low absorption due to its low atomic number (4) [1]. For copper, the 2p-1s transition (Kα, λ = 1.541Å) occurs much more frequently than the 3p-1s transition (Kβ, λ = 1.392Å) and it is this higher intensity radiation that is used in standard laboratory diffraction experiments. In fact, the Kα transition is a doublet, because there are slightly different transition energies for the two

possible spin states of the 2p electron producing $K\alpha_1$ and $K\alpha_2$ radiation where a monochromator is not employed. A monochromator can scatter only $K\alpha_1$ radiation onto a given sample by using Bragg's law and a suitable collimator.

X-ray diffraction data discussed in this thesis has been obtained at a synchrotron source. In a synchrotron, fast-moving electrons are constrained by magnetic fields to move in a circle of large diameter; radiation is emitted tangentially with a continuous spectrum from infra red through to x-ray, from which any wavelength can be selected by use of a monochromator. The intensities of these x-rays are many orders of magnitude greater than those produced using an x-ray tube.

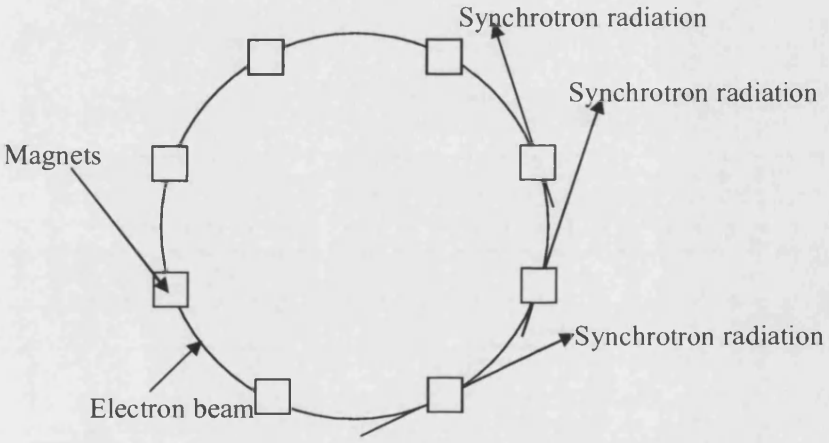

Figure 2.5 – Production of synchrotron radiation from relativistic electrons in a special type of particle accelerator

2.1.2 Neutron Diffraction

The weak, fluctuating dependence of neutron scattering length upon atomic number is in marked contrast with the direct dependence shown by x-rays with number of electrons. Neutrons can therefore be used to locate light atoms in the presence of heavy ones. The neutron also has a magnetic moment, which can interact with the field present in the sample. These advantages have led to the widespread use of neutron powder diffraction for studying a diverse range of polycrystalline materials, from metal hydrides to the oxide superconductors and carbon cage molecules - fullerenes.

Constant Wavelength:

There are two types of sources for neutron diffraction: reactor sources and accelerator-based sources. Reactor sources are more commonly used to perform constant wavelength diffraction experiments, as shown in *figure 2.6*. In a typical experimental arrangement, thermal neutrons from a nuclear reactor (R) are guided through a collimator (horizontal divergence, α_1) to a large single crystal monochromator (M). The monochromatic beam is scattered by the powder sample (S) into a detector (D). The divergence of the monochromatic beam (α_2) and that of the scattered one (α_3) are determined by the collimators between M and D. Additionally, the effective scattered intensity is increased by the use of multiple counter banks, positioned at different scattering angles.

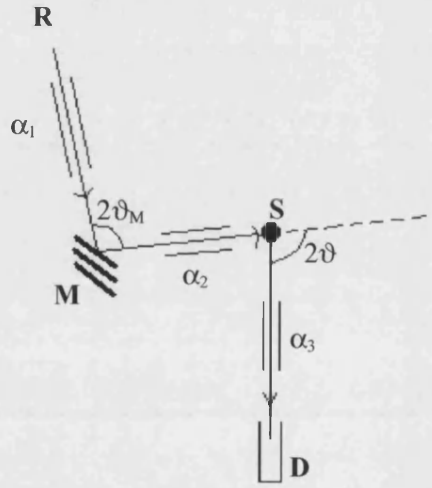

Figure 2.6 – Schematic diagram of a powder neutron diffractometer operating at constant wavelength

This experimental set-up records the intensity scattered by the sample at different values of the scattering angle 2ϑ. The shape of Bragg reflections in this type of experiment are governed by a number of factors, including the geometry of the defining collimators (imperfect collimation), the crystallinity of the sample (particle size effects, finite crystalline strain etc.) and the mosaic structure of the monochromator.

Constant scattering angle:

A second possible experimental arrangement makes use of accelerator-based sources where pulsed neutron beams are scattered. In the case of a spallation source, neutrons are produced by bombarding a heavy metal target, such as uranium or tantalum, with highly energetic protons (~800MeV) at a certain frequency (e.g. 50Hz at ISIS, UK). A high flux, white neutron pulse (typically about 30 neutrons per proton) emerges from the target. These highly energetic neutrons are moderated to increase the proportion of the useful thermal ones; however, moderation of the white neutron beam also creates a significant amount of epithermal neutrons. As a result, the neutron flux extends down to very short wavelength (λ~0.6Å) compared with reactor sources. In a typical experiment, the detector is placed at a fixed scattering angle 2ϑ, and the time that neutrons with different wavelengths take to reach the detector can be measured (*figure 2.7*): the time-of-flight (TOF) method.

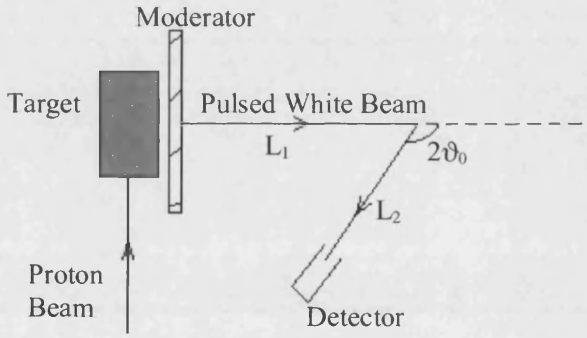

Figure 2.7 – Schematic diagram of a neutron powder diffractometer operating at fixed scattering $2\vartheta_0$

The scattered intensity is determined as a function of the wavelength. The time-of-flight, t_{hkl}, is related to the d-spacing through de Broglie's relation, by substituting the wavelength (λ_{hkl}) from Bragg's law:

$$t_{hkl} = \left(\frac{2m_n L \sin\vartheta_0}{h} \right) d_{hkl}$$

Equation 2.9 – Where m_n is the neutron mass, h is Planck's constant, $L = L_1 + L_2$ is the total flight path and $2\vartheta_0$ is the fixed scattering angle

The spectral distribution of the incident beam is modelled by measuring the isotropic scattering from a standard vanadium sample, which also accounts for corrections in the detector deficiency due to wavelength variation.

2.1.3 Rietveld Refinement

The Rietveld method of analysing powder diffraction patterns was first developed for the case of neutron diffraction at fixed wavelength [2]. Rietveld refinement uses a least-squares minimization technique requiring a good initial structural model which is refined to match the observed data. Least-squares refinement minimises the difference between the calculated and observed profiles, which is expressed mathematically as minimisation of the function:

$$S_y = \sum_i w_i \{y_i - y_{ci}\}^2$$

Equation 2.10 – w_i = weighting factor given to the i^{th} point, calculated as $w_i = \frac{1}{y_i^{obs}}$; y_i = observed intensity at the i^{th} point; y_{ci} = calculated intensity at the i^{th} point.

A powder diffraction pattern can be recorded in numerical form as a function of scattering angles, times of flight or energies. If this scattering variable is referred to as T then the experimental powder diffraction pattern is usually given as two arrays $\{T_i, y_i\}_{i=1,\ldots,n}$. In the case of data that have been manipulated or normalised in some way the three arrays $\{T_i, y_i, \sigma_i\}_{i=1,\ldots,n}$, where σ_i is the standard deviation of the profile intensity y_i, needed in order to properly weight the residuals in the least squares process. The profile can be modelled using the calculated counts y_{cI} at the Ith step by summing the contribution from neighbouring Bragg reflections plus the background:

$$y_{cI} = S \sum_{h_I} L_{h_I} A_{h_I} P_{h_I} C_{h_I} \left| F_{h_I} \right|^2 \Omega(T_I - T_{h_I}) + b_I$$

Equation 2.11 – the vector $\mathbf{h_I}$ labels the Bragg reflections; $\mathbf{S}$ is the scale factor; $\mathbf{L_{hI}}$ is a contribution from the Lorentz, polarisation and multiplicity factors; $\mathbf{A_{hI}}$ is the absorption correction; $\mathbf{P_{hI}}$ is the preferred orientation function; $\mathbf{C_{hI}}$ includes special corrections (non-linearity, efficiencies, special absorption correction); $\mathbf{F_{hI}}$ is the structure factor for the particular hkl reflection; $\boldsymbol{\Omega}$ is the reflection profile function that models both instrumental and sample effects; $\mathbf{T}$ is the scattering variable (angle, time-of-flight or energy); $\mathbf{b_I}$ is the background contribution at the I^{th} point.

There are usually two sets of parameters included within the least-squares Rietveld refinement, the "structural parameters" (for example: fractional coordinates (x_I, y_I, z_I) for the Ith atom in the asymmetric unit, it's fractional occupancy (n_I) and isotropic temperature factor (B_I) or anisotropic temperature factors in the case of anisotropic thermal vibrations) and the "profile parameters" (such as the zero point error in the

detector position ($2\vartheta_0$), the peak asymmetry at high and low scattering angles (P) and the peak shape parameters (U, V, W)). The unit cell dimensions (a, b, c, α, β, γ), which determine the position of the calculated Bragg peaks, with a zero point onset, are also included as variables in the least-squares refinements. The structural parameters depend on the integrated intensities of the Bragg peaks, whereas the profile parameters are strongly affected by the peak shapes.

Powder x-ray diffraction data discussed in this thesis have been refined using Fullprof [3]; neutron powder diffraction data have been refined using the general structure analysis suite, GSAS [4]. In GSAS, the background function is fitted by a Chebyshev function with a variable number of parameters whereas, in Fullprof, the background is interpolated from a list of points taken directly from the data. Both programs use a modified Thompson-Cox-Hastings pseudo-Voigt (TCHZ) peak shape function given by:

$$TCHZ = \eta L = (1-\eta).G$$

Equation 2.12

Where L is the Lorenzian component given by:

$$\Gamma_L = \frac{X}{\cos\vartheta} + Y\tan\vartheta$$

Equation 2.13

G is the Gaussian contribution given by:

$$\Gamma_G^2 = U\tan^2\vartheta + V\tan\vartheta + W$$

Equation 2.14

and η is the mixing parameter given by:

$$\eta = 1.36603q - 0.47719q^2 + 0.1116q^3$$

Equation 2.15

where $q = \frac{\Gamma_L}{\Gamma}$ and $\Gamma = (\Gamma_G^5 + A\Gamma_G^4\Gamma_L + B\Gamma_G^3\Gamma_L^2 + C\Gamma_G^2\Gamma_L^3 + D\Gamma_G\Gamma_L^4 + \Gamma_L^5)^{0.2}$ where A=2.69269, B=2.42843, C=4.47163 and D=0.07842.

After refinement of a particular model, the refinement quality can be estimated by the agreement between observed and calculated profiles as indicated by the following goodness-of-fit factors defined by Rietveld:

$$R_{wp} = \left[\frac{\sum_I w_I \left| y_I(obs) - y_I(calc) \right|^2}{\sum_I w_I y_I^2(obs)} \right]^{1/2} \times 100\%$$

$$R_p = \frac{\sum_I \left| y_I(obs) - y_I(calc) \right|}{\sum_I y_I(obs)} \times 100\%$$

$$R_B = \frac{\sum_k \left| I_k(obs) - I_k(calc) \right|}{\sum_k I_k(obs)} \times 100\%$$

$$R_E = \left[\frac{(N - P + C)}{\sum_I w_I y_I^2(obs)} \right]^{1/2} \times 100\%$$

Equation 2.16-19 – R_{wp} = weighted profile reliability factor; R_p = profile reliability factor; R_B = Bragg or integrated intensities reliability factor; R_E = expected reliability factor; w_I = weighting factor for intensities; $y_I(obs)$ = observed intensities; $y_I(calc)$ = calculated intensities; $I_k(obs)$ = observed integrated intensity at reflection k; $I_k(calc)$ = calculated integrated intensity at reflection k; N = number of observations; P = number of refinable parameters; C = number of constraints used.

The weighted profile reliability factor, R_{wp}, aids in understanding how well the structural model under refinement accounts for relatively small and large Bragg peaks across the diffraction profile. The Bragg reliability factor, R_B, measures the quality of fit on the structural parameters with the use of integrated intensities of each point, I_k, in a similar manner to single crystal analysis. The expected reliability factor, R_E accounts for the statistical quality of the data and the number of variables used in the refinements. During the course of a structural refinement, the goodness of fit is monitored using χ^2, defined as:

$$\chi^2 = \left(\frac{R_{wp}}{R_E} \right)^2 = \frac{\sum_I w_I \left| y_I(obs) - y_I(calc) \right|^2}{N - P + C}$$

Equation 2.20

When a fit to the observed data is particularly accurate, the value of χ^2 is found to be close to one.

2.1.4 Incommensurate Modulations

Normal crystals give rise to a diffraction pattern with fundamental reflections due to the prototype structure. Extra reflections appearing near the fundamental reflections are called satellite reflections: a commensurate superstructure may be detected by the appearance of extra reflections in reciprocal space on both sides of the fundamental reflections at commensurate positions such as a half or a third, and these extra reflections appear in one or more reciprocal lattice directions. When the structure has an incommensurate modulation these satellite reflections occur at positions given by irrational fractions of the reciprocal lattice repeat. Normal crystals exhibit long-range translational order which implies a periodic spacing for the lattice, but when a crystal is incommensurate there is an additional superimposed translational order making the crystal quasiperiodic, characterised by two or more periodicities that are incommensurate with each other. The main reflections, those due to the commensurate part of the structure, give information about the average structure of the crystal; the extra reflections tell us about the incommensurate modulations of the structure. [5]

2.2 Magnetism

2.2.1 Units

There are two systems of magnetic units in common use at present: système international (S.I.) and centimetre, gram, second (c.g.s.). *Table 2.1* shows the conversion factors between the two systems.

Magnetic Quantity	c.g.s. unit	S.I. unit	Conversion factor to S.I.
Magnetic field (H)	Oersted (Oe)	Am^{-1}	$10^3/4\pi$ ($A\ m^{-1}\ Oe^{-1}$)
Magnetic induction (B)	Gauss (G)	Tesla (T)	10^{-4} ($T\ G^{-1}$)
Molar magnetisation (M)	$Oe\ mol^{-1}$	$A\ m^{-1}\ mol^{-1}$	10^3 ($A\ m^{-1}\ Oe^{-1}$)
Molar susceptibility (χ_M)	$emu\ mol^{-1}$	$m^3\ mol^{-1}$	$4\pi10^{-6}$ ($m^3\ emu^{-1}$)

Table 2.1 – Conversion factor of numerical values of magnetic quantities to their corresponding values in S.I. systems.

The basic difference between the S.I. and c.g.s. systems is the definition of flux density, B, with relation to the field strength, H, and magnetisation, M. In the S.I. system the relationship is:

$$B = \mu_0(H + M)$$

*Equation 2.21 – The permittivity of free space, $\mu_0 = 4\pi \times 10^{-7}$ Tm/A; **B** = flux density in Tesla (T); **H** = field strength in A/m; **M** = magnetisation in A/m.*

In the c.g.s. system the relationship is:

$$B = H + 4\pi M$$

*Equation 2.22 – **B** = flux density in Gauss (G); **H** = field strength in Oersted (Oe); **M** = magnetisation in Oe.*

The magnetic moment, μ, is given in J/T in the S.I. system, and in erg/G in the c.g.s. system, also written as e.m.u. The magnetisation, M, is defined as:

$$M = N\langle\mu\rangle$$

*Equation 2.23 – **M** = magnetisation; **N** = number of sites; $\langle\mu\rangle$ = average magnetic moment per site.*

However, magnetisation is quoted for a particular field, so it is more convenient to use magnetic susceptibility, which is defined in the c.g.s. system as:

$$\chi = \frac{M}{H}$$

*Equation 2.24 – χ = magnetic susceptibility; **M** = magnetisation; **H** = magnetic field.*

and may be converted to S.I. units by:

$$\chi^{S.I.} = 4\pi\chi^{C.G.S.}$$

Equation 2.25 – $\chi^{S.I.}$ is the susceptibility in S.I. units, $\chi^{C.G.S.}$ is the susceptibility in c.g.s. units.

There is a caveat to susceptibility: ferromagnets do not follow the linear relationship between magnetisation and magnetic field defined in *equation 2.21*, and their magnetic properties and behaviour must therefore be described in terms of magnetisation, not magnetic susceptibility, which is generally used for all other magnetic systems.

2.2.2 Isolated magnetic moments

If interactions between magnetic moments on different atoms and between magnetic moments and their environments are ignored, what remains is the interaction between isolated atoms, or rather, isolated moments and any applied magnetic field.

Spin and orbital moments:

In an atom the electronic shell as well as the nucleus carry charge and angular momentum, resulting in dipole moments. These moments are given in units of the Bohr or nuclear magneton respectively:

$$\mu_B = \frac{e\hbar}{2m_e} \qquad \mu_N = \frac{e\hbar}{2m_p}$$

Equation 2.26 – m_e = electron mass; m_p = proton mass; $\hbar = h/2\pi$.

The large proton mass relative to that of the electron means that nuclear dipole moments are comparatively small and usually do not need to be considered when discussing the magnetism of atoms.

The electrons of the atomic shell carry the intrinsic spin moment given by S and the orbital moment given by L. Their dipole moments are given by:

$$\mu_S = g_S[S(S+1)]^{1/2}\mu_B \qquad \mu_L = g_L[L(L+1)]^{1/2}\mu_B$$

Equation 2.27 – $g_S = 2.0023 \sim 2$; $g_L = 1$.

These two moments are not independent of each other, but are connected via spin-orbit coupling, resulting in a total angular momentum **J** of the electron shell. The Russell-Saunders coupling scheme is generally used, i.e. **J** = **L** + **S** where **L** is the total orbital momentum of all electrons in the shell and **S** the total spin. The resulting dipole moment is:

$$\mu_J = g_J[J(J+1)]^{1/2}\mu_B$$

Equation 2.28 – g_J is the Landé factor, $g_J = \dfrac{[3J(J+1)+S(S+1)-L(L+1)]}{[2J(J+1)]}$

The values of **S**, **L** and **J** for atoms in their ground state are given by Hund's rules, which state that for closed shells **S** = **L** = **J** = 0, in other words, those atoms carry no dipole moment. A similar diamagnetic state can be reached in molecules if the atomic orbitals are combined accordingly. Magnetism, more specifically, paramagnetism is connected to atoms, ions or molecules with open electron shells [6].

Diamagnetism:

All materials show some degree of diamagnetism: Lenz's Law states that the small magnetic field produced by the motion of electrons around an atom (in the same way that the motion of current carriers around a coil produces a magnetic field) will act

against any applied magnetic field. For a diamagnetic substance, a magnetic field induces a small magnetic moment, which opposes the applied magnetic field that caused it. The magnetisation of a diamagnet is weakly negative, largely temperature independent and proportional to the applied field. Diamagnetism, being a property of electrons in closed shells, is present in all materials, but it is a weak effect that can either be ignored or corrected with the use of Pascal's constants [7].

Paramagnetism:

Paramagnetism corresponds to a positive susceptibility so that an applied magnetic field induces a magnetisation aligning parallel with the applied magnetic field. We have just considered materials that contain no unpaired electrons (diamagnets) and therefore have no magnetic moment unless a field is applied, which is also true for paramagnets as in zero field their normal fluctuation causes the moments to cancel. The positive magnetisation is temperature and field dependent, and typically two orders of magnitude larger than the diamagnetic magnetisation.

The weak interactions between neighbouring atoms causes weak correlation and the electrons can be assumed to be independent. The application of a magnetic field tends to align the moments with field; the degree of alignment (hence the induced magnetisation) is dependent on the strength of the applied magnetic field. Although an increase of magnetic field will tend to align the spins, an increase of temperature will randomise them. It is therefore expected that the magnetisation of a paramagnetic material will depend on the ratio B/T. This can be proved by the classical calculation of the mean orientation of the paramagnetic dipoles [6] to give:

$$M_{para} = Ng_J \mu_B J B_J(y)$$

Equation 2.29

Where the Brillouin function, $B_J(y)$ is given by:

$$B_J(y) = \left(1+\frac{1}{2J}\right)\coth\left[\left(1+\frac{1}{2J}\right)y\right] - \left(\frac{1}{2J}\right)\coth\left(\frac{y}{2J}\right)$$

Equation 2.30

and

$$y = \frac{Jg_J \mu_B B_{ext}}{k_B T}$$

Equation 2.31

Thus it can be seen that the paramagnetic magnetisation is, as expected, dependent on the ratio of field and temperature, and this dependence is different for different values of J.

A typical value of y can be estimated as follows: for $J = ½$, $g_J = 2$ with $B_{ext} = 1T$, $y \sim 2 \times 10^{-3}$ at room temperature. Hence, except at very low temperature and/or in extremely large magnetic fields, the experimental situation will correspond to $y << 1$. For small values of y such as this:

$$B_J(y) = \frac{y(J+1)}{3J}$$

Equation 2.32

Giving:

$$M_{para} = Ng_J\mu_B J\frac{y(J+1)}{3J} = \frac{Ng_J\mu_B y(J+1)}{3}$$

Equation 2.33

Which since:

$$\chi_{para} = \frac{M_{para}}{H} \approx \frac{\mu_0 M_{para}}{B_{ext}}$$

Equation 2.34

Leads to:

$$\chi_{para} = \frac{g_J^2 J(J+1)N\mu_B^2}{3k_BT} = \frac{\mu_{eff}^2 N\mu_B^2}{3k_BT} = \frac{C}{T}$$

Equation 2.35 – the Curie Law, characteristic of paramagnetic behaviour.

The Curie Law states that the paramagnetic susceptibility is inversely proportional to temperature. Measurement of the susceptibility allows deduction, via the Curie Law, of the Curie Constant, C and hence the effective magnetic moment, μ_{eff}, defined as:

$$\mu_{eff} = g_J\mu_B\sqrt{J(J+1)}$$

Equation 2.36

2.2.3 Interactions

When paramagnetic ions are embedded in a close packed solid they interact with each other. Different types of magnetic interaction are possible and important in enabling communication between magnetic moments and potential production of long-range order.

The simplest interaction is dipole-dipole coupling. Two magnetic dipoles μ_1 and μ_2 separated by a distance r have energy:

$$E = \frac{\mu_0}{4\pi r^3}\left[\mu_1 \cdot \mu_2 - \frac{3}{r^2}(\mu_1 \cdot r)(\mu_2 \cdot r)\right]$$

Equation 2.37

Two moments of $1\mu_B$ separated by approximately 1Å have an interaction energy corresponding to about 1K in temperature [7]. This interaction is too weak to account for the ordering of most magnetic materials, for example, iron metal, in which the moments orient themselves parallel at a temperature of 1043K. The magnetic dipolar interaction may at best play a part in ordering at very low temperatures. It is evident from the example of iron however that there must be another, stronger coupling between the moments. This is the exchange interaction, expressed as coupling between two angular momenta. The exchange Hamiltonian (energy) has the form:

$$H_{exc} = -J_{ij} S_i S_j$$

Equation 2.38 – Where J is the coupling energy between the two momenta, called the exchange integral.

The negative sign is a convention meaning that negative exchange energy causes parallel alignment, while positive exchange energy causes antiparallel alignment of the exchange-coupled dipoles. In a solid we have N spins, which are all coupled to each other, which means that the total exchange energy is:

$$H_{exc} = -2\sum_{i>j} J_{ij} S_i S_j$$

Equation 2.39

Origin of exchange – direct exchange:

The exchange energy has its roots in the covalent bond, that is in the overlap of the wave functions of valence electrons between the bonding partners. The simplest case to discuss is the H_2 molecule. Starting from two hydrogen atoms $H_A(1)$ and $H_B(2)$, where (1) and (2) refer to the electron coordinates, if the separation of the atoms is less than the Bohr radius, molecular wave functions are formed by linear combination of the atomic wave functions:

$$\Psi_a = C_a[\psi_A(1)\psi_B(2) - \psi_A(2)\psi_B(1)]$$
$$\Psi_b = C_b[\psi_A(1)\psi_B(2) + \psi_A(2)\psi_B(1)]$$

Equations 2.40-41 – $C_{a,b}$ are normalisation constants

Ψ_b describes the bonding orbital and Ψ_a the antibonding orbital. The bonding wavefunction has symmetric exchange properties, however, by the Pauli principle

antisymmetric wave functions are needed for fermions. Spin must also be considered in the wave functions:

$$\Phi_a = \Psi_a \xi_1 \text{ and } \Phi_b = \Psi_b \xi_0$$

Equations 2.42-43 – where ξ is the Pauli spin function.

In the present case, only two spin states are allowed, the singlet state S = 0 ($\uparrow\downarrow$) and the triplet state S = 1 ($\uparrow\uparrow$). To have an antisymmetric bonding wavefunction one has to combine Ψ_b with ξ_0 as shown in *equation 2.43*. Thus the overlap of valence electron wave functions enforces a definite spin configuration, here the antiparallel configuration. The total energy of the molecular system is given by:

$$E_a = C_a^2[K_{12} + J_{12}] \text{ and } E_b = C_b^2[K_{12} - J_{12}]$$

Equations 2.44-45

K_{12} describes the interaction of electrons with the nucleus:

$$K_{12} = \int \psi_A^*(1)\psi_B^*(2)H_n\psi_A(1)\psi_B(2)dV_1dV_2$$

Equation 2.46

While J_{12} is the exchange energy, i.e. the energy gained by forming the molecular orbitals. It contains by definition the Hamiltonian for the electric electron-electron interaction:

$$J_{12} = \int \psi_A^*(1)\psi_B^*(2)H_e\psi_A(1)\psi_B(2)dV_1dV_2$$

Equation 2.47

According to the solution of the hydrogen molecule by perturbation theory, illustrated in *figure 2.8*, $E_a > E_b$ for all values of r_{AB}, with the consequence that, from *equations 2.44-45*, $J_{12} < 0$, a condition which had previously been introduced for the exchange integral seeking antiparallel spin orientation [6, 7].

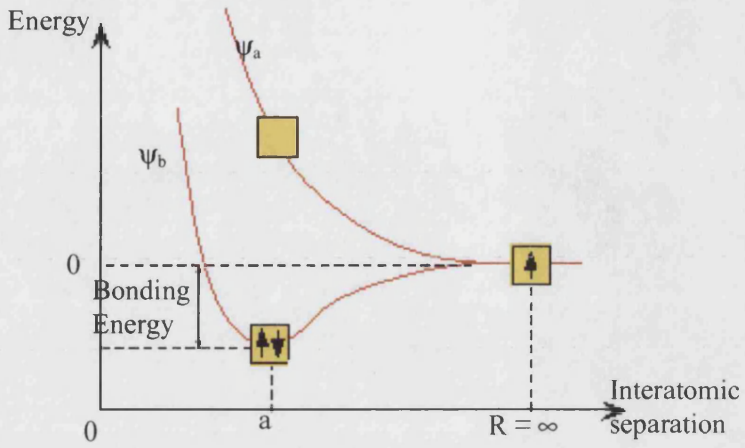

Figure 2.8 – Interatomic separation vs. energy for hydrogen. a is the bond length of H_2.

This example is based on s electron wavefunctions, which have no zero crossover. In the magnetism of transition metals the most important electrons are the d electrons, which do exhibit crossover. This causes a change in the sign of J_{12} from negative to positive as the separation increases, hence both parallel and antiparallel spin orientations are possible depending on the separation of the paramagnetic ions.

Exchange coupling is a quantum mechanical effect based on the rule that electrons in a closed system are indistinguishable. The exchange integral contains the electric electron-electron interaction and is thus of electric and not magnetic nature, despite the fact that it describes spin coupling. The magnetic-magnetic spin interaction is weak and in most cases can be neglected.

Exchange coupling as just described requires the direct overlap of the wave functions of the paramagnetic ions, and thus is only possible if the ions are nearest neighbours and not too widely separated. For example, in the rare earths the 4f electrons are deep in the atomic shell and 4f-4f overlap is excluded. Other cases include metallic materials where the paramagnetic ions are embedded in the sea of conduction electrons. Nevertheless strong exchange coupling often exists in those cases, and has to be transmitted between ions indirectly.

Indirect exchange in metals:

In metals, the conduction electrons can mediate the exchange interaction between magnetic ions. A localised magnetic moment spin-polarises the conduction electrons and this polarisation in turn couples to a neighbouring localised magnetic moment a distance

r away. The exchange interaction is thus indirect because it does not involve direct coupling between magnetic moments. It is known as the RKKY interaction after the discoverers of the effect: Ruderman, Kittel, Kasuya and Yosida. It is sometimes also known as itinerant exchange. The coupling takes the form of an r-dependent exchange interaction $J_{RKKY}(r)$ given by:

$$J(r) = 6\pi Z J^2 N(E_F)\left[\frac{\sin(2k_F r)}{(2k_F r)^4} - \frac{\cos(2k_F r)}{(2k_F r)^3}\right]$$

Equation 2.48 – $\boldsymbol{Z}$ = number of conduction electrons per atom; $\boldsymbol{J}$ = exchange interaction; $\boldsymbol{N(E_F)}$ = density of states at the Fermi level; $\boldsymbol{k_F}$ = Fermi momentum; $\boldsymbol{r}$ = distance between two impurities.

The interaction is long range and has an oscillatory dependence on the distance between the magnetic moments, as shown in *figure 2.9*, hence depending on the separation it may be either ferromagnetic or antiferromagnetic. The coupling is oscillatory with wavelength π/k_F because of the sharpness of the Fermi surface.

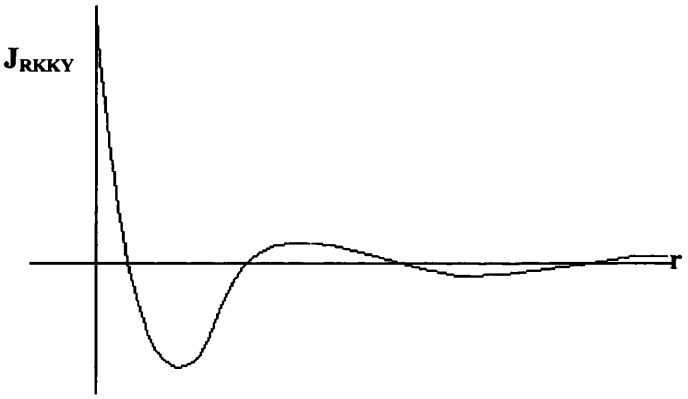

Figure 2.9 – Sketch of the radial dependence of the exchange integral in RKKY exchange

Indirect exchange in ionic solids:

Another type of indirect exchange is superexchange, which plays the central role in oxide materials. For example, MnO and MnF_2 are both antiferromagnets, but there is no direct overlap between the electrons on Mn^{2+} ions in either system. The exchange interaction is normally short ranged, so the longer-ranged interaction taking place in this case must be in some way "super".

Exchange is possible here through the oxygen or fluorine atoms: a non-magnetic ion between the non-neighbouring magnetic ions mediates the exchange interaction. There is a kinetic advantage for antiferromagnetism due to the possibility of delocalisation of electrons over the M-O-M unit, and thus the structure as a whole,

which cannot occur for ferromagnets in this configuration. This is illustrated in *figure 2.10*, on the assumption that the system is perfectly ionic and thus each metal ion has a single unpaired electron in a d orbital and the oxygen has two p electrons in its outermost occupied states.

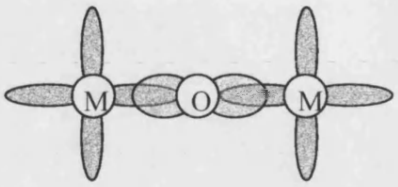

Antiferromagnetic:

a) ↑ ↓↑ ↓

b) ↑↓ ↑↓

c) ↑↓ ↓↑

Ferromagnetic:

d) ↑ ↓↑ ↑

e) ↑↓ ↑↑

f) ↑↓ ↑↑

Figure 2.10 – Superexchange in a magnetic oxide.

The arrows show the spins of four electrons and how they are distributed over the transition metal (M) and oxygen (O) atoms. If the moments on the transition metal ions are coupled antiferromagnetically (a, b, c) the ground state is a) and it can mix with excited configurations such as b) and c). The magnetic electrons can thus be distributed over the M-O-M unit, lowering the kinetic energy. If the moments on the metal (M) atoms are coupled ferromagnetically, (d, e, f), the ground state (d) cannot mix with excited configurations like e) and f) because these configurations are prevented by the exclusion principle

The superexchange integral has two terms: a potential exchange term representing electron repulsion and favouring ferromagnetic ground states which is small when ions are well separated, and a kinetic exchange term which dominates and is discussed above. The latter term is dependent on the degree of overlap of orbitals and thus superexchange is strongly dependent upon the angle of the M-O-M bond.

The additional interactions, mainly exchange, felt by paramagnetic ions in solids cause a change in the temperature dependence of the susceptibility. The linear behaviour

of $1/\chi$ vs. T continues, but the reciprocal susceptibility no longer extrapolates to the origin but cuts the temperature axis at either T > 0 or at T < 0 (obviously not a real temperature) defining the paramagnetic Curie temperature, ϑ_p. The Curie-Weiss law gives the susceptibility:

$$\chi = \frac{C}{T - \vartheta_p}$$

Equation 2.49 – Where C is the Curie constant defined in equation 2.35.

The paramagnetic Curie temperature is related to the exchange integral:

$$\vartheta_p = \left[\frac{2zS(S+1)}{3k_B T}\right] J$$

Equation 2.50 – From the mean field model under the assumption that each ion interacts only with its z nearest neighbours.

$\vartheta_p > 0$ means a positive exchange integral attempting parallel spin alignment (ferromagnetism) while $\vartheta_p < 0$ means a negative exchange integral attempting to align spins antiparallel (antiferromagnetism).

2.2.4 Models of exchange

The Ising model:

The Ising model makes the assumption that all spins are located on lattice points and can only orient themselves along one given axis of preference, the z-axis; therefore only the projection $(S_z)_i$ need be considered. The model also assumes that the exchange interaction is a pure pair interaction between any two spin pairs $(S_z)_i$, $(S_z)_j$, being the same for any pair of spins and can simply be set as *J*.

$$H_{ISING} = -2J \sum_{i>j} (S_z)_i (S_z)_j$$

Equation 2.51

It is important to distinguish between the dimensionality, *d*, of the lattice on which the spins sit, and the dimensionality, *D*, of the spins themselves, also known as the dimensionality of the order parameter. In the case of the Ising model the dimensionality of the order parameter, $D = 1$, as the spins are constrained to point along $\pm z$, however, these one-dimensional spins could be arranged on a lattice with $d = 1, 2, \ldots$ The Ising model plays a central role in the theory of anisotropic and one-dimensional magnets.

The x-y model:

In this case all spins are confined to a plane so only the projections $(S_x)_I$ and $(S_y)_I$ exist formed according to quantization conditions. The spins are of equal size and located on lattice points. Exchange is a pair interaction and the exchange integral is independent of direction within the plane.

$$H_{xy} = -2\sum_{i>j} J_{ij}[(S_x)_i(S_x)_j + (S_y)_i(S_y)_j]$$

Equation 2.52

The order parameter of the x-y model has dimensionality $D = 2$, but as with the Ising model, the lattice dimensionality may vary, $d = 1, 2, \ldots$

The Heisenberg model:

This is the most common model of exchange coupling. In the Heisenberg model all three spin components exist, but it is assumed that exchange is fully isotropic. This is the most serious restriction of the model and strictly speaking it can only be applied to cubic systems, hence the importance of the two previous models if deviations from isotropy are serious. The assumption of the Ising model that the exchange integral is the same for all spin pairs is also usually applied here to give:

$$H_{Heisenberg} = -2J\sum_{i>j}(S_iS_j)$$

Equation 2.53

There is another, more restrictive condition sometimes used, that each spin only interacts with its n nearest neighbours. This gives the simplest form of exchange:

$$H_{Heisenberg} = -2JnS^2$$

Equation 2.54

For the Heisenberg model the dimensionality of the order parameter, $D = 3$, because the spins are free to move in three dimensions, and the lattice dimensionality can vary, $d = 1, 2, \ldots$

2.2.5 Order and magnetic structures

The previous section discussed different types of magnetic interaction operating between magnetic moments in a solid. Here we will consider the different types of magnetic ground states which can be produced by these interactions.

Ferromagnetism:

A ferromagnet has spontaneous magnetisation even in the absence of an applied field. Ferromagnets consist of a number of small regions called domains, within each of which all spins are parallel. The axis of spin orientation changes from one domain to the next. The Hamiltonian for a ferromagnet in an applied magnetic field B is given by:

$$H = -\sum_{ij} J_{ij} S_i \cdot S_j + g\mu_B \sum_j S_j \cdot B$$

Equation 2.55 – The first term on the right hand side is the Heisenberg exchange energy, the second is the energy of an electron in an applied magnetic field B.

The solving of *equation 2.55* is done through the Weiss model of ferromagnetism, in which an effective molecular field at the i^{th} site is defined as:

$$B_{mf} = -\frac{2}{g\mu_B} \sum_j J_{ij} S_j$$

Equation 2.56

and it is assumed that all magnetic ions experience the same magnetic field. For a ferromagnet the molecular field will act so as to align neighbouring magnetic moments because the dominant exchange interactions are positive. Since the molecular field measures the effect of the ordering of the system, it is also assumed that:

$$B_{mf} = \lambda M$$

Equation 2.57 – Where λ is a constant that parameterises the strength of the molecular field as a function of the magnetisation.

This enables the replacement of the initial Hamiltonian with an effective Hamiltonian which is like that for a paramagnet in a magnetic field $B + B_{mf}$ which can be solved graphically.

$$H = g\mu_B \sum_i S_i \cdot (B + B_{mf})$$

Equation 2.58 – Hamiltonian for the Weiss model [7]

The solution of the Weiss model leads to the conclusion that below a certain temperature, the magnetisation of a ferromagnet rises sharply, then more slowly, and finally saturates so that the substance becomes magnetised even in the absence of an external field. In other words, the full parallel orientation of spins is only achieved for T → 0K. At the transition, the Curie temperature is given by:

$$T_C = \frac{g_J \mu_B (J+1)\lambda M_s}{3k_B} = \frac{n\lambda\mu_{eff}^2}{3k_B}$$

Equation 2.59

To reach saturation, a ferromagnetic sample requires the application of an external magnetic field.

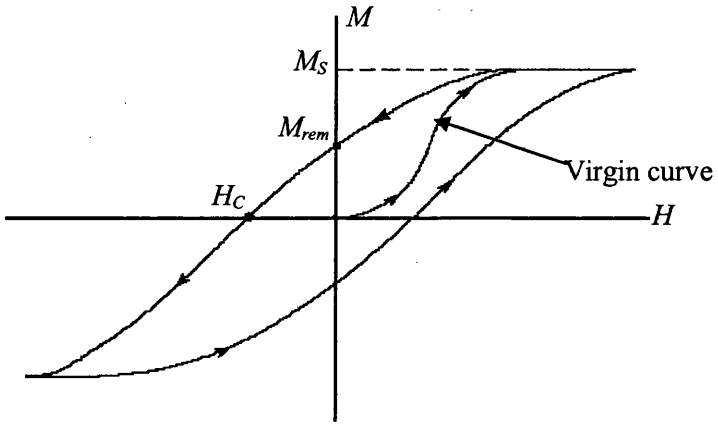

Figure 2.11 – Magnetisation vs. applied field at $T < T_C$, after cooling sample from above T_C. Identified are the initial magnetisation curve (virgin curve), the saturation magnetisation (M_S), the remnant magnetisation (M_{rem}) and the coercive field (H_C).

The first increase in magnetisation at low fields is due to reversible boundary displacements: domains with a small angle between M_{domain} and H shift their boundaries to increase in volume. At intermediate fields a further, irreversible shift of domain boundaries occurs. The jump of domain boundaries is not a continuous process and in high resolution the magnetisation curve is not smooth but is made up of many small steps. Next, M_{domain} starts to rotate into the direction of H and finally, at saturation, a single domain with $M_{domain} = M_{bulk} \parallel H$ is enforced. The "virgin curve" shown in *figure 2.11* starts from the "virgin state", $M_{bulk} = 0$, achieved by zero-field cooling through the transition temperature. Reducing the field after achieving saturation magnetisation (M_s in *figure 2.11*) results in a drop in magnetisation, but not back along the virgin curve. Since some of the domain wall displacements are irreversible, those domain walls do not move back to their original positions, increasing the volume of domains where the magnetisation direction is close to the previously applied field direction. Consequently, at $H = 0$ the bulk magnetisation does not vanish and the ferromagnet remains magnetised in zero field. This finite value of magnetisation is called the remenance (M_{rem}). It requires a field of $-H_C$ in the opposite direction called the coercive field to get back to $M_{bulk} = 0$. Increasing the negative field beyond H_C moves M_{bulk} back to

saturation. Going back to a positive field brings the same irreversibility problem; zero bulk magnetisation is only achieved for $+H_C$ and saturation is approached again when the field is increased beyond this [6].

Magnetisation curves such as that in *figure 2.11* are known as hysteresis loops and are characteristic of ferromagnets. By definition, the susceptibility of a ferromagnet in its ordered state is the slope of the hysteresis curve; since this is clearly dependent on H and the magnetic history of the sample it is not a useful quantity.

Antiferromagnetism:

In antiferromagnets the spin orientation is antiparallel, enforced by a negative exchange integral. An antiparallel spin sequence does not necessarily imply that neighbouring spins must be aligned antiparallel; the main characteristic is that the antiferromagnetic spin lattice can be separated into two intertwined ferromagnetic sublattices of equal strength with their spins cancelling. Again there is a characteristic temperature, the Néel temperature, T_N, below which long-range order is present and each of the ferromagnetic sublattices develops spontaneous magnetisation. These conditions still allow many different spin structures: for example, a linear spin chain may be ↑↓↑↓↑↓... or it may be ↑↑↓↓↑↑... and so on. This usually results in the spin lattice unit cell being larger by a well defined multiple than the chemical lattice unit cell.

An antiferromagnet shows neither large spontaneous magnetisation in low fields, nor hysteresis. The susceptibility below the Néel temperature is well defined and shown in *figure 2.12* for a typical antiferromagnet.

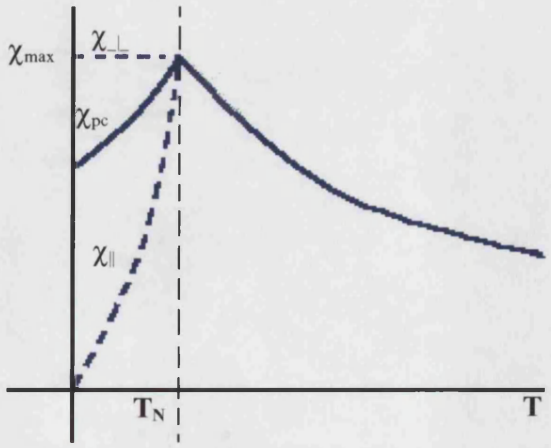

Figure 2.12 – Magnetic susceptibility and inverse susceptibility of an ideal antiferromagnet as a function of temperature.

There are two limiting cases for antiferromagnets which need to be distinguished. A small external field, H, perpendicular to the axis of alignment of the magnetic moments ("easy axis") will cause a slight canting of the two ferromagnetic sublattice magnetisations M_A and M_B in the direction of the field, leading to a weak magnetisation M_{res}. As long as the canting angles are small M_{res} will be proportional to the applied field, H, and the susceptibility is a constant, so that $\chi_{\perp} = \chi(T_N)$ for $T < T_N$. When H is parallel to the easy axis the two sublattice magnetisations M_A and M_B have reached saturation. Small fields do not affect this condition; therefore the susceptibility must drop from $\chi(T_N)$ to zero as the temperature drops, so that $\chi_{\parallel}(0) = 0$ as shown in *figure 2.12*. The susceptibility of a polycrystalline sample is given by:

$$\chi_{pc} = \frac{2}{3}\chi_{\perp} + \frac{1}{3}\chi_{\parallel}.$$

Equation 2.60

If the applied field is increased, at a certain critical field, B_{sf}, the spins will jump from small angle, elastic canting into a distinct canted spin structure with a much larger canting angle. B_{sf} is temperature dependent and the transition into the canted state is called a spin-flop transition. In materials with strong anisotropy the spin-flop state is suppressed, the system goes directly into the paramagnetic state or passes through a mixed state containing different spin structures often including a paramagnetic fraction: this is referred to as metamagnetism [6].

Ferrimagnetism:

Ferrimagnetism can be viewed as a special case of antiferromagnetism where the two ferromagnetic sublattices are inequivalent. In this case, the magnetisations will not cancel each other out and the material will have a net magnetisation. The molecular field on each sublattice is different, resulting in the spontaneous magnetisation of the sublattices to have different temperature dependences; therefore the net magnetisation can have a complicated temperature dependence. For example one sublattice may dominate the magnetisation at low temperature but another dominate at higher temperature; in this case the net magnetisation can be reduced to zero and change sign at a temperature known as the compensation temperature. The magnetic susceptibilities of ferrimagnets therefore do not follow the Curie law, but show hysteresis similar to ferromagnets.

Helimagnetism:

Helimagnets are either special cases of non-collinear structures or structures that are periodically modulated in terms of spin orientation or magnitude, and are generally based on antiferromagnetic spin states. The origin of these complex spin arrangements is the mixture of various interactions the simplest of which is the competition between long-range, oscillatory RKKY interactions and local anisotropy interactions.

Helimagnetism appears predominantly in the rare earths and actinides. Many rare earth metals have a layered structure. Consider a simplified case, relevant for dysprosium, where there is ferromagnetic alignment of magnetic moments within the layers and between the layers there are nearest-neighbour (J_1) and next-nearest-neighbour (J_2) interactions. If the angle between the magnetic moments in successive layers is ϑ, the phase diagram shown in *figure 2.13* may be derived [7].

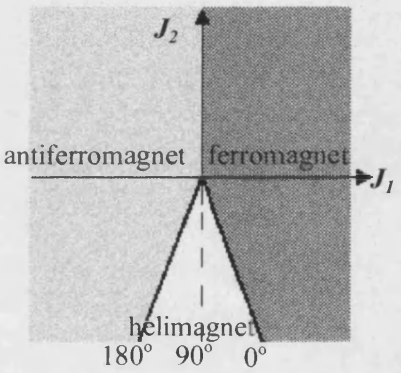

Figure 2.13 – Phase diagram for simplified planar model of Helimagnetism [7].

Helimagnetism is favoured over ferromagnetism or antiferromagnetism when $J_2 < 0$ and $|J_1| < 4|J_2|$. The pitch of the spiral, will not in general be commensurate with the lattice parameter and so no two layers in a crystal will have exactly the same spin directions.

2.2.6 Competing interactions

In some lattices there is no ground state which satisfies all the interactions in the system, leading to a variety of similar low-energy states of the system. The system is said to exhibit magnetic frustration. This is best demonstrated by the case of an antiferromagnet based on a triangular lattice (*figure 2.14*).

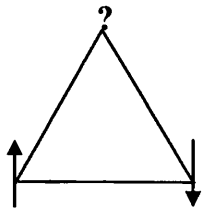

Figure 2.14 – Triangular based antiferromagnet

The first two spins may be placed anti-parallel, but the third cannot be anti-parallel with both of the others; therefore one of the two will not have its energy minimised and the system cannot achieve a state that entirely satisfies its microscopic constraints, although there are a multiplicity of equally dissatisfied states possible. Pyrochlore structures, where magnetic ions occupy a lattice of corner sharing tetrahedra, provide some of the most well studied frustrated systems [8-14].

Spin glasses must possess an element of frustration and competing interactions alongside some degree of chemical disorder. A spin glass is defined as a random, mixed-interacting magnetic system characterised by a random yet cooperative freezing of spins at a well defined temperature T_f, below which a highly irreversible, metastable frozen state appears without magnetic long-range order. Early research into spin glasses were based on systems with a dilute, random distribution of magnetic ions in a metallic lattice, leading to either site-randomness, for example in alloys such as $Cu_{1-x}Mn_x$, or bond randomness, where the nearest neighbour interactions vary. The randomness inherent in a spin glass is as important as the presence of competing interactions. The distribution of distance between moments in a random-site spin glass leads to competing interactions because the interactions are of RKKY-type and therefore their sign (ferromagnetic or antiferromagnetic) depends on the distance between the spins. In a random-bond spin glass, different bonds "pull" the system different ways, introducing frustration so that there is a multidegenerate ground state, but in spin glasses there is also a new effect, a cooperative freezing transition.

At high temperature the behaviour of all magnetic systems is dominated by thermal fluctuations: in a spin glass all the spins are independent. As a spin glass is cooled from high temperature the independent spins slow down and build up into locally correlated units: clusters. The spins that are not in clusters take part in interactions between clusters. As the temperature cools to T_f, the fluctuations in the clusters progressively slow down and the interactions between spins increase in range so that each spin becomes aware of more spins in a progressively growing region around it. At

T_f the system finds one of its many ground states and freezes. This process is not fully understood but appears to be a cooperative phase transition, but not to a magnetically ordered state: there are no magnetic Bragg peaks found in scattering experiments, and below T_f the system appears to be "glassy", possessing metastability and slow relaxation behaviour. There is a divergence between field-cooled and zero-field-cooled magnetic susceptibility below T_f reflecting this metastability [7].

2.2.7 Low dimensionality

Much attention has been devoted to low-dimensional magnetic systems in recent years, because of the many interesting ground states and phenomena unique to low dimensional magnets (for example the spin Peierls transition). Haldane's prediction that there will be an energy gap between the singlet ground state and the first excited state for integer spin one-dimensional Heisenberg antiferromagnets, but not for half-integer spin chains, has led to further interest [15, 16].

The Mermin-Wagner-Berezinskii theorem [17] demonstrates that in dimensions of $d \leq 2$, thermal fluctuations prohibit the existence of long-range magnetic order at non-zero temperature in an isotropic system [7]. In an isotropic Heisenberg ferromagnet with rotational symmetry such that there is free rotation of spin direction, it is possible to excite fluctuations of the spins relatively easily and in one and two dimensions these fluctuations will destroy the long-range order. However, if there is significant anisotropy, there will be an energy cost associated with rotating the spins from their ground state value, and it is possible for this anisotropy to stabilise long-range order in some two dimensional systems. No long-range order exists for the one-dimensional s = ½ Heisenberg antiferromagnet even at T = 0.

The two-dimensional s = ½ square lattice Heisenberg antiferromagnet is of considerable interest, where $Sr_2CuO_2Cl_2$ is regarded as a good approximation. Inelastic neutron scattering has shown that as the temperature is reduced the system does not order but the correlated regions of short-range order increase in size. This size is known as the spin-spin correlation length, ξ, and it diverges at low temperature leading to true long-range order at T = 0. Despite the prohibition of long-range order in one-dimension established by the Mermin-Wagner-Berezinskii theorem as described above, there are still complex excitations and phenomena possible which are not yet entirely understood.

Spin Ladders:

The spin ladder is an interesting intermediary between one-dimensional antiferromagnetic chains and square lattices, obtained by assembling chains next to one another with bonds between them such that the interchain coupling is of a comparable strength to the intrachain coupling, forming "ladders" of increasing width. The transition between one-dimensional Heisenberg antiferromagnetic chain and two-dimensional Heisenberg antiferromagnetic square lattices via spin ladders is not trivial. Ladders made from an even number of chains or "legs" have a finite energy gap to the lowest s = 1 excited state which causes an exponential decay to zero in the susceptibility curve. Ladders with an odd number of legs display similar properties to one-dimensional chains. There is no spin gap in the s = ½ odd-leg ladder and the susceptibility does not fall away to zero but is finite at low temperatures.

Doping the spin ladder with holes breaks up singlets in a spin ladder. For two-leg ladders the number of damaged singlets can be halved if the holes share a rung, hence it is favourable for holes to pair, showing how it could be possible to engineer superconductivity in two-leg spin ladders such as has been discovered in $Sr_{14-x}Ca_xCu_{24}O_{21}$ [18-22].

Spin ladders are an extremely complex area of magnetism with no fixed expressions for the susceptibility, vast differences in properties depending on the number of legs in the ladder and similar properties to many other types of quantum magnets. As a result, there are many examples of ladders in the literature that are disputed. It is very difficult to prove beyond doubt that a compound is a spin ladder.

Spin Peierls Transition:

Although s = ½ antiferromagnetic chains are gapless, they are susceptible to an analogous kind of instability observed in one-dimensional metals and can open up a gap. The spin Peierls transition, which was theoretically predicted in the 1970's, is an unusual effect observed in a limited number of one-dimensional Heisenberg s = ½ antiferromagnets. In this model, a uniform quasi-one-dimensional s = ½ Heisenberg antiferromagnetic chain is coupled to three-dimensional lattice vibrations, which causes the chain to distort into pairs as a function of temperature. Above the transition, the magnetic behaviour is that of a one-dimensional antiferromagnet, below, the dimerisation of the spin lattice system leads to alternating exchange constants. The

dimerisation increases progressively and reaches a maximum at zero temperature. The alternating chain has an energy gap between the singlet ground state and the lowest lying band of triplet excited states. The magnitude of the gap is related to the degree of dimerisation and hence to the degree of lattice distortion.

2.2.8 Low-dimensional models:

Dimer model:

Majumdar and Gosh [23] theoretically predicted that in s = ½ antiferromagnetic chains there are competing nearest neighbour (J_1) and next nearest neighbour (J_2) interactions which are in a dimerised state for $J_2/J_1 = ½$. However, Haldane [24] argued that a spontaneously dimerised state exists for a wider range of J_2/J_1. For an antiferromagnetically interacting pair of s = ½ ions the splitting between the singlet ground state and triplet excited state must be in the order of k_BT to produce a dimerised state. Bleaney and Bowers derived an equation [25] to describe the behaviour of hydrated copper acetate as dimers and Matsuda and Katsumata [26] later obtained the same expression by analysing ESR results between the singlet and triplet states in $Sr_{14}Cu_{24}O_{41}$. The susceptibility of a dimerised state falls rapidly to zero as $T \rightarrow 0$.

$$\chi = \frac{2Ng^2\mu_B^2}{k_BT} \cdot \frac{1}{3 + e^{2J/k_BT}}$$

Equation 2.61 – χ = magnetic susceptibility; N = no. of dimers in the sample; J = exchange interaction between nearest neighbour magnetic moments; T = temperature in Kelvin; k_B = Boltzmann constant; g = gyromagnetic ratio; μ_B = Bohr magneton.

Bonner-Fisher model:

Bonner and Fisher [27] predicted thermal and magnetic properties for varying anisotropy and magnetic fields by calculating the energy levels and eigenvectors on short chains and rings of s = ½ ions. The results for 11- and 12-membered chains of antiferromagnetically exchange coupled s = ½ ions were extrapolated to the infinite chain length. Hall later took these results [28] and fitted the theoretical results obtained by Bonner [29] to a quadratic/cubic function:

$$\chi_M = \frac{(Ng^2\mu_B^2)}{k_B T}\left[\frac{A + Bx + Cx^2}{1 + Dx + Ex^2 + Fx^3}\right]$$

Equation 2.62 – χ_M = molar magnetic susceptibility; N = Avagadro number; g = gyromagnetic ratio; μ_B = Bohr magneton; k_B = Boltzmann constant; T = temperature in Kelvin; $x = \frac{|J|}{k_B T}$ where J = exchange interaction; A, B, C, D, E and F are constants with the values: A = 0.25, B = 0.14995, C = 0.30094, D = 1.9862, E = 0.68854 and F = 6.0626.

The expression is valid for $\mathbf{T > J/2k_B}$. The maximum in reduced susceptibility calculated from this expression occurs at:

$$\frac{k_B T_{max}}{|J|} = 1.297$$

Equation 2.63 – k_B = Boltzmann constant; T_{max} = Temperature in Kelvin at which the maximum in reduced susceptibility occurs; J = exchange interaction.

$$\frac{\chi_{max}|J|}{Ng^2\mu_B^2} = 0.07337$$

Equation 2.64 – χ_{max} = maximum value of reduced susceptibility; J = exchange interaction; N = Avagadro number; g = gyromagnetic ratio; μ_B = Bohr magneton.

In this expression (*equation 2.62*) the magnitude of the maximum on the antiferromagnetic susceptibility is determined by the g value for a given J. A discrepancy in this part of the fit may imply that the given model is inappropriate. The susceptibility of the one-dimensional linear chain approaches a non-zero value as T → 0, in contrast to the dimer model. This is due to the absence of an energy gap in the continuum of energy levels.

Alternating Chain Model:

The Bonner-Fisher model applies to a regular one-dimensional chain, but when J≠αJ as in *figure 2.15*, the Bonner-Fisher model is replaced by the Heisenberg alternating chain model.

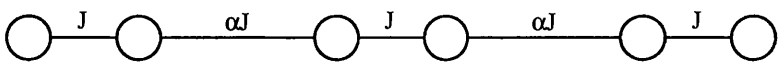

Figure 2.15 – Exchange parameters in an alternating chain.

The Hamiltonian for an antiferromagnetic Heisenberg alternating chain is:

$$H = -2J\sum_{i=1}^{N/2}(S_{2i}.S_{2i-1} + \alpha S_{2i}.S_{2i+1})$$

*Equation 2.65 – **H** = Hamiltonian; **J** = exchange integral between a spin and its right neighbour; **αJ** = exchange integral between the same spin and its left neighbour; **α** = alternation parameter, independent of temperature and has values $0 \leq \alpha \leq 1$.*

When $\alpha = 1$ the model reduces to the linear chain "Bonner-Fisher" model and when $\alpha = 0$ the model reduces to that of magnetically isolated dimers.

Hall [30] repeated calculations done by Duffy and Barr [31] for the reduced susceptibility of short alternating rings of up to ten s = ½ ions for $\alpha = 0$, 0.1, 0.2, 0.3, 0.4, 0.6, 0.8 and 1.0 using the cluster approach and derived the expression given below for the magnetic susceptibility of an s = ½ antiferromagnetic alternating Heisenberg chain:

$$\chi_M = \left[\frac{Ng^2\mu_B^2}{k_BT}\right]\left[\frac{A + Bx + Cx^2}{1 + Dx + Ex^2 + Fx^3}\right]$$

*Equation 2.66 – χ_M = molar magnetic susceptibility; **N** = Avagadro number; **g** = gyromagnetic ratio; μ_B = Bohr magneton; k_B = Boltzmann constant; **T** = temperature in Kelvin; $x = \frac{|J|}{k_BT}$ where **J** = exchange interaction; **A, B, C, D, E & F** are constants.*

In the alternating chain model there are two different sets of values for the constants:

Constant	$0 \leq \alpha \leq 0.4$	$0.4 \leq \alpha \leq 1.0$
A	0.25	0.25
B	$(-0.12587 + 0.22752\alpha)$	$(-0.13695 + 0.26387\alpha)$
C	$(0.019111 - 0.13307\alpha + 0.509\alpha^2 - 1.13167\alpha^3 + 1.0081\alpha^4)$	$(0.017025 - 0.12668\alpha + 0.49113\alpha^2 - 1.1977\alpha^3 + 0.87257\alpha^4)$
D	$(0.10772 + 1.4192\alpha)$	$(0.070509 + 1.3042\alpha)$
E	$(0.00028521 - 0.423462\alpha + 2.1953\alpha^2 - 0.82412\alpha^3)$	$(-0.0035767 - 0.040837\alpha + 3.4862\alpha^2 - 0.73888\alpha^3)$
F	$(0.37754 - 0.067022\alpha + 5.9805\alpha^2 - 2.1678\alpha^3 + 15.838\alpha^4)$	$(0.36184 - 0.065528\alpha + 6.65875\alpha^2 - 20.945\alpha^3 + 15.425\alpha^4)$

Table 2.2 – Values of constants for the alternating chain model.

The expression is valid for $k_BT/|J| > 0.5$ and for negative J values. A is set at 0.25 so the expression converges with the Curie-Weiss law at high temperatures.

Examples of alternating chain compounds are quite rare in the literature with more focus being put on spin ladders because of their link to high temperature superconductors. A third next nearest neighbour interaction may be introduced into an alternating chain as shown in *figure 2.16*. If this exchange is of a comparable size to the other two then the alternating chain model is no longer suitable. It is possible that the third interaction becomes important due to a structural distortion to a zigzag chain (*figure 2.17*). In this case, if it is decided that J_2 is the smallest exchange interaction then the spin-ladder model becomes more appropriate.

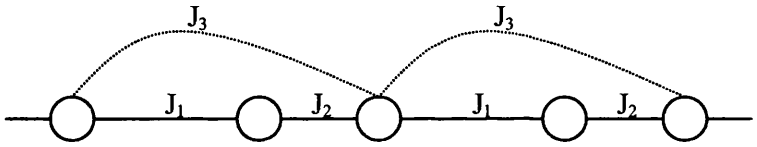

Figure 2.16 – Exchange parameters for next nearest neighbour interactions.

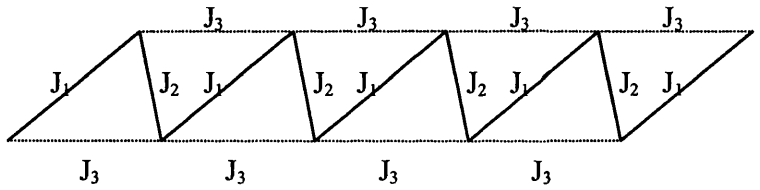

Figure 2.17 – Exchange parameters for zigzag chains.

2.3 μSR: Muon Spin Research

Muons are elementary particles belonging to the Lepton family, along with electrons, tauons and neutrinos. They have the same charge as electrons and protons but their mass is one ninth that of a proton and two hundred times that of an electron. However, while electrons and protons are stable particles, muons have a finite lifetime of approximately 2.2 μs.

A muon primarily acts as a sensitive magnetometer: it has spin one half and a nuclear magnetic moment of $8.8905\mu_n$. The muon spin will feel the effects of local fields at its site, once inside a material, and its precession or resonance allow these fields to be measured: implantation of spin-polarised muons and subsequent measurement of the time evolution of the polarisation enables examination of the distribution and fluctuations of the internal field [32].

2.3.1 Muon production

μSR requires beams of low-energy muons, which will stop in the samples being studied. These are produced at "meson factories", for example at the Paul Scherrer Institut in Switzerland, or at medium energy accelerators such as that of the Rutherford Appleton Lab, UK. A proton beam of 500-800MeV colliding with the nuclei of an intermediate target of a light element such as carbon or beryllium will produce a cloud of positive pions, which produce positive muons via the two-body decay shown in *equation 2.67*. Negative pions stopping in the production target are almost always captured by low-lying orbitals of the target nuclei before they have a chance to decay, hence negative muons must be produced by a different method. This thesis deals only with experiments using positive muons; therefore no more will be said about the production and use of negative muon beams.

$$\pi^+ \longrightarrow \mu^+ + \nu_\mu$$

Equation 2.67 – Decay of a pion to a muon and neutrino.

Due to parity violation in the weak interaction decay of pions, muons are perfectly spin polarised with respect to their momentum or flight path, resulting in a surface muon beam arriving almost 100% spin polarised in the sample. Muons themselves decay as shown in *equation 2.68*:

$$\mu^+ \longrightarrow e^+ + \nu_\mu + \overline{\nu_e}$$

Equation 2.68 – Decay of a muon to positron, neutrino and anti-neutrino.

The positron formed by muon decay is emitted preferentially along the instantaneous direction of the muon spin: hence recording the time dependence of the positron emission directions gives direct information about the spin-polarisation of the ensemble of muons. Since the behaviour of the polarisation depends on the local magnetic field at the muon site we are able to investigate the magnetic interactions taking place within the sample.

There is also an asymmetry in the angular distribution of the emitted positrons, due to parity violating terms in the Hamiltonian representing the interaction. The kinetic energy of the emerging positron may vary between zero and a maximum energy

$$E_{MAX} \cong \frac{1}{2} m_\mu c^2 \cong 52.3keV$$

Equation 2.69 – E_{MAX} = maximum kinetic energy; m_μ = muon mass; c = speed of light.

The emission probability of the positron distribution is given by *equation 2.70*:

$$W(\vartheta) = 1 + A\cos\vartheta$$

Equation 2.70 – $W(\vartheta)$ = emission probability; ϑ = angle between positron trajectory and the initial muon spin direction; $A = P\alpha$ is the asymmetry parameter, P is the beam polarisation and α is an intrinsic asymmetry constant determined by the weak interaction mechanism.

For the positrons of highest energy the asymmetry parameter $\alpha = 1$, but after averaging out over all energies, $\alpha = {}^1/_3$. The μSR technique uses the spin-polarised nature of the muon beams, and the asymmetric distribution of the decay positrons.

2.3.2 The Polarisation function

In muon experiments, t = 0 is defined as the moment a spin polarised positive muon is implanted into the sample. The thermalisation process is very fast (approximately 10^{-13}s) and the muons stop a few μm below the sample surface. Subsequently, their polarisation may become time dependent, **P**(t), under the influence of a magnetic field, **H**, present at the sample position. This field can be of internal or external origin, and has a component that is perpendicular to the magnetic moment of the muon resulting in its Larmor precession. The positron emission rate is monitored along a fixed direction, $\mathbf{r}_0$, which is taken to be the initial muon beam polarisation. What is detected is the number of positrons, dN_{e+}, emitted at an angle ϑ in the time interval dt:

$$\frac{dN_{e^+}(t)}{dt} = \frac{N_0}{\tau_\mu}\exp\left(\frac{-t}{\tau_\mu}\right)\left[1 + \alpha P(t).r_0\right] + B_0$$

Equation 2.71 – B_0 = background factor; N_0 = initial number of muons; P(t) = polarisation vector; τ_μ = muon lifetime.

The first two terms of this equation allow for the natural radioactive decay of the initial number of muons stopped and thermalised by means of electrostatic interactions within the sample. This description allows the polarisation vector P(t) to be determined by monitoring the angular distribution of the positrons:

$$P(t) = \left[P_x(0)\cos(\omega t + \phi), P_y(0)\sin(\omega t + \phi), P_z(0)\right]$$

Equation 2.72 - $\omega = \gamma_\mu H$ is the muon Larmor frequency and $P_x(0)=P(0)\cos\phi$, $P_y(0)=P(0)\sin\phi$ and $P_z(0)$ represent the initial μ^+ polarisation at the instant it enters the field H.

Transverse field:

There are three types of experimental set-up used to collect μSR data: transverse field, longitudinal field and zero field. In transverse field experiments (*figure 2.18*) an external magnetic field is applied perpendicular to the initial beam polarisation, P(0), causing precession of the muon spin, and therefore of the polarisation vector, P(t), in the *xy*-plane, assuming $|P(0)| = P_x(0)$ and $P_y(0) = P_z(0) = 0$. With this geometry, detectors positioned "up" and "down" with respect to the incoming muon beam are used to detect the emitted positrons. Thus *equation 2.71* becomes:

$$\frac{dN_{\perp}(t)}{dt} = \frac{N_0}{\tau_\mu}\exp\left(\frac{-t}{\tau_\mu}\right)\left[1 + \alpha P_x(0)\cos(\omega t + \phi)\right] + B_0$$

Equation 2.73

The Larmor precession of the muon polarisation beam results in an oscillatory modulation of the positron detector rate.

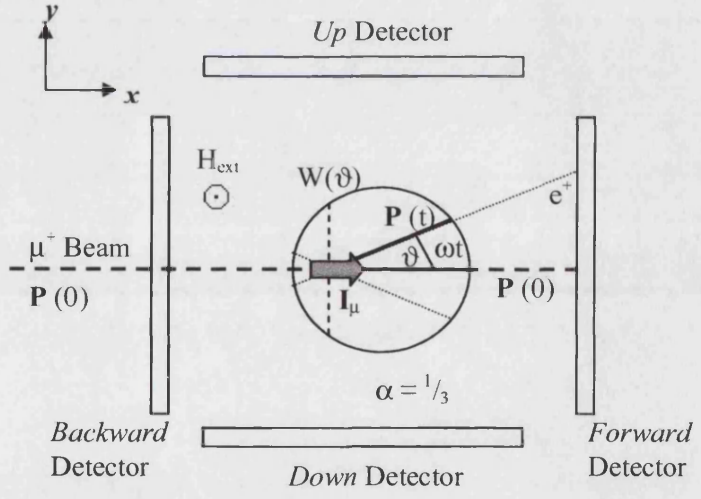

Figure 2.18 – Angular distribution of positrons from the muon decay averaged over all energies. The arrow indicates the polarised nature of the muon beam at the instant of implantation in the target sample. Also shown is the experimental set-up for transverse field geometry μSR.

Longitudinal field:

In the case of longitudinal field configuration, the applied field is along the direction of the initial beam polarisation, P(0), so that if $P_x(0) = P_y(0) = 0$ and $P_z(0) = |P(0)|$ *equation 2.71* becomes:

$$\frac{dN_{\parallel}(t)}{dt} = \frac{N_0}{\tau_\mu}\exp\left(\frac{-t}{\tau_\mu}\right)\left[1 + \alpha P_z(0)\cos\phi\right] + B_0$$

Equation 2.74

In this geometry there is no obvious Larmor precession of the muon spin, and the direction of observation is restricted to the "forward" and "backward" detectors with respect to the incoming muon beam. Zero-field experiments are performed in longitudinal geometry with zero applied external field, again using the "forward" and "backward" detectors.

In practice it is found that the interaction of the muon spin with other magnetic moments of nuclear or electronic origin in its environment leads to a depolarisation by dephasing of its spin precession, so that the initial amplitude of the muon ensemble polarisation is not preserved with time. This could be caused, for example, by an effective distribution of local fields caused by static, randomly oriented spins in the sample. Hence a time dependence is assumed for both transverse, $P_x(0)$, and longitudinal, $P_z(0)$, beam polarisations by ascribing a proper relaxation function to each. Equations *2.73* and *2.74* then become:

$$\frac{dN_{\perp}(t)}{dt} = \frac{N_0}{\tau_\mu}\exp\left(\frac{-t}{\tau_\mu}\right)\left[1 + \alpha P_x(0)G_x(t)\cos(\omega t + \phi)\right] + B_0$$

Equation 2.75 – Transverse field geometry.

$$\frac{dN_{\parallel}(t)}{dt} = \frac{N_0}{\tau_\mu}\exp\left(\frac{-t}{\tau_\mu}\right)\left[1 + \alpha P_z(0)G_z(t)\cos\phi\right] + B_0$$

Equation 2.76 – Longitudinal and zero-field geometry.

$G_x(t) = G_{\perp}(t)$ and $G_z(t) = G_{\parallel}(t)$ are the respective relaxation functions, containing information about the physical mechanism involved in the magnetic interaction of the muon with surrounding moments. For the purposes of this thesis, only longitudinal and zero-field geometry were used.

2.3.3 Relaxation in Longitudinal and Zero Field

Longitudinal and zero-field μSR use the same experimental arrangement, shown in *figure 2.19*.

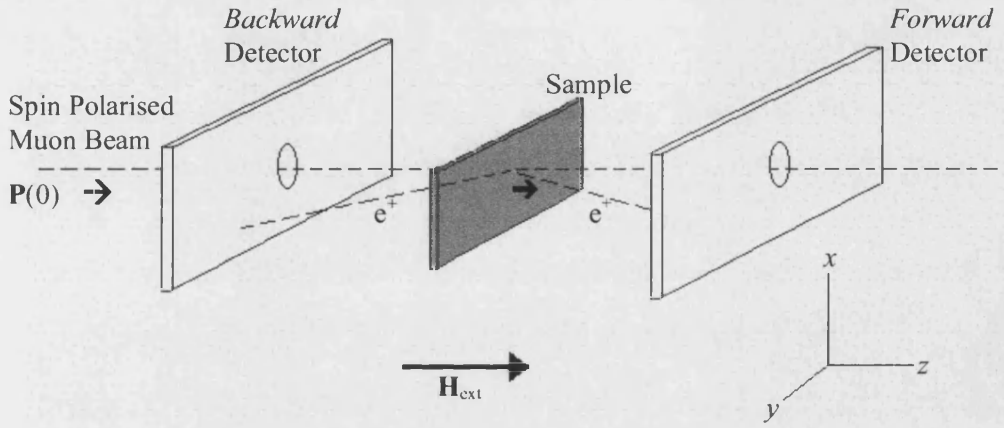

Figure 2.19 – Schematic for the experimental set-up of zero-field and longitudinal field μSR. One set of detectors is placed at 0° (Forward) and 180° (Backward) in respect to the initial muon beam polarisation.

Two time spectra are accumulated, one from each detector. Since the angular distribution of positrons is given by *equation 2.70*, the lifetime histogram of the muons exhibits asymmetry, which reflects the spin polarisation of the muons in the sample-target. The time evolution of the beam polarisation is obtained by taking the time differential ratio of the two spectra:

$$G_{\parallel}(t) = \frac{\frac{dN^{F}(0,t)}{dt} - A_0 \frac{dN^{B}(\pi,t)}{dt}}{\frac{dN^{F}(0,t)}{dt} + A_0 \frac{dN^{B}(\pi,t)}{dt}}$$

Equation 2.77 – $G_{\parallel}(t)$ = relaxation function; A_0 = correction for non-perfect detector geometry.

The correction parameter A_0, is usually determined experimentally by applying a weak transverse field. The relaxation function, $G_{\parallel}(t)$ contains information on the fluctuating components of local fields at directions perpendicular to the initial muon polarisation P(0). It can also discriminate between dynamic and static cases by changing the external field, H_{ext} [33], unlike the transverse field relaxation function, which cannot.

2.3.4 Relaxation in Static Random Fields

In a randomly oriented frozen spin system with a static moment at every lattice point, as illustrated in *figure 2.20*, the dipolar field at a muon site is well approximated by an isotropic Gaussian distribution, where Δ is the width of the Gaussian distribution.

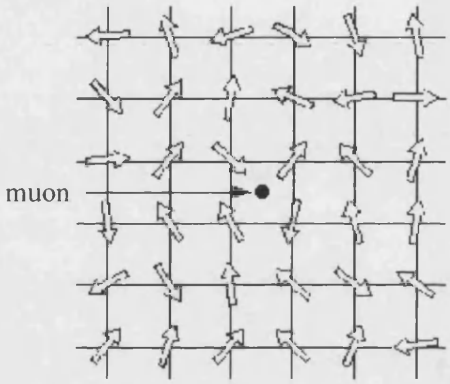

Figure 2.20 – Randomly oriented dense spin system. The local field is well approximated with an isotropic Gaussian distribution.

The relaxation of the muon is given by the static Gaussian Kubo-Toyabe function:

$$G_{\parallel}^{stat}(t) = \frac{1}{3} + \frac{2}{3}(1-\Delta^2 t^2)\exp\left(-\frac{1}{2}\Delta^2 t^2\right)$$

Equation 2.78 – Static Gaussian Kubo-Toyabe

The first term ($^1/_3$-component) originates from the fraction of the local field that is parallel to the initial muon spin polarization. This term is an important signature of static relaxation, because its existence doesn't depend on the shape of the field distribution. The second term ($^2/_3$-component) is the Fourier transform of the field distribution.

In zero magnetic field, the function first decays as a Gaussian and then comes back up to the non-relaxing $^1/_3$-component. With a longitudinal field applied, the amplitude of the flat component increases, because the fraction of the field that is parallel to the initial muon spin polarization increases. In static relaxation, the magnitude of the longitudinal field that decouples the relaxation is comparable to the field distribution width ($H_{LF} \approx \Delta/\gamma_F$). The distribution width can also be extracted from the Gaussian decay-rate at early times before the recovery.

Experimentally, the Gaussian Kubo-Toyabe behaviour of the muon spin relaxation, as well as its longitudinal field dependence, is typically observed in substances with nuclear magnetic moments, such as MnSi [33] and copper [34]. *Figure 2.21* shows $G_{\parallel}(t, H_{ext})$ for different values of the ratio $\gamma_\mu H_{ext}/\Delta$.

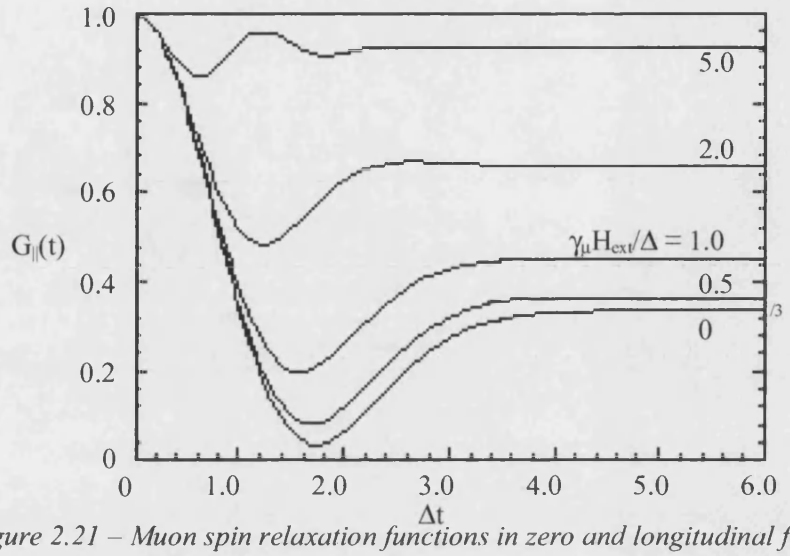

Figure 2.21 – Muon spin relaxation functions in zero and longitudinal fields (Kubo-Toyabe), resulting from a Gaussian distribution of static random moments.

The Gaussian Kubo-Toyabe theory introduced above is based on Gaussian local field distribution, which is often realized in dense spin systems. In dilute spin systems, when the number of the random magnetic dipole moments surrounding the muon is small, as found for example in AuFe, CuMn and dilute spin glass alloys, it is known that the dipolar fields from the local moments take a more Lorenzian distribution. The origin of this Lorenzian distribution is the large variety of the muon sites relative to the local moments (*figure 2.22*). Since some muons are located relatively far from the local moments (site A), and some close (site B), the local field distribution has a sharper peak around zero (from site A's) and a broader tail (from site B's) than the Gaussian field distribution.

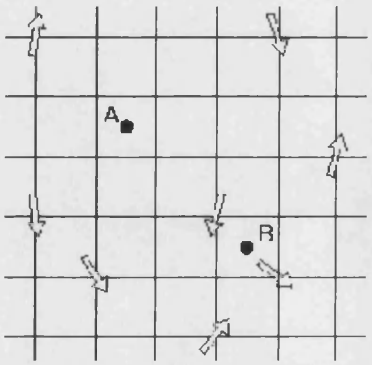

Figure 2.22 – A dilute spin system. The local field takes an isotropic Lorentzian distribution

The appropriate static Lorenzian Kubo-Toyabe function is given by *equation 2.79*:

$$G_{\parallel}^{stat}(t) = \frac{1}{3} + \frac{2}{3}(1 - \alpha t)\exp(-\alpha t)$$

Equation 2.79 - α/γ_μ = half width at the half maximum of the Lorentzian distribution.

Similar to *equation 2.78*, the relaxation function (*figure 2.23*) behaves like that shown in *figure 2.21*, but with an initial exponential damping. The asymmetry recovers towards an asymptotic $^1/_3$ value indicative of the presence of static random fields, which may be selectively decoupled by applying a finite longitudinal magnetic field.

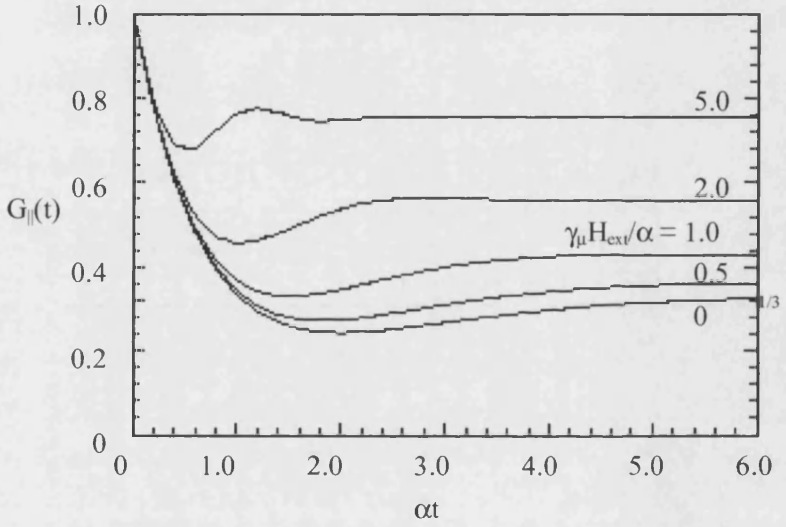

Figure 2.23 – Muon spin relaxation functions in zero and longitudinal fields (Kubo-Toyabe), resulting from a Lorentzian distribution of static random moments.

In conclusion, the presence of a $^1/_3$ tail in the zero-field μSR data is the signature of the static character of the random local fields responsible for the depolarisation of muon spin.

2.3.5 Relaxation in Fluctuating Random Fields

When the magnetic moments of the host fluctuate, the local field at the muon site will be modulated. Hayano and Uemura [33] used the "strong-collision model" [35] to take into account the effect of dynamical modulation of the local field (B_{loc}). The basic features of this model are that when there is a jump from $B_{loc,i}$ to $B_{loc,j}$, ($B_{loc,i}$ being the field at site *i*) the muon spin experiences a sudden change in field rather than a gradual change, and the local field at the muon site has a certain value for a given time interval: at a later time

it takes a new value that is not correlated to the first one. The expression for the relaxation function is given by an integral equation:

$$G_{\parallel}^{d}(t,\Delta,\nu) = G_{\parallel}^{stat}(t)\exp(-\upsilon t) + \upsilon\int_{0}^{t} G_{\parallel}(t-t')G_{\parallel}^{stat}(t')\exp(-\upsilon t')dt'$$

Equation 2.80- ν = fluctuation rate; $e^{-\nu t}$ = factor reflecting the reduction in the fraction of muons which did not collide within time t.

If the field distribution is static, the second term on the right hand side becomes irrelevant and the function for a static field distribution is recovered. The function is illustrated in *figure 2.24*.

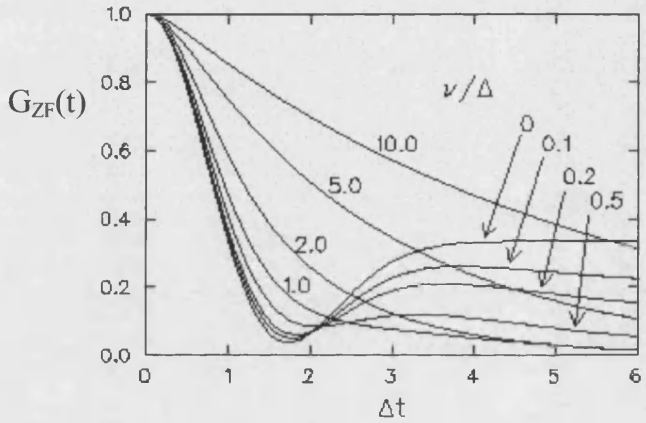

Figure 2.24 – Muon spin relaxation functions in zero field (Kubo-Toyabe) for different values of the magnetic correlation frequency, ν for a Gaussian distribution of fluctuating random moments.

The strong collision model can also be applied to a dilute magnetic system with a Lorenzian field distribution; the appropriate relaxation function decays exponentially in a similar way to the static case:

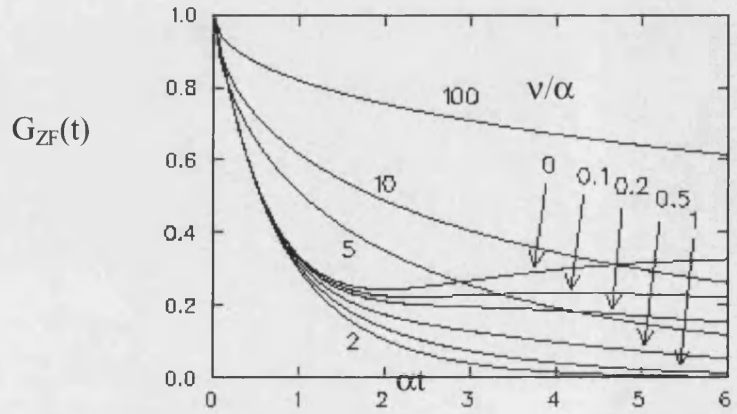

Figure 2.25 – Muon spin relaxation functions in zero field (Kubo-Toyabe) resulting from a Lorentzian distribution of fluctuating random moments.

For dynamic systems with a fluctuation rate $\nu >> \omega_{ext}$ field dependence of the muon polarisation is not expected, unlike the substantial field dependence observed in random static spin systems (*figure 2.21*): hence longitudinal field μSR can be used to differentiate between static and dynamic effects.

2.3.6 Continuous and Pulsed Muon Sources

There are two types of muon source in use at present: continuous and pulsed sources. In continuous sources the muons arrive at more or less random intervals, with the average interval determined by the total rate of the proton beam from a cyclotron, whose repetition frequency is short compared with the muon lifetime of 2.2μs. In a pulsed source the muons arrive at the sample in discrete bursts: the pulse duration is short and the recurrence long compared with the muon lifetime.

Continuous sources use a "time differential" method to collect the time decay histogram of the positron counter rate describing the muon polarisation. This method measures the time elapsed between an incoming muon and an outgoing positron. A sequence of observations of this type (events) is accumulated for every histogram. The measuring electronics are designed so that good events are those that do not overlap. This condition requires only one muon at a time to be present in the sample, and imposes a limit on the rate at which muons are implanted, arising from the intrinsic property of the technique that the decay positron should be observed in a certain time interval (ΔT) after a muon stops in the sample: this is the data-gate interval, usually amounting to several muon lifetimes. There is no such restriction in pulsed source experiments, and the rates of counting are only restricted by instrumental limits such as particle detection and data acquisition. The arrival of a muon burst in a pulse source renders the time-differential method useless: instead, when the muons arrive in the sample a common start-signal sets the beginning of the counting time and ends it when the decay positrons are detected. The statistics are improved by adding together histograms from consecutive bursts.

In addition to the signal arising from the depolarisation of the muon spin, a positron decay histogram versus time contains a background signal, arising from, for example, uncorrelated stopped muons and decay positrons (i.e. accidental second muon in the sample), which can be responsible for simulating false start-stop events. Histograms at continuous sources are more susceptible to background signals, which are

practically absent in a "clean" pulsed muon beam because the beamline is almost free of particles after the occurrence of a burst.

A pulsed muon beam operating with high statistics permits the study of slowly relaxing processes at long times (>10μs). The superior signal-to-noise ratio (the background becomes significant only beyond $10(\tau_\mu)$ at RAL) allows the determination of the longitudinal and/or zero field relaxation functions with good accuracy to much longer elapsed times; in contrast to the limited time range available at a continuous muon source, where the background precludes good statistics at long times. However, the advantages of high flux rates at pulsed sources in accumulating good statistics for a complete histogram in a short time and achieving a very good signal-to-noise ratio for the long times of the μSR histogram, may not always be what we need in order to be able to study fast relaxing phenomena. At early times the positron decay histogram may be distorted because of a large number of events overloading the detectors. In such a case, the early part of the relaxation needs to be excluded by setting an initial "dead-time" (~10ns) for the accumulation electronics. Other important factors resulting in limited time resolution are the finite width of the muon pulse (for example 5ns slice from each of the two initial 70ns long muon pulses at ISIS) and the uncertainty in the time of arrival of different muons with respect to their common start-time signal. Effectively, very fast relaxation processes are inaccessible.

For transverse and zero field studies in magnetically ordered systems, the maximum observed muon Larmor precession frequency is given approximately by the inverse of the pulse width. The finite pulse width imposes an upper limit on the magnitude of the hyperfine fields (frequencies) that can be studied (e.g. ~100MHz at ISIS). However, superb short time resolution is found in a continuous source and the range of frequencies observed may extend up to a few thousand MHz. This is because the highest frequency that can be resolved is closely related to the intrinsic time resolution of the detection electronics. In practice this is measured by the time the light needs to pass from the scintillator detectors to the photomultiplier tubes and usually corresponds to a time window of the order of 1ns.

At the ISIS μSR facility, the double pulse character (2 pulses at 325ns apart) of the muon beam may prevent the observation of certain Larmor precession frequencies from the muon implanted in magnetic materials. Thus for certain values of the internal field, muons from the second pulse may precess 180° out of phase with respect to

muons from the first one. An electronic device (UPPSET) is used, which applies an intense electric field in order to "throw away" the second pulse, with a subsequent reduction in the rate of events. This permits safe observation of any frequency within the previously mentioned limits of the instrument.

1. A.R. West, *Basic Solid State Chemistry*. 1997, Chichester: J. Wiley and Sons.
2. H.M. Rietveld, *J. Appl. Cryst.*, **2,** 65 (1969).
3. J. Rodriguez-Carvajal, *Fullprof*, 2000: Laboratoire Leon Brillouin.
4. A.C. Larson and R.B. Von Dreele, *GSAS*, 1990, Los Alamos National Laboratory: Los Alamos, California.
5. G. Burns and A.M. Glazer, *Space Groups for Solid State Scientists*. 2nd ed. 1990, London: Academic Press Ltd. 343.
6. M. Kalvius. *Magnetism.* in *The first Paul Scherrer Institut summer school on Condensed Matter Research*. 2002. Zuoz, Switzerland: PSI.
7. S. Blundell, *Magnetism in Condensed Matter*. Oxford Master Series in Condensed Matter Physics. 2001: Oxford University Press.
8. T. Fennell, O.A. Petrenko, G. Balakrishnan, S.T. Bramwell, J.D.M. Champion, B. Fak, M.J. Harris, and D.M. Paul, *Appl. Phys. A,* **74,** S889-891 (2002).
9. J.D.M. Champion, S.T. Bramwell, P.C.W. Holdsworth, and M.J. Harris, *Europhys. Lett.,* **57,** 93-99 (2002).
10. V. Bondah-Jagalu and S.T. Bramwell, *2001,* **79,** 1381-1385 (2001).
11. S.T. Bramwell and M.J.P. Gingras, *Science,* **294,** 1495-1501 (2001).
12. S.T. Bramwell and M.J. Harris, *J. Phys. Cond. Matt.,* **10,** L215-220 (1998).
13. M.J. Harris, S.T. Bramwell, T. Zeiske, D.F. McMorrow, and P.J.C. King, *J. Magn. Magn. Mater.,* **177,** 757-762 (1998).
14. M.J. Harris, S.T. Bramwell, D.F. McMorrow, T. Zeiske, and K.W. Godfrey, *Phys. Rev. Lett.,* **79,** 2554-2557 (1997).
15. F.D.M. Haldane, *Phys. Lett.,* **93A,** 464 (1983).
16. F.D.M. Haldane, *Phys. Rev. Lett.,* **50,** 1153 (1983).
17. N.D. Mermin and H. Wagner, *Phys. Rev. Lett.,* **17,** 1133 (1967).
18. J. Akimitsu, *Phys. C,* **259-261,** 1030-1031 (1999).
19. S. Katano, T. Nagata, H. Fujino, J. Akimitsu, M. Nishi, and K. Kakurai, *Physica B,* **259-261,** 1046-1047 (1999).

20. J. Akimitsu, K. Ohishi, T. Yokoo, K. Kakuta, H. Fujino, T. Nagata, R. Kadono, M. Nishi, K. Kakurai, and S. Katano, *Physica B,* **289-290,** 157-160 (2000).
21. R. Bewley, R.S. Eccleston, T. Nagata, and J. Akimitsu, *Physica B,* **276-278,** 662-663 (2000).
22. T. Nagata, H. Fujino, K. Satoh, N. Yamamori, J. Akimitsu, S. Katano, M. Nishi, K. Kakurai, M. Hiroi, M. Sera, N. Kobayashi, K. Tenya, H. Amitsuka, T. Takigawa, H. Inago, and T. Sakakibara, *J. Phys. Soc. Jpn.,* **70,** 2419-2424 (2001).
23. C.K. Majumdar and D.K. Gosh, *J. Math. Phys.,* **10,** 1399 (1969).
24. F.D.M. Haldane, *Phys. Rev. B,* **25,** 4925 (1982).
25. B. Bleaney and K.D. Bowers, *Proc. Inorg. Chem.,* **21,** 209 (1976).
26. M. Matsuda and K. Katsumata, *Phys. Rev. B,* **53,** 12201 (1996).
27. J.C. Bonner and M.E. Fisher, *Physical Review,* **135,** A640 (1964).
28. J.W. Hall, 1977, Univ. North Carolina: Chapel Hill.
29. J.C. Bonner, 1968, Univ. of London: London.
30. J.W. Hall, W.E. Marsh, R.R. Weller, and W.E. Hatfield, *Inorg. Chem.,* **20,** 1033 (1981).
31. W. Duffy and K.P. Barr, *Phys. Rev.,* **165,** 647 (1968).
32. A. Yaouanc and P. Dalmas de Reotier. *Magnetism.* in *The first Paul Scherrer Institut summer school on Condensed Matter Research.* 2002. Zuoz, Switzerland: PSI.
33. R.S. Hayano, Y.J. Uemura, J. Imazato, N. Nishida, T. Yamazaki, and R. Kubo, *Phys. Rev. B,* **20,** (1979).
34. R. Kadono, *Phys. Rev. B,* **39,** (1989).
35. R. Kubo, *J. Phys. Soc. Jpn.,* **9,** 935 (1954).

Chapter Three

Experimental Methods

3.1 Synthetic Methods

3.1.1 Soft Chemistry Preparations

All the compounds discussed in this thesis were prepared by a "chemie douce" method [1-6]: reduction of solid vanadium pentoxide with the appropriate amount of lithium iodide in acetonitrile. The required quantities of lithium iodide and vanadium pentoxide (99.99% purity by assay) were accurately weighed out, mixed and magnetically stirred in acetonitrile solution under flow of nitrogen gas for twenty-four hours. A greenish-blue precipitate (the colour is dependent on the amount of lithium intercalated into the vanadium pentoxide) was formed and separated by filtration using a Buchner funnel. The solid product was washed with acetone and dried at 40°C. The dry powder was pressed to a pellet and annealed at 80°C under vacuum for three days to ensure the complete removal of any remaining solvent. The products are not stoichiometric from the reagents but require an excess of lithium iodide as up to half is lost in synthesis. The lithium content of each product was obtained from magnetic measurements, chemical analysis and the refinement of the fractional occupancy of lithium in neutron powder diffraction data. The non-stoichiometric nature of this synthesis is discussed in more detail in chapter four.

3.2 Diffraction

3.2.1 X-ray diffraction

3.2.1.1 Powder X-ray Diffraction using a Siemens D500

The progress of each reaction was monitored using a Siemens D500 diffractometer operating in Bragg-Bretano geometry with Cu $K_{\alpha 1}$ and $K_{\alpha 2}$ radiation. Samples were mounted on plates, the powder being pressed into a recess and made flush with the surface of the plate using a glass microscope slide. Measurements were of two types: short scans for assessment of sample purity, and longer scans for final assessment and Rietveld refinement. The shorter measurements were taken over the angular range $5° \leq 2\vartheta/° \leq 70°$ with a 2ϑ step size of 0.04° and a counting time of 1 or 2 seconds. Longer scans were taken in the angular range $5° \leq 2\vartheta/° \leq 110°$ with a 2ϑ step size of 0.02° or 0.01° and a counting time of between 10 and 40 seconds, suitable for basic structural refinement using the Rietveld technique. The diffractometer was controlled by use of the Siemens Diffrac-AT software package.

3.2.1.2 Powder X-ray Diffraction using a Bruker D8

X-ray data for further Rietveld refinement were obtained using a Bruker D8 diffractometer operating either in reflection or transmission geometry. Samples were mounted on plates as for the D500 (reflection), or in glass capillary tubes (transmission) on a rotating sample stage. Measurements were taken over the angular range $5° \leq 2\vartheta \leq 110°$, with a step size of 0.01° and a counting time of between 10 and 40 seconds. The use of a position sensitive detector recovers much of the intensity lost in the use of a primary monochromator, giving data at higher resolution and single wavelength. The diffractometer was controlled by use of Bruker AXS software.

3.2.1.3 Powder X-ray Diffraction at the ESRF, Grenoble

Beamline BM01B at the European Synchrotron Research Facility, Grenoble was used to perform powder x-ray diffraction experiments. The beamline is installed on a bending magnet source (dipole BM 1), and the incoming beam divided by a splitter vessel into two separate beams. 10m downstream from the splitter vessel is BM1B and a 1 mrad fan of radiation (from –11.0 mrad to –12.0 mrad) is delivered through a vacuum pipe. Inside BM1B the beam hits a cooled Be-window and then a water-cooled, flat-crystal monochromator – a Si (111) crystal. A fixed, cooled beamstop prevents the white beam from entering the sample hutch, although this can be removed for white beam experiments. The beam cross-section is defined by a set of horizontal and vertical slits, and the beam passes through a final Be window before it hits the sample. The diffractometer is a 2-circle diffractometer, where each circle has a high precision encoder mounted directly on the rotary axis. There are 6 counting chains, i.e. 6 complete patterns are collected simultaneously, with a very small (approximately 1.1°) offset in 2ϑ. The offset is small in order to minimize the total data collection time. Each detector (Na-I scintillation counter) has an Si-111 analyser crystal mounted in front of it, leading to a resolution of approximately 0.01° at a wavelength of around 1Å. The instrument is capable of measuring over a wavelength range of 0.4–1.2Å. It is possible to perform both capillary and flat plate experiments over a wide temperature range using a He cryostat (4-350K) or furnace (room temperature – 1000°C). The environment in the furnace can be controlled with both oxidising and inert atmospheres.

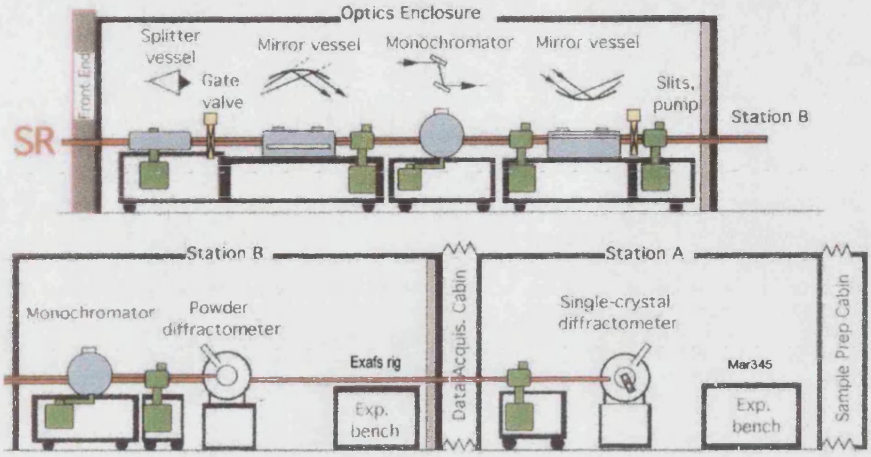

Figure 3.1 - Schematic layout of beamline BM1B, ESRF [7]

Samples were mounted in glass capillary tubes and measurements were taken over the angular range $1.5^{\circ} \leq 2\vartheta \leq 40^{\circ}$ with a step size of 0.0035° and counting time of 0.5 seconds per step. Two experimental set-ups were used, one with and one without the helium cryostat. A silicon capillary sample was used to obtain the exact wavelength for each experimental set-up. The wavelength 0.49956Å was used for the cryostat set-up and wavelength 0.49948Å for the set-up without cryostat. Scans with the cryostat covered the temperature range 15-300K.

3.2.2 Neutron Diffraction

Neutron diffraction experiments reported here were carried out at the spallation source at the ISIS, Rutherford Appleton Laboratory, Didcot, or on the constant wavelength diffractometer at the National Institute of Standards and Technology, Gaithersburg, USA.

3.2.2.1 National Institute of Standards and Technology, NIST, Gaithersburg, USA

The reactor operates using uranium fuel elements producing a thermal flux of 4×10^{14} neutron $cm^{-2}s^{-1}$ at a rated power of 20 MW, with a 7 week operating cycle. The reactor is D_2O moderated, cooled and reflected. The BT-1 diffractometer was used to collect powder neutron diffraction data. BT-1 is a 32 detector high-resolution powder diffractometer that can be used with three different monochromators: Ge [311], Cu [311] or Si [531], with either 15' or 7' collimation. The take off angles for the different

monochromators are shown in *figure 3.2*. The Cu [311], wavelength 1.5401Å, has the optimal balance between intensity and resolution and was used for most of the samples. The Ge [311], wavelength 2.077Å, monochromator yields the highest neutron intensity and best resolution but only at lower scattering angles ($2\vartheta < 40°$).

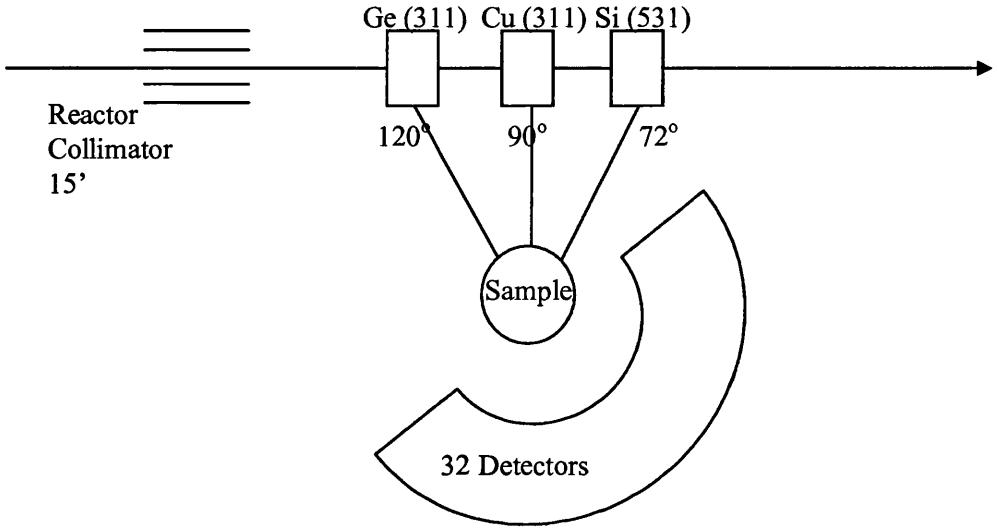

Figure 3.2 – Schematic diagram of diffractometer BT-1

3.2.2.2 ISIS, Rutherford Appleton Laboratory, Didcot, Oxfordshire, UK.

The high resolution powder diffractometer (HRPD) is situated 96m from the ISIS target at the end of a neutron guide. HRPD is the highest resolution neutron powder diffractometer of its type in the world: the main backscattering detection tank has a $\Delta d/d$ resolution $\approx 4 \times 10^{-4}$, which is effectively constant over the wide *d*-spacing range available. Short wavelength epithermal neutrons from the ISIS target allow *d*-spacings below 0.3Å to be recorded leading to the ability to separate peaks resulting from small unit cell changes, and to allow peaks at shorter *d*-spacings to be resolved from complex materials. The highest resolution data at backscattering can be recorded out to *d*-spacings of some 5-6 Å, due to the liquid methane moderator, which provides an incident flux out to a maximum wavelength of some 10-12 Å. Complementary detectors at 90° and low angles extend the measurable *d*-spacing range, albeit at lower resolution, to beyond 20 Å.

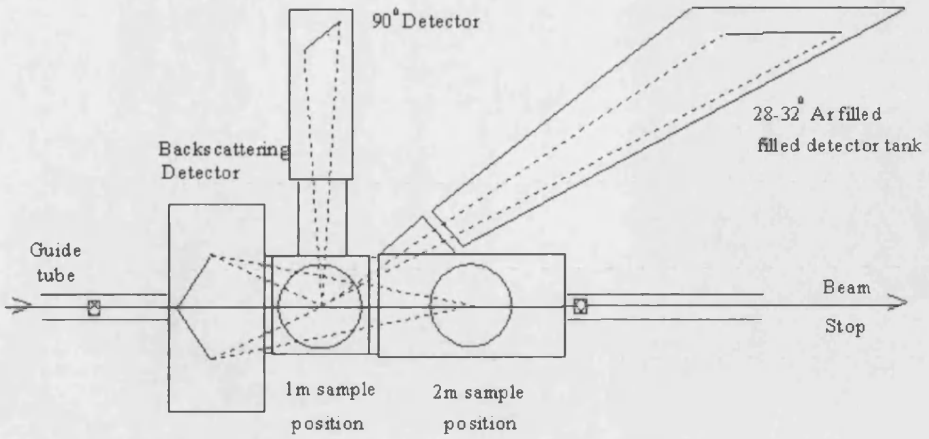

Figure 3.3 - Schematic plan view of the HRPD detector configuration [8]

3.3 Magnetism

3.3.1 SQUID Magnetometers

A Quantum Design MPMS SQUID (Superconducting QUantum Interference Device) was used to obtain all the magnetic data contained within this thesis. A SQUID is an extremely sensitive device for measuring the magnetic response of a material. In a fully calibrated system, measurements of the voltage variations from the SQUID detector as a sample is moved through the detection coils provide an accurate measure of the magnetisation of the sample, which can be performed as a function of temperature and field. The magnetic field produced by the sample is used to induce a supercurrent in a pick-up loop. The loop forms part of a circuit with a coil, which generates a magnetic field in the SQUID. The voltage across the SQUID is measured whilst moving the sample through the pick-up coil. The field inducing the current in the pick-up loop is proportional to the magnetic moment of the sample divided by the cube of the distance between the sample and the loop. Measurement of how the voltage across the SQUID varies with this distance allows the magnetic dipole moment of the sample to be determined and therefore for the magnetisation and susceptibility to be calculated. SQUID measurements can also be used to characterise magnetic behaviour [9].

For measurements reported here, approximately 100mg of accurately weighed powder sample were placed into a gelatine capsule. The capsule was placed into a probe and purged with helium before entering the main chamber. The magnetisation of the samples was measured as a function of temperature on warming after being cooled in the measuring field (FC). Routine measurements spanned the temperature range 1.8K-

300K. Details of measurement conditions for each data set recorded will be described individually. The magnetic data were then converted into the molar susceptibility χ_{mol} (Erg G^{-2} mol^{-1}) using the Microsoft Excel program. A least squares refinement programme was used to fit SQUID data to low-dimensional models.

3.4 μSR Research

3.4.1 EMU, ISIS, Rutherford Appleton Laboratory

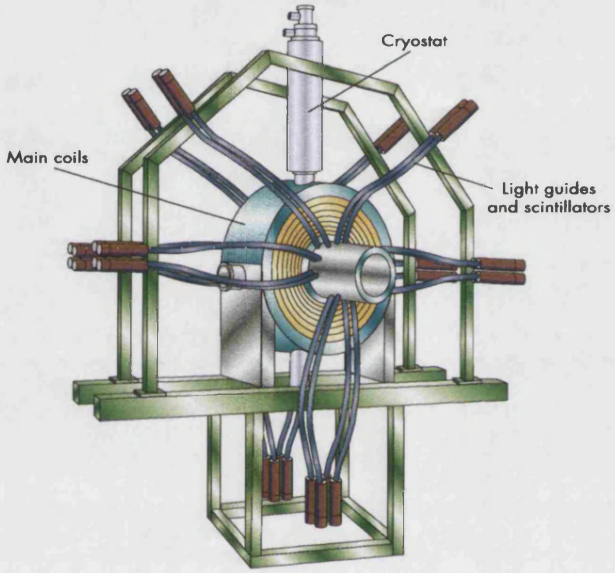

Figure 3.4 - A schematic view of the EMU spectrometer

The μSR experiments reported in this thesis were carried out at the EMU station at the ISIS source at the Rutherford Appleton Laboratory, Didcot, UK. ISIS is a pulsed source, meaning that muons arrive in the sample in discrete bursts. EMU is a 32-detector μSR spectrometer, which is optimised for zero field and longitudinal field measurements. Fields of up to 4000G can be applied, and sample temperatures in the range of 350mK to 1000K can be produced using a variety of sample environment equipment.

Samples were prepared for measurement by pressing approximately 1.5g of sample to form a circular pellet 20mm in diameter and 5mm in depth. The pellet was mounted onto a silver backing plate and covered in thin aluminium foil, secured in place with sticky tape that was kept out of the beam. The backing plate, with sample, was screwed into place in the cryostat. The beam spot was adjusted to cover the appropriate area. Measurements discussed in this thesis were collected in longitudinal field geometry, at fields between 0-1000G over the temperature range 4-40K.

1. J. Galy, *J. Solid State Chem.*, **100,** 229-245 (1992).
2. D.W. Murphy and S.M. Zahurak, *Inorg. Synth.*, **24,** 200 (1986).
3. C. Satto, P. Sciau, E. Dooryhee, J. Galy, and P. Millet, *J. Solid State Chem.*, **146,** 103-109 (1999).
4. J. Galy, C. Satto, P. Sciau, and P. Millet, *J. Solid State Chem.*, **146,** 129-136 (1999).
5. R.J. Cava, A. Santoro, D.W. Murphy, S.M. Zahurak, R.M. Fleming, P. Marsh, and R.S. Roth, *J. Solid State Chem.*, **65,** 63-71 (1986).
6. J. Galy, P. Millet, C. Satto, and P. Sciau, *J. Solid State Chem.*, **136,** 56-62 (1998).
7. B. Holme, *BM1B Swiss-Norwegian CRG*, 1999: http://www.esrf.fr/exp_facilities/BM1B/index.htm.
8. R.M. Ibberson, W.I.F. David, and K.S. Knight, *The High Resolution Neutron Powder Diffractometer (HRPD) at ISIS - A User Guide*, 1992.
9. M. McElfresh, *Fundamentals of Magnetism and Magnetic Measurements*. 1 ed. 1994, Purdue University: Quantum Design. 34.

Chapter Four

Synthesis & Structure of Lithium Vanadates

This chapter describes the synthesis of the series of compounds with the general formula $Li_xV_2O_5$, using "chemie douce" methods described in detail below, and their structure determination through Rietveld refinement of neutron and x-ray diffraction data. Although there have been previous structural studies made of this system (notably by Galy et al [1-15]), none have united a structural neutron and x-ray diffraction study with the electronic properties over a range of temperatures and compositions. There has been extensive work in this area over the past forty years, since the abilities of V_2O_5 as host material for intercalation were recognised [6, 16-18]. Studies of the vanadium oxide bronzes $A_xV_2O_5$, where A = Na, Ca, K, Mg, Cs etc., have been carried out almost entirely using high temperature solid-state synthetic methods. Studies on the lithium family, $Li_xV_2O_5$, however, may be grouped into three distinct categories by synthetic method: high temperature solid-state reactions, room temperature wet methods, and electrochemical methods. A number of distinct structures have been reported, in some instances more than one structure with the same nominal composition, where compounds have been synthesised and studied by different methods. Although phases are sometimes defined by lithium content, i.e. by value of x in $Li_xV_2O_5$, it is more usual to define them with respect to the specific structure of the V_2O_5 network adopted, as this allows easy comparison with other members of the $A_xV_2O_5$ family previously mentioned.

The original phase diagram published by Murphy [19] was constructed from the study of compounds synthesised using soft chemistry methods, which in this case involved the reduction of solid vanadium pentoxide by stirring with the appropriate stoichiometric amount of lithium iodide in acetonitrile at room temperature for twenty-four hours according to *equation 4.1*. The solid reagents used were dried under vacuum while the acetonitrile solvent was distilled from P_2O_5 under argon in order to keep the reaction free of moisture. The phase stability diagram was constructed from differential scanning calorimetry (DSC) and x-ray data.

$$V_2O_5 + xLiI \rightarrow Li_xV_2O_5 + (x/2)I_2$$

Equation 4.1 – Reduction of vanadium pentoxide by lithium iodide.

Galy *et al* used a very similar low temperature method, with the exception of performing the experiment under an inert atmosphere of argon and drying their product under vacuum [20]; hence their phase diagram is very similar to that published by Murphy. Rozier *et al* also mixed stoichiometric amounts of lithium iodide and

vanadium pentoxide in acetonitrile solution and stirred for several hours under argon, filtering and washing the product in acetonitrile and acetone [21], confirming the composition by iodometric titration against a standardized $Na_2S_2O_4$ solution. They reported that the amount of lithium intercalated into the vanadium pentoxide was less than expected: their results indicated that the effective x in $Li_xV_2O_5$ was approximately two thirds of the target value of x. However, Murphy [19] and Galy [20] also confirmed the composition of the products by titration of the iodine produced, yet claim to have found that it was possible to predict accurately the amount of lithium intercalated, in other words, to achieve the target stoichiometry.

The $Li_xV_2O_5$ phases reported in this work have been synthesised via a soft chemistry method similar to those used by Murphy, Galy and Rozier. Stoichiometric quantities of lithium iodide and vanadium pentoxide were mixed in acetonitrile and stirred continuously under nitrogen gas for twenty-four hours. The mixture was filtered and washed with acetonitrile and acetone, and the product dried and annealed by heating to 80°C under vacuum. Samples were stored under nitrogen. The compositions were determined by magnetic susceptibility measurements and refinement of the fractional occupancy of lithium sites from neutron diffraction data obtained at HRPD, ISIS, UK and NIST, USA. A comparison of target lithium content and actual lithium content is given in *table 4.1:*

Target x	Actual x	Difference/%	Rozier's x
0.1	0.13(3)	30	0.07
0.5	0.33(2)	34	0.33
0.6	0.42(2)	30	0.40
0.66	0.50(1)	24	0.44
0.8	0.55(2)	31	0.53
1.0	0.64(1)	36	0.67
1.3	0.72(1)	45	0.87
2.0	0.95(3)	53	1.33

Table 4.1 – Comparison of target lithium content with actual lithium content and predictions by Rozier [21].

From *table 4.1* it can be seen that there is good agreement between Rozier's results and these results for target stoichiometries up to $x = 1$, however for target lithium contents $1 \leq x \leq 2$, up to half the lithium iodide is not intercalated, although diffraction patterns do

not show the formation of any impurity phases. It seems that it becomes increasingly difficult to intercalate lithium into vanadium pentoxide when some lithium is already present. This could be explained by lithium-lithium repulsion and the varying proximity of lithium sites occupied as the content increases.

X-ray and neutron diffraction data were collected on a series of compounds, $Li_xV_2O_5$, where $0 < x < 1$, synthesised by soft chemistry methods as described and discussed in chapters one and three. The sensitivity of these compounds to oxidation in air means that samples gradually degrade, making them unsuitable for study, and fresh samples must be synthesised. This was not immediately realised, as degradation occurs over a long period of time. Diffraction data discussed in this chapter were collected over three years: this period of time between neutron and x-ray diffraction experiments entailed the use of different batches of samples to collect the datasets. Although the magnetic susceptibilities were compared to confirm the compositions of neutron and x-ray samples, the sensitivity of these materials to the exact thermal conditions of synthesis has resulted in larger discrepancies between lattice parameters and atom positions than is wholly desirable, and certainly larger than would be expected had it been possible to use the same samples in collection of both crucial datasets. A small difference in such parameters is to be expected due to neutrons diffracting from the point nucleus while x-rays diffract from the surrounding electron cloud, and the remaining discrepancy may be accounted for by the fact that two different samples were used to collect data so that the exact lithium content may differ slightly between samples. For this reason, simultaneous refinement of neutron and x-ray data would be inappropriate as it would result in an average structure that is not a very good fit to either dataset, and hence not an accurate representation of either the vanadium or lithium environments. Instead, refinement of x-ray and neutron data will be presented and discussed separately in this chapter, the x-ray data being used to obtain detailed information about the vanadium environment, and neutron data to do the same for lithium for each composition: since vanadium does not scatter neutrons coherently its position has been fixed from x-ray data refinement; lithium, as a light atom, will be overpowered by vanadium in the x-ray data, but gives a reasonable contribution to the neutron pattern, thus its position has been determined from neutron data refinement. Lithium atom thermal parameters were held at $0.01Å^2$ in x-ray data refinement, while in neutron data refinement vanadium atom thermal parameters were held fixed at $0.025Å^2$.

4.1 $Li_{0.13}V_2O_5$

X-ray diffraction data were obtained at the ESRF using beamline BM1B; neutron diffraction data were collected at HRPD, ISIS. Refinement of these data based on the structure published by Galy *et al.* [3] that was described in the preceding chapter gave goodness-of-fit factors of χ^2 = 4.3 for the neutron data and χ^2 = 134 for x-ray data refinements. Although all the peaks can be indexed in the Pmmn space group used by Galy, there were significant intensity differences between predicted and observed patterns in refinement of both data sets, implying a problem with the atom positions. Shklover *et al.* [22] and Teller *et al.* [23] studied insertion of small amounts of magnesium into V_2O_5, and produced a model for the structure in the $Pmn2_1$ space group. A drop in symmetry from Pmmn to $Pmn2_1$ allows an extra degree of freedom along the cell depth axis: the vanadium and oxygen atoms in 4*f* sites in Pmmn are no longer restricted to (*x*, 0, *z*) or (*x* + ½, ½, *z*) positions, as the corresponding 4*b* sites in space group $Pmn2_1$ are variable (*x*, *y*, *z*) positions. The oxygen and lithium atoms that are constrained respectively to 2*a* (0, 0, *z*) and 2*b* (0, ½, *z*) positions in Pmmn, are transformed to the corresponding $Pmn2_1$ 2*a* (0, *y*, *z*) position. Refinement based on a $Pmn2_1$ model gave a much better fit than that based on Galy's α-$Li_{0.04}V_2O_5$ phase. However, χ^2 values for the final model are higher than the "ideal" value of one, due to anisotropic peak broadening caused by microstructure size and strain effects within the V_2O_5 layers. The increased FWHM for the neutron diffraction experiments where instrument broadening is greater than sample broadening means that the microstructural effects are not seen. The high-resolution data obtained from synchrotron x-ray diffraction experiments revealed a complex broadening with terms for size and strain effects modelled in Fullprof using the general anisotropic models. Strain broadening is governed by the variance of the factor M_{hkl}, where $M_{hkl} = \frac{1}{d_{hkl}^2}$, given by:

$$\sigma^2 = (M_{hkl}) = (h^2 \quad k^2 \quad l^2 \quad kl \quad hl \quad hk) \begin{bmatrix} S_A^2 & C_{AB} & C_{AC} & C_{AD} & C_{AE} & C_{AF} \\ C_{AB} & S_B^2 & C_{BC} & C_{BD} & C_{BE} & C_{BF} \\ C_{AC} & C_{BC} & S_C^2 & C_{CD} & C_{CE} & C_{CF} \\ C_{AD} & C_{BD} & C_{CD} & S_D^2 & C_{DE} & C_{DF} \\ C_{AE} & C_{BE} & C_{CE} & C_{DE} & S_E^2 & C_{EF} \\ C_{AF} & C_{BF} & C_{CF} & C_{DF} & C_{EF} & S_F^2 \end{bmatrix} \begin{bmatrix} h^2 \\ k^2 \\ l^2 \\ kl \\ hl \\ hk \end{bmatrix}$$

Equation 4.2 – Variance of M_{hkl} [24]

This expression simplifies for the lithium vanadate system to give three terms for strain broadening, S_{400}, S_{004} and S_{112} which are representative of broadening down the *h*, *k* and *l* axes respectively. Size broadening is modelled using the expression:

$$F(\alpha_z) = k_s d^2(\alpha_1 h^2 + \alpha_2 k^2 + \alpha_3 l^2 + \alpha_4 kl + \alpha_5 hl + \alpha_6 hk)$$

Equation 4.3 – Expression for size broadening where $k_s = 360/\pi^2 \times \lambda 10^{-3}$ *[24]*

Although these microstructure parameters vastly improve the quality of the fit, bringing χ^2 down from 8.21 to 3.46, the complete contributions to the peak shape from both sample and instrument broadening terms are not exactly modelled and there are some residual differences between the observed and calculated data on the four main reflections, though the intensities predicted are accurate and this discrepancy is directly related to the peak profile issues, as shown by the inset of *figure 4.1*. Coefficients for size and strain broadening for all compositions and temperatures are given in appendix one, in *tables A1.1-2*.

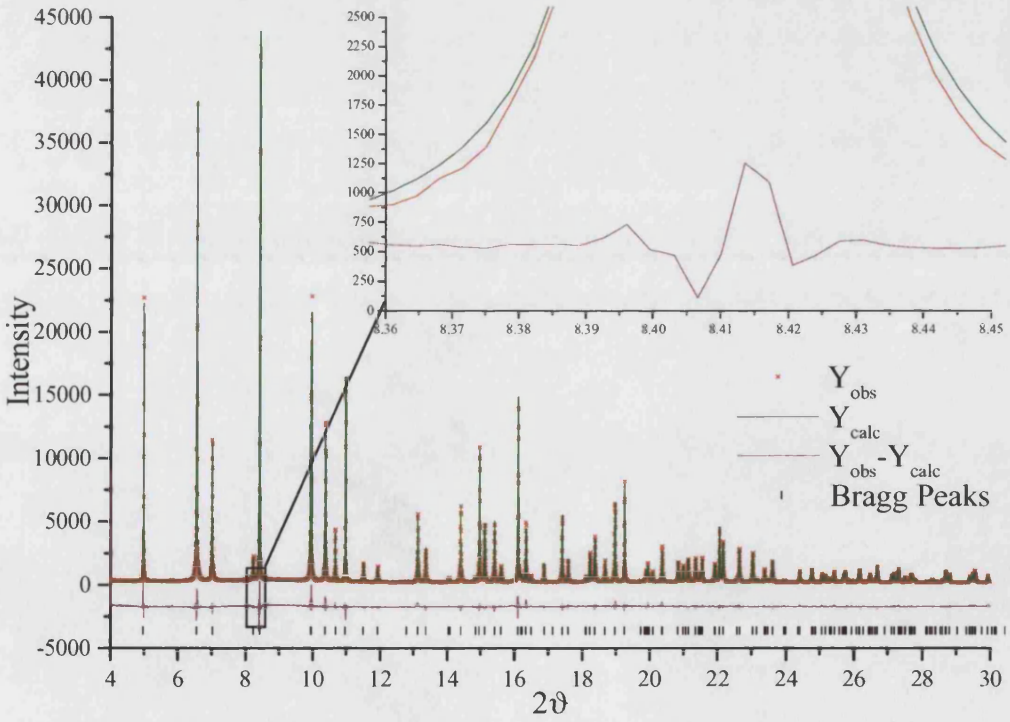

Figure 4.1 – X-ray diffraction data for $Li_{0.13}V_2O_5$*: intensity as a function of 2-theta, refined in the space group* $Pmn2_1$*. Inset is an enlargement of the difference curve for the highest intensity reflection.*

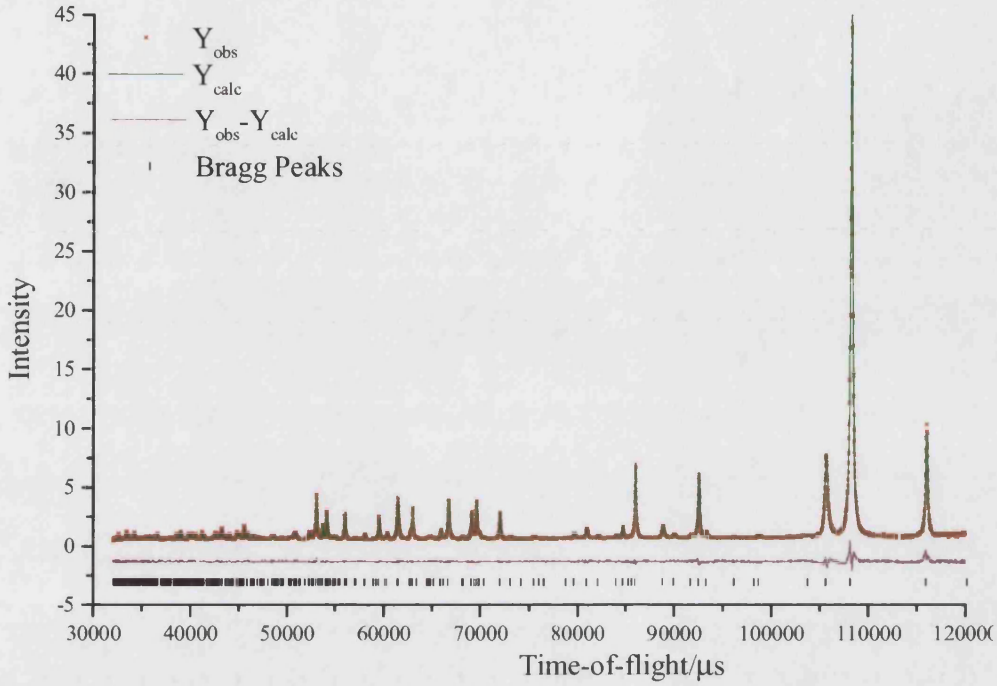

Figure 4.2 – Refined neutron data from HRPD for $Li_{0.13}V_2O_5$ in the $Pmn2_1$ space group: observed pattern in red, calculated pattern in green, difference in purple, Bragg positions in black. Intensity as a function of Time-of-flight.

X-RAY DATA						
χ^2	R_P		R_{WP}		R_B	
3.46	0.0632		0.0805		0.0640	
Space Group	**Lattice Parameters/Å**					
	a		**b**		**c**	
$Pmn2_1$	11.500907(32)		4.366170(12)		3.5610144(93)	
	α		**β**		**γ**	
	90		90		90	
Atom	**x**		**y**	**z**		**Frac.**
V1	0.14891(6)		0.10832(13)	0		1
O2	0.14506(19)		0.46869(38)	-0.0061(30)		1
O3	0.18102(16)		0.00334(41)	0.5001(22)		1
O4	0		-0.00274(58)	0.0365(43)		1
Li5	0.5		0.508	0.414		0.13

Atom	**Anisotropic Thermal Factors x 100/Å^2**					
	B11	**B22**	**B33**	**B12**	**B13**	**B23**
V1	2.73(13)	2.73(13)	2.73(13)	0	0	0
O2	3.91(5)	3.91(5)	3.91(5)	0	0	0
O3	3.91(5)	3.91(5)	3.91(5)	0	0	0
O4	3.91(5)	3.91(5)	3.91(5)	0	0	0
Li5	1	1	1	0	0	0

NEUTRON DATA						
χ^2	R_P		R_{WP}		R_B	
1.917	0.0396		0.0412		0.0481	
Space Group	**Lattice Parameters/Å**					
	a		**b**		**c**	
$Pmn2_1$	11.50329(5)		4.378288(27)		3.565455(15)	
	α		**β**		**γ**	
	90		90		90	
Atom	**x**	**y**		**z**		**Frac.**
V1	0.14891	0.10832		0		1
O2	0.14522(9)	0.46993(29)		0.003(16)		1
O3	0.18047(7)	0.00250(46)		0.498(16)		1
O4	0	-0.00354(67)		0.000(17)		1
Li5	0.5	0.508(18)		0.414(18)		0.13(3)
Atom	**Anisotropic Thermal Factors x 100/Å^2**					
	U11	**U22**	**U33**	**U12**	**U13**	**U23**
V1	2.5	2.5	2.5	0	0	0
O2	2.14(3)	2.14(3)	2.14(3)	0	0	0
O3	1.59(2)	1.59(2)	1.59(2)	0	0	0
O4	1.65(3)	1.65(3)	1.65(3)	0	0	0
Li5	2.5(9)	2.5(9)	2.5(9)	0	0	0

Table 4.2 – Crystallographic data, goodness-of-fit factors and anisotropic thermal parameters obtained by least squares refinement of x-ray and neutron diffraction data for $Li_{0.13}V_2O_5$.

Table 4.2 shows non-zero values for the oxygen positions along the *z*-axis, which corresponds to the constrained Pmmn *y*-axis, although the shifts are small and for the neutron refinement are within the error bar of the constrained value. However, there is a larger shift for the lithium atom position along the previously constrained axis, from ½ to 0.414(18), confirming the lower symmetry space group, $Pmn2_1$, is correct. The structure is shown in *figure 4.3*. The fractional occupancy of lithium was refined from neutron data to be 0.13(3), a composition that was confirmed by magnetic susceptibility measurements described in chapter five. *Table 4.3* gives the bond details of vanadium from refinement of these data.

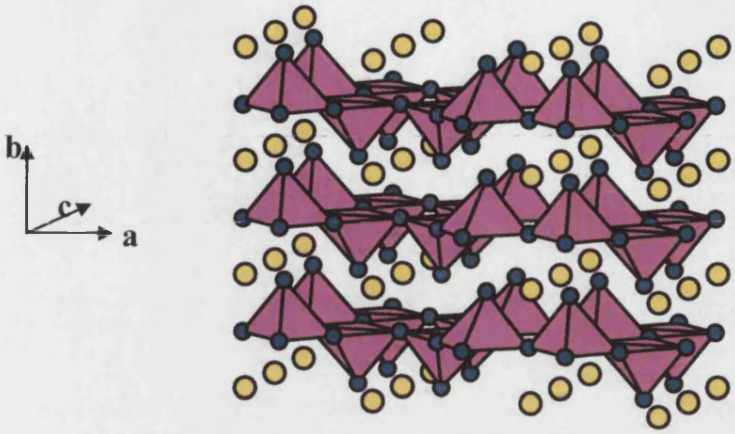

Figure 4.3 – Structure of $Li_{0.13}V_2O_5$ refined from x-ray and neutron diffraction data in space group $Pmn2_1$.

Bond lengths		Bond angles	
Bond	**Bond Length/Å**	**Atoms**	**Angle/°**
V-O2	1.57(2)	O3/O3'-V-O3''	75.51(12)
V-O4	1.78(1)	O3/O3'-V-O4	93.06(13)/101.06(20)
V-O3	1.87(1)	O3/O3'-V-O2	105.24(13)/103.71(21)
V-O3'	1.88(2)	O3''-V-O2	105.61(7)
V-O3''	2.02(1)	O4-V-O2	104.22(11)
V-V1	3.08(1)	V-O3-V1	104.47(13)
V-V2	3.56(1)	V-O3-V2	143.41(14)
V-V2'	3.43(1)	V-O4-V2'	147.32(8)
Puckering angle		4.05(1)	

Table 4.3 – Vanadium-oxygen bond lengths and angles and vanadium-vanadium distances for $Li_{0.13}V_2O_5$ obtained from refinement of x-ray diffraction data. Atom labels correspond to those used in §1.

The vanadium environment obtained from these data is isostructural with that of V_2O_5 as described in chapter one [3, 25]. Puckering in the structure causes a decrease in cell width and increase in layer spacing compared with the undoped compound (section 1.4.1), however, the puckering angle is relatively small and positive, unlike that of the previously reported α-$Li_{0.04}V_2O_5$ structure. In $Li_{0.13}V_2O_5$, lithium atoms are intercalated along the [001] channels and are four-coordinated by oxygen as shown in *figure 4.4*, with shorter lithium-oxygen separations (*table 4.4*) than reported for the eight-fold coordination observed in $Li_{0.04}V_2O_5$ [3, 9]. The average lithium-oxygen distance for this distorted square planar arrangement is 1.96Å, very close to the ideal 1.97Å separation in the preferred tetrahedral coordination, making this a suitable site. The small amount of lithium and therefore large separation and small mutual influence between lithium ions

results in a disordered lithium sublattice [12]. From these data, it appears that insertion of a small amount of lithium does not cause significant distortion in the host lattice vanadium oxide layers.

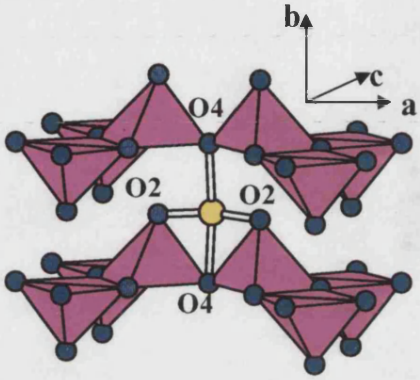

Figure 4.4 – Lithium co-ordination by oxygen within layers of $Li_{0.13}V_2O_5$ (obtained from refinement of neutron diffraction data). Lithium depicted in yellow, oxygen in blue and VO_5 polyhedra in pink.

Li-O	Separation/Å
Li-O4	2.23(8)
Li-O4	2.19(8)
2 x Li-O2	1.70(7)
Average	1.96

Table 4.4 – Lithium-oxygen separations in $Li_{0.13}V_2O_5$.

4.2 $Li_{0.33}V_2O_5$

4.2.1 Room temperature data

Room temperature neutron diffraction data were collected at NIST, USA and x-ray diffraction data at the ESRF. From phase diagrams published previously [7], it was expected that this composition would be made up of a mixture of α and ε phases. The former was refined in the $Pmn2_1$ space group that has been discussed in section 4.1; the latter was refined in the Pmmn space group. Fitted diffraction data are shown in *figures 4.5-6* and the results given in *tables 4.5-6*. The lithium content was refined from the fractional occupancy of lithium atoms to be 0.33(2), confirmed by magnetic susceptibility measurements. The phase mixture was found to consist of 59.5(11)% ε-$Li_{0.33}V_2O_5$ and 40.5(19)% α-$Li_{0.33}V_2O_5$, from refinement of x-ray diffraction data. Low temperature x-ray diffraction data were also obtained on this phase, and have been refined successfully from the same initial model (section 4.2.2). X-ray diffraction data collected at room temperature showed some additional, weak peaks not indexed by either phase, which are discussed in more detail later.

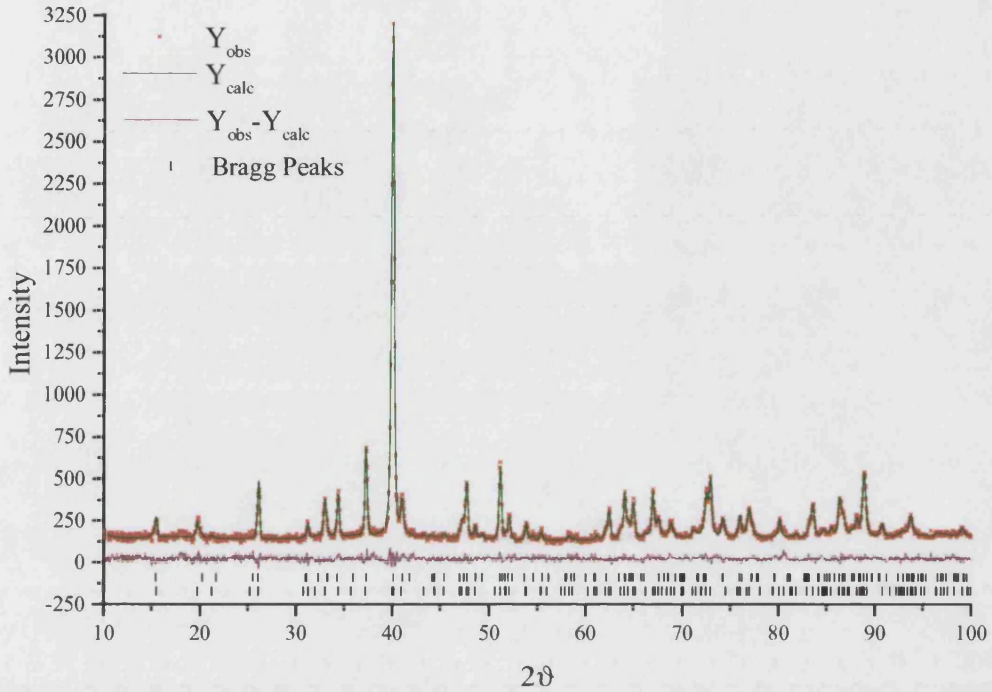

Figure 4.5 - $Li_{0.33}V_2O_5$ neutron diffraction data, Intensity as a function of 2ϑ, refined as alpha and epsilon phases.

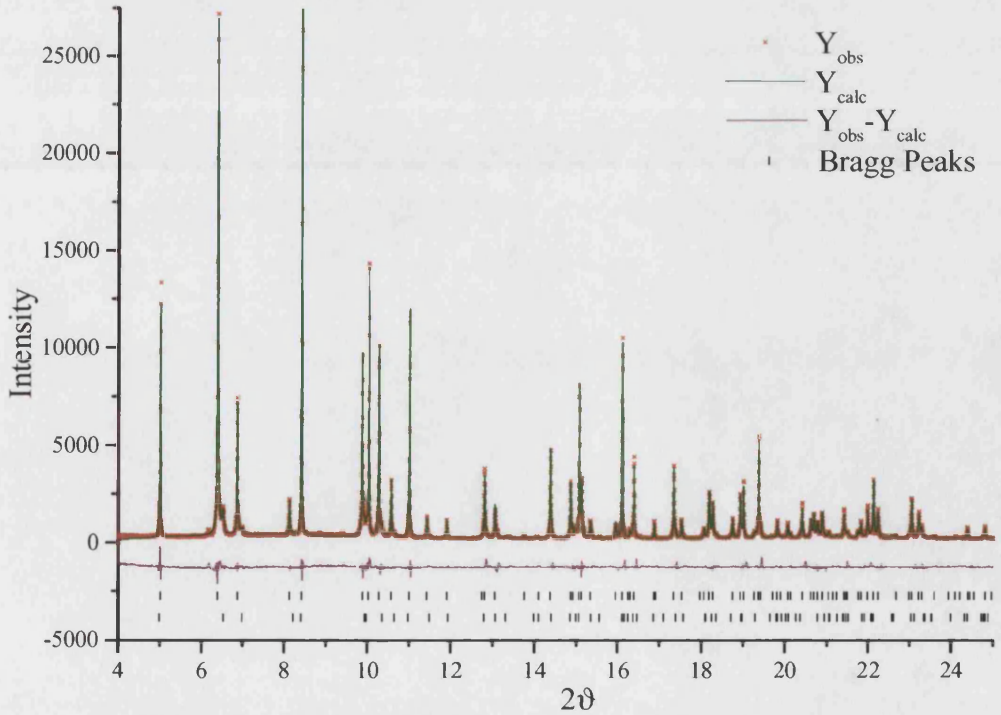

Figure 4.6 – Refinement of $Li_{0.33}V_2O_5$ x-ray diffraction data, intensity as a function of 2ϑ, as alpha and epsilon phases.

X-RAY DATA						
χ^2	R_P		R_{WP}		R_B	
4.06	0.0619		0.0813		0.0641	
α-$Li_{0.33}V_2O_5$ (Weight fraction 40.5(19))						
Space Group	**Lattice Parameters/Å**					
	a		**b**		**c**	
$Pmn2_1$	11.47257(37)		4.38606(23)		3.56320(6)	
	α		β		γ	
	90		90		90	
Atom	**x**		**y**	**z**		**Frac.**
V1	0.14915(65)		0.1063(15)	0		1
O2	0.1354(19)		0.4499(49)	0.9391(58)		1
O3	0.1982(18)		0.0343(79)	0.4811(76)		1
O4	0		0.0257(31)	1.0302(89)		1
Li5	0.5		0.310	0.580		0.33
Atom	**Anisotropic Thermal Factors x 100/Å^2**					
	B11	**B22**	**B33**	**B12**	**B13**	**B23**
V1	5.56(15)	5.56(15)	5.56(15)	0	0	0
O2	1.77(31)	1.77(31)	1.77(31)	0	0	0
O3	1.91(15)	1.91(15)	1.91(15)	0	0	0
O4	2.01(17)	2.01(17)	2.01(17)	0	0	0
Li5	1	1	1	0	0	0
ε-$Li_{0.33}V_2O_5$ (Weight fraction 59.5(11))						
Space Group	**Lattice Parameters/Å**					
	a		**b**		**c**	
Pmmn	11.41518(5)		3.56233(2)		4.47584(2)	
	α		β		γ	
	90		90		90	
Atom	**x**		**y**	**z**		**Frac.**
V1	0.10033(7)		0.75	0.60715(16)		1
O2	0.11152(23)		0.75	0.95862(56)		1
O3	0.07170(18)		0.25	0.49419(53)		1
O4	0.25		0.75	0.48818(76)		1
Li5	0.25		0.25	0.159		0.33
Atom	**Anisotropic Thermal Factors x 100/Å^2**					
	B11	**B22**	**B33**	**B12**	**B13**	**B23**
V1	3.92(12)	3.92(12)	3.92(12)	0	0	0
O2	2.17(22)	2.17(22)	2.17(22)	0	0	0
O3	2.65(35)	2.65(35)	2.65(35)	0	0	0
O4	2.30(51)	2.30(51)	2.30(51)	0	0	0
Li5	1	1	1	0	0	0

Table 4.5 – Crystallographic data, goodness-of-fit factors and anisotropic thermal parameters obtained by least squares refinement of x-ray diffraction data for $Li_{0.33}V_2O_5$.

NEUTRON DATA						
χ^2		R_P		R_{WP}		R_B
1.087		0.0407		0.0444		0.0610
α-$Li_{0.33}V_2O_5$ (Weight fraction 41.9(21))						
Space Group		**Lattice Parameters/Å**				
		a		**b**		**c**
$Pmn2_1$		11.4938(19)		4.3873(6)		3.5687(6)
		α		β		γ
		90		90		90
Atom		**x**	**y**		**z**	**Frac.**
V1		0.14915	0.10634		0	1
O2		0.1481(14)	0.4626(34)		1.04(9)	1
O3		0.1823(10)	-0.0150(49)		0.54(8)	1
O4		0	-0.0048(62)		1.04(8)	1
Li5		0.5	0.31(12)		0.53(31)	0.33(2)
Atom	**Anisotropic Thermal Factors x 100/Å^2**					
	U11	**U22**	**U33**	**U12**	**U13**	**U23**
V1	2.5	2.5	2.5	0	0	0
O2	3.25(9)	3.25(9)	3.25(9)	0	0	0
O3	3.25(7)	3.25(7)	3.25(7)	0	0	0
O4	2.91(8)	2.91(8)	2.91(8)	0	0	0
Li5	3.66(11)	3.66(11)	3.66(11)	0	0	0
ε-$Li_{0.33}V_2O_5$ (Weight fraction 58.1(17))						
Space Group		**Lattice Parameters/Å**				
		a		**b**		**c**
Pmmn		11.4297(4)		3.56584(18)		4.48085(25)
		α		β		γ
		90		90		90
Atom		**x**	**y**		**z**	**Frac.**
V1		0.10033	0.75		0.60715	1
O2		0.11075(40)	0.75		0.9641(14)	1
O3		0.07129(35)	0.25		0.4992(21)	1
O4		0.25	0.75		0.4950(29)	1
Li5		0.25	0.25		0.159(16)	0.33(2)
Atom	**Anisotropic Thermal Factors x 100/Å^2**					
	U11	**U22**	**U33**	**U12**	**U13**	**U23**
V1	2.5	2.5	2.5	0	0	0
O2	1.77(2)	1.77(2)	1.77(2)	0	0	0
O3	2.97(3)	2.97(3)	2.97(3)	0	0	0
O4	1.13(5)	1.13(5)	1.13(5)	0	0	0
Li5	5.46(25)	5.46(25)	5.46(25)	0	0	0

Table 4.6 – Crystallographic data, goodness-of-fit factors and anisotropic thermal parameters obtained by least squares refinement of neutron diffraction data for $Li_{0.33}V_2O_5$.

The structure of α-$Li_{0.33}V_2O_5$ is similar to that of α-$Li_{0.13}V_2O_5$ previously discussed: vanadium-vanadium separations are unchanged, although the vanadium oxygen bonds for this compound (*table 4.7*) are slightly shorter, and there is some rearrangement of lengths amongst the edge-shared oxygen atoms. There are, however, significant differences in the bond angles indicating a more distorted vanadium environment. The most obvious difference is the change in puckering angle, which increases from approximately 4° to approximately 10° with the increase of lithium content. This implies that insertion of more than a small amount of lithium causes significant distortion of the vanadium pentoxide layers, even when the lithium content is sufficiently low to allow formation of an α-$Li_xV_2O_5$ phase, though there is an increase in magnitude of the microstrain parameters, indicating increased internal strain.

Bond Lengths		**Bond Angles**	
Bond	**Bond Length/Å**	**Atoms**	**Angle/°**
V-O2	1.53(2)	O3/O3'-V-O3''	109.53(7)/93.13(10)
V-O4	1.75(1)	O3/O3'-V-O4	102.02(5)/107.84(7)
V-O3	1.83(4)	O3/O3'-V-O2	71.75(3)/68.96(8)
V-O3'	1.96(3)	O3''-V-O2	114.74(11)
V-O3''	1.86(1)	O4-V-O2	96.15(9)
V-V1	3.07(1)	V-O3-V1	112.40(10)
V-V2	3.56(1)	V-O3-V2	140.10(10)
V-V2'	3.42(1)	V-O4-V2'	155.62(11)
Puckering angle		10.43(1)	

Table 4.7 – Vanadium-oxygen bond lengths and angles and vanadium-vanadium distances from α-$Li_{0.33}V_2O_5$ x-ray diffraction data. Atom labels correspond to those used in §1.

Increased lithium content in α-$Li_{0.33}V_2O_5$ also has an effect on the position and environment of lithium ions (*table 4.8*). Although lithium is still four-coordinated by oxygen, lithium-oxygen distances have increased to an average of 2.00Å. The amount of lithium is still relatively small, resulting in a disordered lithium sublattice [12].

Li-O	**Separation/Å**
Li-O4	2.29(8)
Li-O4	2.18(8)
2 x Li-O2	1.77(7)
Average	2.00

Table 4.8 – Lithium-oxygen separations in α-$Li_{0.33}V_2O_5$.

ε-$Li_{0.33}V_2O_5$, has the refined structure shown in *figure 4.7*. The vanadium-oxygen bond details are given in *table 4.9*. Comparison of the parameters with those of α-$Li_{0.33}V_2O_5$ previously described shows a decrease in puckering angle from approximately 10° to approximately 2°, and a decrease in the magnitude of microstructure coefficients for both size and strain broadening. This implies an overall decrease in internal strain within the structure, suggesting the phase transition from α to ε may be driven by the need to reduce distortion in the layers.

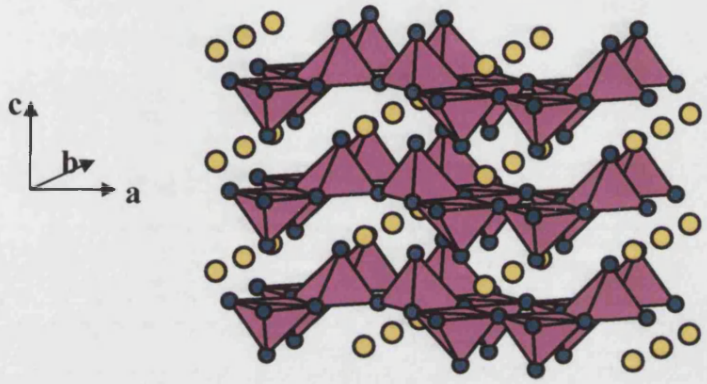

Figure 4.7 – Structure of ε-$Li_{0.33}V_2O_5$

Bond Lengths		Bond Angles	
Bond	**Bond Length/Å**	**Atoms**	**Angle/°**
V-O2	1.58(6)	O3/O3'-V-O3''	76.71(12)
V-O4	1.79(4)	O3/O3'-V-O4	94.93(21)
V-O3	1.88(1)	O3/O3'-V-O2	106.39(23)
V-O3'	1.88(1)	O3''-V-O2	107.65(31)
V-O3''	2.02(4)	O4-V-O2	102.67(4)
V-V1	3.06(1)	V-O3-V1	103.29(4)
V-V2	3.56(1)	V-O3-V2	142.65(4)
V-V2'	3.42(1)	V-O4-V2'	145.38(6)
Puckering angle		2.46(1)	

Table 4.9 – Vanadium-oxygen bond lengths and angles and vanadium-vanadium distances for ε-$Li_{0.33}V_2O_5$ from x-ray diffraction data.

Comparison of the bond lengths for this compound with those for the structure reported by Satto *et al. [20]* shows that the vanadium-oxygen bonds here are shorter than those of the published structure, and more like the separations found in undoped V_2O_5. This is likely to be due to the lower lithium content in this compound, $x = 0.33$ rather than $x = 1.0$ as in the published work, causing less reduction to V^{4+} and therefore less

lengthening of vanadium-oxygen bonds compared with V_2O_5. The bond angles are found to be between the values for V_2O_5 and ε-LiV_2O_5 [20].

Figure 4.8 shows the lithium environment in ε-$Li_{0.33}V_2O_5$:

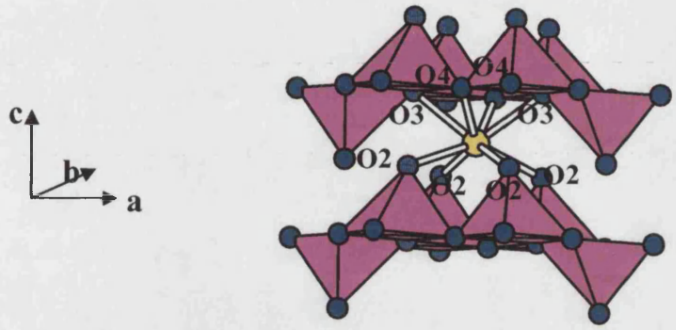

Figure 4.8 – Lithium environment in ε-$Li_{0.33}V_2O_5$ from refinement of neutron diffraction data at room temperature.

Lithium is eight-fold co-ordinated by oxygen in this structure, confirming the results of previous work discussed in chapter one. A comparison of lithium-oxygen separations, given in *table 4.10*, shows that the average separations in ε-$Li_{0.33}V_2O_5$ are similar to those found from previous work, and significantly larger than the lithium-oxygen distance in its preferred tetrahedral (1.97Å) or octahedral (2.14Å) coordination. This is not an energetically favourable site for lithium; transformation from ε-$Li_xV_2O_5$ to other phases, which have more stable lithium sites available will therefore be favoured, and the relative ease of transformation of ε-$Li_xV_2O_5$ with respect to other phases now becomes more understandable.

Li-O	Separation/Å
2 x Li-O4	2.33(5)
2 x Li-O3	2.55(4)
4 x Li-O2	2.54(2)
Average	2.49

Table 4.10 – Lithium-oxygen separations in ε-$Li_{0.33}V_2O_5$.

The relatively low lithium concentration in this compound implies a large separation between lithium ions and therefore small mutual influence, resulting in a disordered lithium sublattice, as observed for α-$Li_xV_2O_5$.

Additional very weak extra peaks are present in both the room temperature and 40K diffraction patterns that cannot be indexed and fitted in a straightforward manner, leading to an increased χ^2 value for refinement at both temperatures. *Figure 4.9* shows one of these extra peaks.

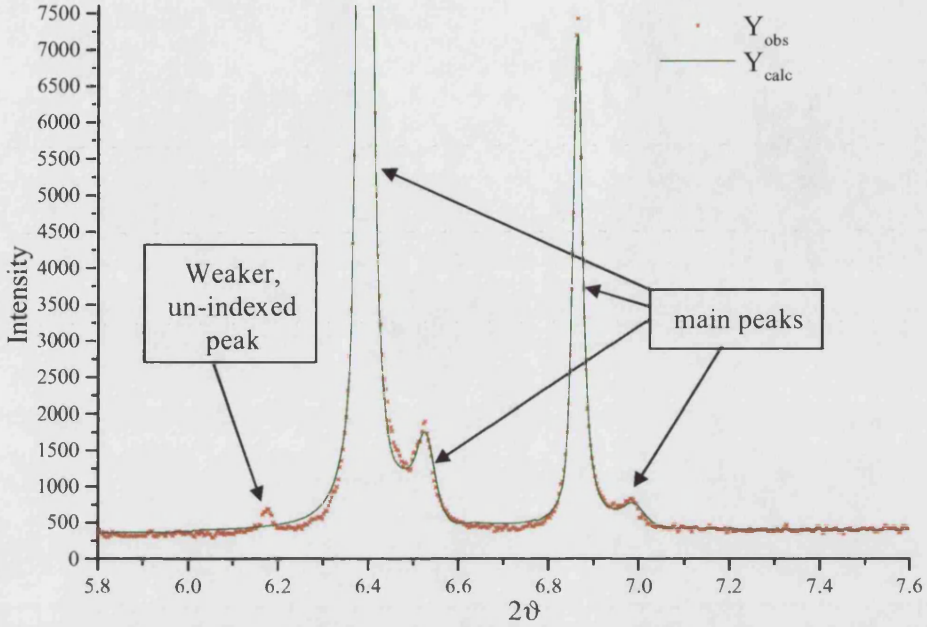

Figure 4.9 – Refined x-ray diffraction data, intensity as a function of 2ϑ, showing very weak extra peak at approximately 6.17°.

Since there are no extra peaks present in the neutron diffraction data, and these reflections do not correspond to a lowering of symmetry to, for example, a monoclinic system as described in section 4.5, a reasonable explanation for their presence is the occurrence of ordering of vanadium: as there is mixed valency of vanadium imposed by the intercalation of lithium, this is likely to be charge ordering. No extra peaks were observed in the α-$Li_{0.13}V_2O_5$ diffraction data, implying that the ordering is associated with the ε-phase. This postulation is supported by the fact that the extra peaks may be indexed as satellite reflections of ε-$Li_{0.33}V_2O_5$ from an incommensurately modulated superstructure, as shown in *table 4.11*. The modulation wave vector, $\mathbf{q}^{rt}$ may be written as:

$$\mathbf{q}^{rt} = 0.6339\mathbf{a}^* + 0.8122\mathbf{b}^* + 0.9107\mathbf{c}^*$$

With this modulation vector, all the reflections may be indexed by four integers (*h*, *k*, *l*, *m*) according to:

$$\mathbf{S} = h\mathbf{a}^* + k\mathbf{b}^* + l\mathbf{c}^* + m\mathbf{q}^{rt}$$

Equation 4.4

The n^{th} order satellites have $m = \pm n$; $m = 0$ corresponds to the main reflections.

h	*k*	*l*	*n*	D*(cal)	D*(obs)	2ϑ(cal)	2ϑ(obs)	2ϑ(obs-cal)
3	1	1	1	0.2148	0.2156	6.1513	6.1730	0.0217
3	0	1	1	0.3088	0.3085	8.8469	8.8396	-0.0073
2	0	0	1	0.3282	0.3282	9.4041	9.4041	0.0000
2	2	1	1	0.3548	0.3548	10.1693	10.1690	-0.0003
5	1	2	1	0.4564	0.4566	13.0920	13.0972	0.0052
-4	0	1	1	0.4660	0.4665	13.3690	13.3830	0.0141
5	0	0	1	0.4896	0.4896	14.0480	14.0479	-0.0001
6	0	1	1	0.5228	0.5218	15.0080	14.9775	-0.0305
3	-1	1	1	0.5497	0.5490	15.7832	15.7647	-0.0186
6	2	1	1	0.5767	0.5754	16.5637	16.5266	-0.0372
3	2	-1	1	0.5800	0.5809	16.6594	16.6844	0.0250

Table 4.11 – Weak satellite peaks from room temperature incommensurate vanadium superstructure, modulation vector (0.6339, 0.8122, 0.9107), R-factor = 0.77%.

4.2.2 $Li_{0.33}V_2O_5$ at 40K

Figure 4.10 shows data collected on $Li_{0.33}V_2O_5$ at 40K, fitted by refinement using the room temperature structure as an initial model. Refinement details are given in *table 4.12*. The slightly high value of χ^2 for this refinement may be explained by the presence of very weak extra peaks.

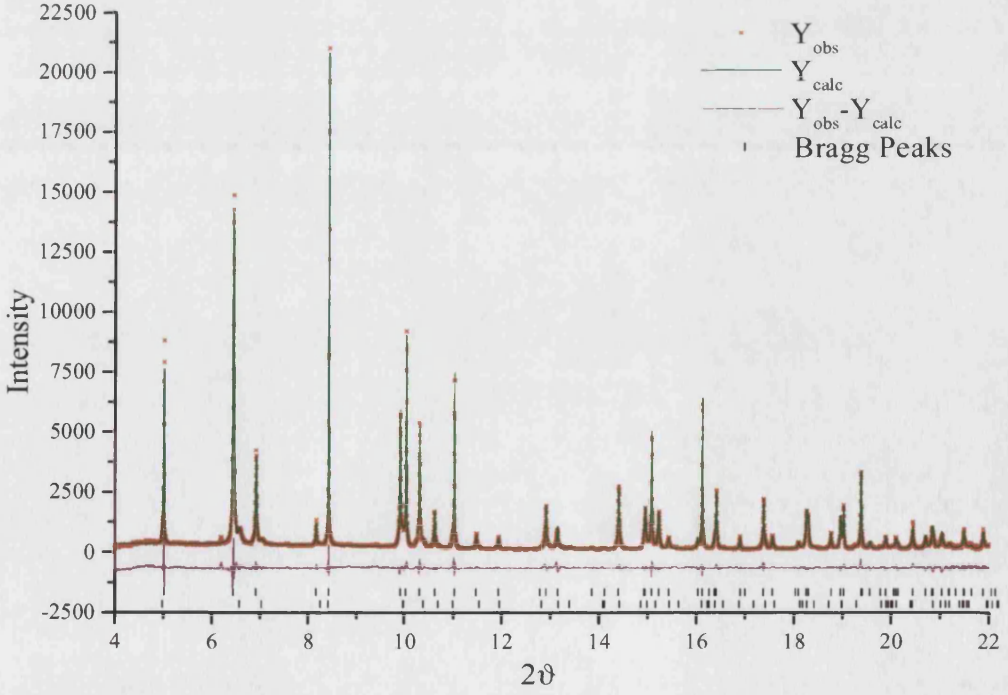

Figure 4.10 – X-ray diffraction data, intensity as a function of 2ϑ, collected at 40K on $Li_{0.33}V_2O_5$.

X-RAY DATA						
χ^2		R_P		R_{WP}		R_B
2.98		0.0695		0.0881		0.0828
α-$Li_{0.33}V_2O_5$ (Weight fraction 45.7(31))						
Space Group		**Lattice Parameters/Å**				
		a		**b**		**c**
$Pmn2_1$		11.47478(61)		4.35465(31)		3.56091(10)
		α		β		γ
		90		90		90
Atom		**x**		**y**	**z**	**Frac.**
V1		0.15198(91)		0.1127(24)	0	1
O2		0.1265(41)		0.4903(62)	1.018(23)	1
O3		0.2172(37)		0.1529(84)	0.443(14)	1
O4		0		0.0188(72)	0.919(26)	1
Li5		0.5		0.31	0.58	0.33
Atom	**Anisotropic Thermal Factors x 100/Å^2**					
	B11	**B22**	**B33**	**B12**	**B13**	**B23**
V1	8.18(19)	8.18(19)	8.18(19)	0	0	0
O2	7.8(12)	7.8(12)	7.8(12)	0	0	0
O3	7.8(12)	7.8(12)	7.8(12)	0	0	0
O4	7.8(12)	7.8(12)	7.8(12)	0	0	0
Li5	1	1	1	0	0	0
ε-$Li_{0.33}V_2O_5$ (Weight fraction 54.3(16))						
Space Group		**Lattice Parameters/Å**				
		a		**b**		**c**
Pmmn		11.41294(7)		3.55865(2)		4.44120(3)
		α		β		γ
		90		90		90
Atom		**x**		**y**	**z**	**Frac.**
V1		0.10078(13)		0.75	0.60818(31)	1
O2		0.11119(30)		0.75	0.96107(99)	1
O3		0.07165(28)		0.25	0.49348(67)	1
O4		0.25		0.75	0.4871(10)	1
Li5		0.25		0.25	0.16	0.33
Atom	**Anisotropic Thermal Factors x 100/Å^2**					
	B11	**B22**	**B33**	**B12**	**B13**	**B23**
V1	2.55(21)	2.55(21)	2.55(21)	0	0	0
O2	1.83(42)	1.83(42)	1.83(42)	0	0	0
O3	1.83(42)	1.83(42)	1.83(42)	0	0	0
O4	1.83(42)	1.83(42)	1.83(42)	0	0	0
Li5	1	1	1	0	0	0

Table 4.12 – Crystallographic data, goodness-of-fit factors and anisotropic thermal parameters obtained by least squares refinement of x-ray diffraction data collected at 40K.

The structure of α-$Li_{0.33}V_2O_5$ at 40K is shown in *figure 4.11*, and is quite different from the room temperature structure. The main differences are in the positions of the oxygen atoms, which have shifted at decreased temperature, twisting the pairs of VO_5 square pyramids. Similar twisting is observed at high temperatures during the phase transition from α-$Li_xV_2O_5$ to β-$Li_xV_2O_5$ [7] resulting in the formation of a tunnel structure as described in chapter one.

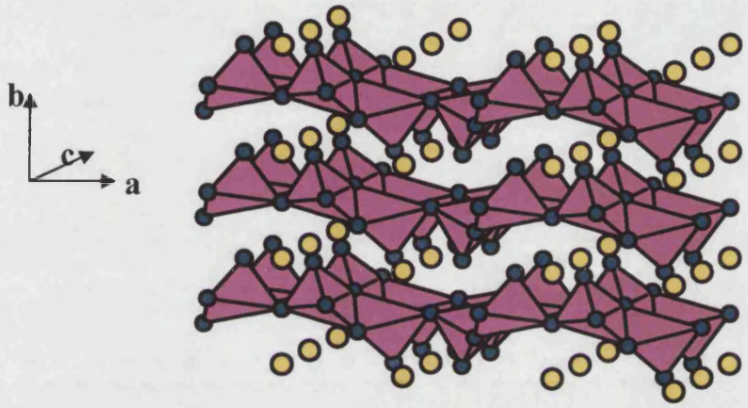

Figure 4.11 – Structure of α-$Li_{0.33}V_2O_5$ at 40K.

Like the room temperature structure, there is one vanadium position, shown in more detail in *figure 4.12*, and described in terms of bond lengths and angles in *table 4.13*:

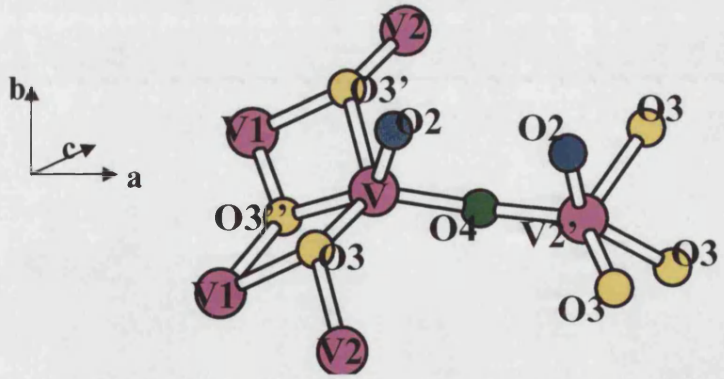

Figure 4.12 – Vanadium environment in α-$Li_{0.33}V_2O_5$ at 40K.

As would be expected from the shifted atom positions, there are some differences in vanadium-oxygen bond lengths and angles, with a general trend being for increased bond lengths.

Bond lengths		Bond angles	
Bond	**Bond Length/Å**	**Atoms**	**Angle/°**
V-O2	1.67(8)	O3/O3'-V-O3''	79.64(8)/70.93(11)
V-O4	1.81(7)	O3/O3'-V-O4	125.11(9)/102.06(5)
V-O3	1.75(5)	O3/O3'-V-O2	86.64(7)/90.99(8)
V-O3'	2.13(3)	O3''-V-O2	137.67(11)
V-O3''	1.91(5)	O4-V-O2	93.41(7)
V-V1	3.03(1)	V-O3-V1	111.80(13)
V-V2	3.56(1)	V-O3-V2	132.83(9)
V-V2'	3.49(1)	V-O4-V2'	148.01(7)
Puckering angle		46.12(1)	

Table 4.13 - Vanadium-oxygen bond lengths and angles and vanadium-vanadium distances at 40K for α-$Li_{0.33}V_2O_5$ from refinement of x-ray diffraction data.

The decrease in temperature has acted to close the angle between square pyramids, increasing the puckering angle from approximately 10° to approximately 46° at 40K, roughly four times its room temperature value. This increase in puckering is accompanied by an increase in magnitude of the microstructure parameters, and is indicative of the increased strain in the system on cooling. There are similarities between this structure and that of the β- and β'-phases, suggesting the possibility of transition to a more stable structure at low temperature, similar to the high temperature α → β → γ transition.

The ratio of phases at 40K is slightly different to that at room temperature, being made up of 45.7(31)% α-$Li_{0.33}V_2O_5$ and 54.3(16)% ε-$Li_{0.33}V_2O_5$ suggesting that there has been a small amount of transformation (~5%) between the two, though cycling experiments would be necessary to confirm this and investigate the reversible nature of the transformation.

Unlike α-$Li_{0.33}V_2O_5$, there are no significant changes in bond lengths and angles for ε-$Li_{0.33}V_2O_5$ at 40K, although there is the expected increase in magnitude of microstructural size coefficients. However, the extra, weaker peaks present at room temperature are still present at 40K and may be indexed by the same method. The modulation wave vector at 40K, $\mathbf{q}^{40}$, differs slightly from $\mathbf{q}^{rt}$ due to contraction of the unit cell at low temperature, and may be written as:

$$\mathbf{q}^{40} = 0.7855\mathbf{a}^* + 0.8075\mathbf{b}^* + 0.1955\mathbf{c}^*$$

With this modulation vector, all the reflections may be indexed, as shown in *table 4.14*, according to *equation 4.4*.

h	*k*	*l*	*n*	D*(cal)	D*(obs)	2ϑ(cal)	2ϑ(obs)	2ϑ(obs-cal)
2	1	1	1	0.2162	0.2162	6.1909	6.1915	0.0006
2	0	1	1	0.3087	0.3087	8.8448	8.8446	-0.0002
-1	0	1	1	0.3293	0.3285	9.4367	9.4142	-0.0225
5	1	1	1	0.4145	0.4142	11.8843	11.8772	-0.0070
4	0	-1	1	0.4514	0.4520	12.9479	12.9661	0.0182
5	1	-1	1	0.4607	0.4602	13.2154	13.2004	-0.0150
-1	0	2	1	0.4902	0.4902	14.0668	14.0669	0.0001
6	0	1	1	0.5410	0.5425	15.5337	15.5761	0.0424
7	1	0	1	0.5490	0.5504	15.7645	15.8046	0.0401
2	0	-2	1	0.5551	0.5552	15.9385	15.9427	0.0042
7	1	1	1	0.5761	0.5757	16.5474	16.5348	-0.0126
4	-1	0	1	0.5825	0.5808	16.7326	16.6821	-0.0505
-1	-1	2	1	0.6684	0.6691	19.2225	19.2418	0.0193

Table 4.14 – Weak satellite peaks from low temperature vanadium superstructure, modulation vector (0.7855, 0.8075, 0.1995), R-factor = 0.99%.

4.3 $Li_{0.42}V_2O_5$

Neutron diffraction data were collected at HRPD, ISIS, and ESRF again provided the x-ray diffraction data. Like $Li_{0.33}V_2O_5$, diffraction data for $Li_{0.42}V_2O_5$ may be refined equally well using any of the three previously published ε structures as an initial model. There is no α-phase present for this composition, and the Pmmn space group has been used to describe the structure of the ε-phase present. Refined data are shown in *figures 4.13-14*, and described in *table 4.15*. There are extra peaks in both sets of diffraction data for this composition: extra reflections in the x-ray diffraction data are a good match to those observed in the $Li_{0.33}V_2O_5$ data, confirming that these are linked to the ε- rather than the α-phase. Extra peaks in the neutron data are also present at this composition however, as indicated in *figure 4.14*, and these are discussed later in this section.

The vanadium environment is similar to that observed in ε-$Li_{0.33}V_2O_5$, with a slight increase in puckering angle from 2.46° to 2.84° in contrast to the large differences observed in the α- phase with increased lithium content. This supports the earlier suggestion that the transformation from α- to ε- is at least partly driven by the need to reduce strain in the layers. Microstructure parameters show an increase in the size effect l^2 and *kl* coefficients, corresponding with an increase along the *c*-axis and in the *bc* plane caused by increased lithium content.

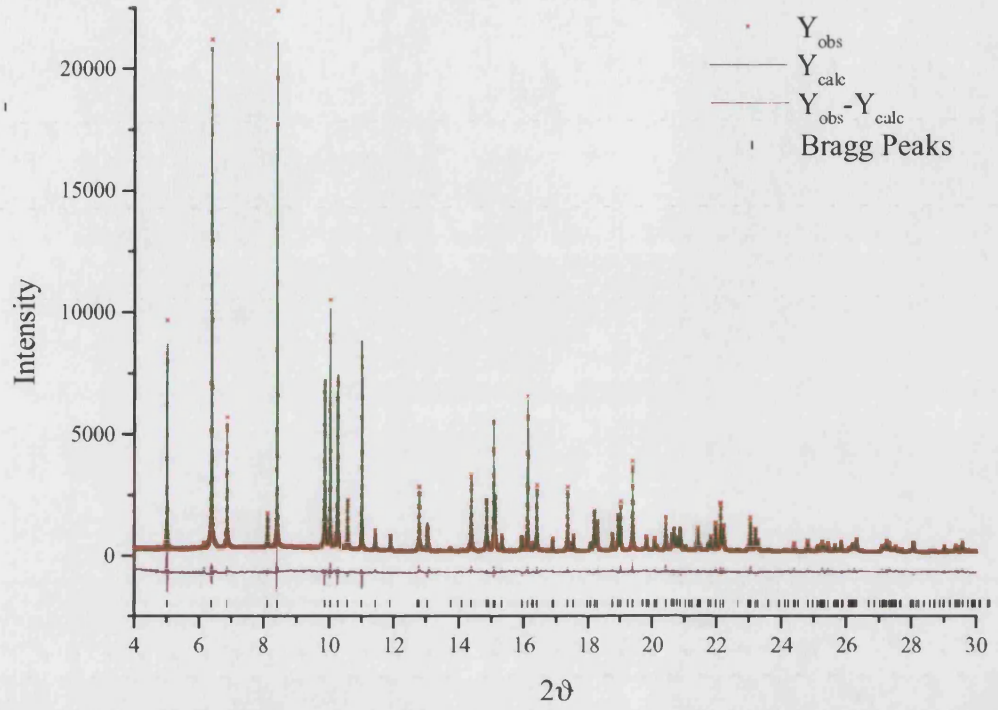

Figure 4.13 – X-ray diffraction data for $Li_{0.42}V_2O_5$: intensity as a function of 2ϑ, refined as epsilon phase in the orthorhombic space group Pmmn.

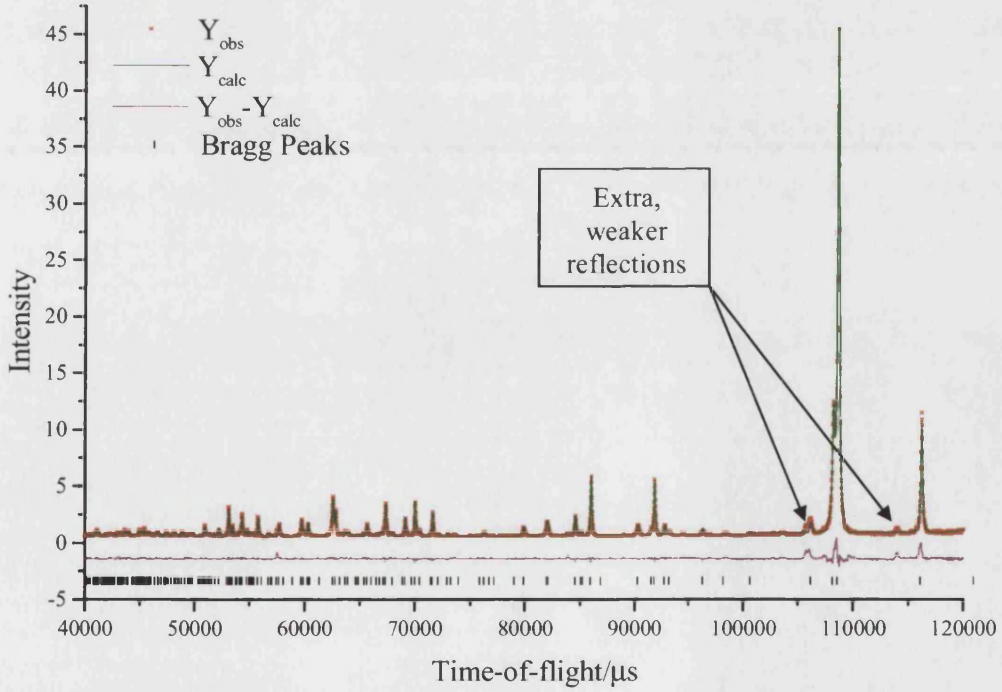

Figure 4.14 – Neutron diffraction data for $Li_{0.42}V_2O_5$: intensity as a function of time-of-flight, refined as epsilon phase.

X-RAY DATA						
χ^2	R_P		R_{WP}		R_B	
2.83	0.0632		0.0833		0.0535	
Space Group	Lattice Parameters/Å					
	a		b		c	
Pmmn	11.41269(3)		3.56203(1)		4.47989(2)	
	α		β		γ	
	90		90		90	
Atom	x		y	z		Frac.
V1	0.10034(8)		0.75	0.60709(16)		1
O2	0.11194(24)		0.75	0.95696(57)		1
O3	0.07088(20)		0.25	0.49304(54)		1
O4	0.25		0.75	0.48669(78)		1
Li5	0.25		0.25	0.180		0.42
Atom	Anisotropic Thermal Factors x 100/Å^2					
	B11	B22	B33	B12	B13	B23
V1	4.50(22)	4.50(22)	4.50(22)	0	0	0
O2	2.21(23)	2.21(23)	2.21(23)	0	0	0
O3	2.67(24)	2.67(24)	2.67(24)	0	0	0
O4	1.67(33)	1.67(33)	1.67(33)	0	0	0
Li5	1	1	1	0	0	0

NEUTRON DATA						
χ^2	R_P		R_{WP}		R_B	
5.881	0.0520		0.0628		0.1028	
Space Group	Lattice Parameters/Å					
	a		b		C	
Pmmn	11.42283(8)		3.564933(25)		4.48395(4)	
	α		β		γ	
	90		90		90	
Atom	x		y	z		Frac.
V1	0.10034		0.75	0.60709		1
O2	0.11072(13)		0.75	0.9600(4)		1
O3	0.07139(11)		0.25	0.4932(5)		1
O4	0.25		0.75	0.4875(8)		1
Li5	0.25		0.25	0.180(5)		0.42(2)
Atom	Anisotropic Thermal Factors x 100/Å^2					
	U11	U22	U33	U12	U13	U23
V1	2.5	2.5	2.5	0	0	0
O2	2.76(11)	6.74(10)	2.89(11)	0	-0.95(11)	0
O3	1.23(7)	1.18(7)	4.08(10)	0	-0.84(10)	0
O4	1.60(9)	3.73(14)	3.15(16)	0	0	0
Li5	11.94(70)	11.94(70)	11.94(70)	0	0	0

Table 4.15 – Crystallographic data, goodness-of-fit factors and anisotropic thermal parameters obtained by least squares refinement of x-ray and neutron diffraction data for ε-$Li_{0.42}V_2O_5$.

Extra peaks present in the x-ray diffraction pattern of this single-phase ε-$Li_{0.42}V_2O_5$ match well with the extra peaks present in the pattern of $Li_{0.33}V_2O_5$, and may be indexed as shown in *table 4.16*, confirming that these are due to vanadium ordering in the ε-phase.

The modulation wave vector, $\mathbf{q}^{rt}$ may be written as:

$$\mathbf{q}^{rt} = 0.9087\mathbf{a}^* + 1.0000\mathbf{b}^* + 0.4003\mathbf{c}^*$$

allowing all the reflections to be indexed as (*h*, *k*, *l*, *m*) according to *equation 4.4*.

h	*k*	*l*	*n*	D*(cal)	D*(obs)	2ϑ(cal)	2ϑ(obs)	2ϑ(obs-cal)
-1	1	1	1	0.2142	0.2149	6.1345	6.1538	0.0193
3	1	1	1	0.2269	0.2269	6.4989	6.4989	0.0000
2	2	0	1	0.3097	0.3090	8.8746	8.8540	-0.0206
2	1	-1	1	0.3269	0.3280	9.3664	9.3994	0.0329
-1	2	1	1	0.3531	0.3545	10.1208	10.1600	0.0392
6	1	0	1	0.4550	0.4558	13.0506	13.0754	0.0248
6	1	1	1	0.4658	0.4668	13.3616	13.3925	0.0309
7	1	0	1	0.5412	0.5420	15.5370	15.5616	0.0246
0	-1	0	1	0.5741	0.5749	16.4889	16.5133	0.0245
1	1	3	1	0.5804	0.5803	16.6702	16.6698	-0.0004
-1	-1	2	1	0.6861	0.6855	19.7355	19.7187	-0.0168

Table 4.16 – Weak satellite peaks from vanadium superstructure, modulation vector (0.9087, 1.0000, 0.4003), R-factor 1.56%.

The modulation vector for vanadium ordering in ε-$Li_{0.42}V_2O_5$ has a commensurate component along the cell depth axis, *b*, and incommensurate components along the cell width (*a*) and layer spacing (*c*) directions.

There are similarities in lithium environment between ε-$Li_{0.33}V_2O_5$ and ε-$Li_{0.42}V_2O_5$: eight-fold coordination by oxygen with a slightly shorter average separation (*table 4.17*).

Li-O	Separation/Å
2 x Li-O4	2.25(1)
2 x Li-O3	2.48(1)
4 x Li-O2	2.58(1)
Average	2.47

Table 4.17 – Lithium-oxygen separations in ε-$Li_{0.42}V_2O_5$.

Although the differences in lithium environment are small, there is a more significant difference with increased lithium content: neutron data show extra, weaker peaks. Since neutrons are insensitive to vanadium, this is due to ordering of lithium ions within the layered structure, as proposed by Katzke *et al.* [12]. When the lithium content is low, as in ε-$Li_{0.33}V_2O_5$, the neighbouring lithium ions are well separated and therefore have

little mutual influence, leading to a disordered sublattice. However, when the lithium content is increased, it is possible for repulsive Li^+-Li^+ forces and/or elastic strain to cause a regular distribution of the intercalated lithium ions resulting in the formation of an ordered commensurate or incommensurate superstructure.

Katzke *et al.* carried out electron diffraction experiments on various ε-$Li_xV_2O_5$ phases, and proposed a modulation vector for lithium ordering:

$$\mathbf{q}^{KATZKE} = \gamma\mathbf{b}^* + \tfrac{1}{2}\mathbf{c}^*$$

where **b*** and **c*** are the reciprocal lattice vectors of the basic structure, which has lattice parameters **a** (cell width), **b** (cell depth) and **c** (layer spacing), and γ is stoichiometry dependent [10-15, 26]. In other words, he proposed that the lithium ordered superstructure is commensurate with the basic structure along the cell width and layer spacing axes, and incommensurate along the cell depth axis, and is dependent upon lithium content. Satellite peaks observed in the neutron diffraction pattern were found to give a modulation vector:

$$\mathbf{q} = 0.4212\mathbf{b}^* + \tfrac{1}{2}\mathbf{c}^*$$

allowing all peaks to be indexed according to *equation 4.4*.

h	*k*	*l*	*n*	D*(cal)	D*(obs)	D*(obs-cal)
1	-1	1	1	0.4231	0.4235	0.0004
3	1	2	1	0.4552	0.4498	-0.0054
3	1	2	1	0.4552	0.4566	0.0014
5	0	1	1	0.4669	0.4661	-0.0008
5	0	1	1	0.4669	0.4698	0.0029
4	1	2	1	0.5108	0.5108	0.0000
5	1	2	1	0.5743	0.5758	0.0015
7	0	1	1	0.6340	0.6279	-0.0061
7	1	1	1	0.6437	0.6377	-0.0060
4	2	2	1	0.6563	0.6565	0.0002
5	-1	2	1	0.6800	0.6806	0.0006
2	-1	3	1	0.7074	0.7124	0.0050
3	2	3	1	0.7589	0.7528	-0.0061
6	0	3	1	0.7751	0.7783	0.0032
4	3	1	1	0.8114	0.8163	0.0049
4	-2	2	1	0.8341	0.8404	0.0063
7	0	3	1	0.8369	0.8454	0.0085
0	3	3	1	0.9133	0.9178	0.0045
2	-3	1	1	0.9819	0.9831	0.0012
5	3	3	1	1.0128	1.0117	-0.0011

Table 4.18 – Weak satellite peaks from lithium superstructure, modulation vector (0.0000, 0.4212, 0.5000), R-factor = 1.87%.

The modulation wave-vector obtained here has $\gamma = 0.4212$: according to Katzke's work, this corresponds to a lithium content of approximately $x = 0.42$ [11]. This is consistent with the lithium content obtained from refinement of lithium fractional occupancies, and magnetic susceptibility measurements giving $x = 0.42(2)$.

Although the diffraction data may be refined to give equally good results in any of the three published space groups, refinement in Pmmn is the only way to index the extra, satellite peaks in a manner consistent with the electron diffraction work of Katzke. The satellite peaks may be indexed using lattice parameters obtained by refinement in space groups $Pmn2_1$ and $P2_1mn$ but the difference between calculated and observed peaks is greater.

4.4 $Li_{0.50}V_2O_5$

4.4.1 Room temperature data

Diffraction data were refined as ε-$Li_{0.50}V_2O_5$, using the Pmmn space group. Refined diffraction data collected at room temperature are shown in *figures 4.15-16*, and the results described in *table 4.19*. Goodness-of-fit factors for refinement of neutron diffraction data for $Li_{0.50}V_2O_5$ are reasonable; the low χ^2 value signals the absence of any extra peaks in the neutron data for this compound. It is surprising that there are no satellite peaks due to lithium ordering in this $x = 0.50$ compound when ordering has been observed in the $x = 0.42$ compound: increase in lithium content would be expected to maintain the ordering previously observed, but there are no unindexed peaks in the data collected at NIST. The lithium content obtained from refinement of the fractional occupancy of lithium was 0.50(1), confirmed by magnetic susceptibility measurements.

Although there are no unindexed peaks in neutron diffraction data, there are extra peaks observed in the x-ray diffraction data collected at ESRF, which are a good match to those observed in $Li_{0.42}V_2O_5$ and $Li_{0.33}V_2O_5$. Microstructure parameters show a small overall increase in size coefficients, particularly for effects along the *c*-axis, indicative of increased strain within the system. However, the puckering angle is unexpectedly reduced from 2.84° to 2.22° with this increase in lithium content.

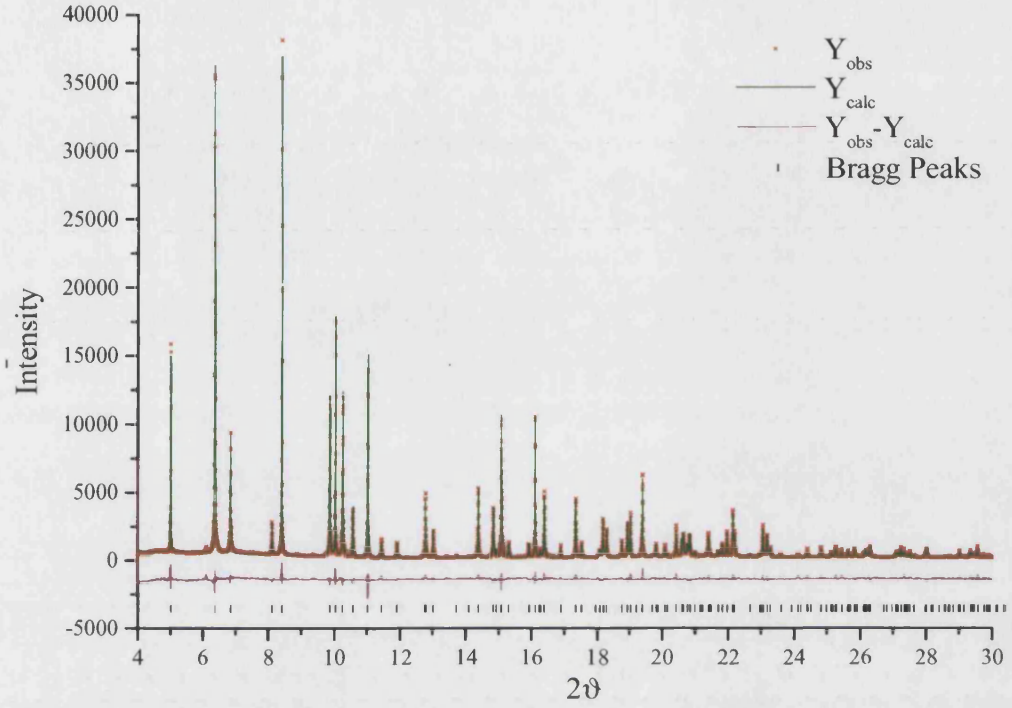

Figure 4.15 – Refined room temperature x-ray data from ESRF for $Li_{0.50}V_2O_5$: intensity as a function of 2ϑ.

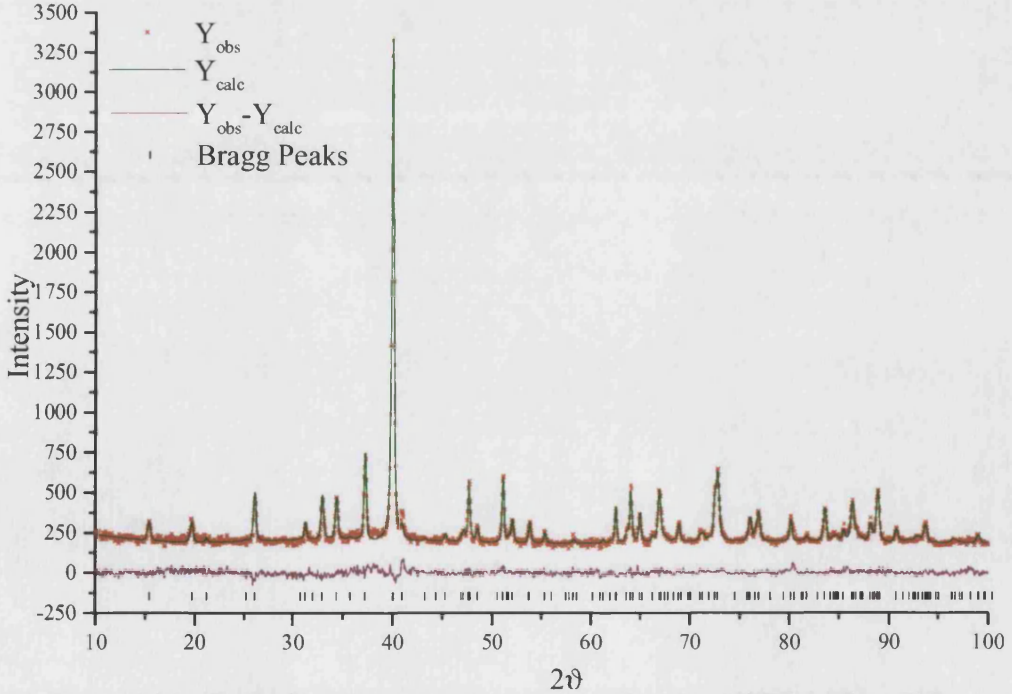

Figure 4.16 – Refined room temperature neutron data from NIST for $Li_{0.50}V_2O_5$: intensity as a function of 2ϑ.

X-RAY DATA						
χ^2	R_P		R_{WP}		R_B	
4.15	0.0642		0.0839		0.0529	
Space Group	Lattice Parameters/Å					
	a		b		c	
Pmmn	11.40585(3)		3.56048(1)		4.48859(2)	
	α		β		γ	
	90		90		90	
Atom	x	y	z	Frac.		
V1	0.10020(7)	0.75	0.60608(14)	1		
O2	0.11297(22)	0.75	0.95691(53)	1		
O3	0.07160(18)	0.25	0.49502(47)	1		
O4	0.25	0.75	0.48914(69)	1		
Li5	0.25	0.25	0.178	0.50		
Atom	Anisotropic Thermal Factors x 100/Å^2					
	B11	B22	B33	B12	B13	B23
V1	4.48(21)	4.48(21)	4.48(21)	0	0	0
O2	2.59(21)	2.59(21)	2.59(21)	0	0	0
O3	2.45(22)	2.45(22)	2.45(22)	0	0	0
O4	2.18(29)	2.18(29)	2.18(29)	0	0	0
Li5	1	1	1	0	0	0

NEUTRON DATA						
χ^2	R_P		R_{WP}		R_B	
1.107	0.0415		0.0470		0.1003	
Space Group	Lattice Parameters/Å					
	a		b		c	
Pmmn	11.42498(33)		3.56631(11)		4.48667(22)	
	α		β		γ	
	90		90		90	
Atom	x	y	z	Frac.		
V1	0.10020	0.75	0.60608	1		
O2	0.11065(24)	0.75	0.9622(10)	1		
O3	0.07144(19)	0.25	0.4950(13)	1		
O4	0.25	0.75	0.4848(19)	1		
Li5	0.25	0.25	0.178(9)	0.50(1)		
Atom	Anisotropic Thermal Factors x 100/Å^2					
	U11	U22	U33	U12	U13	U23
V1	2.5	2.5	2.5	0	0	0
O2	2.35(18)	6.42(19)	2.70(23)	0	-0.99(19)	0
O3	0.96(12)	1.43(12)	3.47(21)	0	-1.26(17)	0
O4	1.24(15)	2.98(26)	3.37(35)	0	0	0
Li5	11.7(15)	11.7(15)	11.7(15)	0	0	0

Table 4.19 – Crystallographic data and goodness-of-fit factors for $Li_{0.50}V_2O_5$ from refinement of diffraction data.

A modulation wave vector, $\mathbf{q}^{rt}$, allowing all satellite reflections to be indexed according to *equation 4.4*, may be written as:

$$\mathbf{q}^{rt} = 0.8272\mathbf{a}^* + 0.4399\mathbf{b}^* + 0.5475\mathbf{c}^*$$

h	*k*	*l*	*n*	D*(cal)	D*(obs)	2ϑ(cal)	2ϑ(obs)	2ϑ(obs-cal)
2	1	1	1	0.2133	0.2132	6.1071	6.1066	-0.0005
-1	0	1	1	0.2260	0.2259	6.4731	6.4690	-0.0042
-2	1	1	1	0.3104	0.3097	8.8935	8.8728	-0.0207
4	0	0	1	0.3279	0.3267	9.3961	9.3623	-0.0338
0	0	2	1	0.3539	0.3549	10.1426	10.1728	0.0302
5	1	0	1	0.4165	0.4170	11.9428	11.9577	0.0149
3	1	-1	1	0.4241	0.4258	12.1630	12.2104	0.0474
2	2	0	1	0.4663	0.4676	13.3774	13.4142	0.0368
3	2	0	1	0.4931	0.4928	14.1502	14.1417	-0.0085
1	2	2	1	0.5449	0.5442	15.6457	15.6255	-0.0202
3	-1	2	1	0.5519	0.5505	15.8463	15.8062	-0.0400
7	1	1	1	0.5725	0.5732	16.4440	16.4623	0.0183
6	1	2	1	0.5789	0.5787	16.6284	16.6230	-0.0054
4	0	3	1	0.6254	0.6271	17.9756	18.0221	0.0465
7	-1	0	1	0.6865	0.6859	19.7479	19.7297	-0.0182

Table 4.20 – Weak satellite peaks from vanadium superstructure, modulation vector (0.8272, 0.4399, 0.5475), R-factor = 1.43%.

The vanadium environment in $Li_{0.50}V_2O_5$ does not differ significantly from that observed in the x = 0.33 and x = 0.42 ε-phases. The lithium environment is also unchanged from that of ε-$Li_{0.42}V_2O_5$.

4.4.2 $Li_{0.50}V_2O_5$ at 200K

X-ray diffraction data were collected at the temperatures 200K, 50K and 15K for $Li_{0.50}V_2O_5$. 200K data were successfully refined in the same Pmmn space group as the room temperature data: refined data are shown in *figure 4.17* and details of the refinement given in *table 4.21*. The structure of ε-$Li_{0.50}V_2O_5$ at 200K is very similar to that at room temperature, with slightly difference lattice parameters. Microstructure parameters indicate an increase in strain in the *a* and *b* directions, with a decrease along the *c*-axis. Strain also increases in the *bc* plane.

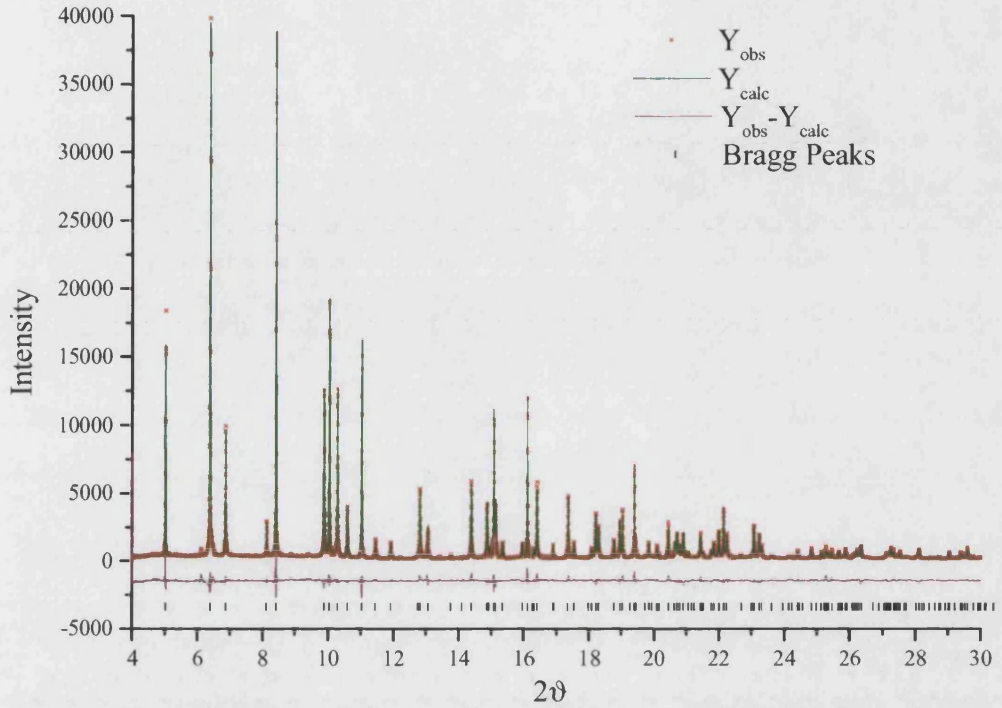

Figure 4.17 – Refined x-ray diffraction data collected at 200K at ESRF for $Li_{0.50}V_2O_5$.

X-RAY DATA						
χ^2	R_P		R_{WP}		R_B	
5.21	0.0509		0.0680		0.0931	
Space Group	**Lattice Parameters/Å**					
	a		**b**		**c**	
Pmmn	11.40445(5)		3.55889(1)		4.47359(2)	
	α		**β**		**γ**	
	90		90		90	
Atom	**x**	**y**		**z**		**Frac.**
V1	0.10035(7)	0.75		0.60645(15)		1
O2	0.11221(24)	0.75		0.95964(52)		1
O3	0.07114(18)	0.25		0.49311(50)		1
O4	0.25	0.75		0.48723(73)		1
Li5	0.25	0.25		0.178		0.5

Atom	**Anisotropic Thermal Factors x 100/Å²**					
	B11	**B22**	**B33**	**B12**	**B13**	**B23**
V1	4.97(21)	4.97(21)	4.97(21)	0	0	0
O2	1.88(20)	1.88(20)	1.88(20)	0	0	0
O3	3.43(22)	3.43(22)	3.43(22)	0	0	0
O4	2.32(30)	2.32(30)	2.32(30)	0	0	0
Li5	1	1	1	0	0	0

Table 4.21 – Crystallographic data for $Li_{0.50}V_2O_5$ (data collected at 200K).

The vanadium environment at 200K shows no significant differences from the room temperature structure, apart from an increase in puckering angle from 2.22° to 2.75°. This is consistent with the observed strain increases shown by the microstructure effect coefficients. There are still extra, weaker peaks present at 200K, thus again there is an inflated value of χ^2. The main difference between room temperature and 200K diffraction data is in the modulation vector needed to index these satellite peaks. The modulation wave vector, $\mathbf{q}^{200}$ may be written as:

$$\mathbf{q}^{200} = 0.8354\mathbf{a}^* + 0.5755\mathbf{b}^* + 0.3812\mathbf{c}^*$$

which allows all satellite reflections to be indexed as (*h*, *k*, *l*, *m*) in *table 4.22*, according to *equation 4.4*.

h	*k*	*l*	*n*	D*(cal)	D*(obs)	2ϑ(cal)	2ϑ(obs)	2ϑ(obs-cal)
1	0	1	1	0.2133	0.2133	6.1077	6.1077	0.0000
0	0	1	1	0.2251	0.2262	6.4450	6.4793	0.0343
-1	1	1	1	0.2434	0.2430	6.9721	6.9610	-0.0111
-2	1	1	1	0.3085	0.3100	8.8389	8.8811	0.0422
-2	0	1	1	0.3273	0.3269	9.3774	9.3685	-0.0088
0	0	-1	1	0.3561	0.3562	10.2073	10.2075	0.0002
0	2	0	1	0.4157	0.4170	11.9211	11.9566	0.0355
3	1	2	1	0.4257	0.4260	12.2068	12.2174	0.0106
3	2	0	1	0.4511	0.4523	12.9394	12.9735	0.0342
0	-1	1	1	0.4696	0.4678	13.4708	13.4208	-0.0500
5	1	-1	1	0.4929	0.4928	14.1426	14.1425	-0.0001
4	2	1	1	0.5063	0.5079	14.5307	14.5770	0.0462
1	1	-2	1	0.5457	0.5447	15.6673	15.6384	-0.0290
5	2	0	1	0.5485	0.5511	15.7483	15.8242	0.0759
7	0	0	1	0.5706	0.5733	16.3882	16.4671	0.0788
7	0	1	1	0.5809	0.5804	16.6864	16.6724	-0.0141
-4	-1	0	1	0.6189	0.6170	17.7852	17.7318	-0.0535

Table 4.22 – Weak satellite peaks from vanadium superstructure, modulation vector (0.8354, 0.5755, 0.3812), R-factor = 2.09%.

The change in modulation vector with temperature will be further discussed in section 4.4.4.

4.4.3 $Li_{0.50}V_2O_5$ at 50K

Diffraction data collected at 50K were also refined as ε-phase, in the Pmmn space group. Refined data are shown in *figure 4.18* and refinement details given in *table 4.23*. The 50K structure remains very similar to that at room temperature, with the expected contraction in unit cell parameters. There is an increase in puckering angle to 2.85°, and an increase in strain coefficient along the *c*-axis.

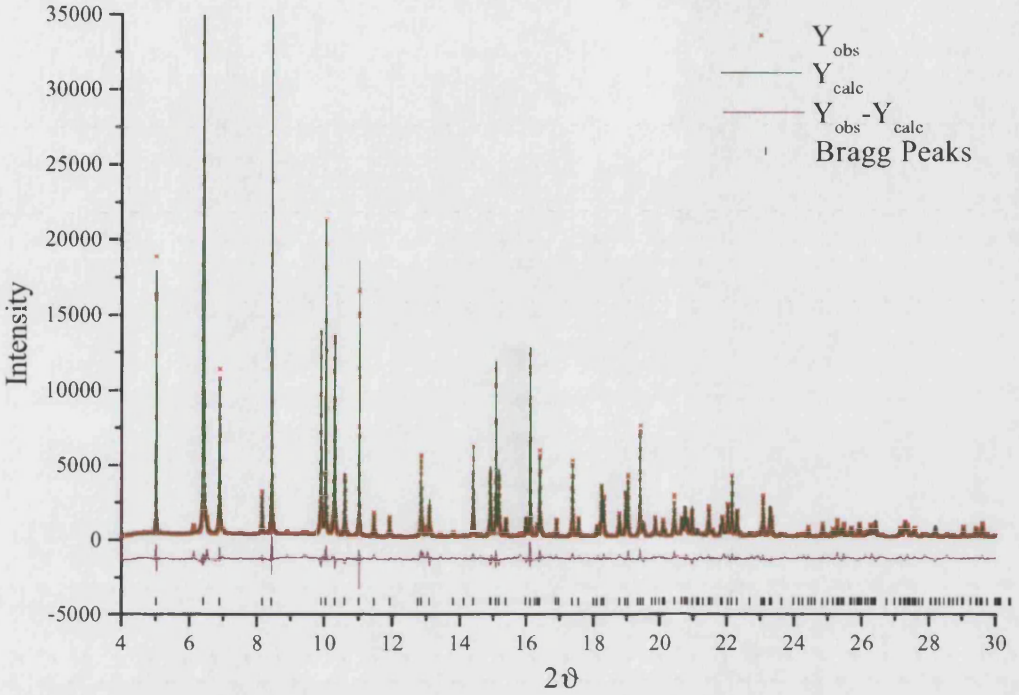

Figure 4.18 – Refined x-ray diffraction data collected at 50K at ESRF for $Li_{0.50}V_2O_5$

X-RAY DATA						
χ^2	R_P		R_{WP}		R_B	
11.0	0.0556		0.0827		0.1130	
Space Group	**Lattice Parameters/Å**					
	a		**b**		**c**	
Pmmn	11.40470(6)		3.55715(2)		4.45872(2)	
	α		**β**		**γ**	
	90		90		90	
Atom	**x**	**y**		**z**		**Frac.**
V1	0.10041(9)	0.75		0.60602(19)		1
O2	0.11196(26)	0.75		0.95999(67)		1
O3	0.07123(23)	0.25		0.49333(66)		1
O4	0.25	0.75		0.48625(96)		1
Li5	0.25	0.25		0.178		0.5

Atom	**Anisotropic Thermal Factors x 100/Å^2**					
	B11	**B22**	**B33**	**B12**	**B13**	**B23**
V1	4.50(25)	4.50(25)	4.50(25)	0	0	0
O2	2.06(26)	2.06(26)	2.06(26)	0	0	0
O3	3.76(31)	3.76(31)	3.76(31)	0	0	0
O4	3.11(43)	3.11(43)	3.11(43)	0	0	0
Li5	1	1	1	0	0	0

Table 4.23 – Crystallographic data for $Li_{0.50}V_2O_5$ at 50K from refinement of x-ray diffraction data.

There are no significant changes in vanadium environment in terms of bond lengths or angles, apart from the slight increase in puckering angle previously mentioned. At 50K, the value of χ^2 for refinement as ε-$Li_{0.50}V_2O_5$ has increased to 11.00, compared with 4.15 at room temperature and 5.21 at 200K. This increase is due to the increasing intensity of the satellite peaks, as can be seen in *figure 4.21*. Satellite peaks can be indexed by the modulation wave vector, $\mathbf{q}^{50}$:

$$\mathbf{q}^{50} = 0.9541\mathbf{a}^* + 0.6979\mathbf{b}^* + 0.3487\mathbf{c}^*$$

which allows all satellite reflections to be indexed as (*h, k, l, m*) in *table 4.24*, according to *equation 4.4*.

h	*k*	*l*	*n*	D*(cal)	D*(obs)	2ϑ(cal)	2ϑ(obs)	2ϑ(obs-cal)
3	1	0	1	0.2133	0.2138	6.1090	6.1223	0.0133
0	0	0	1	0.2272	0.2272	6.5058	6.5062	0.0004
1	0	1	1	0.2446	0.2435	7.0065	6.9728	-0.0337
2	0	1	1	0.2612	0.2622	7.4824	7.5089	0.0265
-2	1	1	1	0.3093	0.3100	8.8608	8.8830	0.0223
2	1	-1	1	0.3273	0.3273	9.3785	9.3786	0.0001
2	1	-1	1	0.3273	0.3295	9.3785	9.4411	0.0626
-1	1	-1	1	0.3579	0.3569	10.2568	10.2295	-0.0273
5	1	0	1	0.3731	0.3720	10.6938	10.6638	-0.0300
3	2	0	1	0.4151	0.4175	11.9021	11.9710	0.0689
0	0	2	1	0.4274	0.4260	12.2561	12.2170	-0.0391
4	0	-1	1	0.4487	0.4495	12.8696	12.8938	0.0241
-1	0	2	1	0.4528	0.4523	12.9876	12.9741	-0.0135
6	1	0	1	0.4573	0.4545	13.1165	13.0366	-0.0799
-3	1	-1	1	0.4679	0.4679	13.4228	13.4228	0.0000
6	0	0	1	0.4903	0.4928	14.0681	14.1420	0.0739
3	2	-1	1	0.5076	0.5091	14.5685	14.6121	0.0435
7	1	0	1	0.5425	0.5446	15.5771	15.6362	0.0590
5	0	2	1	0.5491	0.5505	15.7663	15.8058	0.0395
2	-1	-1	1	0.5725	0.5737	16.4425	16.4777	0.0352
6	2	0	1	0.5795	0.5796	16.6464	16.6495	0.0032
7	0	1	1	0.5838	0.5822	16.7707	16.7232	-0.0475
7	1	-1	1	0.6162	0.6178	17.7086	17.7540	0.0454

Table 4.24 – Weak satellite peaks from vanadium superstructure, modulation vector (0.9541, 0.6979, 0.3487), R-factor = 3.60%.

4.4.4 $Li_{0.50}V_2O_5$ at 15K

X-ray and neutron data were collected at 15K for $Li_{0.50}V_2O_5$: refined diffraction patterns are shown in *figures 4.19-20* and refinement details given in *table 4.25*. Microstructure effects remain similar to those found at 50K.

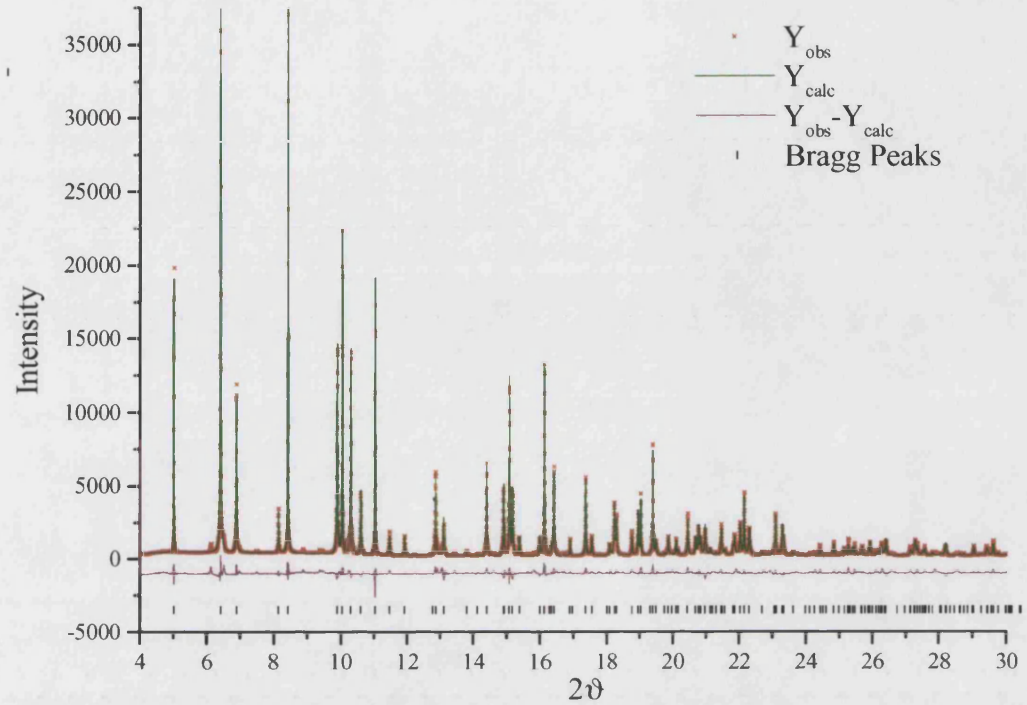

Figure 4.19 – Refined x-ray diffraction data collected at 15K at ESRF for $Li_{0.50}V_2O_5$: intensity as a function of 2ϑ.

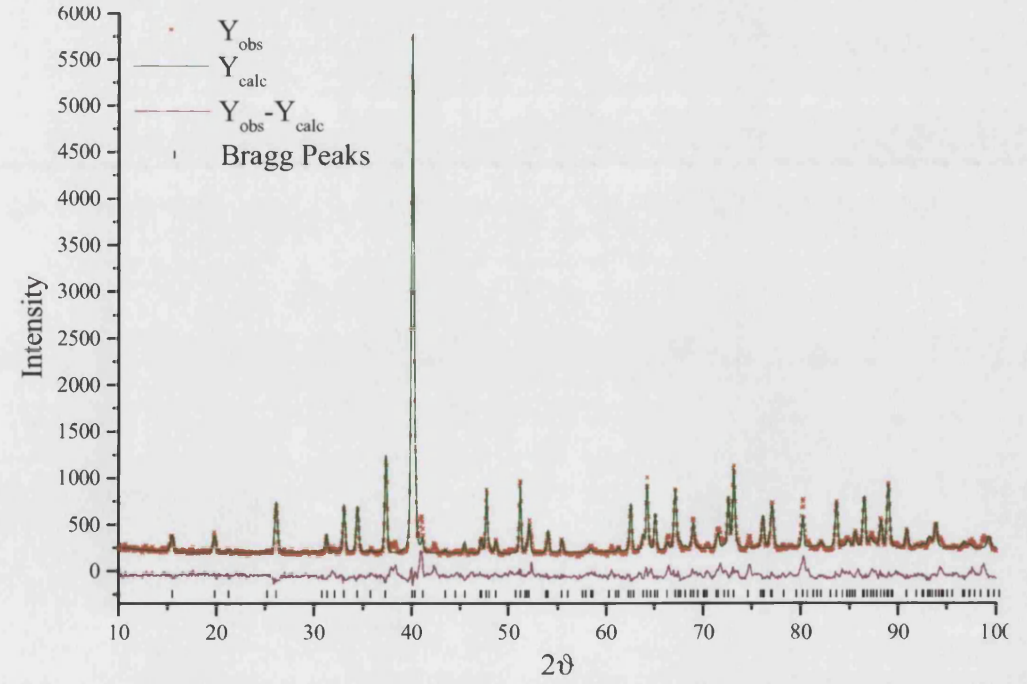

Figure 4.20 – Refined neutron diffraction data, collected at 15K at NIST for $Li_{0.50}V_2O_5$: intensity as a function of 2ϑ.

X-RAY DATA						
χ^2	R_P		R_{WP}		R_B	
38.5	0.0739		0.1070		0.0538	
Space Group	Lattice Parameters/Å					
	a		b		c	
Pmmn	11.40403(6)		3.55704(2)		4.45855(2)	
	α		β		γ	
	90		90		90	
Atom	x		y	z		Frac.
V1	0.10037(8)		0.75	0.60592(18)		1
O2	0.11176(26)		0.75	0.96044(62)		1
O3	0.07131(21)		0.25	0.49388(59)		1
O4	0.25		0.75	0.48647(88)		1
Li5	0.25		0.25	0.175		0.5
Atom	Anisotropic Thermal Factors x 100/Å^2					
	B11	B22	B33	B12	B13	B23
V1	4.55(24)	4.55(24)	4.55(24)	0	0	0
O2	1.78(24)	1.78(24)	1.78(24)	0	0	0
O3	3.36(28)	3.36(28)	3.36(28)	0	0	0
O4	2.64(39)	2.64(39)	2.64(39)	0	0	0
Li5	1	1	1	0	0	0
NEUTRON DATA						
χ^2	R_P		R_{WP}		R_B	
4.076	0.0659		0.0890		0.1855	
Space Group	Lattice Parameters/Å					
	a		b		c	
Pmmn	11.4184(6)		3.56223(21)		4.46559(32)	
	α		β		γ	
	90		90		90	
Atom	x		y	z		Frac.
V1	0.10037		0.75	0.60592		1
O2	0.11116(25)		0.75	0.9612(12)		1
O3	0.07120(19)		0.25	0.4958(13)		1
O4	0.25		0.75	0.4835(23)		1
Li5	0.25		0.25	0.175(9)		0.5
Atom	Anisotropic Thermal Factors x 100/Å^2					
	U11	U22	U33	U12	U13	U23
V1	2.5	2.5	2.5	0	0	0
O2	1.56(19)	6.85(24)	2.70(27)	0	-1.11(18)	0
O3	0.47(13)	1.41(14)	3.02(22)	0	-2.38(15)	0
O4	0.68(16)	2.31(29)	5.13(43)	0	0	0
Li5	8.7(12)	8.7(12)	8.7(12)	0	0	0

Table 4.25 – Crystallographic data for $Li_{0.50}V_2O_5$ at 15K from refinement of neutron and x-ray diffraction data.

Barring the predictable contraction of the lattice parameters with a decrease in temperature, the structure is fundamentally unchanged at 15K. The vanadium environment is again largely unchanged apart from a slight alteration in puckering angle from 2.85° to 2.74°. Likewise, the lithium environment is mainly unaffected by the decrease in temperature. The retention of structure on cooling is in contrast to the behaviour of the α-phase discussed in section 4.2. The lower puckering angle and microstructure coefficients imply less strain in the ε- structure, suggesting the distortion observed on cooling α-$Li_{0.33}V_2O_5$ is related to the need to reduce strain in the layers.

The value of χ^2 for refinement of x-ray diffraction data collected at 15K has increased from the already high value found at 50K. Although the satellite peaks at 15K correspond well to those already present at higher temperatures, their intensity has further increased, leading to an inflated χ^2 value:

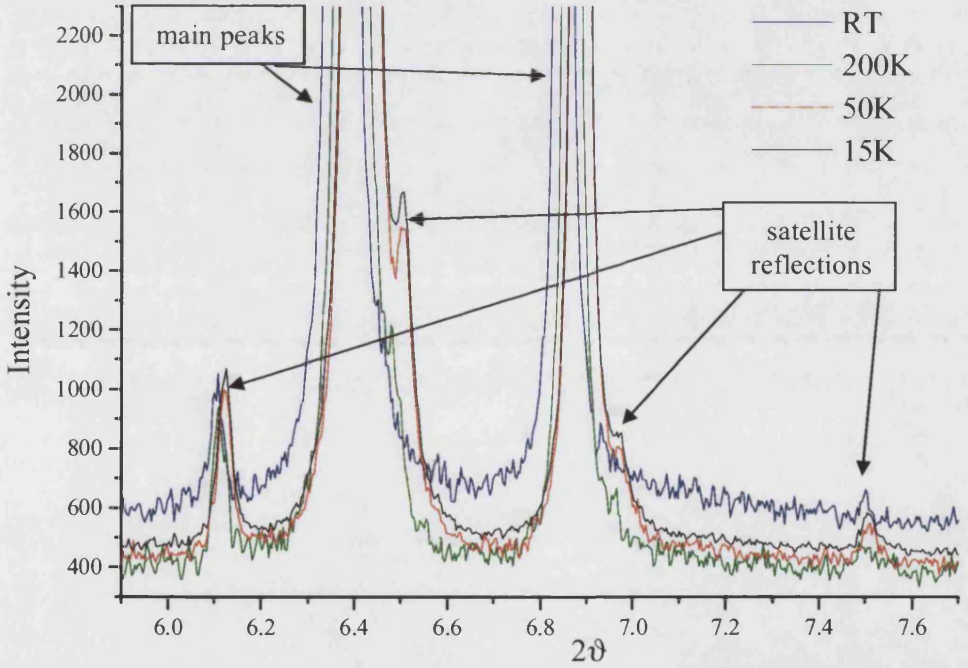

Figure 4.21 – Raw diffraction data, intensity as a function of 2ϑ, showing increasing intensity of satellite peaks in $Li_{0.50}V_2O_5$ as temperature is decreased from room temperature (blue), through 200K (green) and 50K (red) to 15K (black).

Satellite peaks at 15K can be indexed by the modulation wave vector, $\mathbf{q}^{15}$:

$$\mathbf{q}^{15} = 0.8757\mathbf{a}^* + 0.6909\mathbf{b}^* + 0.2938\mathbf{c}^*$$

which allows all satellite reflections to be indexed as (*h*, *k*, *l*, *m*) in *table 4.26*, according to *equation 4.4*.

h	*k*	*l*	*n*	D*(cal)	D*(obs)	2ϑ(cal)	2ϑ(obs)	2ϑ(obs-cal)
3	1	0	1	0.2159	0.2140	6.1813	6.1273	-0.0539
2	0	0	1	0.2276	0.2271	6.5172	6.5043	-0.0129
-1	1	1	1	0.2443	0.2435	6.9974	6.9750	-0.0224
0	0	1	1	0.2621	0.2621	7.5082	7.5080	-0.0002
3	0	1	1	0.3123	0.3102	8.9472	8.8871	-0.0601
4	1	1	1	0.3282	0.3272	9.4037	9.3762	-0.0275
4	1	1	1	0.3282	0.3297	9.4037	9.4465	0.0428
1	0	-1	1	0.3494	0.3475	10.0124	9.9602	-0.0522
3	1	-1	1	0.3556	0.3571	10.1919	10.2355	0.0437
4	0	1	1	0.3713	0.3720	10.6432	10.6629	-0.0197
5	0	0	1	0.4158	0.4173	11.9219	11.9656	0.0438
-1	1	2	1	0.4255	0.4263	12.2019	12.2246	0.0226
-2	2	0	1	0.4510	0.4495	12.9355	12.8920	-0.0435
-2	2	0	1	0.4510	0.4522	12.955	12.9715	0.0360
-3	1	-1	1	0.4553	0.4549	13.0589	13.0496	-0.0093
-1	0	2	1	0.4596	0.4581	13.1838	13.1395	-0.0443
3	0	2	1	0.4678	0.4678	13.4207	13.4207	0.0000
6	0	0	1	0.4939	0.4929	14.1740	14.1445	-0.0295
4	0	2	1	0.5091	0.5093	14.6126	14.6179	0.0052
4	2	-1	1	0.5429	0.5447	15.5865	15.6398	0.0534
4	-1	0	1	0.5526	0.5507	15.8677	15.8137	-0.0540
7	0	0	1	0.5749	0.5738	16.5113	16.4816	-0.0296
3	0	-2	1	0.5806	0.5795	16.6774	16.6457	-0.0317
6	2	0	1	0.5845	0.5824	16.7914	16.7297	-0.0617
7	1	-1	1	0.6166	0.6179	17.7184	17.7582	0.0398

Table 4.26 – Weak satellite peaks from vanadium superstructure, modulation vector (0.8757, 0.6909, 0.2938), R-factor = 5.15%.

As the temperature decreases and the unit cell contracts, the modulation vector for vanadium ordering observed in ε-$Li_{0.50}V_2O_5$ changes as shown in *table 4.27*:

Temperature	q^a	q^b	q^c
Room temp.	0.8272	0.4399	0.5475
200K	0.8354	0.5755	0.3812
50K	0.9541	0.6979	0.3487
15K	0.8757	0.6909	0.2938

Table 4.27 – Change in modulation vector with temperature in ε-$Li_{0.50}V_2O_5$.

4.5 $Li_{0.55}V_2O_5$

4.5.1 Room Temperature Data

Refinements of room temperature diffraction data for ε'-$Li_{0.55}V_2O_5$ are shown in *figures 4.22-23* and described in *table 4.28*. Lithium content, calculated from refinement of fractional occupancy of lithium atoms in neutron diffraction data, was found to be x = 0.55(2), a value that has been confirmed by magnetic susceptibility measurements. The ε-phase region is generally accepted to be split into two regions, ε or ε_1 ($0.33 \leq x \leq 0.52$) which does not undergo a phase transition on cooling (as sections 4.2-4 have shown), and ε' or ε_2 ($0.52 \leq x \leq 0.8$) in which, according to Katzke *et al.*, there is a continuous ferro-elastic structural phase transition on cooling [12]. It is perhaps unsurprising therefore to observe severe broadening of certain peaks in room temperature x-ray diffraction data for $Li_{0.55}V_2O_5$, as shown in the inset of *figure 4.22*, foreshadowing a phase transition from orthorhombic to monoclinic at lower temperature. There are no extra reflections present at room temperature in either the neutron or x-ray diffraction data for this composition; therefore charge ordering is not thought to occur. However, microstructure coefficients are indicative of increased internal strain with the increase in lithium content to x = 0.55. The magnitude of coefficients for size effects have increased slightly along the *a* and *b* axes and decreased slightly along the c-axis compared with room temperature data for ε-$Li_{0.50}V_2O_5$, but the most noticeable difference is a large increase in magnitude of the size coefficient in the *bc* plane. There is increased strain, but instead of charge ordering there is a continuous phase transition in the ε'- phase, suggesting that the lack of charge ordering of vanadium is due to the phase transition relieving internal strain in the layers. This supports the postulation that charge ordering observed in the ε- phase is not solely an electronic effect, but is also driven by the need to reduce strain within the layers: since it is the lithium ions that cause increased strain, the charge ordering will differ slightly for each composition, as has been observed, and will be incommensurate in nature due to the mobility of lithium ions within the layers.

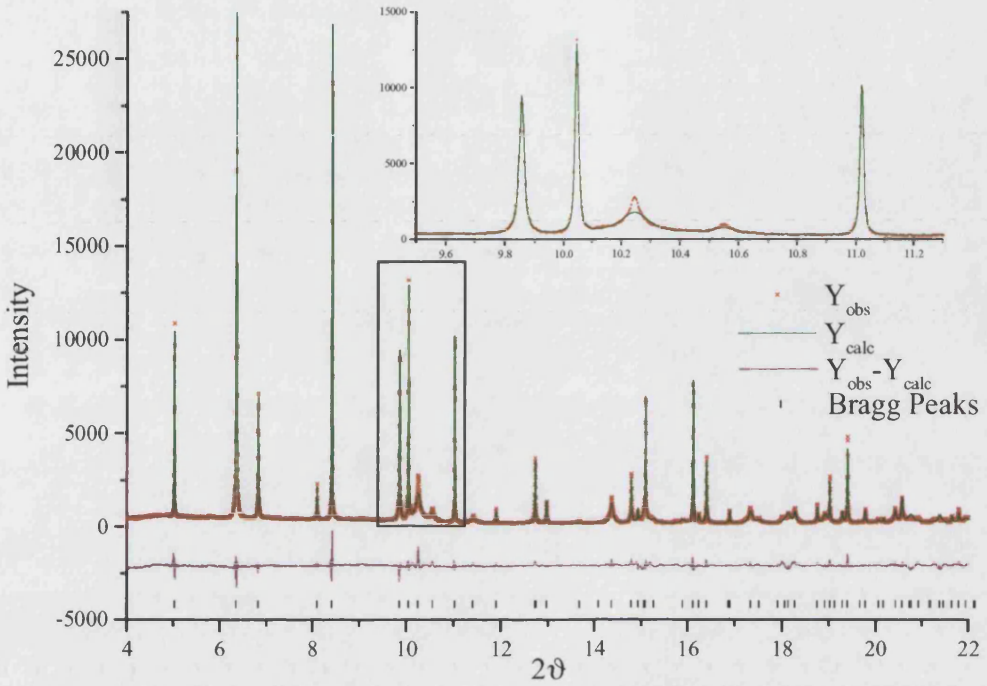

Figure 4.22 – X-ray diffraction data collected at room temperature on $Li_{0.55}V_2O_5$ refined in orthorhombic Pmmn space group: intensity as a function of 2ϑ. Inset is enlargement to show anisotropic peak broadening due to the phase transition.

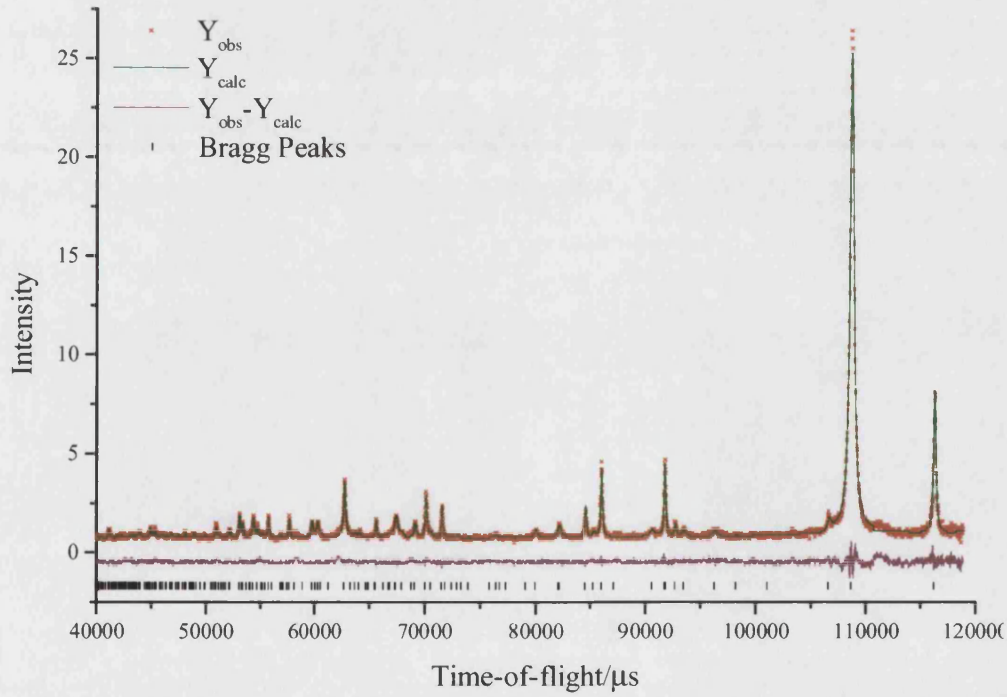

Figure 4.23 – Room temperature neutron data from HRPD for $Li_{0.55}V_2O_5$: intensity as a function of time-of-flight.

X-RAY DATA						
χ^2	R_P		R_{WP}		R_B	
4.77	0.0796		0.1010		0.0616	
Space Group	Lattice Parameters/Å					
	a		b		c	
Pmmn	11.39777(8)		3.56130(2)		4.50595(3)	
	α		β		γ	
	90		90		90	
Atom	x		y		z	Frac.
V1	0.10093(12)		0.75		0.60609(34)	1
O2	0.11400(33)		0.75		0.95191(94)	1
O3	0.07039(26)		0.25		0.48726(89)	1
O4	0.25		0.75		0.4788(11)	1
Li5	0.25		0.25		0.195	0.55

Atom	Anisotropic Thermal Factors x 100/Å^2					
	B11	B22	B33	B12	B13	B23
V1	11.03(63)	11.03(63)	11.03(63)	0	0	0
O2	0.58(36)	0.58(36)	0.58(36)	0	0	0
O3	3.82(55)	3.82(55)	3.82(55)	0	0	0
O4	0.27(55)	0.27(55)	0.27(55)	0	0	0
Li5	1	1	1	0	0	0

NEUTRON DATA						
χ^2	R_P		R_{WP}		R_B	
1.462	0.0482		0.0547		0.0999	
Space Group	Lattice Parameters/Å					
	a		b		C	
Pmmn	11.41026(13)		3.56409(6)		4.50454(12)	
	α		β		γ	
	90		90		90	
Atom	x		y		z	Frac.
V1	0.10093		0.75		0.60609	1
O2	0.11256(16)		0.75		0.9599(8)	1
O3	0.07262(15)		0.25		0.4880(11)	1
O4	0.25		0.75		0.4903(13)	1
Li5	0.25		0.25		0.195(7)	0.55(2)

Atom	Anisotropic Thermal Factors x 100/Å^2					
	U11	U22	U33	U12	U13	U23
V1	2.5	2.5	2.5	0	0	0
O2	1.79(12)	8.50(17)	2.12(19)	0	-0.85(16)	0
O3	1.77(10)	1.00(12)	4.19(18)	0	-0.56(17)	0
O4	0.61(12)	3.73(25)	3.50(30)	0	0	0
Li5	12.27(90)	12.27(90)	12.27(90)	0	0	0

Table 4.28 – Crystallographic data, goodness-of-fit factors and anisotropic thermal parameters obtained by least squares refinement of x-ray and neutron diffraction data for ε'-$Li_{0.55}V_2O_5$

The ε'-$Li_{0.55}V_2O_5$ structure (*figure 4.24*) shows only slight differences from that of ε-$Li_{0.50}V_2O_5$. Vanadium bond details are given in *table 4.29*.

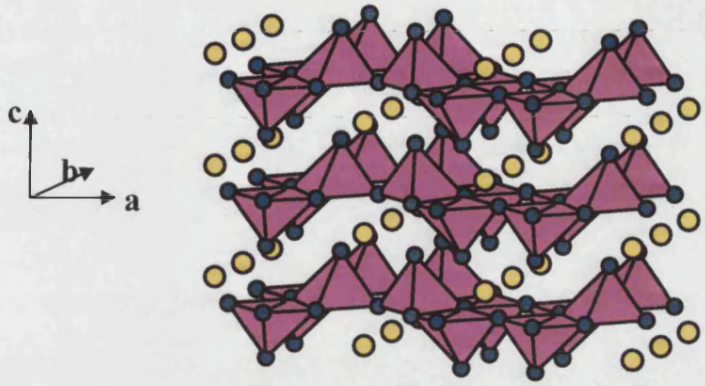

Figure 4.24 – Structure of $Li_{0.55}V_2O_5$.

Bond Lengths		Bond Angles	
Bond	**Bond Length/Å**	**Atoms**	**Angle/°**
V-O2	1.57(3)	O3/O3'-V-O3''	76.14(6)
V-O4	1.79(1)	O3/O3'-V-O4	94.81(9)
V-O3	1.89(1)	O3/O3'-V-O2	107.41(14)
V-O3'	1.89(1)	O3''-V-O2	107.62(14)
V-O3''	2.00(2)	O4-V-O2	103.20(20)
V-V1	3.06(1)	V-O3-V1	103.86(13)
V-V2	3.56(1)	V-O3-V2	140.54(8)
V-V2'	3.40(1)	V-O4-V2'	142.69(12)
Puckering angle		4.80(1)	

Table 4.29 – Vanadium-oxygen bond lengths and angles and vanadium-vanadium distances for ε'-$Li_{0.55}V_2O_5$ x-ray diffraction data.

Bond lengths and angles for ε'-$Li_{0.55}V_2O_5$ have values between those published for V_2O_5 and ε-LiV_2O_5 [20]. The puckering angle has increased from approximately two degrees for ε-$Li_{0.50}V_2O_5$, to almost five degrees in ε'-$Li_{0.55}V_2O_5$, but is still less than that reported for ε-LiV_2O_5 [20]. The lithium environment has not been significantly affected by the increase in lithium content having, on average, slightly shorter lithium-oxygen distances (*table 4.30*) than were found in ε-$Li_{0.50}V_2O_5$ and slightly longer distances than were published for ε-LiV_2O_5.

Li-O	Separation/Å
2 x Li-O4	2.22(2)
2 x Li-O3	2.42(2)
4 x Li-O2	2.60(1)
Average	2.46

Table 4.30 – Lithium-oxygen separations in ε'-$Li_{0.55}V_2O_5$.

4.5.2 $Li_{0.55}V_2O_5$ at 50K

From previous work, there is expectation of a phase transition in ε'-$Li_xV_2O_5$ at lower temperature [10-15, 26]. Thus it is not surprising that refinement of x-ray diffraction data collected at 50K for $Li_{0.55}V_2O_5$ using the room temperature orthorhombic structure as an initial model is not entirely satisfactory, giving $\chi^2 \sim 10$, due to the presence of additional peaks at this temperature. The extra peaks may be fitted by refinement using a monoclinic model structure obtained from symmetry transformation of the orthorhombic unit cell. However, refinement using only the monoclinic cell is also unsatisfactory, giving $\chi^2 \sim 30$ and leaving some of the orthorhombic peaks unindexed. Refinement as a mixture of orthorhombic and monoclinic phases gives the best fit to the data and allows indexing of all peaks, as shown in *figure 4.25* and described in *table 4.31*. Comparison of the microstructure coefficients shows a massive size effect in the *bc* plane of the orthorhombic layers, a factor of ten greater than the large value observed in the room temperature orthorhombic structure. The corresponding coefficient in the monoclinic layers is much smaller, although there is a general increase in the magnitude of other microstructure coefficients indicative of increased strain in comparison with the orthorhombic layers at room temperature and 50K, particularly along the *c*-axis.

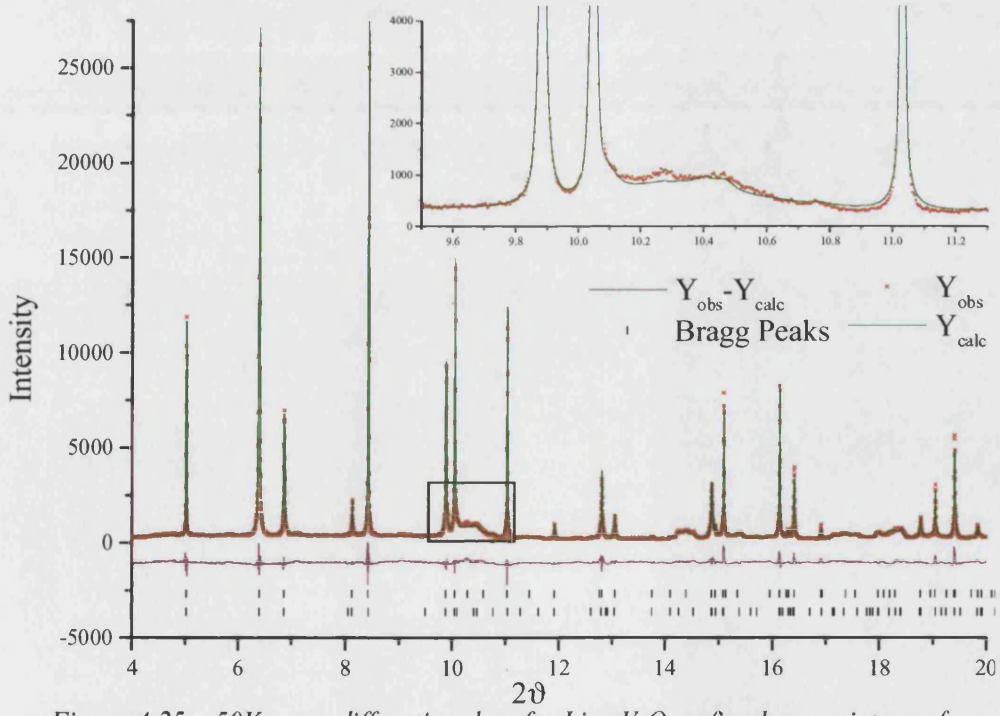

Figure 4.25 – 50K x-ray diffraction data for $Li_{0.55}V_2O_5$ refined as a mixture of orthorhombic and monoclinic phases. Inset shows anisotropic peak broadening.

X-RAY DATA						
χ^2	R_P		R_{WP}		R_B	
6.78	0.0802		0.1060		0.0918	
Orthorhombic (Weight fraction 82.6(8))						
Space Group	**Lattice Parameters/Å**					
	a		**b**		**c**	
Pmmn	11.39763(9)		3.55556(3)		4.47446(4)	
	α		**β**		**γ**	
	90		90		90	
Atom	**x**	**y**	**z**	**Frac.**		
V1	0.10152(21)	0.75	0.60700(43)	1		
O2	0.10951(50)	0.75	0.9642(11)	1		
O3	0.06733(38)	0.25	0.4997(13)	1		
O4	0.25	0.75	0.4709(19)	1		
Li5	0.25	0.25	0.195	0.55		
Atom	**Anisotropic Thermal Factors x 100/Å²**					
	B11	**B22**	**B33**	**B12**	**B13**	**B23**
V1	2.5	2.5	2.5	0	0	0
O2	0.25(0)	0.25(0)	0.25(0)	0	0	0
O3	0.25(0)	0.25(0)	0.25(0)	0	0	0
O4	0.25(0)	0.25(0)	0.25(0)	0	0	0
Li5	1	1	1	0	0	0
Monoclinic (Weight fraction 17.4(4))						
Space Group	**Lattice Parameters/Å**					
	a		**b**		**c**	
$P2_1/m$	4.48123(17)		11.39487(30)		3.55385(41)	
	α		**β**		**γ**	
	90		92.15343(557)		90	
Atom	**x**	**y**	**z**	**Frac.**		
V1	0.3851(19)	0.59713(85)	0.2496(24)	1		
O2	0.0989(42)	0.66300(21)	0.0425(71)	1		
O3	0.32800(54)	0.0972(24)	0.2685(70)	1		
O4	0.5491(78)	0.25	0.808(11)	1		
Li5	0.195	0.25	0.25	0.55		
Atom	**Anisotropic Thermal Factors x 100/Å²**					
	B11	**B22**	**B33**	**B12**	**B13**	**B23**
V1	2.5	2.5	2.5	0	0	0
O2	0.25(0)	0.25(0)	0.25(0)	0	0	0
O3	0.25(0)	0.25(0)	0.25(0)	0	0	0
O4	0.25(0)	0.25(0)	0.25(0)	0	0	0
Li5	0	0	0	0	0	0

Table 4.31 – Crystallographic data, goodness-of-fit factors and anisotropic thermal parameters obtained by least squares refinement of x-ray diffraction data collected at 50K for ε'-$Li_{0.55}V_2O_5$.

The phase mixture was determined to be 82.6(8)% orthorhombic and 17.4(4)% monoclinic; the phase transition from orthorhombic to monoclinic is not universal at 50K, and it is likely that the structure at this temperature is made up of a mixture of orthorhombic and monoclinic layers, shown in *figure 4.26*, stacked in a disordered arrangement. The occurrence of stacking faults within vanadium oxide layers would allow for increased anisotropic broadening, as is observed here compared with lower lithium content phases previously discussed, for example around 10°, as shown in the inset of *figure 4.25*. When there are profile problems, such as those caused by anisotropic broadening, the thermal parameters can act as a dumping ground for systematic errors in peak shape; for this reason the thermal parameters have been fixed in this refinement.

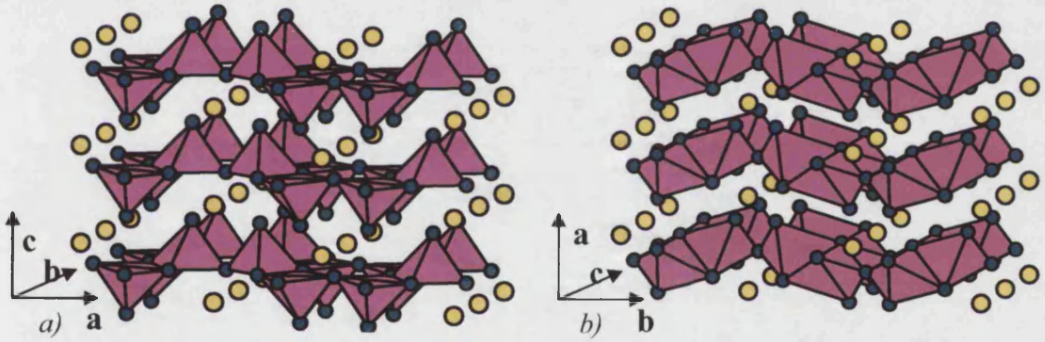

Figure 4.26 – a) Pmmn layers, b) $P2_1/m$ layers in ε'-$Li_{0.55}V_2O_5$ at 50K

Both the monoclinic and orthorhombic structures have one crystallographic vanadium site, shown in its environment coordinated by oxygen in *figure 4.27*, and described in *table 4.32*.

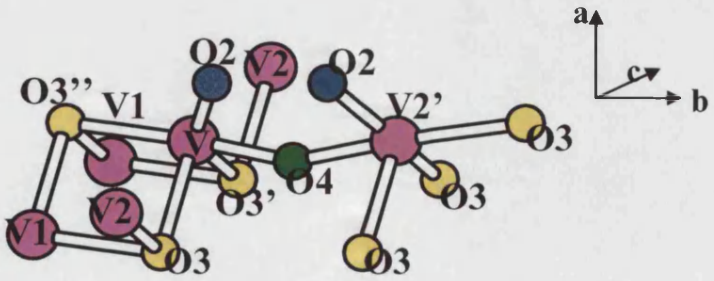

Figure 4.27 – Vanadium environment within monoclinic layers in ε'-$Li_{0.55}V_2O_5$ at 50K.

Monoclinic, $P2_1/m$			
Bond Lengths		**Bond Angles**	
Bond	**Bond Length/Å**	**Atoms**	**Angle/°**
V-O2	1.64(1)	O3/O3'-V-O3''	96.82(9)/91.20(6)
V-O4	1.78(2)	O3/O3'-V-O4	78.87(7)/89.44(9)
V-O3	2.34(1)	O3/O3'-V-O2	94.45(11)/144.93(3)
V-O3'	2.04(1)	O3''-V-O2	113.11(9)
V-O3''	2.23(2)	O4-V-O2	68.28(9)
V-V1	3.04(1)	V-O3-V1	83.18(7)
V-V2	3.55(1)	V-O3-V2	107.87(5)
V-V2'	3.48(1)	V-O4-V2'	156.29(6)
Puckering angle		18.95(1)	

Table 4.32 – Vanadium-oxygen bond lengths and angles and vanadium-vanadium distances for ε'-$Li_{0.55}V_2O_5$ x-ray diffraction data collected at 50K.

The vanadium environment in the orthorhombic, Pmmn, space group is essentially unchanged from that at room temperature, having a similar puckering angle of 4.16°. This is surprising given the very large size coefficient in the *bc* plane. The monoclinic environment differs significantly: bonds to edge-shared oxygen atoms in the VO_5 square pyramids are much longer than are found in the orthorhombic structure, and bond angles are generally more wide-ranging, giving a less regular structure; hence the reduction in symmetry. The puckering angle is much larger than that for the orthorhombic layers at either temperature, consistent with more strain along the *c*-axis.

4.6 $Li_{0.64}V_2O_5$

4.6.1 Room Temperature Data

Refinement of diffraction data using the orthorhombic Pmmn system, as for the previous compounds, gives reasonable goodness-of-fit factors. Refined diffraction patterns are shown in *figures 4.28-29*, and results described in *table 4.33*. The structure of ε'-$Li_{0.64}V_2O_5$ is very similar to that of ε'-$Li_{0.55}V_2O_5$. Changes in vanadium-oxygen bond lengths and angles are small, with a slight increase in puckering angle to 5.45°. Comparison with V_2O_5 and ε-LiV_2O_5 [20] shows that there has been a gradual shift towards the $x = 1$ values with increasing lithium content. The lithium environment in ε'-$Li_{0.64}V_2O_5$ is the same as observed in the previously discussed ε and ε' phases. Although there are no significant changes in lithium environment there are extra,

weaker peaks in neutron diffraction data for ε'-$Li_{0.64}V_2O_5$, which are not present in ε'-$Li_{0.55}V_2O_5$.

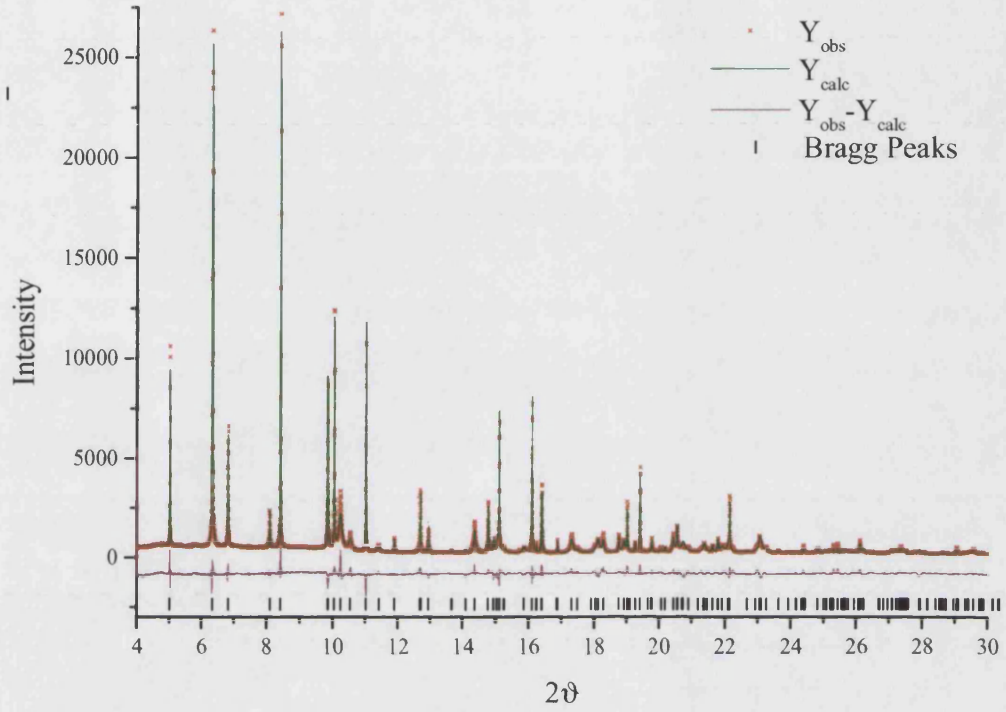

Figure 4.28 – Refined x-ray diffraction data for $Li_{0.64}V_2O_5$: intensity as a function of 2ϑ.

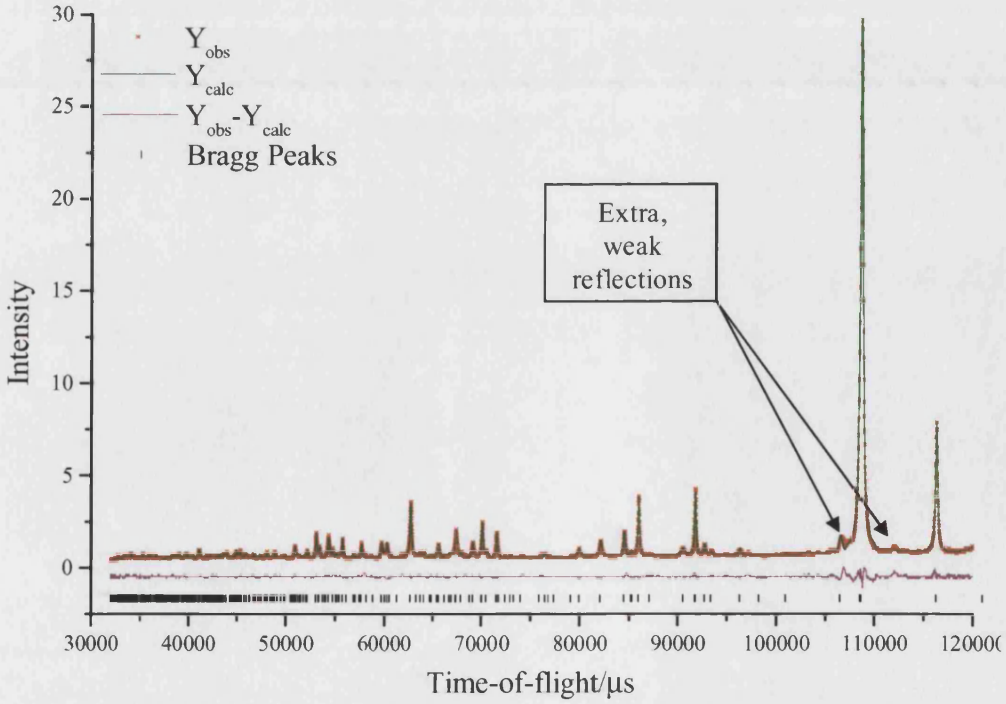

Figure 4.29 – Refined neutron data collected at HRPD for $Li_{0.64}V_2O_5$: intensity as a function of time-of-flight.

X-RAY DATA						
χ^2	R_P		R_{WP}		R_B	
5.40	0.0738		0.0989		0.0779	
Space Group	Lattice Parameters/Å					
	a		b		c	
Pmmn	11.38806(8)		3.56244(2)		4.51144(3)	
	α		β		γ	
	90		90		90	
Atom	x		y	z		Frac.
V1	0.10031(11)		0.75	0.60720(25)		1
O2	0.11434(30)		0.75	0.95570(76)		1
O3	0.07096(25)		0.25	0.48423(87)		1
O4	0.25		0.75	0.4771(11)		1
Li5	0.25		0.25	0.1616		0.64
Atom	Anisotropic Thermal Factors x 100/Å^2					
	B11	B22	B33	B12	B13	B23
V1	10.72(36)	10.72(36)	10.72(36)	0	0	0
O2	1.02(29)	1.02(29)	1.02(29)	0	0	0
O3	5.78(44)	5.78(44)	5.78(44)	0	0	0
O4	1.88(48)	1.88(48)	1.88(48)	0	0	0
Li5	1	1	1	0	0	0

NEUTRON DATA						
χ^2	R_P		R_{WP}		R_B	
5.831	0.0303		0.0375		0.1329	
Space Group	Lattice Parameters/Å					
	a		b		c	
Pmmn	11.41364(17)		3.56401(5)		4.50052(7)	
	α		β		γ	
	90		90		90	
Atom	x		y	z		Frac.
V1	0.10031		0.75	0.60720		1
O2	0.11178(11)		0.75	0.9607(4)		1
O3	0.07183(9)		0.25	0.4902(6)		1
O4	0.25		0.75	0.4855(7)		1
Li5	0.25		0.25	0.1616(22)		0.64(1)
Atom	Anisotropic Thermal Factors x 100/Å^2					
	U11	U22	U33	U12	U13	U23
V1	2.5	2.5	2.5	0	0	0
O2	1.81(9)	7.50(12)	2.57(13)	0	-0.27(10)	0
O3	0.81(8)	0.53(8)	4.09(12)	0	-0.32(9)	0
O4	0.58(9)	3.43(15)	3.00(18)	0	0	0
Li5	16.4(11)	21.6(18)	2.0(6)	0	0	0

Table 4.33 – Crystallographic data, goodness-of-fit factors and anisotropic thermal parameters obtained by least squares refinement of x-ray and neutron diffraction data for ε'-$Li_{0.64}V_2O_5$.

As discussed in section 4.4, the extra peaks present in the neutron diffraction data are caused by ordering of the lithium atoms. The phase transition to monoclinic that occurs on cooling the ε' phases could be explained by a decrease in thermal energy of lithium ions as the temperature decreases: at room temperature lithium ions have enough thermal energy to move between sites, giving a simpler ordering scheme to that observed at low temperature. The structure is therefore orthorhombic, but as the temperature drops the lithium atoms are less mobile and have a preference for certain sites causing a transition to a monoclinic structure, intrinsically linked to strain in the lattice. However, this neutron data suggests that there is some lithium ordering even at room temperature, and ordering has also been observed in lower lithium content phases, which do not undergo a phase transition at all [11]. The current explanation for the observed phase transition above a certain lithium content is that Li^+-Li^+ repulsion favours a shear strain [13-15].

A search for a commensurate supercell that would allow indexing of the extra peaks in this pattern was unsuccessful, but the best incommensurate modulation vector was found to fit the $\mathbf{q}^{\mathbf{KATZKE}}$ model [12] described in section 5.3. Satellite peaks observed in the HRPD pattern were found to give a modulation vector:

$$\mathbf{q} = 0.5550\mathbf{b}^* + \tfrac{1}{2}\mathbf{c}^*$$

allowing all peaks to be indexed (*table 4.34*) according to *equation 4.4*.

h	*k*	*l*	*n*	D*(cal)	D*(obs)	D*(obs-cal)
1	2	1	1	0.4294	0.4302	0.0008
3	0	2	1	0.4521	0.4520	-0.0001
5	1	1	1	0.4689	0.4676	-0.0013
4	1	2	1	0.4995	0.4979	-0.0016
4	0	2	1	0.5081	0.5083	0.0002
0	-1	2	1	0.5490	0.5499	0.0009
4	-1	2	1	0.6513	0.6513	0.0000
0	-1	3	1	0.7063	0.7070	0.0003
1	-2	1	1	0.7307	0.7307	0.0000
6	0	3	1	0.7805	0.7801	-0.0004
7	-1	2	1	0.8232	0.8234	0.0002
5	-1	3	1	0.8311	0.8330	0.0019

Table 4.34 – Weak satellite peaks from lithium superstructure, modulation vector (0.0000, 0.5550, 0.5000), R-factor = 1.19%.

Lithium content for this compound was determined to be 0.64(1) from refinement of lithium fractional occupancies. This is consistent with the value of γ in the modulation

vector ($\gamma = 0.5550$) which, according to Katzke [11], corresponds to a lithium content of approximately $x = 0.64$.

4.6.2 $Li_{0.64}V_2O_5$ at 50K

Like ε'-$Li_{0.55}V_2O_5$, ε'-$Li_{0.64}V_2O_5$ is a mixture of orthorhombic and monoclinic phases at 50K. Although it appears that all the peaks can be indexed by the monoclinic phase alone, refinement using only this model is unsatisfactory, giving $\chi^2 \sim 12$. Refined x-ray diffraction data are shown in *figure 4.30*, and details given in *table 4.35*. The mixture of phases was determined to consist of 78.1(1)% orthorhombic and 21.9(5)% monoclinic at this temperature: the monoclinic phase contributes slightly more than for ε'-$Li_{0.55}V_2O_5$ at 50K. The gradual nature of the phase transition is consistent with a relationship to strain in the structure, rather than, for example, electronic effects that would cause a first order transition.

Microstructure effects are similar to those observed for ε'-$Li_{0.55}V_2O_5$ at 50K: a massive coefficient for size effect in the *bc* plane of the orthorhombic layers, while the monoclinic layers show a noticeable decrease of coefficient for the *bc* plane and increase along the *c*-axis, with an overall increase in magnitude compared with room temperature coefficients. However, the puckering angles are somewhat different to those found for the $x = 0.55$ composition at 50K. Orthorhombic layers have relaxed from the room temperature value of approximately 5° to a puckering angle of 2.24°, in contrast to the $x = 0.55$ composition which showed little change in the corresponding puckering angle on cooling. The monoclinic layers have a large puckering angle of 23.69°, larger than the angle of approximately 18° observed in the $x = 0.55$ composition. Together these suggest that at higher lithium content, the orthorhombic layers become less distorted and the monoclinic layers more distorted on cooling.

The vanadium bond details in orthorhombic and monoclinic layers are quite different. The orthorhombic phase shows little difference from the room temperature environment, or from the ε'-$Li_{0.55}V_2O_5$ orthorhombic environment at 50K. The monoclinic phase is much more distorted than the orthorhombic, to take up internal strain, and has longer vanadium-oxygen bonds. In comparison with the environment in monoclinic layers of ε'-$Li_{0.55}V_2O_5$ at 50K, vanadium-oxygen bond lengths are similar, but longer in the $x = 0.64$ compound.

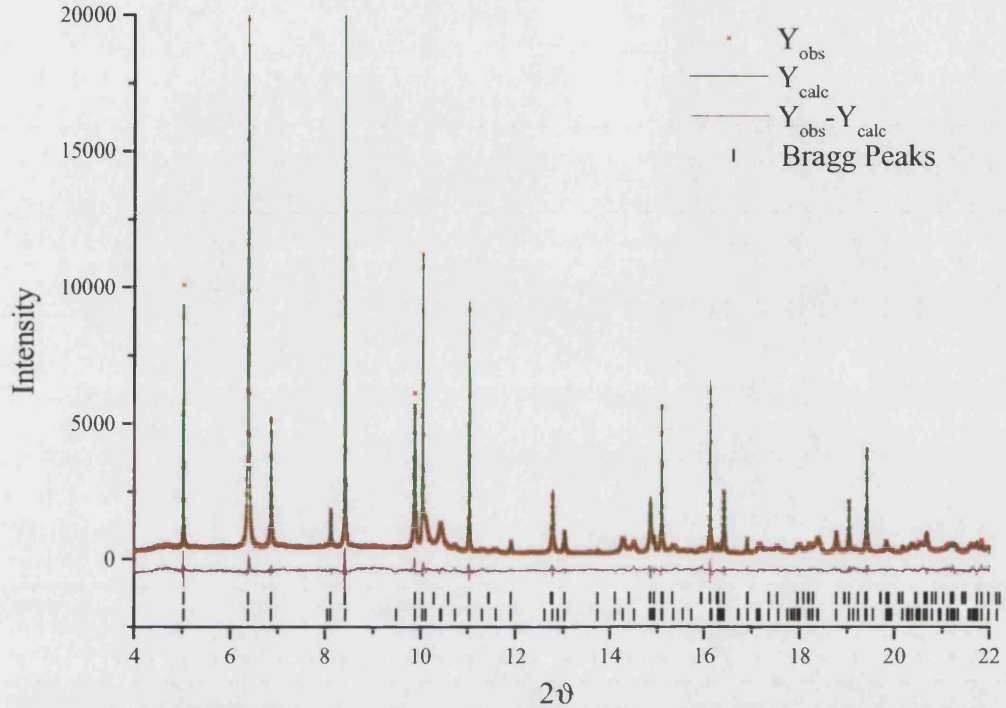

Figure 4.30 – X-ray diffraction data collected at 50K on $Li_{0.64}V_2O_5$, at BM1B, ESRF, refined as a mixture of orthorhombic and monoclinic phases; intensity as a function of 2ϑ.

X-RAY DATA						
χ^2	R_P		R_{WP}		R_B	
3.81	0.0655		0.0843		0.0553	
Orthorhombic (Weight fraction 78.1(1))						
Space Group	**Lattice Parameters/Å**					
	a		**b**		**c**	
Pmmn	11.39291(9)		3.55740(2)		4.48192(4)	
	α		**β**		**γ**	
	90		90		90	
Atom	**x**	**y**		**z**		**Frac.**
V1	0.10383(38)	0.75		0.5999(12)		1
O2	0.10362(76)	0.75		0.9753(15)		1
O3	0.06503(52)	0.25		0.5295(32)		1
O4	0.25	0.75		0.4548(18)		1
Li5	0.25	0.25		0.1616		0.64

Atom	**Anisotropic Thermal Factors x 100/Å^2**					
	B11	**B22**	**B33**	**B12**	**B13**	**B23**
V1	4.74(18)	4.74(18)	4.74(18)	0	0	0
O2	3.99(69)	3.99(69)	3.99(69)	0	0	0
O3	5.34(92)	5.34(92)	5.34(92)	0	0	0
O4	1.55(13)	1.55(13)	1.55(13)	0	0	0
Li5	1	1	1	0	0	0

Monoclinic (Weight fraction 21.9(5))						
Space Group	**Lattice Parameters/Å**					
	a		**b**		**c**	
$P2_1/m$	4.48418(14)		11.39249(13)		3.55677(17)	
	α		**β**		**γ**	
	90		91.8598(34)		90	
Atom	**x**	**y**	**z**		**Frac.**	
V1	0.3755(15)	0.60487(58)	0.2534(19)		1	
O2	0.1031(30)	0.6828(12)	-0.0171(33)		1	
O3	0.3341(45)	0.09127(86)	0.2845(33)		1	
O4	0.4931(51)	0.25	0.7804(40)		1	
Li5	0.1616	0.25	0.25		0.64	
Atom	**Anisotropic Thermal Factors x 100/Å²**					
	B11	**B22**	**B33**	**B12**	**B13**	**B23**
V1	4.38(19)	4.38(19)	4.38(19)	0	0	0
O2	1.40(16)	1.40(16)	1.40(16)	0	0	0
O3	5.25(29)	5.25(29)	5.25(29)	0	0	0
O4	2.53(28)	2.53(28)	2.53(28)	0	0	0
Li5	1	1	1	0	0	0

Table 4.35 – Crystallographic data obtained from refinement of 50K x-ray diffraction data collected at ESRF on $Li_{0.64}V_2O_5$.

4.6.3 $Li_{0.64}V_2O_5$ at 30K

Refinement as a mixture of orthorhombic and monoclinic phases again gives the best fit to the x-ray diffraction data collected at 30K. Refined data is shown in *figure 4.31*, and details given in *table 4.36*. The mixture of phases was determined to be 56.5(14)% orthorhombic and 43.6(11)% monoclinic at this temperature: the monoclinic contribution has doubled between 50K and 30K. Microstructure coefficients for the orthorhombic layers show an increase in coefficients for size effects along the *a* and *b* axes and in the *bc* plane, with a decrease along the *c*-axis compared to values at 50K. Monoclinic layers show a large overall decrease in coefficients for size effects, noticeably along the *c*-axis, indicating reduced strain in the structure. This is supported by the decrease in puckering angle from approximately 23° to 6.15°. There is an increase in puckering angle for the orthorhombic layers however, from approximately 2° at 50K to 5.52° at 30K. The puckering angles for both types of layers are closer in value at 30K, suggesting strain in the layers is similar in contrast to the situation at 50K where the monoclinic layers were highly distorted to take most of the internal strain.

At 30K there are additional, weak reflections present in the x-ray diffraction data, which are assigned to charge ordering of vanadium. It is likely that the relaxation

of monoclinic layers at this temperature is linked to the occurrence of charge ordering, supporting the earlier postulation that charge ordering is at least partially driven by the need to relieve internal strain.

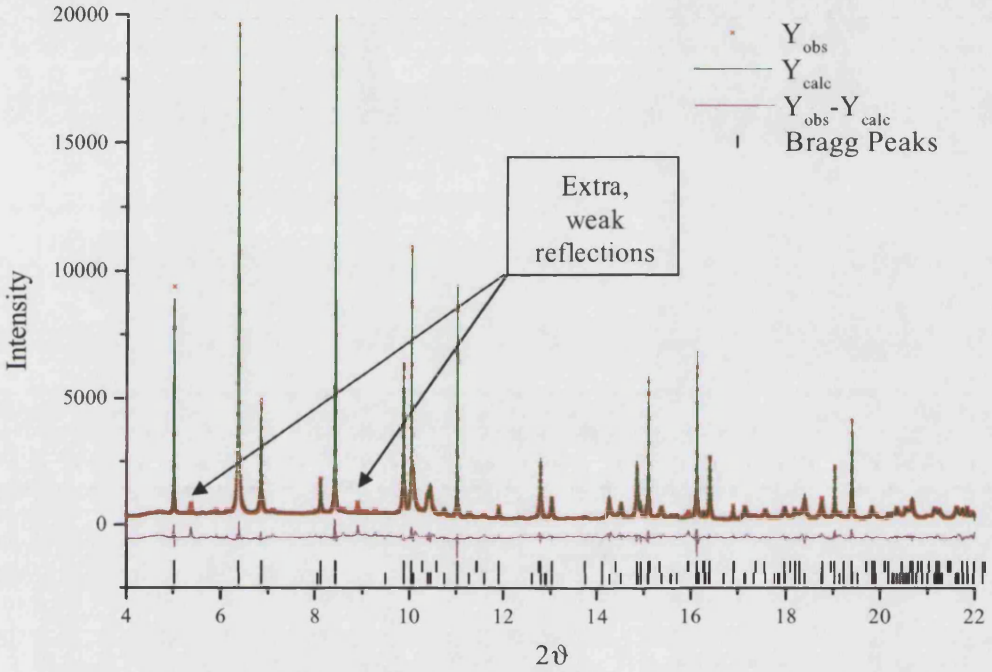

Figure 4.31 – X-ray diffraction collected at 30K on $Li_{0.64}V_2O_5$ at BM1B, ESRF: intensity as a function of 2ϑ.

X-RAY DATA				
χ^2	R_P	R_{WP}	R_B	
22.9	0.0692	0.0937	0.0613	
Orthorhombic (Weight fraction 56.5(14))				
Space Group	**Lattice Parameters/Å**			
	a	**b**	**c**	
Pmmn	11.39416(11)	3.55676(3)	4.48147(5)	
	α	**β**	**γ**	
	90	90	90	
Atom	**x**	**y**	**z**	**Frac.**
V1	0.09924(33)	0.75	0.6086(13)	1
O2	0.11669(83)	0.75	0.9630(31)	1
O3	0.07373(67)	0.25	0.49700(31)	1
O4	0.25	0.75	0.4633(31)	1
Li5	0.25	0.25	0.1616	0.64

Atom	Anisotropic Thermal Factors x 100/Å^2					
	B11	B22	B33	B12	B13	B23
V1	4.89(15)	4.89(15)	4.89(15)	0	0	0
O2	3.8(11)	3.8(11)	3.8(11)	0	0	0
O3	5.0(19)	5.0(19)	5.0(19)	0	0	0
O4	3.5(12)	3.5(12)	3.5(12)	0	0	0
Li5	1	1	1	0	0	0
Monoclinic (Weight fraction 43.6(11))						
Space Group	**Lattice Parameters/Å**					
	a		**b**		**c**	
$P2_1/m$	4.48232(9)		11.39186(18)		3.55999(6)	
	α		**β**		**γ**	
	90		92.08088(18)		90	
Atom	**x**	**y**	**z**	**Frac.**		
V1	0.3880(11)	0.60070(54)	0.2537(14)	1		
O2	0.0407(29)	0.6101(17)	0.2127(53)	1		
O3	0.4592(33)	0.0686(18)	0.2622(34)	1		
O4	0.5181(38)	0.25	0.7835(42)	1		
Li5	0.1616	0.25	0.25	0.64		
Atom	**Anisotropic Thermal Factors x 100/Å^2**					
	B11	**B22**	**B33**	**B12**	**B13**	**B23**
V1	4.25(21)	4.25(21)	4.25(21)	0	0	0
O2	1.60(35)	1.60(35)	1.60(35)	0	0	0
O3	1.41(36)	1.41(36)	1.41(36)	0	0	0
O4	3.5(18)	3.5(18)	3.5(18)	0	0	0
Li5	1	1	1	0	0	0

Table 4.36 – Crystallographic data obtained from refinement of x-ray diffraction data collected at 30K on $Li_{0.64}V_2O_5$ at BM1B, ESRF.

The structure of monoclinic layers is shown in *figure 4.32*, and the vanadium environment is described in *table 4.37*.

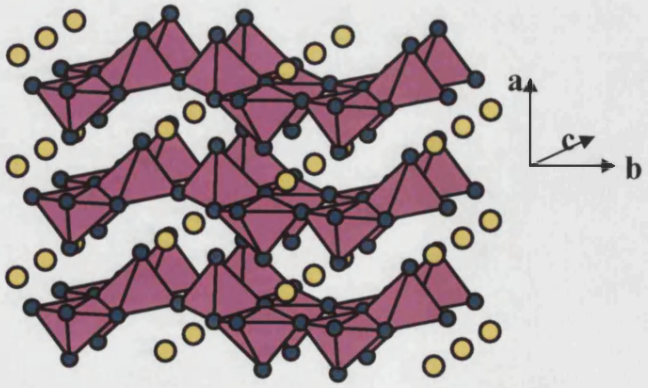

Figure 4.32 – Monoclinic layers in ε'-$Li_{0.64}V_2O_5$ at 30K.

Monoclinic, $P2_1/m$			
Bond Lengths		**Bond Angles**	
Bond	**Bond Length/Å**	**Atoms**	**Angle/°**
V-O2	1.56(1)	O3/O3'-V-O3''	76.98(7)/74.84(6)
V-O4	1.76(2)	O3/O3'-V-O4	90.94(12)/100.26(11)
V-O3	2.02(1)	O3/O3'-V-O2	107.32(9)/115.50(7)
V-O3'	1.87(2)	O3''-V-O2	103.36(8)
V-O3''	1.96(1)	O4-V-O2	99.61(8)
V-V1	3.11(1)	V-O3-V1	103.02(7)
V-V2	3.56(1)	V-O3-V2	132.82(9)
V-V2'	3.40(1)	V-O4-V2'	150.62(7)
Puckering angle		6.15(1)	

Table 4.37 – Vanadium-oxygen bond lengths and angles and vanadium-vanadium distances for ε'-$Li_{0.64}V_2O_5$ x-ray diffraction data at 30K.

Monoclinic layers at 30K contain a regular VO_5 square pyramids when compared to those at 50K; the range of bond angles is smaller, and angles are closer to the values observed in the orthorhombic layers at this temperature. Bond lengths are shorter at 30K than 50K, and comparable to those seen in the orthorhombic layers.

The χ^2 value here is quite high, much higher than at 50K, due to the presence of extra peaks in the pattern at this temperature, some of which are shown in *figure 4.33*:

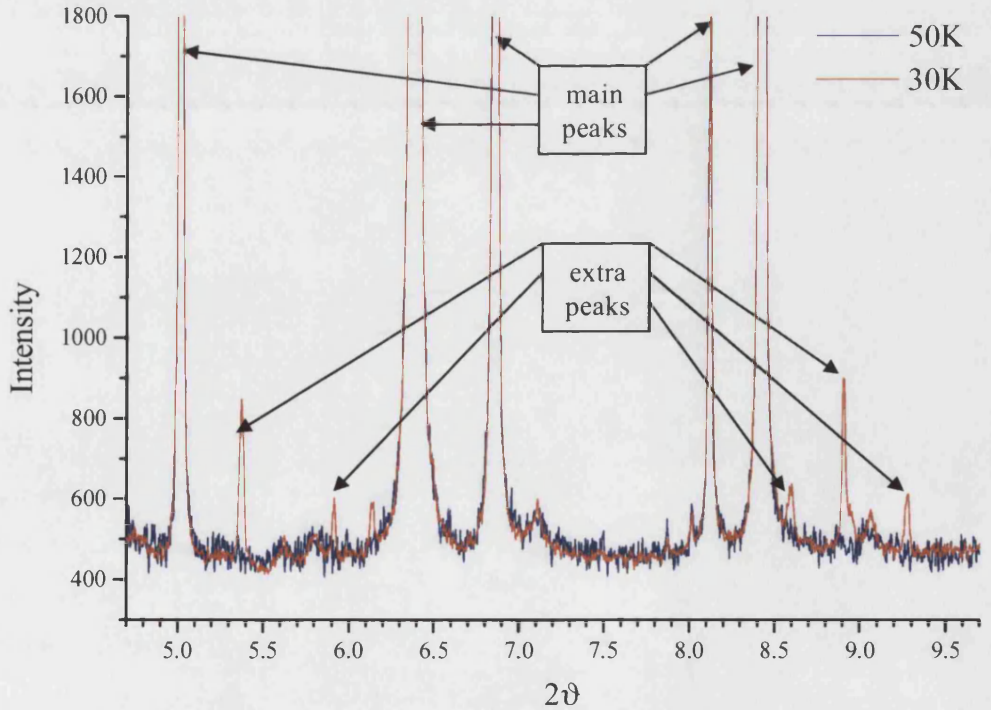

Figure 4.33 – X-ray diffraction data for $Li_{0.64}V_2O_5$ at 50K (blue) and 30K (red) showing extra peaks present at the lower temperature.

The extra peaks can be indexed with a modulation vector from the orthorhombic or monoclinic layers. Neither gives a perfect fit, but the fit from monoclinic cell parameters is slightly better than that from orthorhombic. The modulation wave vector, $\mathbf{q}^{30}$ may be written as:

$$\mathbf{q}^{30} = 0.4545\mathbf{a}^* + 0.1545\mathbf{b}^* + 0.4216\mathbf{c}^*$$

which allows all satellite reflections to be indexed as (*h*, *k*, *l*, *m*) in *table 4.38*, according to *equation 4.4*.

h	*k*	*l*	*n*	D*(cal)	D*(obs)	2ϑ(cal)	2ϑ(obs)	2ϑ(obs-cal)
1	1	0	1	0.1826	0.1878	5.2280	5.3759	0.1479
1	-1	0	1	0.1952	0.1965	5.5891	5.6266	0.0375
1	0	1	1	0.2071	0.2066	5.9303	5.9168	-0.0135
1	1	1	1	0.2196	0.2146	6.2879	6.1449	-0.1430
1	-2	0	1	0.2522	0.2482	7.2228	7.1097	-0.1131
1	-2	1	1	0.2801	0.2799	8.0243	8.0178	-0.0065
1	3	0	1	0.3004	0.3003	8.6050	8.6023	-0.0027
0	3	1	1	0.3129	0.3129	8.9660	8.9660	0.0000
1	-3	0	1	0.3233	0.3164	9.2626	9.0648	-0.1978
1	3	1	1	0.3242	0.3239	9.2887	9.2799	-0.0089
2	1	0	1	0.3683	0.3745	10.5566	10.7351	0.1785
2	2	0	1	0.3954	0.3938	11.3372	11.2901	-0.0471
2	-1	1	1	0.3998	0.4037	11.4621	11.5751	0.1130
2	-2	1	1	0.4305	0.4309	12.3457	12.3561	0.0104
2	3	0	1	0.4388	0.4324	12.5840	12.4016	-0.1824
2	-3	0	1	0.4548	0.4521	13.0444	12.9668	-0.0776
2	3	1	1	0.4604	0.4655	13.2063	13.3549	0.1486
2	-3	1	1	0.4756	0.4747	13.6461	13.6185	-0.0276
1	3	-1	1	0.4831	0.4870	13.8613	13.9742	0.1130
2	4	0	1	0.4940	0.4991	14.1766	14.3229	0.1462
1	-3	-1	1	0.4977	0.5037	14.2813	14.4568	0.1755
2	4	1	1	0.5133	0.5108	14.7330	14.6605	-0.0724

Table 4.38 – Weak satellite peaks from vanadium superstructure, modulation vector (0.4545, 0.1545, 0.4216), R-factor = 10.75%.

The changes in atom separation and bond angles within monoclinic layers between 50K and 30K, tending back towards room temperature values at 30K where there is charge ordering, indicate the relieving of strain firstly by transformation to a monoclinic structure and secondly by a transformation within the monoclinic structure linked to charge ordering, beginning at around 50K and completed by 30K.

4.6.4 $Li_{0.64}V_2O_5$ at 5K

Neutron diffraction data collected at 5K was refined as a mixture of orthorhombic and monoclinic phases, using the 30K structures as a starting model. Refined data is shown in *figure 4.34*, and structural details given in *table 4.39*. The composition of the phase mixture was determined as 70.9(12)% orthorhombic and 29.1(8)% monoclinic.

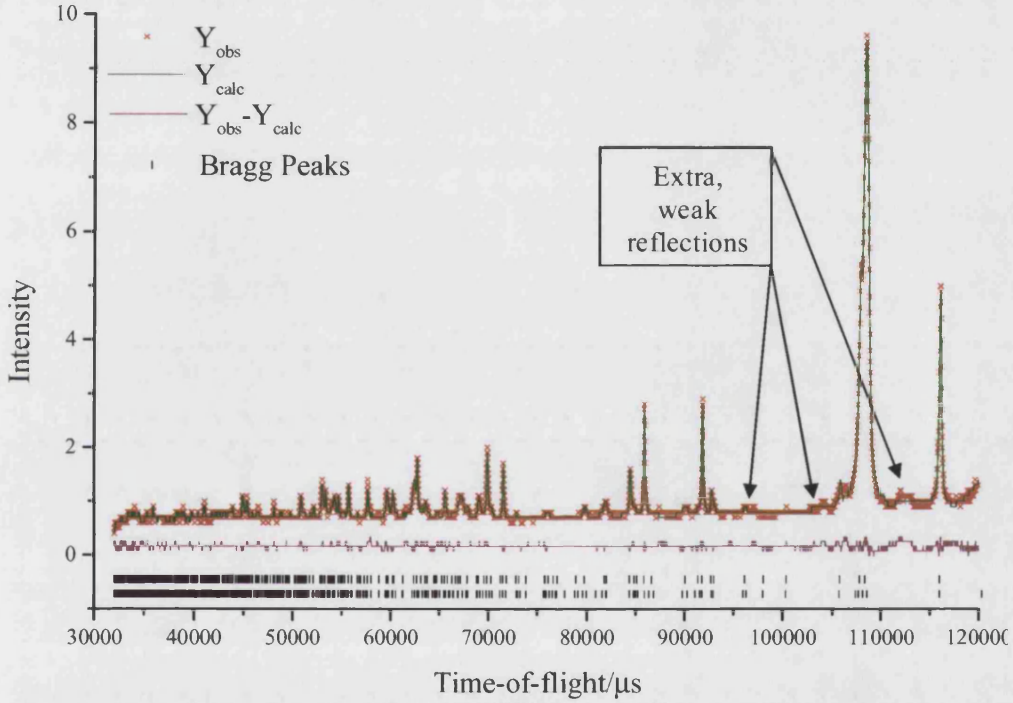

Figure 4.34 – Refined neutron data from HRPD at 4-5K on $Li_{0.64}V_2O_5$: intensity as a function of time-of-flight.

NEUTRON DATA				
χ^2	R_P	R_{WP}	R_B	
6.454	0.0289	0.0339	0.1006	
Orthorhombic (Weight fraction 70.9(12))				
Space Group	**Lattice Parameters/Å**			
	a	**b**	**c**	
Pmmn	11.41275(20)	3.55998(6)	4.47077(11)	
	α	**β**	**γ**	
	90	90	90	
Atom	**x**	**y**	**z**	**Frac.**
V1	0.09924	0.75	0.60860	1
O2	0.11628(31)	0.75	0.9553(9)	1
O3	0.07178(26)	0.25	0.4978(14)	1
O4	0.25	0.75	0.4866(17)	1
Li5	0.25	0.25	0.1783(30)	0.64

Atom	Anisotropic Thermal Factors x 100/Å^2					
	U11	U22	U33	U12	U13	U23
V1	2.5	2.5	2.5	0	0	0
O2	2.50(26)	2.50(26)	2.50(26)	0	0	0
O3	3.79(25)	3.79(25)	3.79(25)	0	0	0
O4	4.84(45)	4.84(45)	4.84(45)	0	0	0
Li5	12.2(9)	12.2(9)	12.2(9)	0	0	0
Monoclinic (Weight fraction 29.1(8))						
Space Group	**Lattice Parameters/Å**					
	a		**b**		**c**	
$P2_1/m$	4.4669(5)		11.41224(21)		3.56218(27)	
	α		**β**		**γ**	
	90		90.367(9)		90	
Atom	**x**	**y**	**z**	**Frac.**		
V1	0.38799	0.60070	0.25371	1		
O2	-0.0039(33)	0.6024(7)	0.2553(28)	1		
O3	0.5486(31)	0.0724(5)	0.2066(37)	1		
O4	0.4831(45)	0.25	0.7398(71)	1		
Li5	0.174(13)	0.25	0.233(19)	0.64		
Atom	**Anisotropic Thermal Factors x 100/Å^2**					
	U11	**U22**	**U33**	**U12**	**U13**	**U23**
V1	2.5	2.5	2.5	0	0	0
O2	1.21(28)	1.21(28)	1.21(28)	0	0	0
O3	5.0(8)	5.0(8)	5.0(8)	0	0	0
O4	1.96(62)	1.96(62)	1.96(62)	0	0	0
Li5	15.0(6)	15.0(6)	15.0(6)	0	0	0

Table 4.39 – Crystallographic data, goodness-of-fit factors and anisotropic thermal parameters obtained by least squares refinement of neutron diffraction data collected at 4-5K for ε'-$Li_{0.64}V_2O_5$.

The lithium environment in both orthorhombic and monoclinic layers is very similar to that observed at room temperature: eight-fold coordination by oxygen in a bicapped trigonal prismatic arrangement. Average lithium-oxygen distances are the same in the orthorhombic layers as that at room temperature, but are slightly longer in the monoclinic layer. *Table 4.40* gives the interatomic distances for comparison.

Li-O	Pmmn Separation/Å	Li-O	$P2_1/m$ Separation/Å
2 x Li-O4	2.25(1)	2 x Li-O4	2.27(2), 2.24(2)
2 x Li-O3	2.49(2)	2 x Li-O3	2.63(1)
4 x Li-O2	2.55(1)	4 x Li-O2	2.54(1) x 2, 2.60(1) x 2
Average	2.46	Average	2.51

Table 4.40 – Lithium-oxygen separations in ε'-$Li_{0.64}V_2O_5$.

The relatively high value of χ^2 for refinement of these data may be explained by the presence of extra, weaker, peaks at 5K. As previously discussed, this is believed to be indicative of ordering of lithium ions, but again there is no satisfactory commensurate supercell which will account for all the extra peaks. Satellite peaks may be indexed in either the monoclinic or orthorhombic systems to give very similar modulation vectors, allowing for the necessary interchange of axes:

$$\mathbf{q}^5_{\text{orthorhombic}} = 0.0910\mathbf{b}^* + \tfrac{1}{2}\mathbf{c}^*$$

allowing all peaks to be indexed (*table 4.41*) according to *equation 4.4*.

h	*k*	*l*	*n*	D*(cal)	D*(obs)	D*(obs-cal)
4	1	-1	1	0.5483	0.5517	0.0034
3	1	-1	1	0.4969	0.4971	0.0002
1	-1	-1	1	0.4628	0.4676	0.0048
1	-1	-1	1	0.4628	0.4635	0.0107
2	1	-1	1	0.4566	0.4535	-0.0031
3	0	-1	1	0.4270	0.4309	0.0039
3	0	-1	1	0.4270	0.4274	0.0004

Table 4.41 – Weak satellite peaks from lithium ordered superstructure, modulation vector (0.0000, 0.0910, 0.5000), R-factor = 2.22%.

$$\mathbf{q}^5_{\text{monoclinic}} = \tfrac{1}{2}\mathbf{a}^* + 0.0830\mathbf{c}^*$$

allowing all peaks to be indexed (*table 4.42*) according to *equation 4.4*.

h	*k*	*l*	*n*	D*(cal)	D*(obs)	D*(obs-cal)
-1	4	1	1	0.5484	0.5517	0.0033
-1	3	1	1	0.4970	0.4971	0.0001
-1	1	-1	1	0.4628	0.4676	0.0048
-1	1	-1	1	0.4628	0.4635	0.0007
1	4	1	1	0.4495	0.4535	-0.0040
-1	3	0	1	0.4272	0.4309	0.0037
-1	3	0	1	0.4272	0.4274	0.0002

Table 4.42 – Weak satellite peaks from lithium ordered superstructure, modulation vector (0.5000, 0.0000, 0.0830), R-factor = 2.05%.

It can be seen from these modulation vectors that there is almost a commensurate supercell possible: (002) in the orthorhombic system, or (200) in the monoclinic. In either system, this would mean a doubling along the axis of layer spacing; in other words, a doubled cell height, as is observed in the delta phases reviewed in chapter one. However, doubling of the unit cell height observed in the δ-phases is attributed to a shift of vanadium oxide layers by half the unit cell width, along that axis, rather than ordering of lithium [20, 27, 28].

4.7 $Li_{0.72}V_2O_5$

Refinements of x-ray diffraction data as solely ε'-$Li_{0.72}V_2O_5$ were unsatisfactory, as major peaks were left unmatched. These peaks can be matched to the δ-phase, however, the δ-phase alone also leaves unmatched peaks. Refinement of the x-ray diffraction data as a mixture of a slightly distorted ε'- and δ-phases in the space groups $Pmn2_1$ and Cmcm [27, 28] respectively, gave good results. Refined data are shown in *figures 4.35-36* and results are described in *tables 4.43-44*. The phase mixture was determined to be 92.1(14)% ε'-$Li_{0.72}V_2O_5$, and 7.9(13)% δ-$Li_{0.72}V_2O_5$ from x-ray diffraction data. Lithium content was determined to be 0.72(1) from refinement of the fractional occupancy of lithium atoms, confirmed by magnetic susceptibility measurements.

Refinement of neutron diffraction data for $Li_{0.72}V_2O_5$ using the usual Pmmn space group for the ε'-phase gave $\chi^2 \sim 8$, due to intensity and peak shape problems. A drop in symmetry to $Pmn2_1$ allows an extra degree of freedom along the cell depth axis; the vanadium and oxygen atoms now occupy (*x*, *y*, *z*) positions, and oxygen and lithium atoms that are constrained respectively to 2*a* (0, 0, *z*) and 2*b* (0, ½, *z*) positions in Pmmn, are transformed to the 2*a* (0, *y*, *z*) position in $Pmn2_1$. For vanadium and oxygen atoms there is a small shift, within error bars of the constrained value, but there is a larger shift in lithium position, along the previously constrained *z*-axis, leading to less intensity problems, as shown in *figure 4.36*, and a reduced $\chi^2 \sim 2$, as described in *table 4.44*. X-ray diffraction data has a smaller improvement in χ^2 when symmetry is lowered to $Pmn2_1$; since the lithium position shows the most significant shift and x-ray data for this compound will be dominated by the position of vanadium atoms, this is not surprising.

Microstructure effects show an overall decrease in size effect coefficients for both phases compared with the $x = 0.64$ composition, particularly in the *bc* plane. Between phases, there is an increase in coefficients for the *bc* plane and the axis corresponding to cell depth (*c* for ε', *a* for δ). Strain coefficients show an increase for the ε'-phase compared with those of the lower lithium content $x = 0.64$ composition.

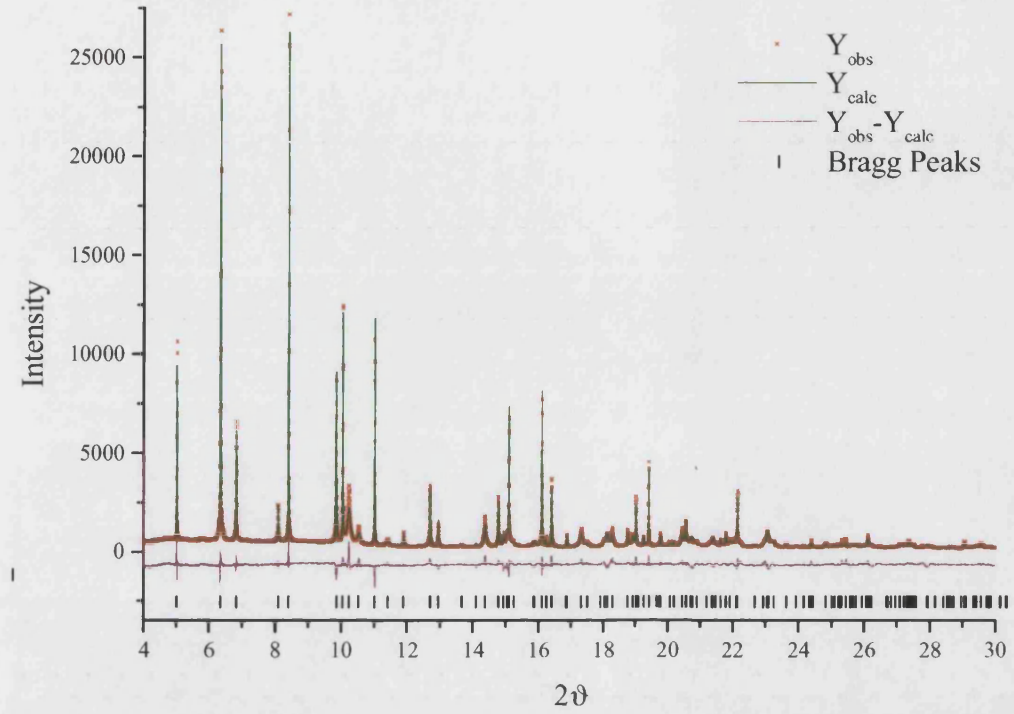

Figure 4.35 – X-ray diffraction data for $Li_{0.72}V_2O_5$ collected at BM1B, ESRF, refined as orthorhombic phases in $Pmn2_1$ and Cmcm space groups: intensity as a function of 2ϑ.

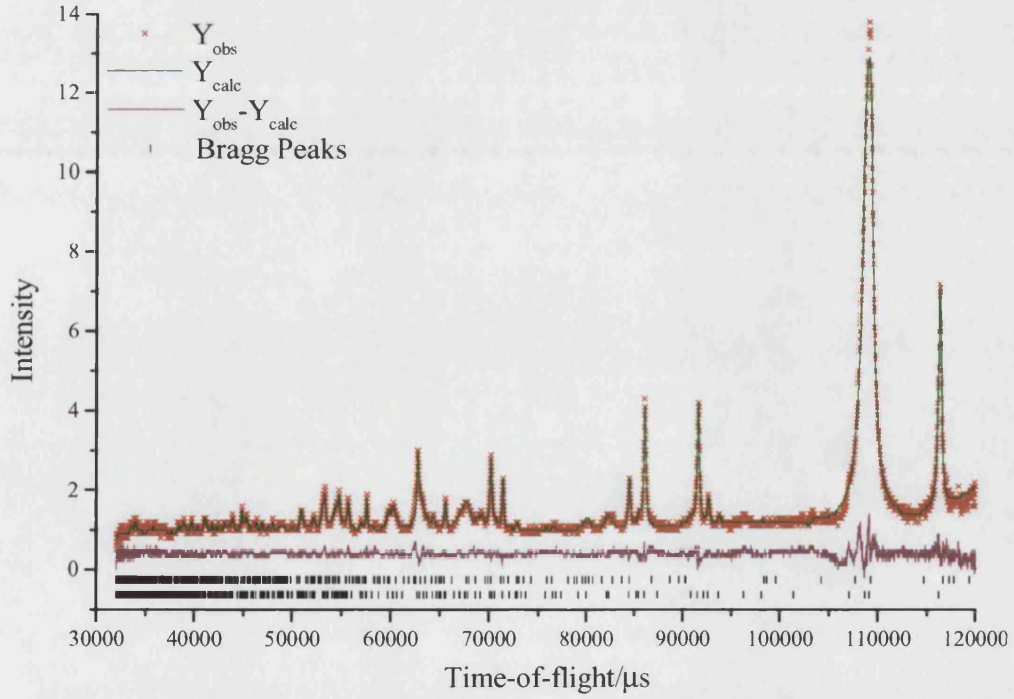

Figure 4.36 – Neutron data from HRPD on $Li_{0.72}V_2O_5$ refined as $Pmn2_1$ and Cmcm space group phases: intensity as a function of time-of-flight.

X-RAY DATA						
χ^2	R_P		R_{WP}		R_B	
5.89	0.0605		0.0766		0.0938	
ε'-$Li_{0.72}V_2O_5$ (Weight fraction 92.1(14))						
Space Group	**Lattice Parameters/Å**					
	a		**b**		**c**	
$Pmn2_1$	11.37106(9)		4.53240(4)		3.56688(2)	
	α		**β**		**γ**	
	90		90		90	
Atom	**x**	**y**		**z**		**Frac.**
V1	0.15141(22)	0.10847(63)		0		1
O2	0.13431(41)	0.4542(15)		0.9458(40)		1
O3	0.17483(58)	-0.0139(12)		0.5088(37)		1
O4	0	-0.0395(19)		1.0481(52)		1
Li5	0.5	0.258		1.102		0.72

Atom	**Anisotropic Thermal Factors x 100/Å²**					
	B11	**B22**	**B33**	**B12**	**B13**	**B23**
V1	3.83(11)	3.83(11)	3.83(11)	0	0	0
O2	2.61(53)	2.61(53)	2.61(53)	0	0	0
O3	2.02(76)	2.02(76)	2.02(76)	0	0	0
O4	2.41(93)	2.41(93)	2.41(93)	0	0	0
Li5	1	1	1	0	0	0

δ-$Li_{0.72}V_2O_5$ (Weight fraction 7.9(13))						
Space Group	**Lattice Parameters/Å**					
	a		**b**		**c**	
Cmcm	3.60082(3)		9.90616(13)		11.23564(11)	
	α		**β**		**γ**	
	90		90		90	
Atom	**x**	**y**		**z**		**Frac.**
V1	0	0.20224(37)		0.39458(28)		1
O2	0	0.04180(92)		0.37196(73)		1
O3	0	0.24445(77)		0.57034(59)		1
O4	0	0.2976(15)		0.25		1
Li5	0.5	0.399		0.25		0.72

Atom	**Anisotropic Thermal Factors x 100/Å²**					
	B11	**B22**	**B33**	**B12**	**B13**	**B23**
V1	1.82(11)	1.82(11)	1.82(11)	0	0	0
O2	1.39(13)	1.39(13)	1.39(13)	0	0	0
O3	1.31(28)	1.31(28)	1.31(28)	0	0	0
O4	2.7(13)	2.7(13)	2.7(13)	0	0	0
Li5	1	1	1	0	0	0

Table 4.43 – Crystallographic data, goodness-of-fit factors and anisotropic thermal parameters obtained by least squares refinement of x-ray diffraction data for $Li_{0.72}V_2O_5$

NEUTRON DATA						
χ^2	R_P		R_{WP}		R_B	
2.328	0.0408		0.0490		0.0999	
ε'-$Li_{0.72}V_2O_5$ (Weight fraction 91.5(19))						
Space Group	**Lattice Parameters/Å**					
	a		**b**		**c**	
$Pmn2_1$	11.39058(15)		4.52591(15)		3.56727(6)	
	α		**β**		**γ**	
	90		90		90	
Atom	**x**		**y**	**z**		**Frac.**
V1	0.15141		0.10847	0		1
O2	0.13670(13)		0.5310(12)	0.995(26)		1
O3	0.17586(16)		0.0089(13)	0.508(26)		1
O4	0		-0.0060(19)	0.989(27)		1
Li5	0.5		0.258(6)	1.102(26)		0.72(1)
Atom	**Anisotropic Thermal Factors x 100/Å^2**					
	U11	**U22**	**U33**	**U12**	**U13**	**U23**
V1	2.5	2.5	2.5	0	0	0
O2	5.75(13)	5.75(13)	5.75(13)	0	0	0
O3	2.51(9)	2.51(9)	2.51(9)	0	0	0
O4	1.48(10)	2.75(23)	2.78(25)	0	0	0
Li5	13.71(90)	13.71(90)	13.71(90)	0	0	0
δ-$Li_{0.72}V_2O_5$ (Weight fraction 8.5(8))						
Space Group	**Lattice Parameters/Å**					
	a		**b**		**C**	
Cmcm	3.60213(16)		9.90821(14)		11.23799(10)	
	α		**β**		**γ**	
	90		90		90	
Atom	**x**		**y**	**z**		**Frac.**
V1	0		0.20224	0.39458		1
O2	0		0.0443(11)	0.3723(15)		1
O3	0		0.2447(16)	0.5721(19)		1
O4	0		0.2848(12)	0.25		1
Li5	0.5		0.399(7)	0.25		0.72(1)
Atom	**Anisotropic Thermal Factors x 100/Å^2**					
	U11	**U22**	**U33**	**U12**	**U13**	**U23**
V1	2.5	2.5	2.5	0	0	0
O2	2.73(8)	0.55(11)	0.91(6)	0	0.65(14)	0
O3	2.80(31)	2.75(18)	0.77(3)	0	1.53(12)	0
O4	1.16(9)	0.73(4)	0.05(7)	-0.03(2)	0.04(7)	-0.10(9)
Li5	12.08(23)	12.08(23)	12.08(23)	0	0	0

Table 4.44 – Crystallographic data, goodness-of-fit factors and anisotropic thermal parameters obtained by least squares refinement of neutron diffraction data for $Li_{0.72}V_2O_5$

The vanadium environment of ε'-$Li_{0.72}V_2O_5$ is described in *table 4.45*. Vanadium-oxygen bond lengths are similar to those in ε'-$Li_{0.64}V_2O_5$, the average vanadium-oxygen distance is slightly longer, but vanadium-vanadium distances remain almost unchanged with increased lithium content. Bond angles for the $x = 0.72$ compound have a greater range of values than lower lithium content compounds: in particular, the puckering angle has increased from approximately 5° to 8.64°, indicative of the greater distortion in the structure with increased lithium content.

Bond Lengths		Bond Angles	
Bond	**Bond Length/Å**	**Atoms**	**Angle/°**
V-O2	1.59(1)	O3/O3'-V-O3''	79.11(8)/77.77(7)
V-O4	1.86(3)	O3/O3'-V-O4	96.45(5)/86.38(3)
V-O3	1.86(3)	O3/O3'-V-O2	101.36(3)/114.66(2)
V-O3'	1.92(2)	O3''-V-O2	109.28(2)
V-O3''	2.02(2)	O4-V-O2	104.70(3)
V-V1	3.03(1)	V-O3-V1	102.59(4)
V-V2	3.57(1)	V-O3-V2	141.92(4)
V-V2'	3.44(1)	V-O4-V2'	136.21(6)
Puckering angle		8.64(1)	

Table 4.45 – Vanadium-oxygen bond lengths and angles and vanadium-vanadium distances for ε'-$Li_{0.72}V_2O_5$ x-ray diffraction data.

Lithium ions in ε'-$Li_{0.72}V_2O_5$ are in the same type of eight-fold coordination by oxygen atoms as has been previously observed in lower lithium content phases. The shift in lithium position in this composition has an effect on the lithium-oxygen separations as shown in *table 4.46*. Two of the oxygen atoms surrounding the lithium ion are now so far removed that the ion could almost be considered to be six-coordinated, as shown in *figure 4.37*. If the two longest lithium-oxygen bonds are not included in calculation of the average lithium-oxygen distance there is a larger decrease to 2.26Å.

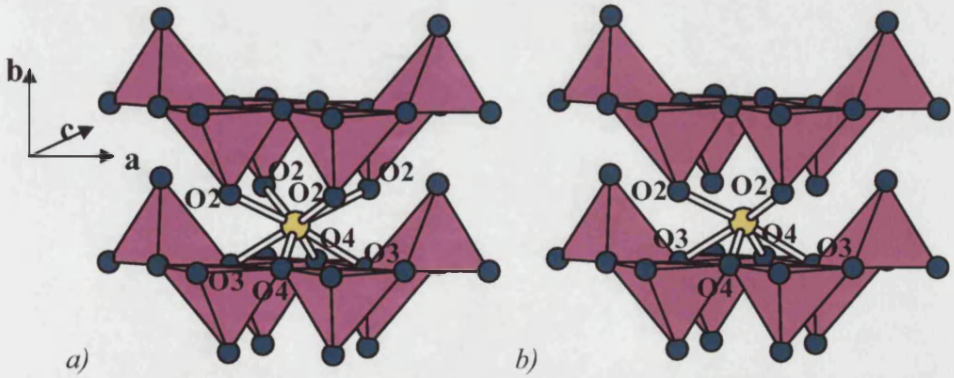

Figure 4.37 – Lithium environment in $Li_{0.72}V_2O_5$ $Pmn2_1$ phase, from neutron diffraction data.

Li-O	Separation/Å
2 x Li-O4	1.79(3), 2.47(4)
2 x Li-O3	2.36(1)
4 x Li-O2	2.30(1) x 2, 2.83(1) x 2
Average	2.41

Table 4.46 – Lithium-oxygen separations in ε'-$Li_{0.72}V_2O_5$.

The structure of δ-$Li_{0.72}V_2O_5$ (*figure 4.38*) shows very small differences in atom position and lattice constant compared with the structure published by Cava *et al.* [27, 28]. There is a shift of $^a/_2$ along [100] resulting in a doubling of the cell height, *b*.

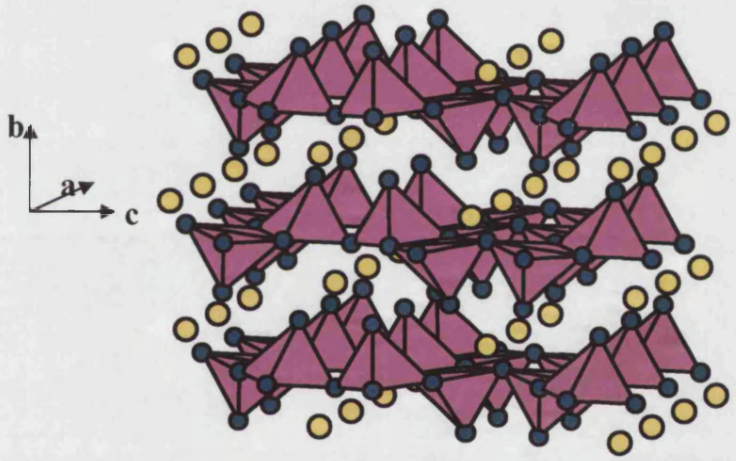

Figure 4.38 – Structure of δ-$Li_{0.72}V_2O_5$ from refinement of diffraction data.

The vanadium site is shown in more detail in *figure 4.39*, and described in *table 4.47*. It would be expected that increased lithium content leading to increased reduction of vanadium would result in an increased vanadium-oxygen bond length, yet the average bond length for δ-$L_{0.72}V_2O_5$ is 1.87Å, slightly longer than the 1.85Å average bond length in δ-LiV_2O_5 [27, 28] and ε'-$Li_{0.72}V_2O_5$. The nearest-neighbour vanadium distance is longer, while the next-nearest distance is shorter in this compound than in δ-LiV_2O_5. Bond angles also differ from those previously reported, and the puckering angle of 16.65° is significantly larger in δ-$Li_{0.72}V_2O_5$ than the 11.14° calculated for δ-LiV_2O_5: this is unexpected, as increased lithium content is expected to cause increased puckering in the layers.

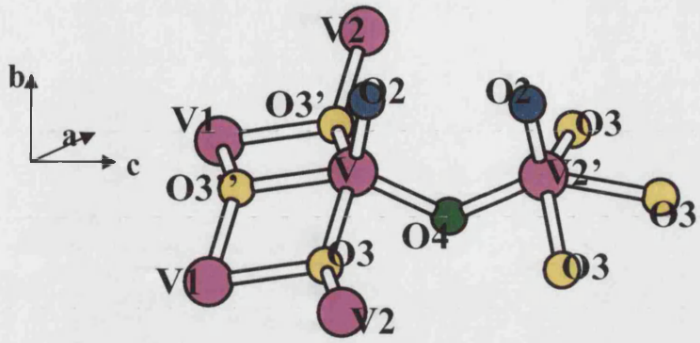

Figure 4.39 – Vanadium environment in δ-$Li_{0.72}V_2O_5$ from x-ray diffraction data.

Bond Lengths		Bond Angles	
Bond	**Bond Length/Å**	**Atoms**	**Angle/°**
V-O2	1.61(3)	O3/O3'-V-O3''	75.04(9)
V-O4	1.88(2)	O3/O3'-V-O4	92.25(8)
V-O3	1.92(1)	O3/O3'-V-O2	107.73(3)
V-O3'	1.92(1)	O3''-V-O2	111.04(3)
V-O3''	2.02(2)	O4-V-O2	111.10(5)
V-V1	3.12(1)	V-O3-V1	104.96(7)
V-V2	3.60(1)	V-O3-V2	136.79(6)
V-V2'	3.25(1)	V-O4-V2'	119.64(6)
Puckering angle		16.65(1)	

Table 4.47 – Vanadium-oxygen bond lengths and angles and vanadium-vanadium distances for δ-$Li_{0.72}V_2O_5$ from refinement of x-ray diffraction data.

The shift along {100} in the δ-phase allows more favourable six-fold coordination of lithium ions by oxygen, as shown in *figure 4.40*. The average lithium-oxygen distance has decreased to 2.17Å, close to the ideal value for octahedral coordination of lithium (2.14Å [12]), making this a favourable site, much more stable than the cuboctahedral site available in the ε- and ε'- phases. The distances here are similar to those for the published δ-LiV_2O_5 phase, although the average distance is slightly shorter in the x = 0.72 compound.

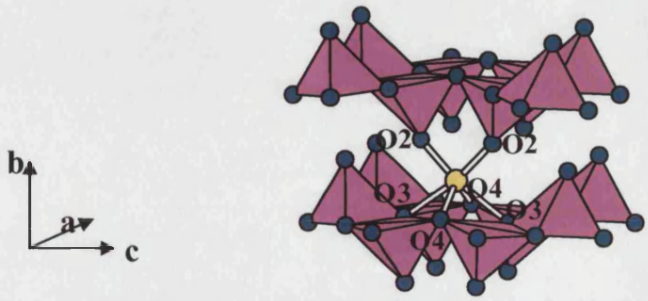

Figure 4.40 – Lithium environment in δ-$Li_{0.72}V_2O_5$, from refinement of neutron diffraction data.

Li-O	Separation/Å
2 x Li-O4	2.06(2)
2 x Li-O3	2.47(1)
2 x Li-O2	1.97(1)
Average	2.17

Table 4.48 – Lithium-oxygen separations in δ-$Li_{0.72}V_2O_5$.

4.8 $Li_{0.95}V_2O_5$

$Li_{0.95}V_2O_5$, like $Li_{0.72}V_2O_5$, was found to consist of a mixture of ε'- and δ-phases, in the proportions 5.9(5)% ε'- and 94.1(12)% δ-$Li_{0.95}V_2O_5$. Refined data are shown in *figure 4.41* and described in *table 4.49*. Microstructure coefficients show an overall increase in coefficients for size effects compared with the values obtained for the $x = 0.72$ phases. The small amount of ε'-phase present at the higher $x = 0.95$ composition is very strained, size coefficients having increased by approximately a factor of ten. There is an increase in the size coefficients for δ-$Li_{0.95}V_2O_5$ in comparison with δ-$Li_{0.72}V_2O_5$, however, overall the coefficients correspond to a much less strained structure than the ε' phase at this high lithium content composition.

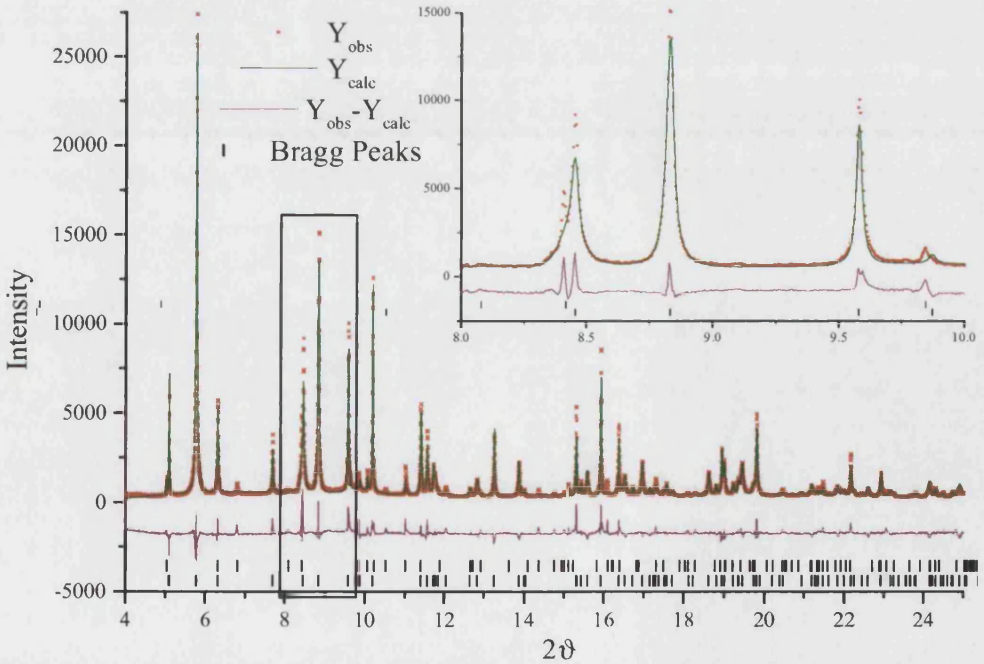

Figure 4.41 – Refined x-ray diffraction data for $Li_{0.95}V_2O_5$ as Pmmn and Cmcm phases: intensity as a function of 2ϑ. Inset is enlargement of 8-10° showing anisotropic broadening.

X-RAY DATA						
χ^2	R_P		R_{WP}		R_B	
9.33	0.0820		0.1040		0.0925	
ε'-$Li_{0.95}V_2O_5$ (Weight fraction 5.9(5))						
Space Group	**Lattice Parameters/Å**					
	a		**b**		**c**	
Pmmn	11.37725(26)		3.56585(7)		4.52431(18)	
	α		β		γ	
	90		90		90	
Atom	**x**	**y**	**z**	**Frac.**		
V1	0.1031(12)	0.75	0.6355(42)	1		
O2	0.1200(17)	0.75	0.9711(48)	1		
O3	0.0585(19)	0.25	0.5165(61)	1		
O4	0.25	0.75	0.4739(72)	1		
Li5	0.25	0.25	0.1616	0.95		
Atom	**Anisotropic Thermal Factors x 100/Å^2**					
	B11	**B22**	**B33**	**B12**	**B13**	**B23**
V1	2.02(19)	2.02(19)	2.02(19)	0	0	0
O2	8.4(16)	8.4(16)	8.4(16)	0	0	0
O3	22.5(48)	22.5(48)	22.5(48)	0	0	0
O4	21.1(34)	21.1(34)	21.1(34)	0	0	0
Li5	1	1	1	0	0	0
δ-$Li_{0.95}V_2O_5$ (Weight fraction 94.1(12))						
Space Group	**Lattice Parameters/Å**					
	a		**b**		**c**	
Cmcm	3.60067(4)		9.90578(14)		11.23687(13)	
	α		β		γ	
	90		90		90	
Atom	**x**	**y**	**z**	**Frac.**		
V1	0	0.20559(18)	0.40200(17)	1		
O2	0	0.04314(58)	0.37447(45)	1		
O3	0	0.24307(68)	0.58971(59)	1		
O4	0	0.28954(91)	0.25	1		
Li5	0.5	0.3994	0.25	0.95		
Atom	**Anisotropic Thermal Factors x 100/Å^2**					
	B11	**B22**	**B33**	**B12**	**B13**	**B23**
V1	4.80(17)	4.80(17)	4.80(17)	0	0	0
O2	1.36(87)	1.36(87)	1.36(87)	0	0	0
O3	1.20(84)	1.20(84)	1.20(84)	0	0	0
O4	3.71(19)	3.71(19)	3.71(19)	0	0	0
Li5	1	1	1	0	0	0

Table 4.49 – Crystallographic data, goodness-of-fit factors and anisotropic thermal parameters obtained by least squares refinement of x-ray diffraction data for $Li_{0.95}V_2O_5$.

The structure of ε'-$Li_{0.95}V_2O_5$ does not differ significantly from lower lithium content phases, although the reversion to Pmmn from the lower symmetry $Pmn2_1$ space group required in ε'-$Li_{0.72}V_2O_5$ is noteworthy. This may be due to the small percentage of the ε'-phase present: the difference between the space groups in refinement of the x-ray data is very small, as the lithium is drowned out by the heavier vanadium atom position, which does not change much between Pmmn and $Pmn2_1$ in this case.

The vanadium environment in ε'-$Li_{0.95}V_2O_5$, described in *table 4.50*, is similar but has a much smaller puckering angle than was observed in the lower lithium content ε'-phases.

Bond Lengths		**Bond Angles**	
Bond	**Bond Length/Å**	**Atoms**	**Angle/°**
V-O2	1.53(1)	O3/O3'-V-O3''	69.87(7)
V-O4	1.82(2)	O3/O3'-V-O4	97.43(8)
V-O3	1.93(1)	O3/O3'-V-O2	108.04(7)
V-O3'	1.93(1)	O3''-V-O2	117.73(3)
V-O3''	1.96(2)	O4-V-O2	106.42(7)
V-V1	3.19(1)	V-O3-V1	110.13(6)
V-V2	3.57(1)	V-O3-V2	134.92(5)
V-V2'	3.34(1)	V-O4-V2'	132.73(5)
Puckering angle		1.42(1)	

Table 4.50 – Vanadium-oxygen bond lengths and angles and vanadium-vanadium distances for ε'-$Li_{0.95}V_2O_5$ x-ray diffraction data.

The structure of δ-$Li_{0.95}V_2O_5$ is similar to that of δ-$Li_{0.72}V_2O_5$ in terms of lattice parameters and atom positions. Bond values given in *table 4.51* are more revealing of structural differences with increased lithium content. The average bond length, 1.88Å is slightly longer than that in the $x = 0.72$ compound, which is consistent with a higher lithium content causing more reduction of vanadium and therefore longer bonds. Vanadium-vanadium distances have changed to be more like those reported for δ-LiV_2O_5, and those observed in ε'-phases with a decrease in the nearest-neighbour distance and an increase in the next-nearest neighbour distance. Puckering angle has also decreased and is now between the value observed for the $x = 0.72$ compound and that of the reported $x = 1$ compound.

Bond Lengths		Bond Angles	
Bond	**Bond Length/Å**	**Atoms**	**Angle/°**
V-O2	1.64(1)	O3/O3'-V-O3''	84.49(5)
V-O4	1.90(1)	O3/O3'-V-O4	85.75(3)
V-O3	1.87(2)	O3/O3'-V-O2	106.02(2)
V-O3'	1.87(1)	O3''-V-O2	110.86(2)
V-O3''	2.14(2)	O4-V-O2	105.08(4)
V-V1	2.98(1)	V-O3-V1	95.51(6)
V-V2	3.60(1)	V-O3-V2	147.95(4)
V-V2'	3.42(1)	V-O4-V2'	128.08(3)
Puckering angle		13.75(1)	

Table 4.51 – Vanadium-oxygen bond lengths and angles and vanadium-vanadium distances for δ-$Li_{0.95}V_2O_5$ x-ray diffraction data.

4.9 General Trends

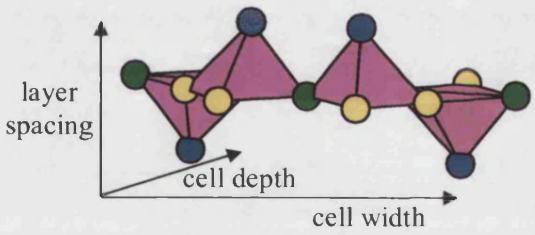

Figure 4.42 – Definition of cell width, cell depth and layer spacing for purposes of discussion here.

To compare the change in the lattice parameters across the series in a meaningful way, it is necessary to allow for the differences in space group. *Table 4.52* gives the room temperature lattice parameters in terms of the cell width, cell depth and layer spacing, which is the height of one layer of VO_5 square pyramids. The changes in cell width and layer spacing are graphically represented for ease of comparison in *figures 4.43-44*. Cell depth remains approximately unchanged across the series and therefore has not been plotted.

X-RAY DATA					
x	χ	Space Group	Cell width	Cell depth	Layer spacing
α-$Li_xV_2O_5$					
0.13	3.46	$Pmn2_1$	11.500907(32)	3.5610144(93)	4.3661695(119)
0.33	4.06	$Pmn2_1$	11.47257(37)	3.56320(6)	4.38606(23)
ε-$Li_xV_2O_5$					
0.33	4.06	Pmmn	11.41518(5)	3.56233(2)	4.47584(2)
0.42	2.83	Pmmn	11.41269(3)	3.56203(1)	4.47989(2)
0.50	4.15	Pmmn	11.40585(3)	3.56048(1)	4.48859(2)
ε'-$Li_xV_2O_5$					
0.55	4.77	Pmmn	11.39777(8)	3.56130(2)	4.50595(3)
0.64	5.40	Pmmn	11.39906(8)	3.56244(2)	4.51144(3)
0.72	5.89	$Pmn2_1$	11.37106(9)	3.56688(2)	4.53240(2)
0.95	9.33	Pmmn	11.37725(26)	3.56585(7)	4.52431(18)
δ-$Li_xV_2O_5$					
0.72	5.89	Cmcm	11.23564(11)	3.60082(3)	4.95308(13)
0.95	9.33	Cmcm	11.23687(13)	3.60067(4)	4.95289(14)
NEUTRON DATA					
α-$Li_xV_2O_5$					
0.13	1.917	$Pmn2_1$	11.50329(5)	3.565455(15)	4.378288(27)
0.33	1.087	$Pmn2_1$	11.4638(19)	3.5687(6)	4.3873(6)
ε-$Li_xV_2O_5$					
0.33	1.087	Pmmn	11.4297(4)	3.56584(18)	4.48085(25)
0.42	5.881	Pmmn	11.42283(8)	3.564933(25)	4.48395(4)
0.50	1.107	Pmmn	11.42498(33)	3.56631(11)	4.48667(22)
ε'-$Li_xV_2O_5$					
0.55	1.462	Pmmn	11.41026(13)	3.56409(6)	4.50454(12)
0.64	5.831	Pmmn	11.41364(17)	3.56401(5)	4.50052(7)
0.72	2.328	$Pmn2_1$	11.39058(15)	3.56727(6)	4.52591(15)
0.95	4.06	Pmmn	11.372(15)	3.564(4)	4.515(5)
δ-$Li_xV_2O_5$					
0.72	2.238	Cmcm	11.23799(10)	3.60213(16)	4.954105(14)
0.95	4.06	Cmcm	11.24967(20)	3.60328(7)	4.9556415(27)

Table 4.52 – Comparison of lattice parameters for $Li_xV_2O_5$ where $0 \leq x \leq 1$.

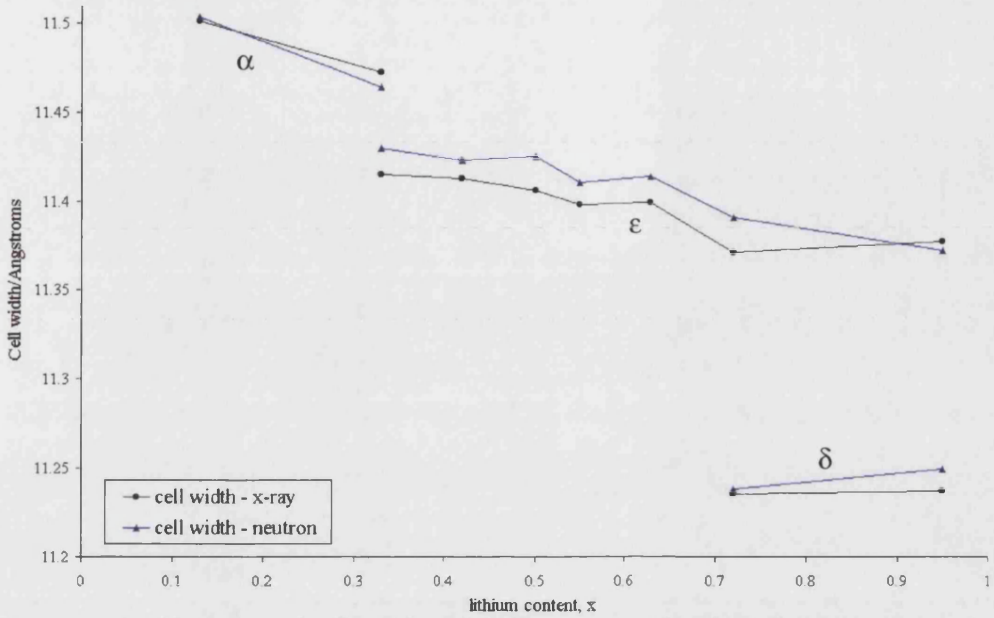

Figure 4.43 – Variation of cell width with lithium content by phase from neutron and x-ray diffraction data.

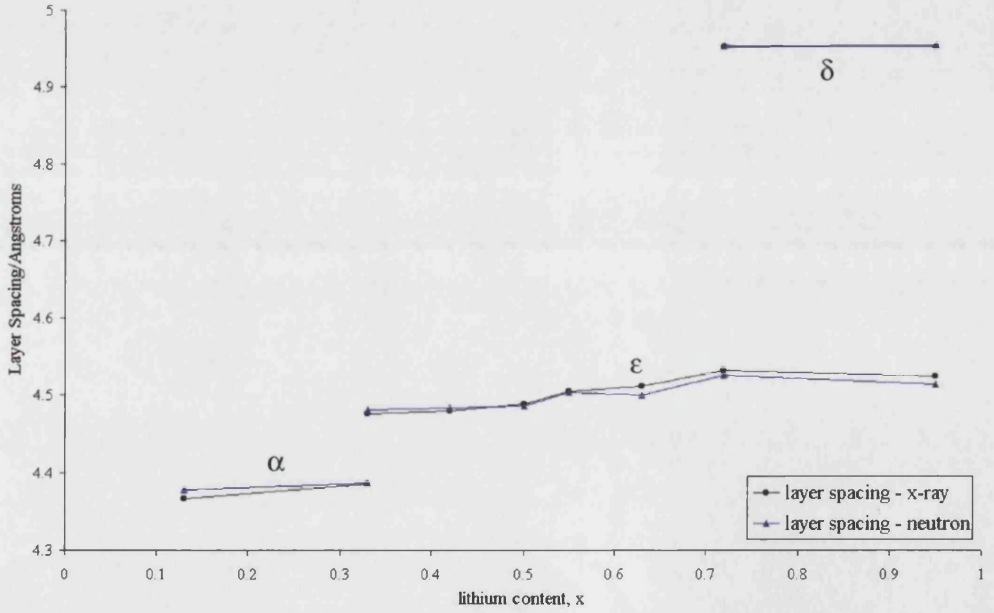

Figure 4.44 – Variation of layer spacing with lithium content by phase from neutron and x-ray diffraction data.

From the graphs it is evident that there is a decrease in cell width and an increase in layer separation as more lithium is intercalated. This supports the conclusion drawn from earlier work that the insertion of more lithium between the layers leads to the increased layer spacing and decreased unit cell width.

Table 4.53 gives the variation with lithium content of average bond length and puckering angles. From these data, depicted in *figure 4.45*, it can be seen that within the α-, ε- and ε'-phases there is an increase in puckering angle as more lithium is intercalated; in other words, distortion in the host lattice layers increases as more guest molecules are introduced.

x	Phase	Average V-O bond length/Å	Puckering angle/°	Average Li-O distance/Å	Coordination number of lithium
0.13	α	1.82	4.05	1.96	4
0.33	α	1.79	10.43	2.00	4
0.33	ε	1.83	2.46	2.49	8
0.42	ε	1.82	2.84	2.47	8
0.50	ε	1.83	2.22	2.48	8
0.55	ε'	1.83	4.80	2.46	8
0.64	ε'	1.83	5.45	2.46	8
0.72	ε'	1.85	8.64	2.41	8
0.95	ε'	1.83	1.42	2.49	8
0.72	δ	1.87	16.65	2.17	6
0.95	δ	1.88	13.75	2.17	6

Table 4.53 – Variation of vanadium-oxygen bond length, puckering angle, lithium-oxygen distance and coordination number with lithium content.

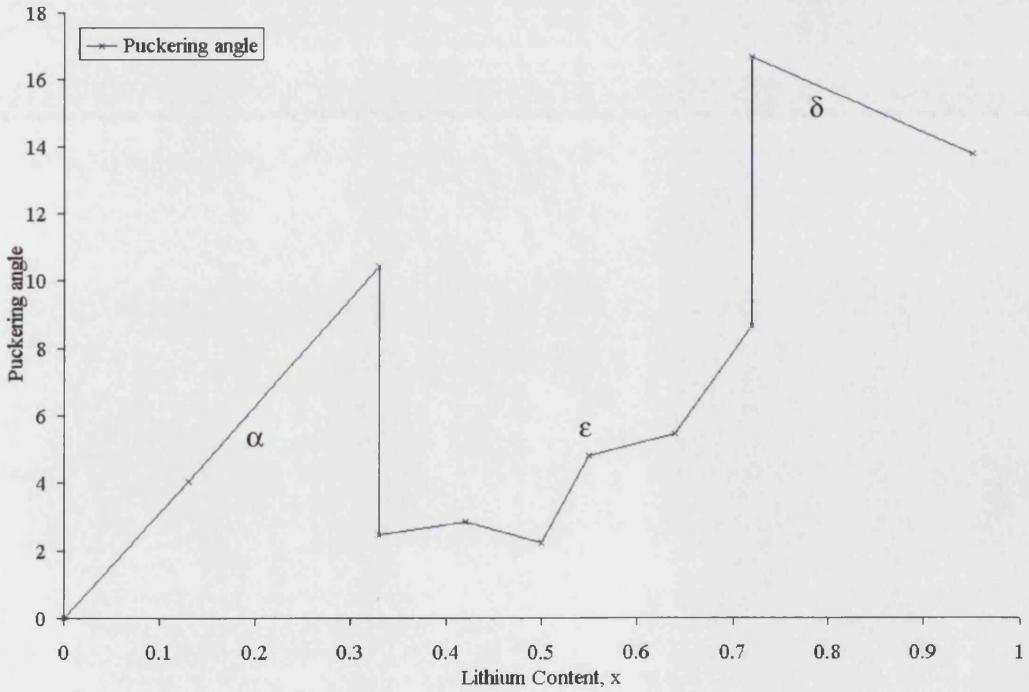

Figure 4.45 – Variation of puckering angle with lithium content.

It is noteworthy that the ε phase is less puckered than the α-phase: this may be accounted for by the change in lithium site from a four-coordinated site to a larger cuboctahedral eight-coordinated site, which, although less stable for lithium, causes less distortion to the host lattice layers. The puckering angle in ε'-phases is comparable to that observed in the α-phases, and increases with lithium content up to the mixed ε'/δ-phase region, when shifting of the V_2O_5 layers along the cell depth axis occurs, forming a new site where lithium can be in its preferred six-coordinated state, with more favourable lithium-oxygen distances.

It seems that when the lithium content is low, it is energetically favourable to have a relatively unstable lithium site within less distorted host lattice layers; as the lithium content increases, there comes a point when the distortions in the host lattice are outweighed by the stability of the lithium site and the structure is thus driven ultimately towards a layer shift enabling more stable coordination of lithium.

1. J. Galy and A. Hardy, *Bulletin de la Societe Chimique de France,* **1964,** 2808-2811 (1964).
2. J. Galy and A. Hardy, *Acta. Crys.,* **19,** 432-435 (1965).
3. J. Galy, A. Hardy, A. Casalot, and M. Pouchard, *Bulletin de Societe Chimie de France,* **1965,** 1056-1065 (1965).
4. J. Galy, *Theses,* (1965, 1966).
5. J. Galy, J. Darriet, A. Casalot, and J.B. Goodenough, *J. Solid State Chem.,* 339-348 (1970).
6. J. Galy, J. Darriet, and P. Hagenmuller, *Rev. Chim. Miner.,* **8,** 509 (1971).
7. J. Galy, *J. Solid State Chem.,* **100,** 229-245 (1992).
8. J. Galy, P. Millet, C. Satto, and P. Sciau, *J. Solid State Chem.,* **136,** 56-62 (1998).
9. J. Galy, C. Satto, P. Sciau, and P. Millet, *J. Solid State Chem.,* **146,** 129-136 (1999).
10. H. Katzke and W. Depmeier, *Phase Transitions,* **59,** 91-104 (1996).
11. H. Katzke, M. Czank, W. Depmeier, and S. van Smaalen, *Journal of Physics-Condensed Matter,* **9,** 6231-6239 (1997).

12. H. Katzke, M. Czank, W. Depmeier, and S. van Smaalen, *Philosophical Magazine B-Physics of Condensed Matter Statistical Mechanics Electronic Optical and Magnetic Properties,* **75,** 757-767 (1997).
13. H. Katzke, K. Kato, and R.E. Dinnebier, *Zeitschrift Fur Kristallographie,* **214,** 392-397 (1999).
14. H. Katzke, K. Kato, and R.E. Dinnebier, *Zeitschrift Fur Kristallographie,* **214,** 398-401 (1999).
15. H. Katzke, *Zeitschrift Fur Kristallographie,* **216,** 278-283 (2001).
16. A. Hardy, J. Galy, A. Casalot, and M. Pouchard, *Bull. Chim. Soc. Fr.,* **4,** 1056 (1965).
17. P. Hagenmuller, J. Galy, M. Pouchard, and A. Casalot, *Mat. Res. Bull.,* **1966,** 45 (1966).
18. J. Galy, J. Darriet, A. Casalot, and J. Goodenough, *J. Solid State Chem.,* **1970,** 339 (1970).
19. D.W. Murphy, P.A. Christian, F.J. DiSalvo, and J.V. Waszczak, *Inorganic Chemistry,* **18,** 2800 (1979).
20. C. Satto, P. Sciau, E. Dooryhee, J. Galy, and P. Millet, *Journal of Solid State Chemistry,* **146,** 103-109 (1999).
21. P. Rozier, *European Journal of Solid State and Inorganic Chemistry,* **33,** 1-13 (1996).
22. V. Shklover, T. Haibach, F. Reid, R. Nesper, and P. Novak, *Journal of Solid State Chemistry,* **123,** 317-323 (1996).
23. G.R. Teller, M.R. Antonio, J.F. Bradzil, and R.K. Grasselli, *J. Solid State Chem.,* **64,** 249-260 (1986).
24. J. Rodriguez-Carvajal, *Fullprof,* 2000: Laboratoire Leon Brillouin.
25. R. Enjalbert and J. Galy, *Acta Crys. Sect. C,* **42,** 1467-1469 (1986).
26. H. Katzke and K. Kato, *Zeitschrift Fur Kristallographie,* **214,** 103-107 (1999).
27. R.J. Cava, A. Santoro, D.W. Murphy, S.M. Zahurak, R.M. Fleming, P. Marsh, and R.S. Roth, *J.Solid State Chem.,* **65,** 63-71 (1986).
28. R.J. Cava, A. Santoro, D.W. Murphy, S.M. Zahurak, R.M. Fleming, P. Marsh, and R.S. Roth, *J. Solid State Chem.,* **65,** 63-71 (1986).

Chapter Five

Magnetic Susceptibility

5.1 Introduction

Lithium vanadates have been widely studied with respect to their structural phases and transitions [1-13]. However, there has been little research into the physical properties, specifically the magnetic properties. Furthermore, research has concentrated on stoichiometric LiV_2O_5, rather than the series $Li_xV_2O_5$. Anderson carried out a study in 1971 on γ-LiV_2O_5 [14], and more recently a large body of work has been published on the comparative magnetic properties of the oxide bronzes MV_2O_5 where M represents an alkali or alkali earth metal [15-22]. Murphy *et al.* published their work on $Li_xV_2O_5$ in 1979 [12], which briefly described the variation of magnetic susceptibility with temperature for α-$Li_{0.1}V_2O_5$, ε-$Li_{0.5}V_2O_5$, δ-LiV_2O_5 and γ-LiV_2O_5. More recently Doumerc *et al.* [23] have published a comparison of the magnetic behaviour of δ-$Li_{0.9}V_2O_5$ and γ-$Li_{0.9}V_2O_5$, also touching on the variation of susceptibility with temperature in α-$Li_{0.03}V_2O_5$ and ε-$Li_{0.55}V_2O_5$. Samples in this study were synthesised by both high temperature and electrochemical routes.

It has been shown that δ-LiV_2O_5 and γ-LiV_2O_5 have double-linear or zigzag chain structures [12, 16, 23]. Both of these arrangements can be regarded as being quasi one-dimensional since each magnetic chain is isolated by nonmagnetic $V^{5+}O_5$ chains. There has been no systematic study into how the variation of lithium content (x) in $Li_xV_2O_5$ affects the magnetic properties, only general comparison between phases. We have, therefore, carried out such a study with investigation into the correlation of magnetic susceptibility with structural aspects. The general formula of this series is usefully written as $Li_xV^{4+}{}_xV^{5+}{}_{(2-x)}O_5$. Long-range magnetic order is more likely to exist in these $3d^1$ systems compared with $4d^1$ and $5d^1$ transition metal oxides, due to increased localisation. Throughout the $A_xV_2O_5$ series there are interesting low dimensional spin configurations with limited insight into the factors that determine them, which will be provided by such a systematic study. The susceptibility curves can be grouped into sections based on their magnetic behaviour. These are discussed separately below and the lithium content refers to that determined from powder neutron diffraction (see §4) in all cases.

The spin-only magnetic moment was calculated using *equation 5.1*:

$$\mu_{SO}^2 = [4s(s+1)]x = 3x$$

$$\mu_{SO} = \sqrt{3x}$$

*Equation 5.1 – μ_{SO} is spin-only magnetic moment; **x** is lithium content.*

5.2 Low lithium content phases, $Li_xV_2O_5$, $0 < x \leq 0.42$

Low lithium content phases exhibit paramagnetic behaviour, as shown in *figure 5.1* for phases $x = 0.13$, 0.33 and 0.42.

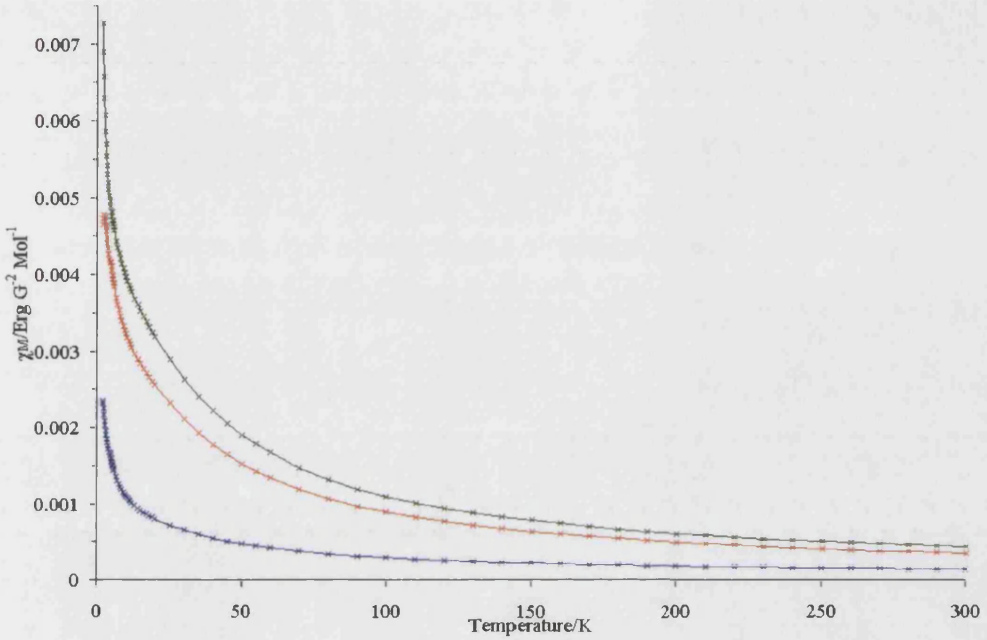

Figure 5.1 – Susceptibility as a function of temperature for paramagnetic low lithium content phases field-cooled data collected at 1T (10000G) over the temperature range 1.8-300K: $Li_{0.13}V_2O_5$ shown in blue, $Li_{0.33}V_2O_5$ in red and $Li_{0.42}V_2O_5$ in green.

Diffraction data collected on $Li_{0.33}V_2O_5$ and $Li_{0.42}V_2O_5$ suggests the occurrence of charge ordering of mixed valence vanadium ions, although from these susceptibility measurements there is no apparent magnetic ordering. This is probably due to the concentration of lithium ions being relatively low, and the spin concentration therefore quite weak.

The magnitude of magnetic susceptibility in this range increases with increasing lithium content as expected. The fit of the inverse magnetic susceptibility to the Curie-Weiss law with a small temperature independent paramagnetic (TIP) contribution, over the temperature range 70-300K, is shown in *figure 5.2*.It shows deviation from the Curie-Weiss law below approximately 50K, which is around three to four times the Weiss constant of between –11 to –16 (given with all other parameters in *table 5.1*). Such behaviour is typical in such systems. What is unusual is the lack of ordering given the relatively high Weiss constants, which is assigned to the randomness of the system. The high Weiss constants clearly show strong antiferromagnetic interaction between the

V^{4+} (d^1) ions. However, their dilute nature does not, presumably, allow long-ranged correlations within the lattice to order them onto specific sites. The V^{4+} ions may also be bound to the Li^+ potential, and therefore be affected by the randomness and mobility of the Li^+ ions.

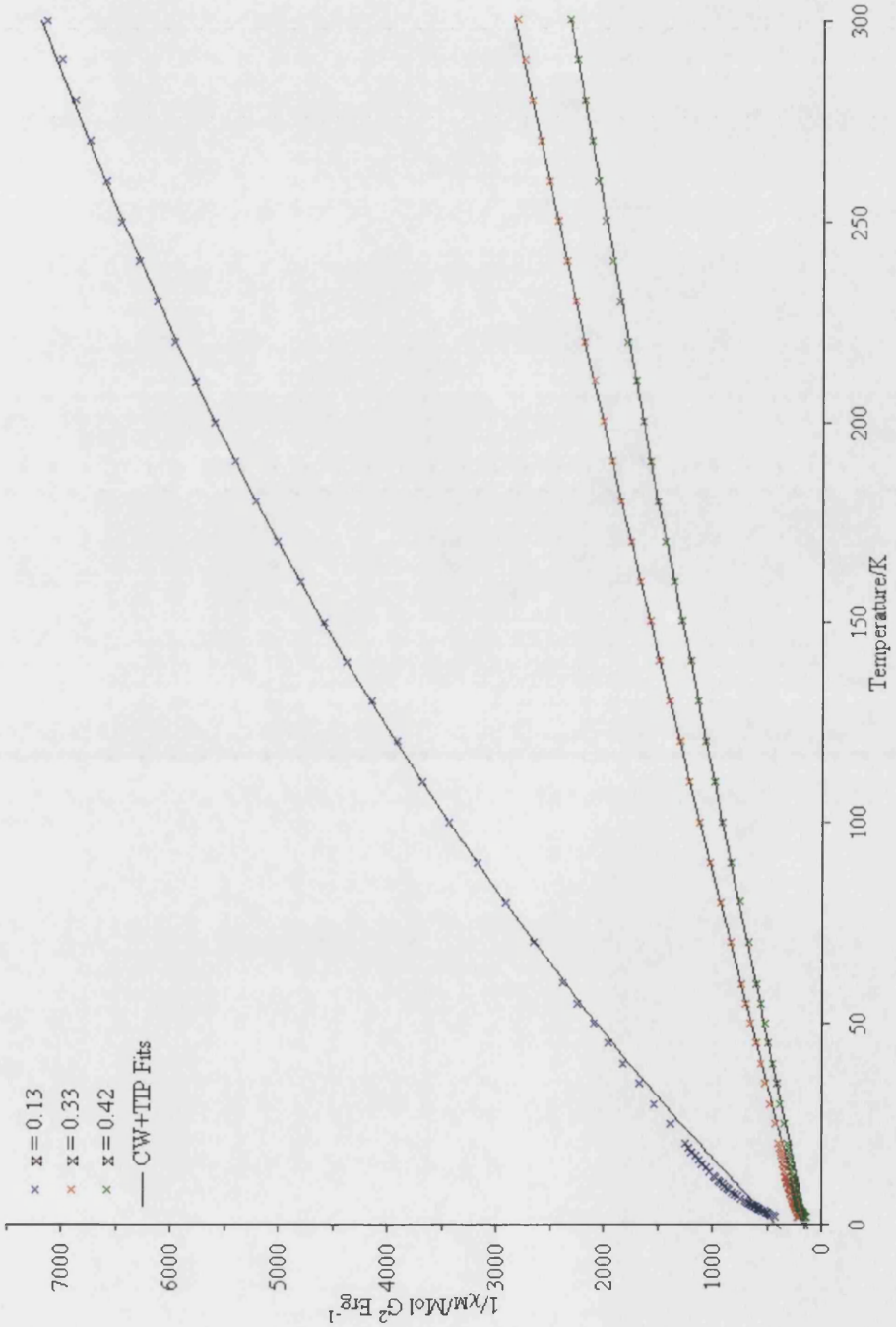

Figure 5.2 – Inverse susceptibility as a function of temperature fitted to the Curie-Weiss law with TIP for $Li_{0.13}V_2O_5$, (blue), $Li_{0.33}V_2O_5$ (red) and $Li_{0.42}V_2O_5$ (green). Fits shown in black.

Lithium content x	Curie constant C	Weiss constant ϑ	TIP term $\alpha/10^5$	Spin-only moment μ_{calc}	Experimental moment μ_o
0.13	0.2628(32)	-11.23(84)	5.42(10)	0.62	0.46
0.33	0.9822(35)	-15.43(27)	4.01(11)	0.99	0.89
0.42	1.221(8)	-16.00(51)	4.30(9)	1.12	0.99

Table 5.1 – Results of Curie-Weiss with T.I.P. fit for $0 < x \leq 0.42$ over the temperature range 70-300K. The lithium content in column one is that determined from neutron diffraction data (see §4).

Murphy *et al.* reported a Weiss constant of approximately -17K for α-$Li_{0.1}V_2O_5$ [12], which is in the region of the values obtained here. There is good agreement between the theoretical spin-only magnetic moment, μ_{calc}, determined using the lithium composition obtained from the neutron diffraction data (see §4), and the experimental magnetic moment, μ_o, calculated from the magnetic susceptibility data, demonstrating the direct reduction of the vanadium ions with lithium intercalation.

5.3 Medium Lithium content phases, $Li_xV_2O_5$, $0.42 < x \leq 0.72$

The value of $x = 0.42$ is an interesting threshold leading to more complex magnetic behaviour. The magnetic susceptibility can be fitted to the Curie-Weiss law with a TIP term at high temperature, followed by a distinct maximum in magnetic susceptibility between approximately 20-35K. The maxima vary in breadth and temperature, as exemplified by the susceptibility data shown in *figure 5.3*. The susceptibility is indicative of a low-dimensional system and various models have been investigated. At very low temperature, around 10-15K, there is a second turning point in the curve; this increase in susceptibility at low temperature has been observed in most low dimensional systems and accepted as a "Curie tail", caused by the presence of paramagnetic impurities or breaks in the ordered chains of spins [16, 23].

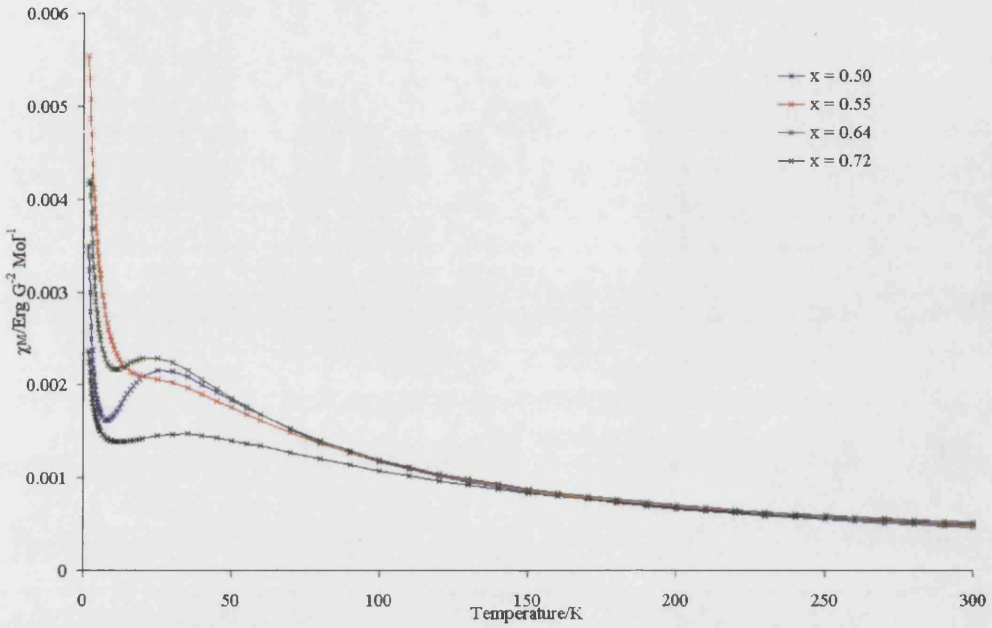

Figure 5.3 – Susceptibility as a function of temperature for $Li_xV_2O_5$ where $0.42 < x \leq 0.72$ medium lithium content phases. Field-cooled data collected at 1T (10000G) over the temperature range 1.8-300K: $Li_{0.50}V_2O_5$ shown in blue, $Li_{0.55}V_2O_5$ in red, $Li_{0.64}V_2O_5$ in green and $Li_{0.72}V_2O_5$ in black.

Applying the Curie-Weiss law with a TIP contribution to these medium lithium content phases yields the fits shown in *figure 5.4*. The marked deviation from Curie-Weiss behaviour occurs below approximately 50K; that is the same temperature as the dilute systems, despite large increases in the Weiss constant. Fit parameters are given in *table 5.2*.

Lithium content x	Curie constant C	Weiss constant ϑ	TIP term $\alpha/10^5$	Spin-only moment μ_{calc}	Exper'tal moment μ_o	T_{max}/K
0.50	1.558(6)	-32.13(34)	0.58(6)	1.22	1.12	25.0
0.55	1.693(4)	-42.91(22)	0.60(11)	1.28	1.16	27.5
0.64	1.455(3)	-29.32(16)	7.4(8)	1.39	1.08	22.5
0.72	2.384(15)	-102.29(75)	10.2(3)	1.47	1.38	35.0

Table 5.2 – Results of Curie-Weiss with T.I.P. fit for $0.42 < x \leq 0.72$ over the temperature range 70-300K.

The variation in magnetic behaviour in this region of lithium content is such that each compound will be discussed individually, but with the exception of $Li_{0.64}V_2O_5$, the increase in magnitude of the Weiss constant with lithium content that was noted for the low lithium content phases continues here, although the x = 0.64 is somewhat

anomalous to the other compositions. Negative Weiss constants and maxima in susceptibility are indicative of antiferromagnetic exchange; if one-dimensional in nature due to the formation of chains, this exchange will be consistent with the Bonner-Fisher theory and no long-range magnetic order will exist at low temperature [12].

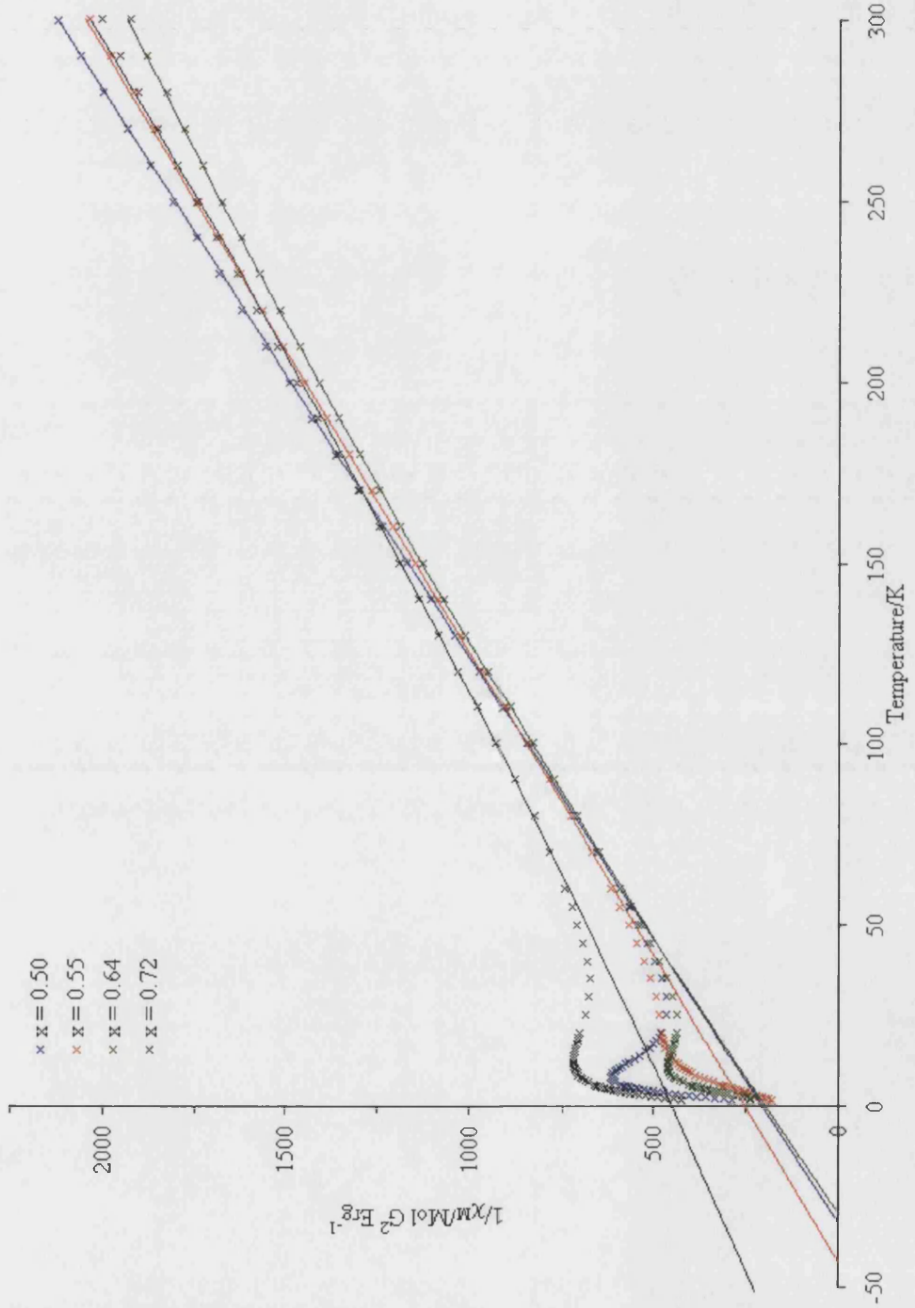

Figure 5.4 – Inverse susceptibility as a function of temperature, fitted to the Curie-Weiss law with TIP for $Li_{0.50}V_2O_5$, (blue), $Li_{0.55}V_2O_5$ (red), $Li_{0.64}V_2O_5$ (green) and $Li_{0.72}V_2O_5$ (black). Fits are shown in the same colour as data.

The question remains as to the origin of the maxima in the susceptibility for all compositions. It is obvious from the low temperature neutron diffraction that no long-range antiferromagnetic state is achieved. If the V^{4+} ions and, therefore, the spins in the system are randomly distributed the maxima could represent the freezing of the moments into a spin glass state, which leads to a significant difference between the zero field cooled (ZFC) and field cooled (FC) measurements. However, *figure 5.5* does not show such behaviour and thus the magnetic structure is more complex.

5.3.1 ε-$Li_{0.50}V_2O_5$

Given the previous background of the $A_xV_2O_5$ system (see §1), it is expected that charge ordering of vanadium ions is causing low-dimensional correlations at low temperature, which would be associated with the presence of a charge-ordered "supercell" below the characteristic temperature, 25K.

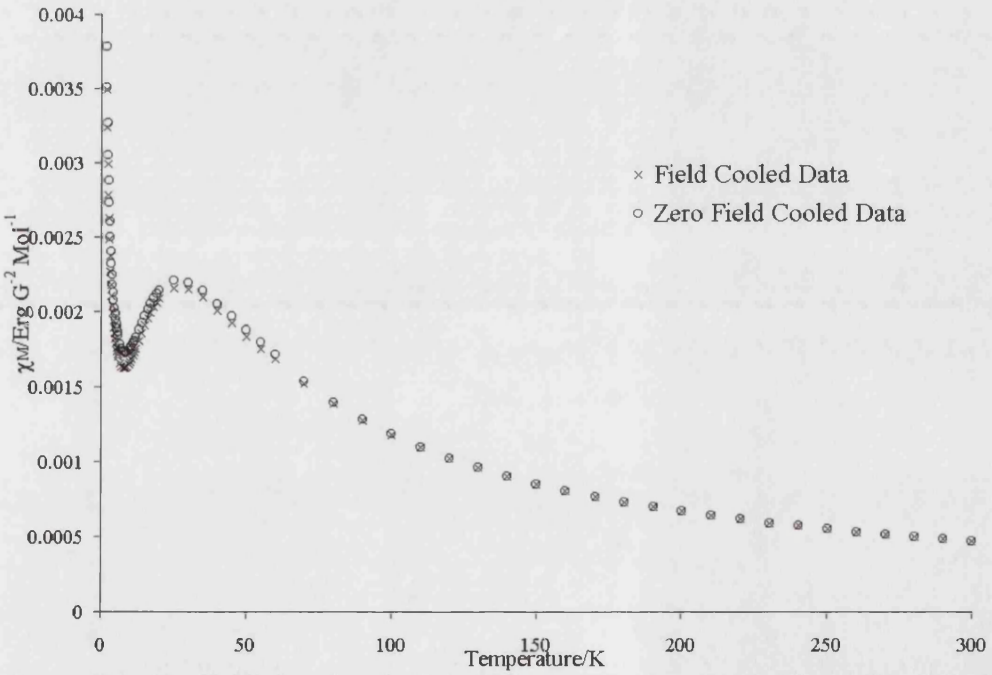

Figure 5.5 – Susceptibility data for $Li_{0.50}V_2O_5$ measured in zero field cooled and field cooled conditions.

Figure 5.6 shows two possible arrangements consistent with the $x = 0.5$ composition, that is a $d^1d^1d^0d^0d^0d^0d^0d^0d^1$... (*a*) or a $d^1d^0d^0d^0d^1$... (*b*) configuration. This would possibly offer an explanation for the maxima seen in the susceptibility, which cannot be accounted for in a random distribution scheme.

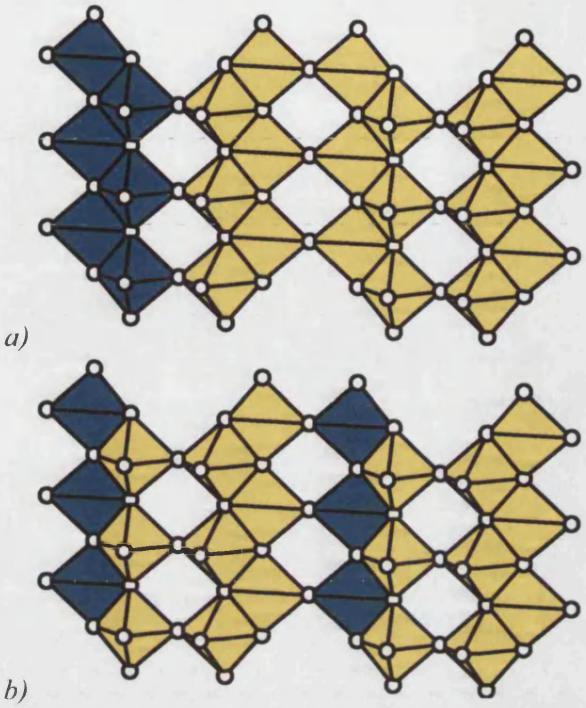

Figure 5.6 – Potential supercells for $Li_{0.50}V_2O_5$ with rational ratio of V^{4+}:V^{5+} of 1:3, $V^{4+}O_5$ square pyramids shown in blue, $V^{5+}O_5$ square pyramids shown in yellow. a) zigzag chain structure, b) double linear chain structure

High-resolution x-ray diffraction data (§4) has shown the presence of extra, weak reflections that increase in intensity as the sample is cooled. These were indexed using an incommensurately modulated cell. As these reflections are not seen in the neutron data, they are likely to originate from an ordering of vanadium producing a larger cell. It is, however, unexpected that these reflections index to an incommensurate cell for the stoichiometric $x = 0.5$ composition. One can conclude from this that the two supercells given in *figure 5.6* do not represent significantly more stable structures. The fact that the system orders in an incommensurate structure results from an as yet undetermined, more complex arrangement of V^{4+} ions. Though, as with well-characterised compositions such as γ-LiV_2O_5 and NaV_2O_5, the susceptibility still suggests a V^{4+} correlation down the *b*-axis, the nature of which can be investigated from fitting low-dimensional models to the susceptibility. The Bonner-Fisher model describes the susceptibility as a function of temperature for a uniform s = ½ linear Heisenberg chain. *Figure 5.7* shows the fit to this model, along with others (described in §2), which clearly describes the behaviour well.

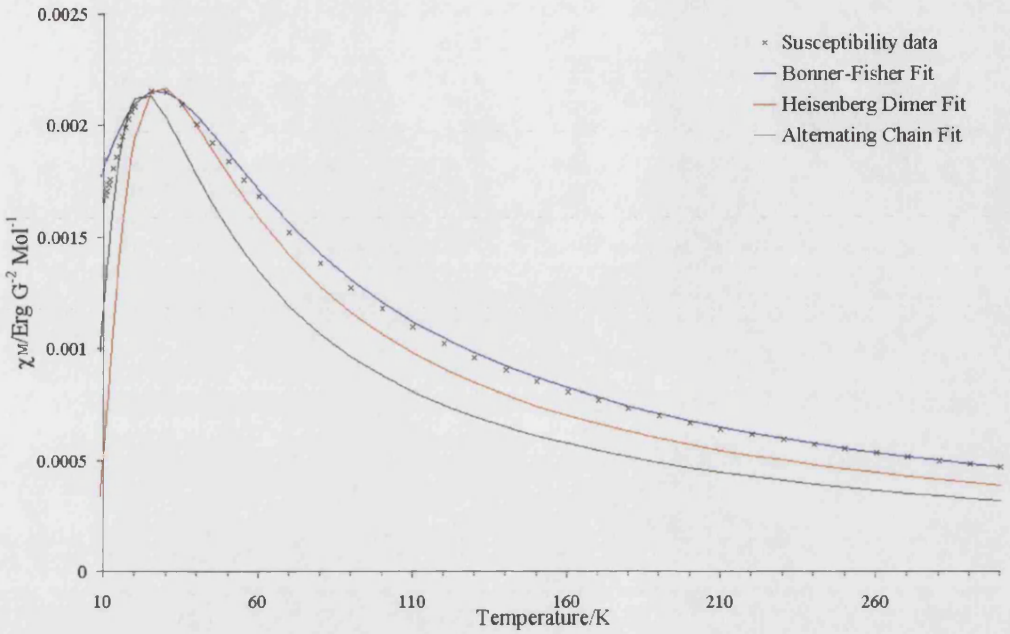

Figure 5.7 – Susceptibility as a function of temperature for $Li_{0.50}V_2O_5$ fitted to low dimensional models: Bonner-Fisher model (blue), Heisenberg Dimer model (red) and Alternating chain model (green).

The Heisenberg dimer and alternating chain models do not correspond to the experimentally determined susceptibility. The preferred Bonner-Fisher model implies the existence of one-dimensional linear chains of V^{4+} ions rather than dimerised chains in the system, consistent with the work of Ueda *et al.* on γ-LiV_2O_5 [16].

Table 5.3 compares the values of gyromagnetic ratio and exchange energy calculated from the data using different low dimensional models.

Variable	Bonner-Fisher model
Range of fit/K	**10-50K**
g	1.283(2)
J/k/JK^{-1}	-21.01(10)

Table 5.3 – Variables from fit of Bonner-Fisher model to susceptibility data for $Li_{0.50}V_2O_5$.

5.3.2 ε'-$Li_{0.55}V_2O_5$

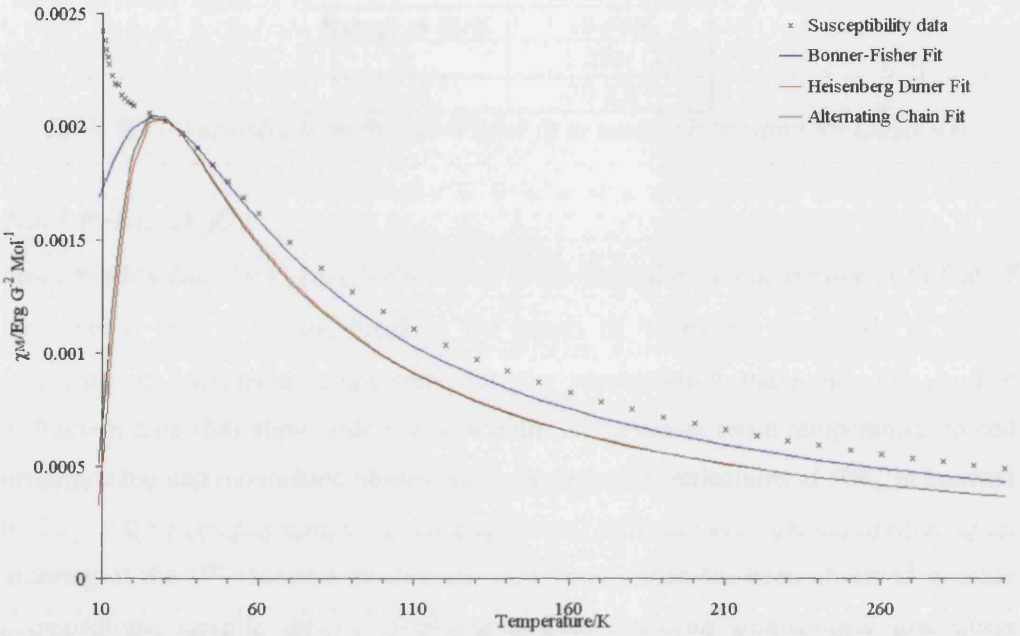

Figure 5.8 – Susceptibility as a function of temperature for $Li_{0.55}V_2O_5$ fitted to low dimensional models: Bonner-Fisher model (blue), Heisenberg Dimer model (red) and Alternating chain model (green).

While $Li_{0.50}V_2O_5$ shows a distinct maximum in magnetic susceptibility, the maximum in $Li_{0.55}V_2O_5$ data is broader, as shown in *figure 5.8*. ε'-$Li_{0.55}V_2O_5$ undergoes a continuous phase transition from orthorhombic to monoclinic on cooling [16], and has a more disordered layered structure than ε-$Li_{0.50}V_2O_5$. Diffraction data showed no additional peaks indicative of charge ordering as low as 50K. It is therefore envisaged that the degree of disorder afforded by the $x = 0.55$ composition is sufficient to hinder charge ordering, at least at high temperature (above 50K), in a long-ranged fashion accessible to diffraction techniques, thus an average environment is observed. Furthermore, this causes a similarly disordered range of coupling schemes, which combine to produce such a broad feature.

Since the maximum in susceptibility is at a lower temperature than diffraction data were collected, it is possible that there may be some charge ordering occurring below 50K, as was found for ε'-$Li_{0.64}V_2O_5$. *Figure 5.8* demonstrates the poor agreement in the fits to low dimensional models.

Variable	Bonner-Fisher model
Range of fit/K	**10-50K**
g	1.224(1)
J/k/JK^{-1}	-20.23(7)

Table 5.4 – Variables from Bonner-Fisher fit to susceptibility data for $Li_{0.55}V_2O_5$.

5.3.3 ε'-$Li_{0.64}V_2O_5$

Susceptibility data for ε'-$Li_{0.64}V_2O_5$ shows some anomalies in comparison with that of the other ε- and ε'-phases, breaking the trends of increasing magnitude of Weiss constant and increasing temperature for the susceptibility maximum (T_{max}). The diffraction data (§4) show ordering of lithium ions even at room temperature, mixed orthorhombic and monoclinic phases and no superlattice reflections at 50K, in contrast to the $x = 0.50$ composition, with some additional reflections at 30K demonstrating an ordering of the V^{4+} ions at a much lower temperature than has been observed in other compositions. Despite the $x = 0.64$ composition have an anomalously low Curie constant it is one of the systems to demonstrate a relatively well defined peak in the susceptibility at approximately 22.5K, which can be well fitted to the Bonner-Fisher model, as shown in *figure 5.9* and described in *table 5.5*, implying a linear chain model.

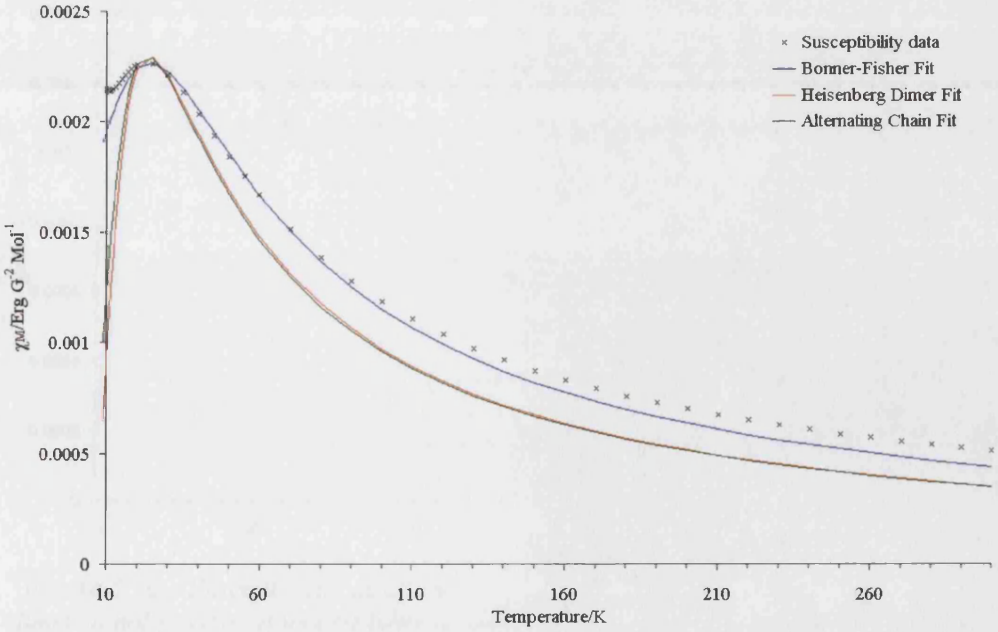

Figure 5.9 – Susceptibility as a function of temperature for $Li_{0.64}V_2O_5$ fitted to low dimensional models: Bonner-Fisher model (blue), Heisenberg Dimer model (red) and Alternating chain model (green).

Variable	Bonner-Fisher model
Range of fit/K	**10-50K**
g	1.233(1)
$J/k/JK^{-1}$	-18.8(7)

Table 5.5 – Comparison of variables from different low dimensional fits to data for $Li_{0.64}V_2O_5$.

5.3.4 ε'/δ-$Li_{0.72}V_2O_5$

Susceptibility data for $Li_{0.72}V_2O_5$ are similar to those of lower lithium content ε- and ε'-phases (x = 0.50, 0.55 and 0.64): the presence of a small amount of δ-phase does not have an immediately obvious effect on the magnetic behaviour. The increase in lithium content to x = 0.72 resumes the general trend of increasing Weiss constant and therefore enhanced antiferromagnetic interactions, with a corresponding increase in the maximum of the susceptibility (T_{max} = 35K). *Figure 5.10* shows the susceptibility data fitted to low dimensional models; the Bonner-Fisher model remains the best at low temperature (10-50K). *Table 5.6* gives the parameters obtained from that model.

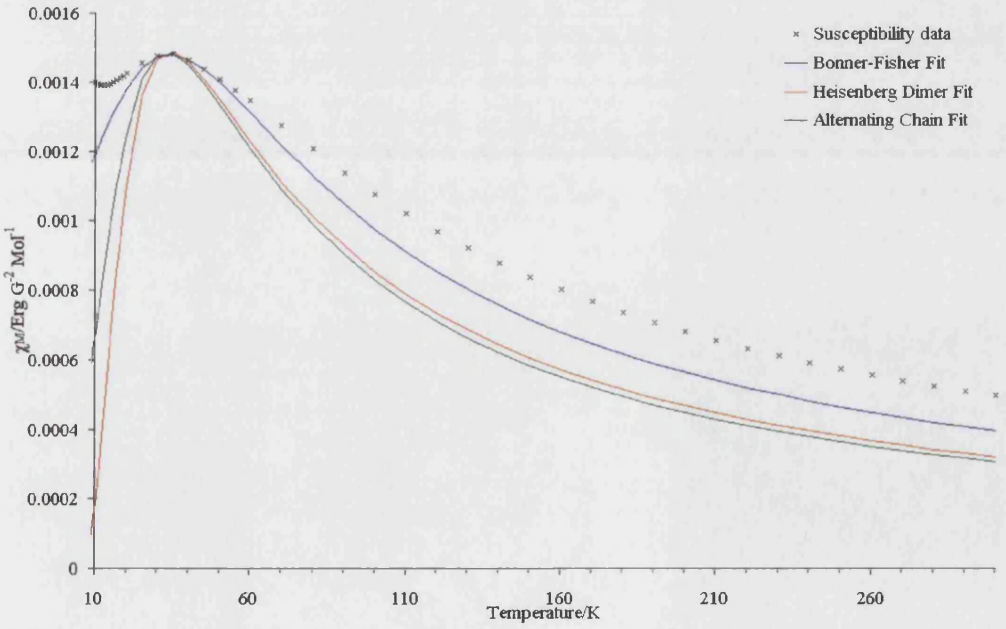

Figure 5.10 – Susceptibility as a function of temperature for $Li_{0.72}V_2O_5$ fitted to low dimensional models: Bonner-Fisher model (blue), Heisenberg Dimer model (red) and Alternating chain model (green).

Variable	Bonner-Fisher model
Range of fit/K	**10-50K**
g	1.186(2)
J/k/JK^{-1}	-26.20(13)

Table 5.6 – Variables from Bonner-Fisher model fit to susceptibility data for $Li_{0.72}V_2O_5$.

5.4 High lithium content phases, $Li_xV_2O_5$, $0.72 < x \leq 1$

The change in susceptibility with increased lithium content in this region can be seen in *figure 5.11*; δ-$Li_{0.95}V_2O_5$ appears to be almost temperature independent, although there is still an increased susceptibility below approximately 15K, and a very broad maximum.

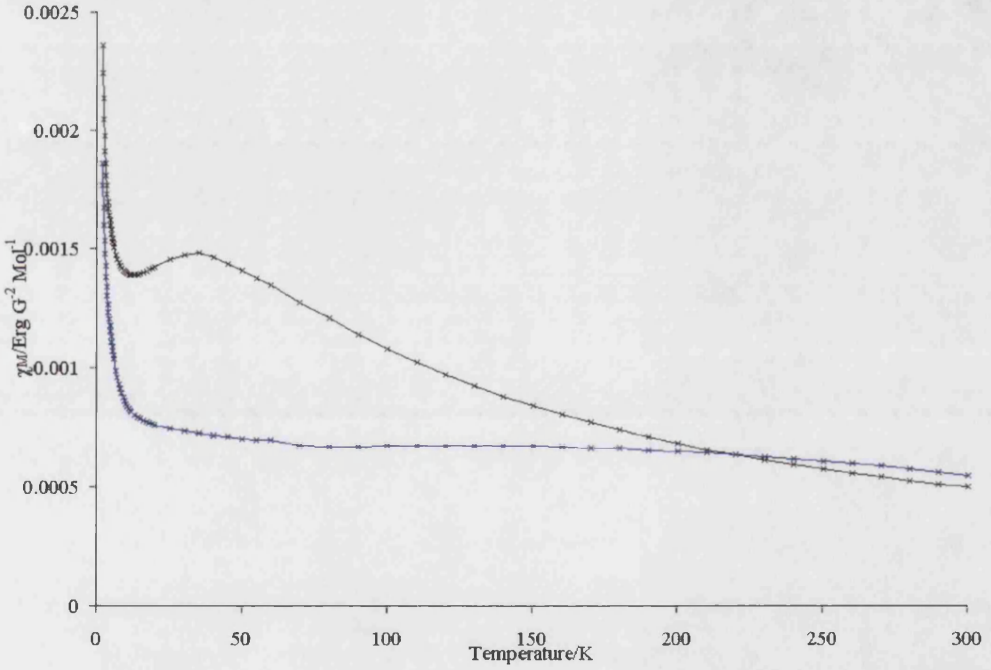

Figure 5.11 – Susceptibility as a function of temperature for $Li_xV_2O_5$ where $0.72 < x \leq 1.0$ high lithium content phases. Field-cooled data collected at 1T (10000G) over the temperature range 1.8-300K: $Li_{0.72}V_2O_5$ shown in black and $Li_{0.95}V_2O_5$ in blue.

The susceptibility is clearly not consistent with any of the models described previously and its temperature independent nature suggests that it is moving into a delocalised regime.

5.5 General Trends

The magnetic susceptibility of the series shows a gradual development of the magnetic behaviour alongside an anomaly at $x = 0.64$. Throughout this series, except for $x = 0.64$, there remains good agreement between predicted and observed magnetic moments, and Curie constants obtained experimentally give values of lithium content (x_{mag}) that agree well with those obtained from diffraction data (x_{dat}), as shown in *table 5.7*.

x_{diff}	μ_{calc}	μ_o	Predicted Curie constant, C	Experimental Curie constant, C	x_{mag}
0.13(3)	0.62	0.46	0.3460	0.2628(32)	0.100(1)
0.33(2)	0.99	0.89	0.9610	0.9822(35)	0.336(1)
0.42(2)	1.12	0.99	1.2705	1.221(8)	0.406(3)
0.50(1)	1.22	1.12	1.5625	1.558(6)	0.499(2)
0.55(2)	1.28	1.16	1.7530	1.693(4)	0.534(2)
0.64(1)	1.39	1.08	2.1120	1.455(3)	0.471(1)
0.72(1)	1.47	1.38	2.4480	2.384(15)	0.705(6)
0.95(3)	1.69	1.66	3.5030	3.447(12)	0.939(5)

Table 5.7 – Predicted and observed values of magnetic moments and Curie constants and extrapolated lithium content.

Where $x > 0.42$ the lithium content, and therefore number of V^{4+} ions, is high enough to support low dimensional magnetic correlation, where the single chain Bonner-Fisher model is preferred. There is a gradual decrease in gyromagnetic ratio as the lithium content is increased. Although the gyromagnetic ratio remains small, below the value commonly used as an approximation ($g \approx 2$), this is consistent with previous work: Isobe *et al.* found γ-LiV_2O_5 to have $g = 1.8$ [16].

x	Bonner-Fisher Model		
	g	J/k/JK^{-1}	Range of fit/K
0.50	1.283(2)	-21.01(10)	10-50
0.55	1.224(1)	-20.23(7)	10-50
0.64	1.233(1)	-18.80(7)	10-50
0.72	1.186(2)	-26.20(13)	10-50

Table 5.8 – Variation of constants for Bonner-Fisher model with lithium content

There is an increase in the Weiss constant and therefore the degree of antiferromagnetic interactions with x. The feature at approximately 25K was clearly

better defined at particular compositions, these include $x = 0.50$ and $x = 0.64$, the latter being very close to $x = 0.67$; that is a 1:2 ratio of V^{4+}:V^{5+} ions. The former, at a ratio of 1:3, can also be thought of as a "magic" number, where the association of other factors with disorder causing the broadening of this feature were not observed. This is heavily linked with the observation of V^{4+} ion ordering, facilitating a more ordered exchange scheme. Previous work carried out on the gamma phase γ-LiV_2O_5 has asserted there to be charge ordering within that structure, [13] and within analogous structures such as α'-NaV_2O_5. Charge ordering is implicit in the occurrence of well-defined features in the magnetic susceptibility of these compounds.

1. J. Galy and A. Hardy, *Acta. Crys.*, **19,** 432-435 (1965).
2. J. Galy, A. Hardy, A. Casalot, and M. Pouchard, *Bulletin de Societe Chimie de France,* **1965,** 1056-1065 (1965).
3. J. Galy, *Theses,* (1965, 1966).
4. J. Galy, J. Darriet, and P. Hagenmuller, *Rev. Chim. Miner.*, **8,** 509 (1971).
5. J. Galy, *J. Solid State Chem.*, **100,** 229-245 (1992).
6. J. Galy, P. Millet, C. Satto, and P. Sciau, *J. Solid State Chem.*, **136,** 56-62 (1998).
7. J. Galy, C. Satto, P. Sciau, and P. Millet, *J. Solid State Chem.*, **146,** 129-136 (1999).
8. R.J. Cava, A. Santoro, D.W. Murphy, S.M. Zahurak, R.M. Fleming, P. Marsh, and R.S. Roth, *J. Solid State Chem.*, **65,** 63-71 (1986).
9. R.J. Cava, A. Santoro, D.W. Murphy, S.M. Zahurak, R.M. Fleming, P. Marsh, and R.S. Roth, *J. Solid State Chem.*, **16,** 393 (1976).
10. A. Hardy, J. Galy, A. Casalot, and M. Pouchard, *Bull. Chim. Soc. Fr.*, **4,** 1056 (1965).
11. D.W. Murphy and S.M. Zahurak, *Inorg. Synth.*, **24,** 200 (1986).
12. D.W. Murphy, P.A. Christian, F.J. DiSalvo, and J.V. Waszczak, *Inorganic Chemistry,* **18,** 2800 (1979).
13. Y. Ueda, *Chem. Mater.*, **10,** 2653-2664 (1998).
14. D.N. Anderson and R.D. Willett, *Acta Crystallographica B (24,1968-38,1982),* 1477-1478 (1971).
15. R. Valenti and T. Saha-Dasgupta, *Phys. Rev. B,* **65,** 144445-1 (2002).

16. M. Isobe and Y. Ueda, *J. Phys. Soc. Jpn.*, **65**, 3142-3145 (1996).

17. M. Isobe, Y. Ueda, K. Yakushi, M.J. Konstantinovic, J. Dong, M.E. Ziaei, B.P. Clayman, and J.C. Irwin, *Phys. Rev. B*, **63**, 121102-1 (2001).

18. M. Isobe, Y. Ueda, K. Takizawa, and T. Goto, *J. Phys. Soc. Jpn.*, **67**, 755-758 (1997).

19. H. Yamada and Y. Ueda, *J. Phys. Soc. Jpn.*, **69**, 1437-1442 (1999).

20. Z.V. Popovic, V. Stergiou, Y.S. Raptis, M.J. Konstantinovic, M. Isobe, Y. Ueda, and V.V. Moshchalkov, *J. Phys. Condens. Matter*, **14**, L583-L589 (2002).

21. H. Iwase, M. Isobe, Y. Ueda, and H. Yasuoka, *J. Phys. Soc. Jpn.*, **65**, 2397-2400 (1996).

22. H. Sawa, E. Ninomiya, T. Ohama, H. Nakao, K. Ohwada, Y. Murakami, Y. Fujii, Y. Noda, M. Isobe, and Y. Ueda, *J. Phys. Soc. Jpn.*, **71**, 385-388 (2002).

23. J.P. Doumerc, J.M. Cocciantelli, J.C. Grenier, M. Pouchard, and P. Hagenmuller, *Zeitschrift Fur Anorganische Und Allgemeine Chemie*, **619**, 748-752 (1993).

Chapter Six

Muon Spin Research

6.1 Introduction

Muon spin research techniques have been applied to probe the magnetic behaviour of a wide range of systems [1] including the frustrated spinels LiV_2O_4 and ZnV_2O_4 [2], Ruddlesden-Popper phases exhibiting colossal magnetoresistance, for example $Sr_2RMn_2O_7$ (R = Pr, Nd, Sm, Eu, Gd, Tb, Dy, Ho) [3], organic spin ladder systems like $[(DT\text{-}TTF)_2][Au(mnt)_2]$ [3] and inorganic spin ladders such as the $Sr_{n-1}Cu_{n+1}O_{2n}$ series [4]. μSR has been used to investigate many of the charge ordered compounds that were discussed in chapter one, in order to understand further the unusual magnetic behaviour observed. For instance, μSR studies of the "stripe-ordered" series' $La_{2-x}Sr_xNiO_{4+\delta}$ and $La_{2-x}Sr_xCu_{1-y}Zn_yO_4$ [5-9], revealed composition-dependence of the magnetic transition temperature below which magnetic order is observed in the former series [10], while in the latter series stabilisation of copper spin fluctuations by a small amount of zinc to form a static ordered state, compared with the destruction of magnetic correlations by a larger zinc doping, was established [6].

Of particular interest is the work of Green *et al.* in establishing the occurrence of long-range magnetic order in the dilute spin system $Nb_{12}O_{29}$ [11]. This mixed valence Nb^{5+}/Nb^{4+}, d^0/d^1 compound contains two unpaired electrons per formula unit, one of which contributes to metallic conduction in the system: although the most likely magnetic state for a localized electron randomly embedded in a sea of conduction electrons is the formation of a spin glass state, in this case charge ordering allows the formation of well-separated chains of Nb^{4+}, d^1 ions, in which long-range magnetic order of an antiferromagnetic nature occurs.

Despite the successful use of μSR to elucidate magnetic behaviour in low-dimensional systems [11-13], this technique has not previously been used to probe the magnetic properties of vanadium oxide bronzes. We have carried out zero-field (ZF) and longitudinal field (LF) measurements on $Li_xV_2O_5$ compounds with x = 0.50, 0.55, 0.64 and 0.72 in order to obtain information about local magnetic interactions (ZF) and to decouple the static and dynamic local magnetic fields to investigate associated spin-freezing mechanisms (LF).

6.2 $Li_{0.50}V_2O_5$

Zero-field μSR spectra do not contain any oscillations that would support the occurrence of long-range antiferromagnetic order in $Li_{0.50}V_2O_5$. *Figure 6.1* shows zero-field muon data at a range of temperatures fitted with a product of LF-Keren [14] and Lorentzian functions [13], reflecting muon depolarisation due to coexisting nuclear dipolar fields, from V^{5+} ions and electronic spin-lattice relaxation due to V^{4+}, which is likely to be a realistic representation of the physical behaviour occurring in these dilute spin systems.

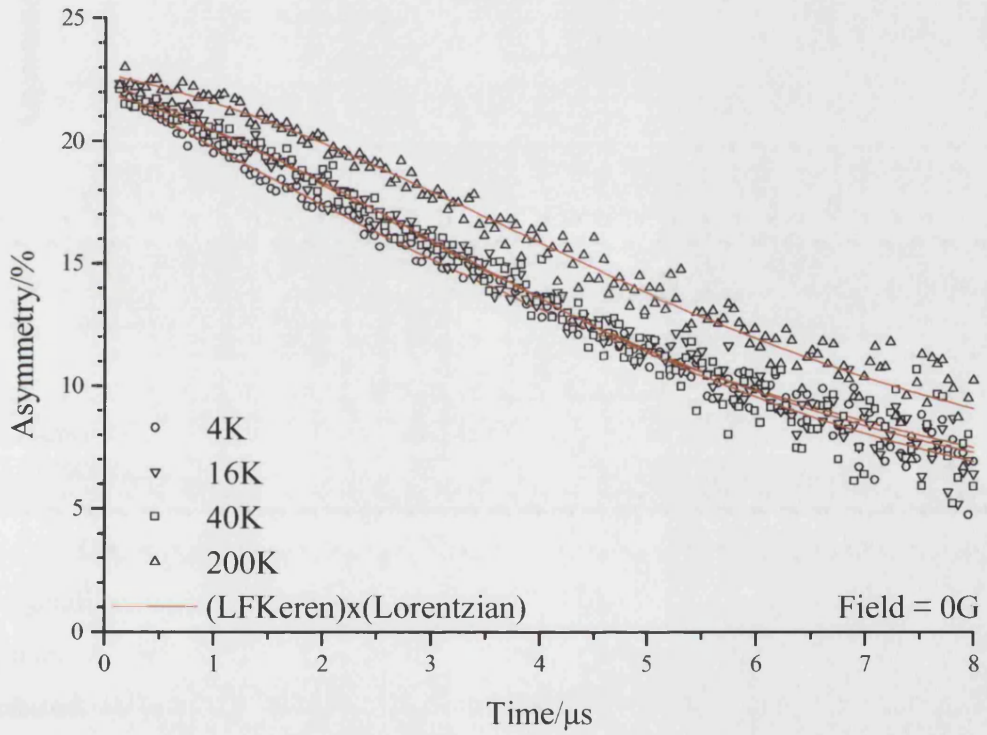

Figure 6.1 – Time-evolution of muon depolarisation in $Li_{0.50}V_2O_5$, at zero-field, fitted with the product of LF-Keren and Lorentzian functions.

In longitudinal field experiments rapid quenching of muon depolarisation was observed; an applied field as low as 25G gives a much smaller asymmetry loss as time progresses. Increase of the applied magnetic field as high as 1000G gives increased quenching, but 25G is sufficient to quench most of the muon depolarisation, as shown in *figure 6.2*. The application of a longitudinal magnetic field has a large effect on the muon depolarisation if the dynamics are weak, and is much less effective when the dynamics are fast; thus the significant effect of a relatively small longitudinal field here

is indicative of weak dynamics: in other words, the internal field experienced by the muon has a static character [1].

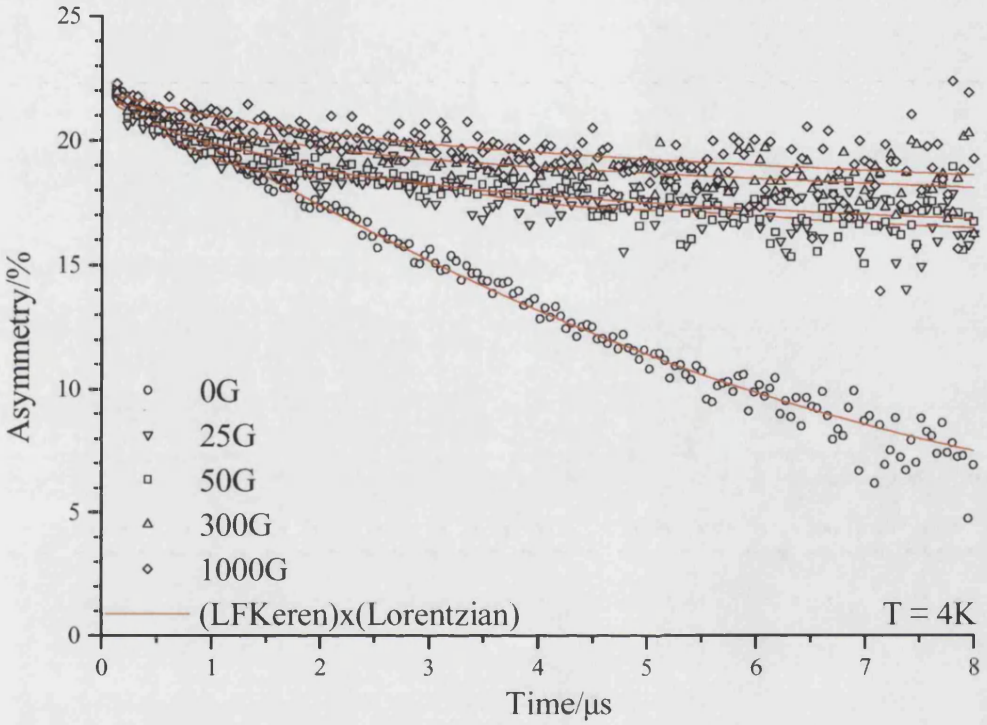

Figure 6.2 – Time-evolution of muon depolarisation in $Li_{0.50}V_2O_5$, with variation in longitudinal field, fitted with the product of LF-Keren and Lorentzian functions.

The nuclear relaxation rate, δ, decreases rapidly with the application of a small longitudinal field, while the electronic relaxation rate, λ, increases at the expense of the former. A similar effect is observed at zero-field: δ decreases as the temperature is reduced, while λ is enhanced (*figure 6.3*). The maximum observed around 25 K in the susceptibility data of $Li_{0.50}V_2O_5$ correlates well with the observed zero-field and longitudinal field μSR changes in the relaxation rates, λ and δ, supporting the postulation of a quasi-static character for the observed magnetic ordering transition.

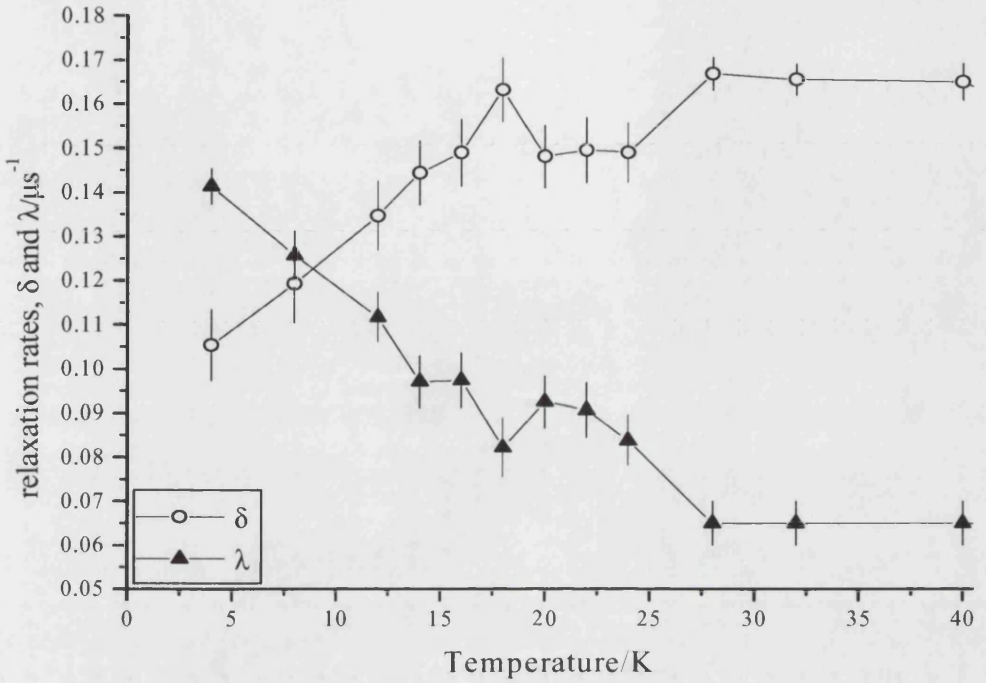

Figure 6.3 – Variation of relaxation rates with temperature in zero-field experiments for $Li_{0.50}V_2O_5$. The lines connecting points provide a guide for the eye.

6.3 $Li_{0.55}V_2O_5$

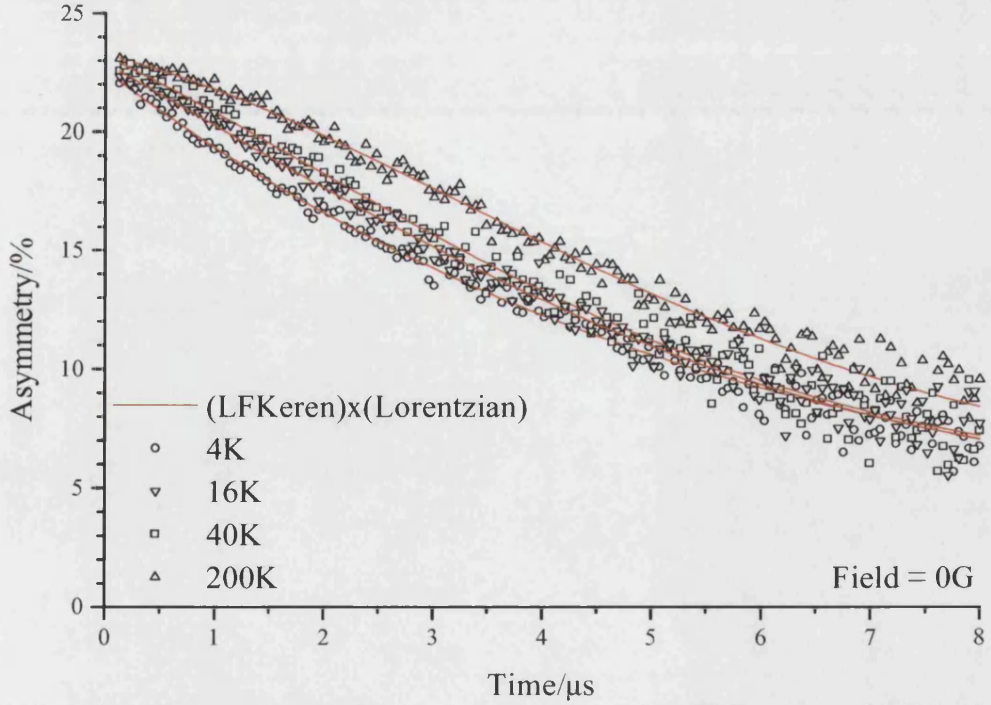

Figure 6.4 – Time-evolution of muon depolarisation in $Li_{0.55}V_2O_5$, at zero-field, fitted with the product of LF-Keren and Lorentzian functions.

As was found for $Li_{0.50}V_2O_5$, there are no oscillations observed in zero-field μSR data for $Li_{0.55}V_2O_5$ (*figure 6.4*). Again the product of LF-Keren and Lorentzian functions gives a good fit to the data at zero-field, and the application of a small longitudinal field results in rapid quenching of muon depolarisation (*figure 6.5*) indicative of static character.

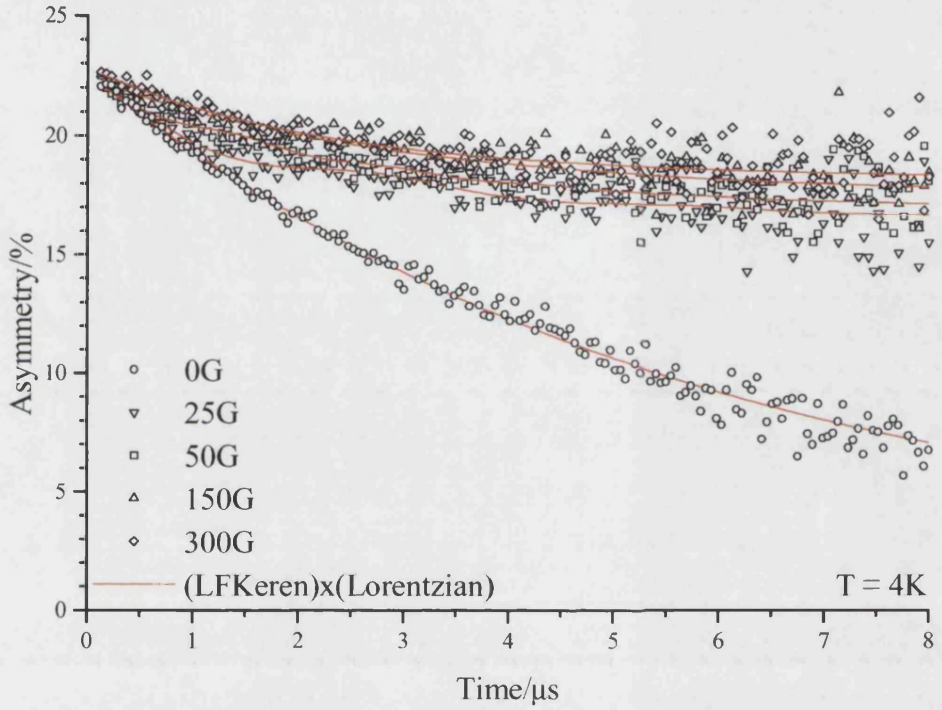

Figure 6.5 – Time-evolution of muon depolarisation in $Li_{0.55}V_2O_5$, with variation in longitudinal field, fitted with the product of LF-Keren and Lorentzian functions.

The nuclear relaxation rate, δ, due to the V^{5+} ions present, becomes very small when a longitudinal field is applied, and data are dominated by the electronic relaxation rate, λ. Zero-field relaxation rates differ in value from those obtained for $Li_{0.50}V_2O_5$, however the same pattern of decreasing nuclear relaxation and increasing electronic relaxation rate with decreasing temperature is observed (*figure 6.6*). The susceptibility maximum observed at approximately 28K coincides with the gradual increase in electronic and decrease in nuclear relaxation rates.

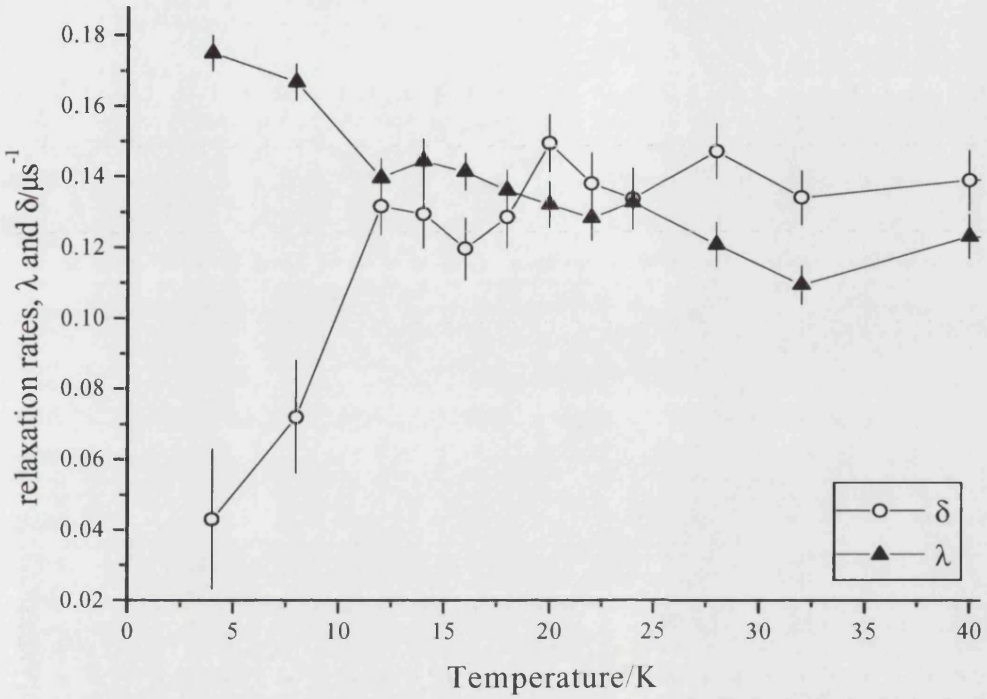

Figure 6.6 – Variation of relaxation rates with temperature in zero-field experiments for $Li_{0.55}V_2O_5$. The solid lines provide a guide for the eye.

6.4 $Li_{0.64}V_2O_5$

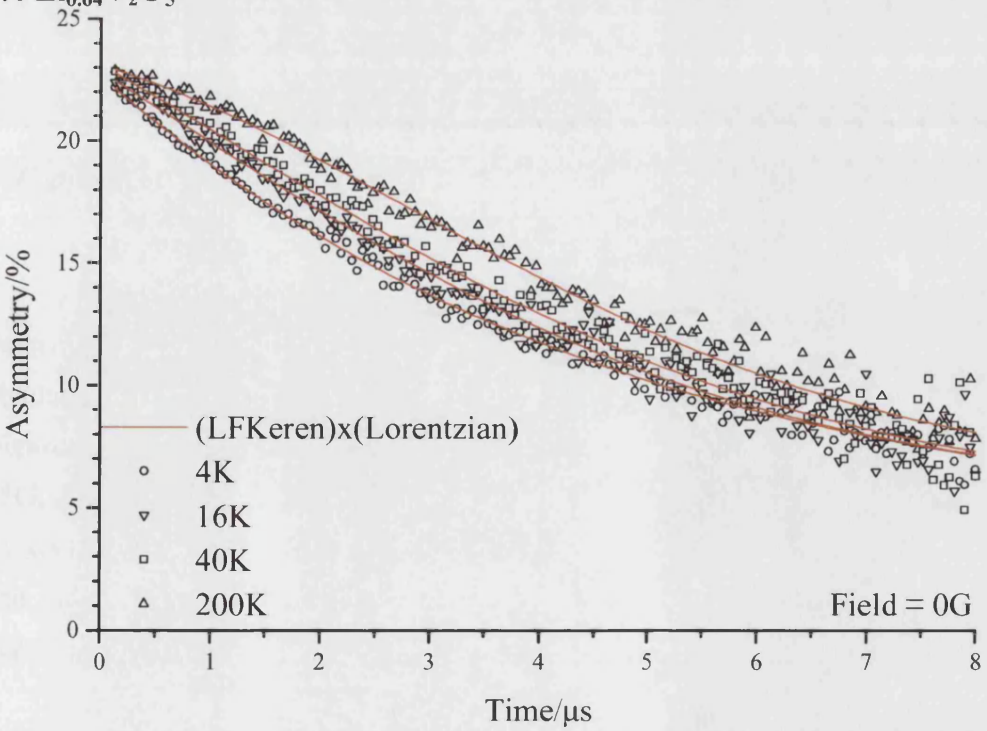

Figure 6.7 – Time-evolution of muon depolarisation in $Li_{0.64}V_2O_5$, at zero-field, fitted with the product of LF-Keren and Lorentzian functions.

Like the lower lithium content phases, no oscillations are observed in zero-field μSR data for $Li_{0.64}V_2O_5$ indicating the absence of long-range magnetic ordering in this compound (*figure 6.8*). The data are well-fitted by a product of LF-Keren and Lorentzian functions, representative of the nuclear dipole contribution of V^{5+} ions and the electronic spin-lattice relaxation of V^{4+}, s = ½ ions in a single volume fraction.

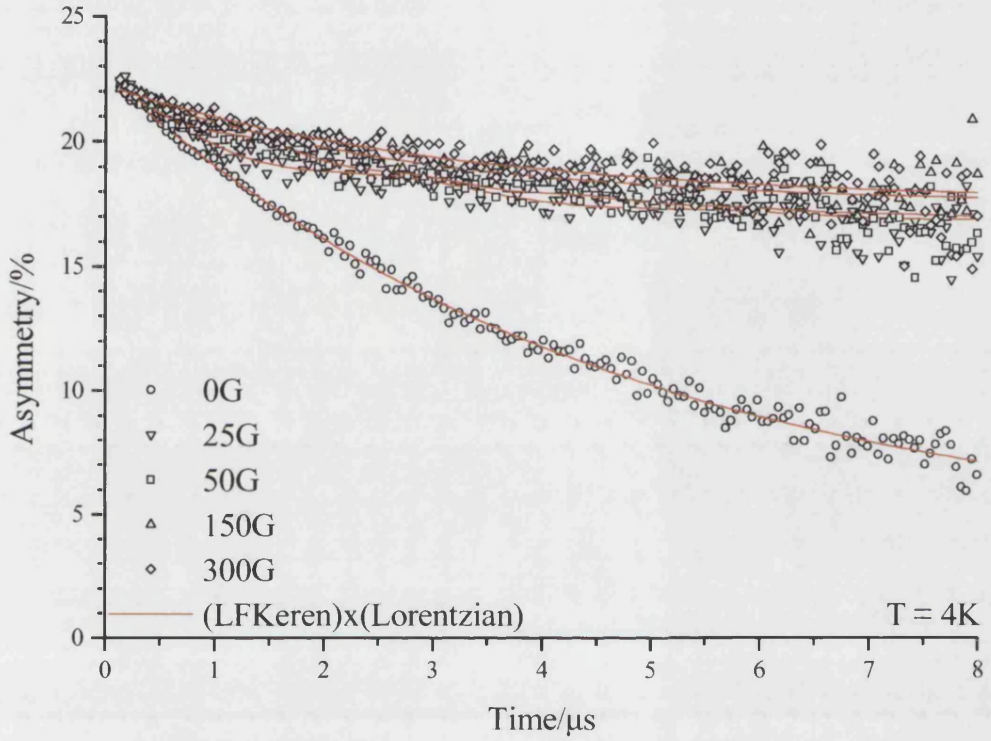

Figure 6.8 – Time-evolution of muon depolarisation in $Li_{0.64}V_2O_5$, with variation in longitudinal field, fitted with the product of LF-Keren and Lorentzian functions.

The anomalies observed in susceptibility measurements for this compound, described in chapter six are not reflected in the μSR data at first glance. Similar data are obtained and can be well fitted by the same model as for lower lithium content phases (*figure 6.8-9*). Rapid quenching occurs on application of a small longitudinal field of 25G, with a drop in nuclear relaxation rate, δ, as previously observed for $Li_{0.50}V_2O_5$ and $Li_{0.55}V_2O_5$. As the temperature is reduced there is a decrease in nuclear relaxation rate and increase in electronic relaxation rate, slowly at first and more markedly below approximately 15K (*figure 6.9*).

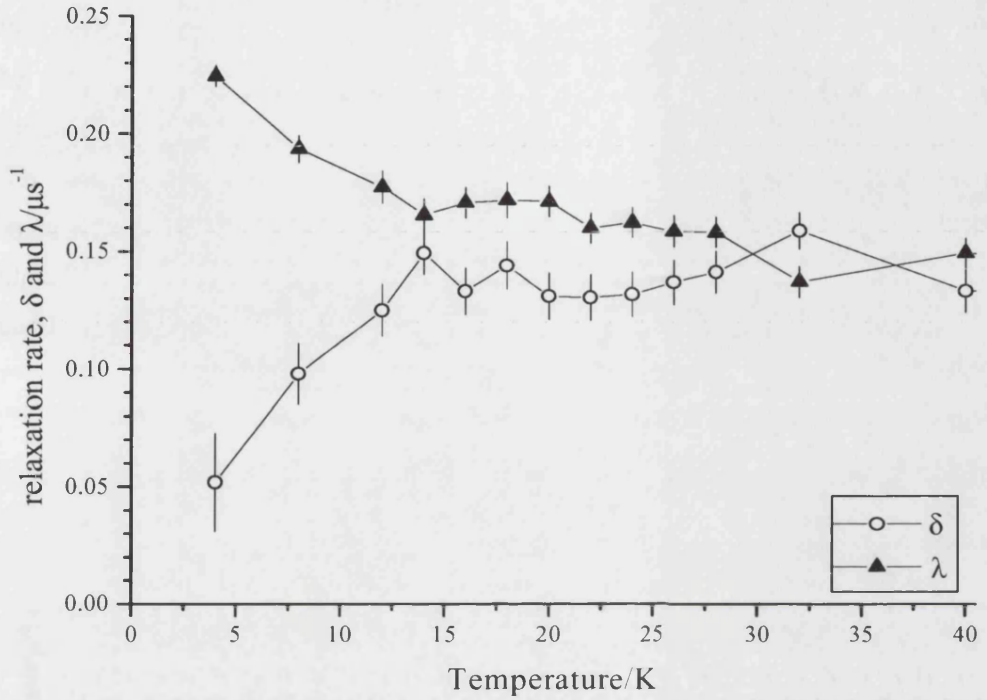

Figure 6.9 – Variation of relaxation rates with temperature in zero-field experiments for $Li_{0.64}V_2O_5$. The solid lines provide a guide for the eye.

6.5 $Li_{0.72}V_2O_5$

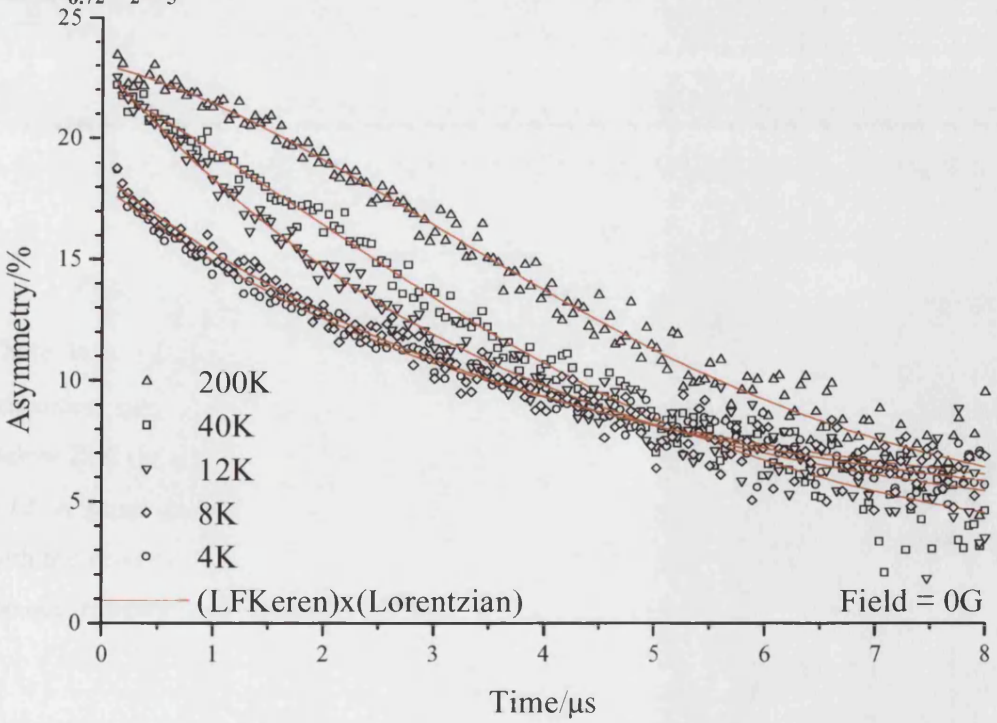

Figure 6.10 – Time-evolution of muon depolarisation in $Li_{0.72}V_2O_5$, at zero-field, fitted with the product of LF-Keren and Lorentzian functions

μSR data collected on $Li_{0.72}V_2O_5$ show some differences in magnetic behaviour from the previous compounds. Although there are still no oscillations supportive of the presence of long-range magnetic ordering, zero-field data change significantly between 12K and 8K, as shown in *figure 6.10*, where a considerable drop in the initial asymmetry value is observed. *Figure 6.11* shows the variation in initial asymmetry with lithium content and temperature; the abrupt reduction in asymmetry for $Li_{0.72}V_2O_5$ is readily apparent.

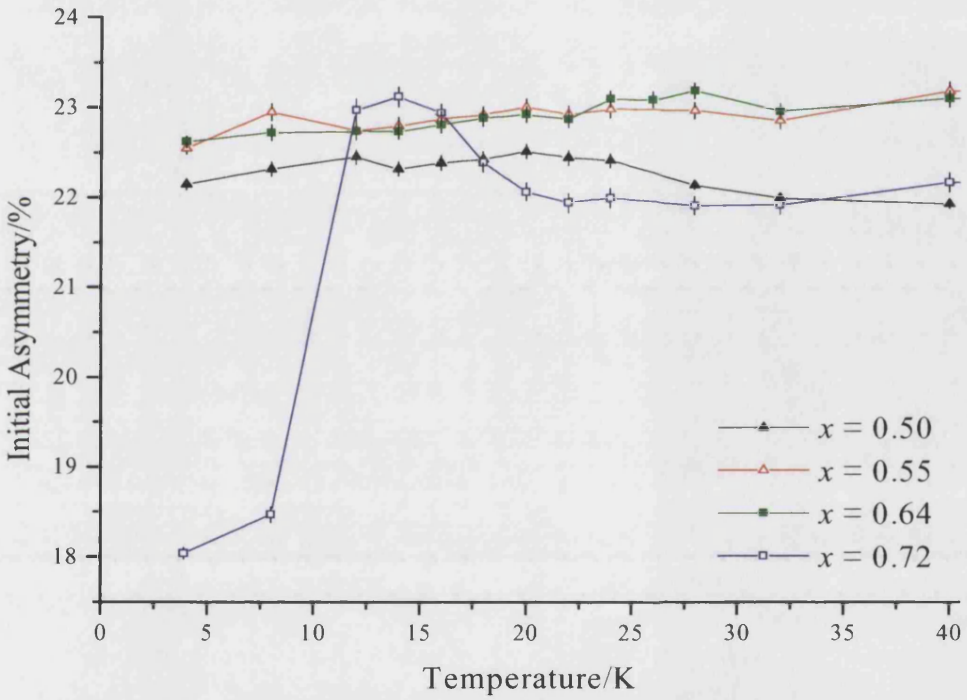

Figure 6.11 – Temperature variation of the initial asymmetry in $Li_xV_2O_5$.

There is a slow decrease in nuclear relaxation rate, δ, and increase in electronic relaxation rate, λ, as the temperature is reduced from 200K to approximately 28K. Below 28K the changes in relaxation rates become more significant, as shown in *figure 6.12*. A small peak is apparent in the electronic relaxation rate, λ, at 12K, coincident with the drop in initial asymmetry observed at this temperature. This is consistent with the occurrence of a static magnetic transition at this temperature.

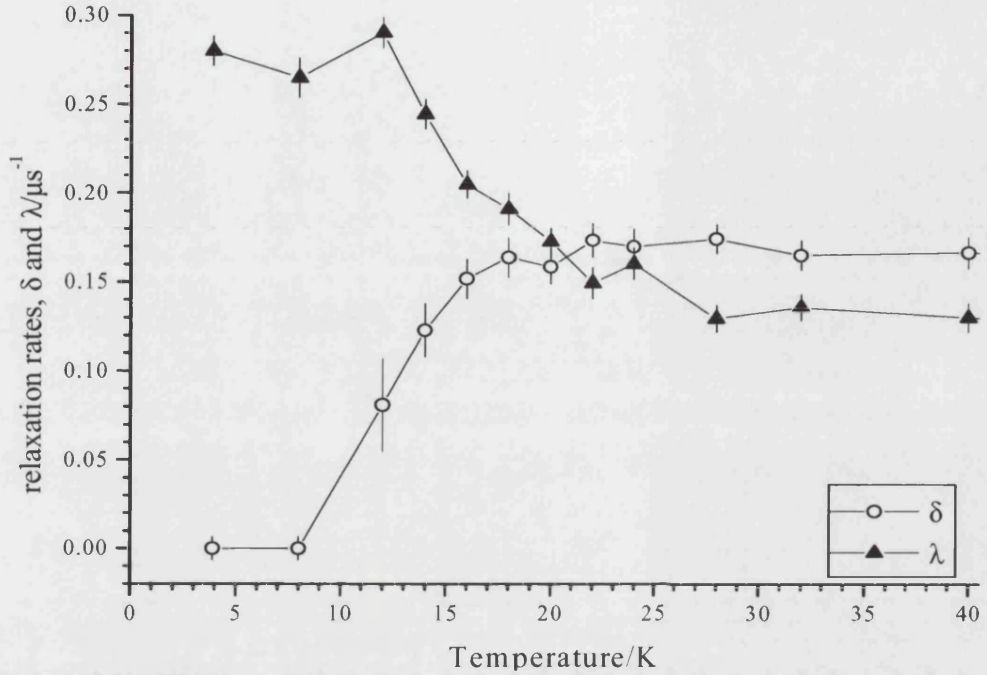

Figure 6.12 – Variation of relaxation rates with temperature in zero-field experiments for $Li_{0.72}V_2O_5$. The solid lines provide a guide for the eye.

Longitudinal field experiments do not show any significant differences from the lower lithium content compounds: rapid quenching of the muon depolarisation occurs, well modelled by the product of LF-Keren and Lorentzian functions (*figure 6.13*).

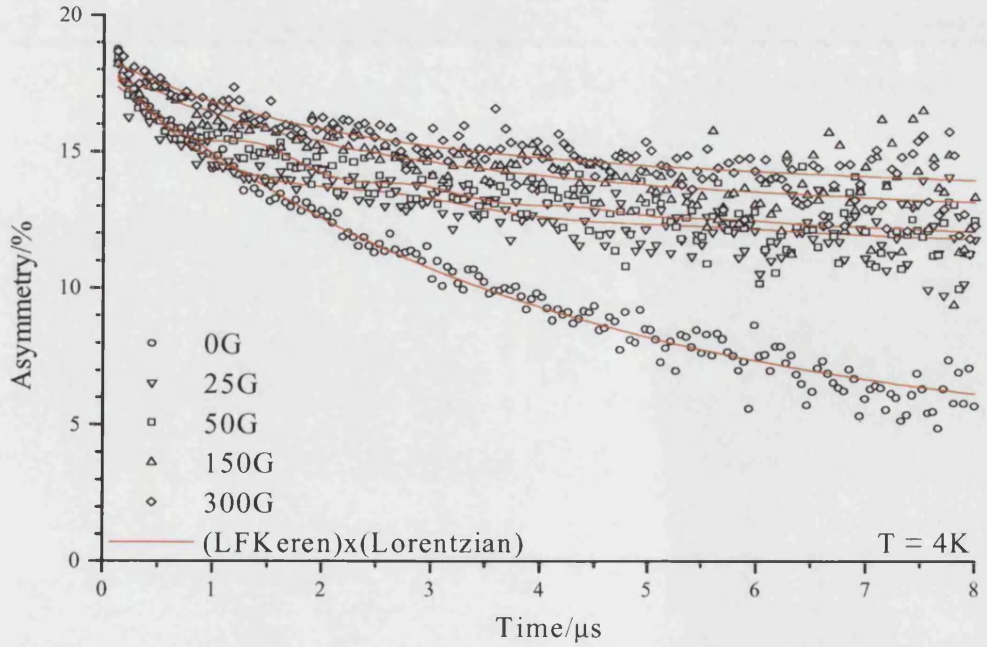

Figure 6.13 – Time-evolution of muon depolarisation in $Li_{0.72}V_2O_5$, with variation in longitudinal field, fitted with the product of LF-Keren and Lorentzian functions.

6.6 General Trends

No oscillating signal supporting the occurrence of long-range antiferromagnetic order is seen at any temperature in zero-field μSR data of $Li_xV_2O_5$. The μSR spectra for all compositions were best fitted by the double relaxation function:

$$P_\mu(t) = \exp(-\lambda t) P_\mu(t)^K (B, \omega_C, \langle \Delta h^2 \rangle)$$

where the first term describes the spin-lattice relaxation and the second is the Keren analytical approximation of the Kubo-Toyabe function [14]. The physical origin of this muon spin relaxation rests on arguments of coexisting relaxation mechanisms in the same sample volume [11]: electronic moments on V^{4+} act as an independent channel of depolarisation in addition to dipolar fields arising from the randomly frozen nuclear spins of V^{5+} ions.

Relaxation rates for different doping levels of lithium are compared in *figure 6.14* and *figure 6.15*. $Li_xV_2O_5$ compounds show an overall increase in electronic relaxation rate, λ, as the lithium content is increased, and as the temperature is reduced, while the nuclear relaxation rates, initially of similar magnitude for all the compounds studied, decrease as the temperature is reduced.

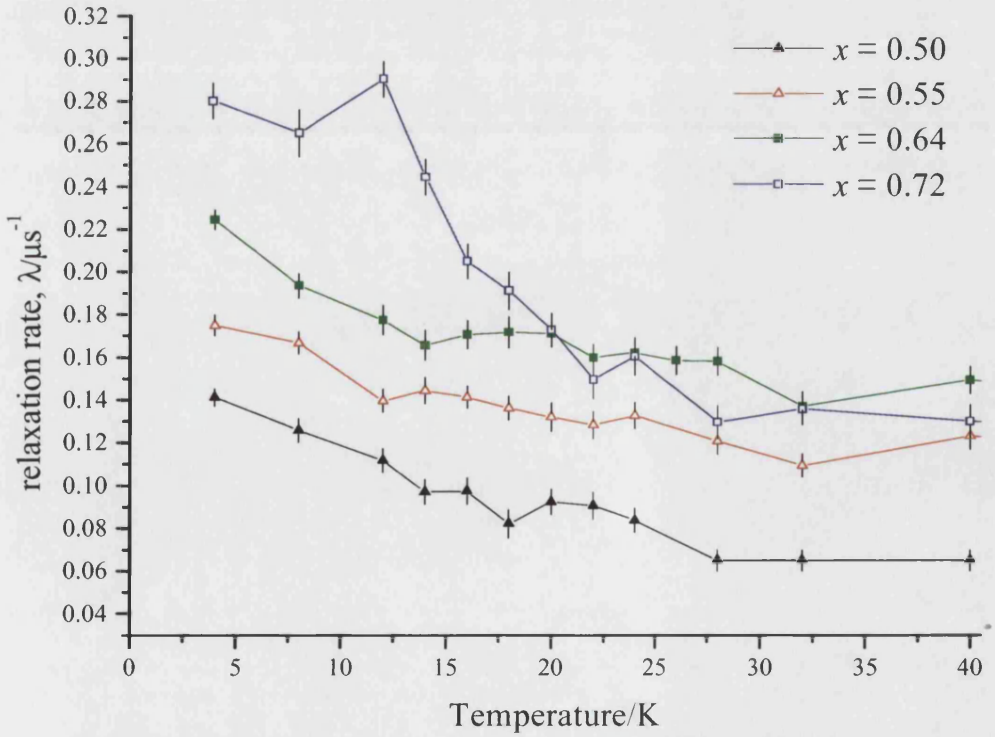

Figure 6.14 – Temperature variation of the ZF relaxation rate, λ, in $Li_xV_2O_5$.

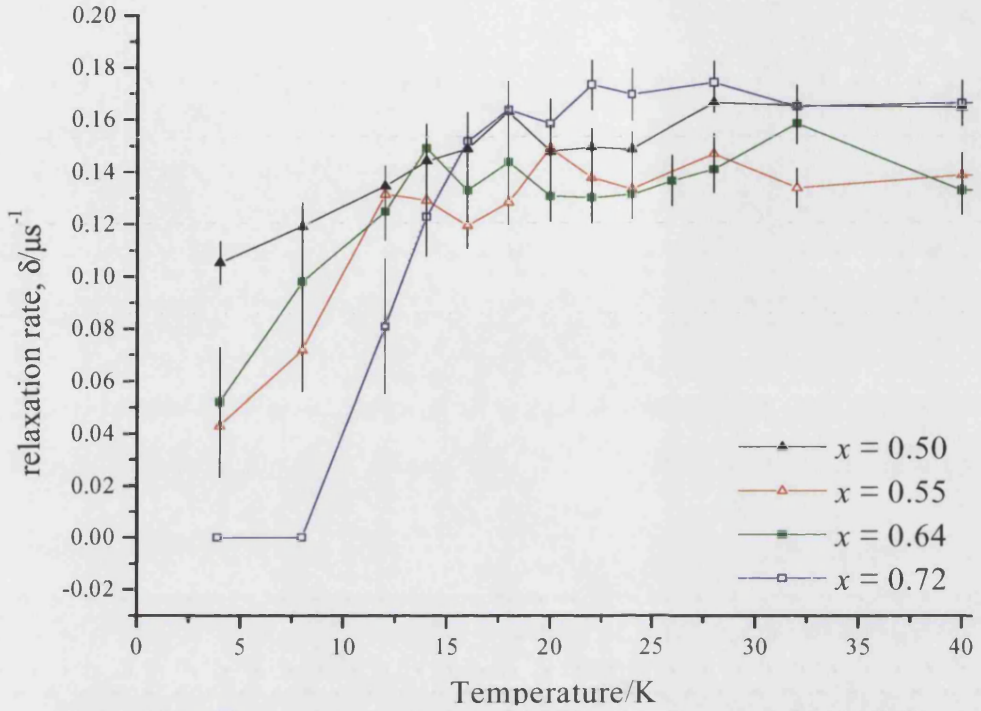

Figure 6.15 – Temperature variation of the ZF relaxation rate, δ, in $Li_xV_2O_5$.

The increase in electronic relaxation rate observed below approximately 25-30K in $Li_xV_2O_5$ could be attributed to either fluctuating and/or static internal fields. Longitudinal field experiments can distinguish between these two possibilities, allowing depolarisation due to dynamic or fluctuating components to be decoupled from that due to static contributions [12]. Longitudinal field experiments on $Li_xV_2O_5$ show rapid quenching of the muon depolarisation, indicating the increase in electronic relaxation rate, λ, is due to static internal fields. The nuclear relaxation rates drop rapidly when a longitudinal field is applied, and the electronic relaxation rates increase to compensate. An increase in λ on application of a longitudinal field, and further increase as the field is increased is unexpected, and seems to suggest either a broader field distribution, or faster fluctuation of the electronic moments in the higher fields.

1. S.J. Blundell, *Contemporary Physics,* **40,** 175-192 (1999).

2. N. Buettgen, A. Krimmel, A. Loidl, M. Klemm, S. Horn, D.R. Noakes, E. Schreier, and G.M. Kalvius, *Physica B,* **312-313,** 703-705 (2002).

3. R.I. Bewley, S.J. Blundell, B.W. Lovett, T. Jestaedt, F.L. Pratt, K.H. Chow, W. Hayes, P.D. Battle, M.A. Green, J.E. Millburn, M.J. Rosseinsky, L.E. Spring, and J.F. Vente, *Phys. Rev. B,* **60,** 12286-12293 (1999).
4. K. Kojima, A. Keren, G.M. Luke, B. Nachumi, W.D. Wu, Y.J. Uemura, M. Azuma, and M. Takano, *Phys. Rev. Lett.,* **74,** 2812 (1995).
5. H.H. Klauss, D. Baabe, D. Mienert, M. Birke, H. Luetkens, F.J. Litterst, M. Huecker, B. Buechner, and S.W. Cheong, *Hyperfine Interactions,* **136-137,** 711-715 (2001).
6. I. Watanabe, A. Adachi, S. Yairi, Y. Koike, and K. Nagamine, *Physica B,* **326,** 305-311 (2003).
7. T. Adachi, I. Watanabe, S. Yairi, K. Takahashi, Y. Koike, and K. Nagamine, *J. Low Temp. Phys.,* **131,** 843-847 (2003).
8. R. Kadono, W. Higemoto, A. Koda, M.I. Larkin, G.M. Luke, A.T. Savici, Y.J. Uemura, K.M. Kojima, T. Okamoto, T. Kakeshita, S. Uchida, T. Ito, and K. Oka, *Physica C,* **388-389,** 631-632 (2003).
9. H. Goka, K. Kubo, T. Uefuji, M. Fujita, K. Yamada, M. Matsuda, I. Watanabe, and K. Nagamine, *Physica C,* **378-381,** 390-394 (2002).
10. T. Jestaedt, K.H. Chow, S.J. Blundell, W. Hayes, F.L. Pratt, B.W. Lovett, M.A. Green, J.E. Millburn, and M.J. Rosseinsky, *Phys. Rev. B,* **59,** 3775-3782 (1999).
11. A. Lappas, J.E.L. Waldron, M.A. Green, and K. Prassides, *Phys. Rev. B,* **65,** 134405 (2002).
12. D. Arcon, A. Lappas, S. Margadonna, K. Prassides, E. Ribera, J. Veciana, C. Rovira, R.T. Henriques, and M. Almeida, *Phys. Rev. B,* **60,** 4191-4194 (1999).
13. P. Carretta, R. Melzi, N. Papinutto, and P. Millet, *Phys. Rev. Lett.,* **88,** 047601(4) (2002).
14. A. Keren, *Phys. Rev. B,* **50,** 10039-10042 (1994).

Chapter Seven

Conclusions

As the amount of lithium intercalated into the host layers is increased, there are gradual changes in structure and magnetic behaviour, described and discussed in detail in chapters 4, 5 and 6.

Structurally, there is a decrease in cell width, increase in layer separation, and increase in puckering angle within each phase as more lithium is intercalated; in other words, distortion in the host layers increases as more guest molecules are introduced. The change in lithium coordination between phases allows an initial decrease in distortion, well demonstrated by comparison of α and ε phases: although less stable for lithium, the larger eight-coordinated site observed in the ε phase causes less distortion to the host layers. The puckering angle in ε' phases is comparable to that observed in α phases, and increases with lithium content up to the mixed ε'/δ phase region, where shifting of the V_2O_5 layers along the cell depth axis occurs, allowing lithium to be in its preferred six-coordinated state, with more favourable lithium-oxygen distances. Thus we conclude that for low lithium content, it is energetically favourable to have a relatively unstable lithium site within less distorted host lattice layers. However, as the lithium content increases, the energy cost of distortions in the host lattice is outweighed by the stability of the lithium site and the structure is thus driven ultimately towards a layer shift enabling more stable coordination of lithium.

The magnetic susceptibility of the series shows a gradual development of magnetic behaviour: from paramagnetic, through a region of low-dimensional antiferromagnetic correlation, towards metallic behaviour as lithium content increases. Throughout the series there is good agreement between predicted and observed magnetic moments, and Curie constants obtained experimentally give values of lithium content that agree well with those obtained from diffraction data and elemental analysis. There is a gradual increase in Weiss constant and therefore the degree of antiferromagnetic interactions as the lithium content, and therefore number of V^{4+} ions, is increased. Where $x > 0.42$ the lithium content is high enough to support low dimensional magnetic correlation, where the single chain Bonner-Fisher model is preferred. The lack of an oscillating signal at any temperature in zero-field μSR data of $Li_xV_2O_5$, gives conclusive evidence that the feature observed between 25-30K in the susceptibility data for compositions with $x > 0.42$ is not due to the occurrence of long-range antiferromagnetic order, but may be assigned to shorter-range antiferromagnetic correlations.

For certain compositions, such as $x = 0.50$ and $x = 0.64$, the feature at approximately 25K was clearly better defined. The latter composition is very close to $x = 0.67$, that is a 1:2 ratio of V^{4+}:V^{5+} ions, while the former, at a ratio of 1:3, can also be thought of as a "magic" number, where the association of other factors with disorder causing the broadening of this feature were not observed. This is heavily linked with the observation of V^{4+} ion ordering, facilitating a more ordered exchange scheme: high-resolution x-ray diffraction revealed the occurrence of incommensurate charge ordering of vanadium ions for these compositions. We can conclude therefore that charge ordering is implicit in the occurrence of well-defined features in the susceptibility of these compounds: previous work carried out on the dimer chain compound γ-LiV_2O_5 has asserted there to be charge ordering within that structure and within analogous structures such as the quarter-filled spin ladder system α'-NaV_2O_5.

Appendix One

Microstructure Effects

Lithium Composition x	Phase	Space Group	T/K	S_{400}	S_{004}	S_{112}
0.13	α	$Pmn2_1$	295	-0.00045(1)	-0.24276(1)	0.00684(1)
0.33	α	$Pmn2_1$	295	0.0438(57)	-0.66(13)	-0.05(15)
0.33	ε	Pmmn	295	-0.00020(1)	0.01700(1)	-0.01664(1)
0.33	α	$Pmn2_1$	40	0.04340(98)	-1.96(27)	-0.02(30)
0.33	ε	Pmmn	40	-0.00020(1)	0.01701(1)	-0.01664(1)
0.42	ε	Pmmn	295	-0.00020(1)	0.01699(1)	-0.01664(1)
0.50	ε	Pmmn	295	-0.00020(1)	0.01699(1)	-0.01664(1)
0.50	ε	Pmmn	200	-0.00020(1)	0.01699(1)	-0.01664(1)
0.50	ε	Pmmn	50	-0.00020(1)	0.01699(1)	-0.01664(1)
0.50	ε	Pmmn	15	-0.00020(1)	0.01699(1)	-0.01664(1)
0.55	ε'	Pmmn	295	-0.00020(1)	0.01700(1)	-0.01664(1)
0.55	ε'	Pmmn	50	0	0	0
0.55	ε'	$P2_1/m$	50	-0.00028(1)	-0.24266(1)	0.00647(1)
0.64	ε'	Pmmn	295	-0.00020(1)	0.01701(1)	-0.01664(1)
0.64	ε'	Pmmn	50	0	0	0
0.64	ε'	$P2_1/m$	50	-0.00028(1)	-0.24266(1)	0.00647(1)
0.64	ε'	Pmmn	30	0	0	0
0.64	ε'	$P2_1/m$	30	-0.00028(1)	-0.24266(1)	0.00647(1)
0.72	ε'	$Pmn2_1$	295	0	-0.25845(1)	-0.04561(1)
0.72	δ	Cmcm	295	0	0	0
0.95	ε'	Pmmn	295	-0.00020(1)	0.01699(1)	-0.01664(1)
0.95	δ	Cmcm	295	0	0	0

Table A1.1 – Comparison of strain coefficients with variable lithium composition.

x	Space Group	T/K	$\alpha_1 \times 10^3$	$\alpha_2 \times 10^3$	$\alpha_3 \times 10^3$	$\alpha_4 \times 10^3$	$\alpha_5 \times 10^3$	$\alpha_6 \times 10^3$
0.13	$Pmn2_1$	295	-1.4(1)	-9.8(3)	-13.1(4)	9.7(5)	-0.9(2)	4.8(2)
0.33	$Pmn2_1$	295	-72(1)	11(6)	-211(9)	37(9)	38(4)	55(4)
0.33	Pmmn	295	1.5(1)	21.5(9)	18.1(4)	12.8(8)	4.3(2)	-0.7(3)
0.33	$Pmn2_1$	40	-51.9(1)	23.6(1)	-233(1)	42.6(1)	40.3(1)	45.9(1)
0.33	Pmmn	40	-1.1(1)	-22.3(8)	32.1(6)	27(1)	3.1(3)	0.3(3)
0.42	Pmmn	295	-1.6(1)	-21.3(7)	10.6(4)	15.1(7)	4.4(2)	-0.2(2)
0.50	Pmmn	295	-1.7(1)	-21.8(6)	12.2(3)	15.4(6)	5.0(2)	-0.1(2)
0.50	Pmmn	200	-2.4(13)	-27(14)	5.2(86)	21.6(7)	5.6(2)	-0.5(2)
0.50	Pmmn	50	-1.4(1)	-18.0(8)	13.5(4)	20.6(9)	5.2(3)	-1.1(3)
0.50	Pmmn	15	-1.4(1)	-18.1(8)	13.5(4)	20.8(8)	5.3(3)	-0.7(3)
0.55	Pmmn	295	-2.2(1)	-23.7(8)	3.5(4)	388(6)	3.7(3)	-1.4(3)
0.55	Pmmn	50	-2.0(1)	-20.8(9)	12.0(6)	1233(24)	4.9(3)	-2.1(3)
0.55	$P2_1/m$	50	-58(9)	-16(1)	279(29)	45(6)	-13(9)	13(3)
0.64	Pmmn	295	-1.8(1)	-21.2(8)	10.3(4)	343(5)	5.4(3)	-1.8(3)
0.64	Pmmn	50	-1.6(1)	19.2(9)	23(1)	1477(60)	12.7(6)	-1.9(4)
0.64	$P2_1/m$	50	-82(4)	-14.8(4)	382(19)	46(4)	55(9)	2.1(15)
0.64	Pmmn	30	-2.4(1)	-32(1)	5.4(11)	1950(73)	8.9(6)	-2.8(6)
0.64	$P2_1/m$	30	-27(3)	-12.0(4)	-65(5)	-17(2)	-9(3)	3(1)
0.72	$Pmn2_1$	295	-0.9(1)	10.1(5)	-18(1)	27(1)	-2.8(5)	4.1(4)
0.72	Cmcm	295	-55(3)	0.5(2)	-3.8(2)	2.6(3)	-7.9(1)	48(2)
0.95	Pmmn	295	-27(14)	-98(6)	262(54)	9289(548)	-82(9)	725(35)
0.95	Cmcm	295	-111(2)	-0.9(3)	-8.4(5)	1.6(2)	-2.6(7)	58(1)

Table A1.2 – Comparison of size coefficients with variable lithium composition.